

Fall 12-15-2023

Floating Offshore-wind and Controls Advanced Laboratory Program: 1:70-scale Testing of a 15 Mw Floating Wind Turbine

Matthew J. Fowler
University of Maine, matthew.fowler@maine.edu

Follow this and additional works at: <https://digitalcommons.library.umaine.edu/etd>



Part of the [Ocean Engineering Commons](#)

Recommended Citation

Fowler, Matthew J., "Floating Offshore-wind and Controls Advanced Laboratory Program: 1:70-scale Testing of a 15 Mw Floating Wind Turbine" (2023). *Electronic Theses and Dissertations*. 3903.
<https://digitalcommons.library.umaine.edu/etd/3903>

This Open-Access Dissertation is brought to you for free and open access by DigitalCommons@UMaine. It has been accepted for inclusion in Electronic Theses and Dissertations by an authorized administrator of DigitalCommons@UMaine. For more information, please contact um.library.technical.services@maine.edu.

THE FLOATING OFFSHORE-WIND AND CONTROLS ADVANCED LABORATORY

PROGRAM: 1:70-SCALE TESTING OF A 15 MW FLOATING WIND TURBINE

By

Matthew John Lombard Fowler

BS, University of Maine, 2009

M.A. University of Maine, 2014

M.B.A. University of Maine, 2018

A DISSERTATION

Submitted in Partial Fulfillment of the

Requirements for the Degree of

Doctor of Philosophy

(in Mechanical Engineering)

The Graduate School

The University of Maine

December 2023

Advisory Committee:

Andrew J. Goupee, Donald A. Grant Associate Professor of Mechanical Engineering, Co-advisor

Richard W. Kimball, Presidential Professor in Ocean Engineering and Energy, Co-advisor

Anthony M. Viselli, Assistant Director and Chief Engineer, Ocean Energy and Engineering, Advanced Structures and Composites Center

Amrit S. Verma, Assistant Professor of Mechanical Engineering

Todd Griffith, Associate Professor of Mechanical Engineering, University of Texas-Dallas

UNIVERSITY OF MAINE GRADUATE SCHOOL LAND ACKNOWLEDGMENT

The University of Maine recognizes that it is located on Marsh Island in the homeland of Penobscot people, where issues of water and territorial rights, and encroachment upon sacred sites, are ongoing. Penobscot homeland is connected to the other Wabanaki Tribal Nations—the Passamaquoddy, Maliseet, and Micmac—through kinship, alliances, and diplomacy. The University also recognizes that the Penobscot Nation and the other Wabanaki Tribal Nations are distinct, sovereign, legal and political entities with their own powers of self-governance and self-determination.

**THE FLOATING OFFSHORE-WIND AND CONTROLS ADVANCED LABORATORY
PROGRAM: 1:70-SCALE TESTING OF A 15 MW FLOATING WIND TURBINE**

By Matthew John Lombard Fowler

Dissertation Advisors: Dr. Andrew Goupee and Dr. Richard Kimball

An Abstract of the Dissertation Presented
in Partial Fulfillment of the Requirements for the
Degree of Doctor of Philosophy
(in Mechanical Engineering)
December 2023

This thesis presents results from the Floating Offshore-wind and Controls Advanced Laboratory (FOCAL) Experiment which performed 1:70-scale model testing of a 15 mega-watt floating offshore wind turbine (FOWT) at the University of Maine's Alfond Wind/Wave Ocean Engineering Laboratory (W2). The experimental campaigns supported the application of controls co-design to FOWTs by incorporating real-time wind turbine control and hull mounted tuned-mass damper (TMD) elements. A performance-matched scaling strategy was proposed and analysis in OpenFAST performed to design the scale models, including integration of the Reference OpenSource Controller (ROSCO) and modeling of the TMDs in the hull. Four test campaigns were conducted, first characterizing the performance of the turbine and hull separately in wind and wave only environments, respectively. The combined system was then characterized in wind and wave environments, investigating effects of control strategies such as thrust peak shaving, floating feedback, and different TMD frequencies. Data were collected and used to validate OpenFAST models developed by the FOCAL team as well as mid- and high-fidelity tools developed by other ATLANTIS teams.

Key outcomes consisted of demonstrating the ability to tune ROSCO and control the scale model turbine and investigating the impacts of ROSCO on system behavior, including attenuation of platform pitch

motion and tower base bending moments in response to the thrust peak shaving and floating feedback control. The TMDs demonstrated effective attenuation of platform pitch and tower bending moments at their respective resonant frequencies, as well as synergistic performance when combined with ROSCO's floating feedback control. These findings identified opportunities for further optimization of FOWT systems through controls co-design and areas of future work to advance ROSCO and scale model testing of FOWTs with controls. Three datasets were generated and uploaded to the Atmosphere to Electrons portal including time history data, technical reports describing the experimental setup and test articles, and numerical models in Bladed and OpenFAST. Ten publications from the FOCAL team describe the design of the scale model, results of the numerical model validation, and discussion of the experimental results including the effects of ROSCO and TMDs on the performance of the floating wind turbine system.

DEDICATION

To my wife, Rachel, who has supported me tirelessly through this transformational journey, and my daughters Tera and Ivy who remind me what is most important in life.

ACKNOWLEDGEMENTS

I would like to acknowledge contributions of the staff and students at the University of Maine's Alfond Ocean Engineering Laboratory. Their innovation and hard work were essential to completing the FOCAL experimental program, especially during the extraordinarily difficult conditions conducting work during the COVID-19 pandemic. Significant contributions from graduate students Amber Parker and Mitchell York were definitive in the design and construction of the scale model turbine and hull, respectively, and are gratefully acknowledged. I am especially grateful for the guidance and insight from my co-advisors Dr. Andrew Goupee and Dr. Richard Kimball who have performed foundational work in floating offshore wind research and provided much needed support as I developed and managed this program over its near four-year duration. I also want to acknowledge the work of Eben Lenfest in processing and analyzing the dataset, Casey Bourque in construction of the model turbine, Mike DiBona and Matt Cameron for designing and building the model hull, and Nate Faessler for helping organize the testing and manage day to day operations. This work required the coordinated efforts of this team, and the contributions of each member are gratefully acknowledged.

I would also like to thank Dr. Amy Robertson for managing the program and interfacing with the sponsor, as well as leading the team from NREL. I gratefully acknowledge the expertise provided by Dr. Alan Wright, Dr. Nikhar Abbas, and Dr. Daniel Zalkind in understanding ROSCO and the work of Dr. Nicole Mendoza, Roger Bergua, and Dr. Lu Wang in validating numerical models and publishing results. It has been a humbling and inspiring opportunity to work with this team of experts and I am grateful for the connections I have made.

The FOCAL program was executed in part by the University of Maine for the U.S. Department of Energy under Award No. DE-AR0001183. Funding provided by the U.S. Department of Energy Advanced

Research Projects Agency-Energy under the Aero-dynamic Turbines, Lighter and Afloat, with Nautical Technologies and Integrated Servo-control program is gratefully acknowledged.

TABLE OF CONTENTS

DEDICATION	iv
ACKNOWLEDGEMENTS	v
LIST OF TABLES	xiii
LIST OF FIGURES.....	xvii
Chapter 1	
1. INTRODUCTION	1
1.1. Executive Summary.....	1
1.2. Background.....	4
1.3. Research Objectives	8
1.4. Scale Model Testing Methodologies	11
1.5. Outline	15
Chapter 2	
2. CAMPAIGN 1: WIND ONLY TURBINE TESTING.....	17
2.1. Research Objectives.....	17
2.2. Methodology	18
2.2.1. Full-Scale Design.....	18
2.2.2. Scaling Approach.....	19
2.2.3. Water Density Mismatch	23
2.2.4. Wind Speed Adjustment	24
2.2.5. Model Turbine Design	25
2.2.6. Model Rotor and Nacelle Construction	32

2.2.7. Controller Design.....	37
2.3. Experiment Setup.....	42
2.3.1. Initial Wind Surveys	42
2.3.2. Wind Conditions	46
2.3.3. Calibrated Environments	50
2.3.4. Test Matrix.....	52
2.4. Results and Discussion	55
2.4.1. Steady-State Performance and Performance-Matching	55
2.4.2. Turbine Performance Under ROSCO Control	62
2.5. Conclusions	66
Chapter 3	
3. CAMPAIGNS 2 AND 3: WAVE ONLY HULL AND TMD TESTING	69
3.1. Research Objectives.....	69
3.2. Design Methodology.....	70
3.2.1. Full-Scale Design.....	71
3.2.2. Scaling Methodology	72
3.2.3. Turbine Scaling Methodology	72
3.2.4. TMD Design	73
3.3. Model Design.....	78
3.3.1. System Overview	80
3.3.2. Hull Design	80
3.3.3. Hull Properties	82
3.3.4. Internal Load Measurement	82
3.3.5. Tower Properties.....	83

3.3.6. Mooring Properties	84
3.3.7. RNA Properties.....	86
3.3.8. TMD Structural Design.....	87
3.4. Experimental Setup.....	89
3.4.1. Orientation and Coordinate Systems.....	89
3.4.2. Wave Measurement Locations.....	91
3.4.3. Tuned Mass Dampers	92
3.5. Instrumentation and Data Acquisition	93
3.5.1. Instrumentation	93
3.5.2. Sample Rates.....	95
3.6. Test Program.....	95
3.6.1. Wind Conditions	95
3.6.2. Wave Conditions.....	96
3.6.3. Calibrated Environments	97
3.6.4. Test Matrices.....	99
3.7. System Characterization	101
3.7.1. System Natural Frequencies	101
3.7.2. Tower Frequency	101
3.7.3. TMD Characterization	102
3.8. Results	114
3.8.1. System Characterization	115
3.8.2. Load Cases.....	117
3.8.3. Internal Load Measurements.....	120

3.9. Conclusions.....	120
Chapter 4	
4. Campaign 4: Floating Turbine Wind/Wave Testing	122
4.1. Research Objectives.....	122
4.2. Airfoil Performance Tuning.....	122
4.2.1. Power And Thrust Coefficient Determination	123
4.2.2. Tuning Lift and Drag Polars	125
4.3. TMD Tuning	129
4.4. ROSCO Floating Feedback Control Tuning	130
4.5. Experimental Setup.....	132
4.5.1. Hull Properties	136
4.5.2. Tuned Mass Damper Properties.....	136
4.5.3. Mooring Properties	137
4.5.4. Tower Properties.....	139
4.5.5. RNA Properties	140
4.6. Turbine Controller	140
4.6.1. Floating Feedback.....	141
4.6.2. Peak Shaving.....	142
4.7. Instrumentation and Data Acquisition	143
4.7.1. A Note on Rotor Thrust	144
4.7.2. Internal Load Cells.....	144
4.8. Test Program	145
4.8.1. Wind Conditions	145
4.8.2. Wave Conditions.....	147

4.8.3. Test Matrices.....	150
4.9. Results	153
4.9.1. Baseline – No Load Mitigation.....	154
4.9.2. Wave Only - Effect of TMDs	155
4.9.3. Wind Only.....	156
4.9.4. Wind/Wave – DLC 1.6	158
4.9.5. Combined Effect of ROSCO and TMDs	161
4.10. Conclusions	162
Chapter 5	
5. Campaign 4 OpenFAST Simulations	164
5.1. Materials and Methods.....	164
5.1.1. Model Description	165
5.1.2. Wind Environment.....	167
5.1.3. Wave Environment	168
5.1.4. Mooring	169
5.1.5. Instrumentation	170
5.2. Results	171
5.2.1. Free Decay	171
5.2.2. Above-Rated Conditions.....	172
5.2.3. Wave Only	172
5.2.4. Wind Only.....	174
5.2.5. Combined Wind and Wave.....	176
5.3. Discussion.....	181

5.3.1. Surge Resonant Response	181
5.3.2. Effect of ROSCO Above-Rated Torque Control	182
5.3.3. Performance of Floating Feedback Control Loop.....	185
5.4. Conclusions.....	186
Chapter 6	
6. Conclusions and Future Work.....	188
6.1. Summary	188
6.2. Significant Findings	190
6.3. Challenges.....	193
6.4. Impact and Future Work	195
6.5. Publications.....	197
BIBLIOGRAPHY	199
APPENDICES	209
APPENDIX A: CAMPAIGN 1 SUPPLEMENTALS.....	209
APPENDIX B: CAMPAIGN 2/3 SUPPLEMENTALS.....	215
APPENDIX C: CAMPAIGN 4 SUPPLEMENTALS	224
BIOGRAPHY OF THE AUTHOR	228

LIST OF TABLES

Table 1.1:	Main parameters of reference turbines	9
Table 2.1:	Main parameters of the IEA Wind 15 MW RWT.....	18
Table 2.2:	Scaling parameters for Froude-scale model test campaign.....	23
Table 2.3:	Main particulars of the IEA Wind 15 MW RWT	26
Table 2.4:	As-designed distributed blade properties, 1:70 scale.....	33
Table 2.5:	As-built rotor blade properties	35
Table 2.6:	Campaign 1 instrumentation	36
Table 2.7:	Controller strategies considered for the IEA Wind 15 MW RWT.....	42
Table 2.8.	Wind shear sensitivity study, OpenFAST simulation mean responses.....	46
Table 2.9:	Wind Types.....	47
Table 2.10:	Wind Environments	48
Table 2.11:	Wind Survey statistics	50
Table 2.12:	Test Matrix.....	53
Table 3.1:	Main parameters of the VolturnUS-S reference hull	72
Table 3.2:	TMD design wave environment definitions.....	75
Table 3.3:	TMD Effects on Global Performance, Load Case DLC 1.2	77
Table 3.4:	TMD Effects on Global Performance, Load Case DLC 6.1	77
Table 3.5:	As-Built System Structural Properties – including hull, tower, dummy RNA (locations relative to centerline of structure at bottom – keel, full-scale).....	80
Table 3.6:	Hull Properties	82
Table 3.7:	Tower Properties.....	83
Table 3.8:	Fairlead and anchor locations	84

Table 3.9:	Stiffness properties of the mooring lines	85
Table 3.10:	Dummy RNA properties.....	86
Table 3.11:	Dummy RNA dimensions.....	86
Table 3.12:	Axis Definitions (x,y,z locations relative to bottom of keel center)	91
Table 3.13:	Location of wave probes and anchors (relative to O coordinate system; Full Scale)	92
Table 3.14:	Tuned Mass Damper Settings	93
Table 3.15:	Tuned Mass Damper CG locations	93
Table 3.16:	Instruments List	94
Table 3.17:	Pink noise wave properties	96
Table 3.18:	Regular wave case properties.....	96
Table 3.19:	Irregular wave case properties	97
Table 3.20:	Water Properties	97
Table 3.21:	System ID Test Matrix.....	100
Table 3.22:	Active Wave Test Matrix.....	100
Table 3.23:	As-Built System Free-Decay Properties	101
Table 3.24:	Tower Natural Frequencies.....	102
Table 3.25:	TMD characterization data	105
Table 3.26:	Full and model scale target frequencies and corresponding spring stiffness setpoint required to achieve that frequency.	107
Table 3.27:	FOCAL TMD Initial Setpoint Values.....	112
Table 3.28:	List of load cases (LCs) from (Wang et al., 2023a).....	118
Table 4.1:	As-Built System Structural Properties	135
Table 4.2:	As-Built System Free Decay Periods.....	135
Table 4.3:	Floating System Buoyancy Characteristics	135
Table 4.4:	Hull Properties	136

Table 4.5:	Tuned Mass Damper Settings	137
Table 4.6:	Tuned Mass Damper CG locations	137
Table 4.7:	Fairlead and anchor locations	138
Table 4.8:	Stiffness properties of the mooring lines	138
Table 4.9:	Tower Properties.....	139
Table 4.10:	Tower Natural Frequencies.....	139
Table 4.11:	RNA Mass Properties	140
Table 4.12:	Controller strategies for FOCAL Campaign 4.....	141
Table 4.13:	Instrumentation list	144
Table 4.14:	Wind environments.....	145
Table 4.15:	Pink noise wave properties	147
Table 4.16:	Regular wave case properties.....	147
Table 4.17:	Irregular wave case properties	148
Table 4.18:	System ID Test Matrix.....	151
Table 4.19:	“No-Umbilical” Test Matrix	151
Table 4.20:	“With-Umbilical” Test Matrix	152
Table 4.21:	Measured values - Wind only	157
Table 4.22:	Comparison of statistics for key metrics.....	160
Table 5.1:	Floating turbine system properties for OpenFAST model	166
Table 5.2:	Wave environment parameters	168
Table 5.3:	Linearized mooring stiffnesses	170
Table 5.4:	Mooring model parameters	170
Table 5.5:	Instrumentation and data channel list	170
Table 5.6:	Additional linear stiffness, linear damping, and quadratic damping terms.....	171

Table 5.7:	Natural periods for experiment and simulation.....	171
Table 5.8:	Key frequency ranges for PSD analysis.....	172
Table 5.9:	Wave-only statistics.....	174
Table 5.10:	Wind-only statistics	176
Table 5.11:	Wind/wave statistics with baseline ROSCO (RO).....	177
Table 5.12:	Wind/wave statistics comparison, effect of Floating Feedback control	180
Table 5.13:	Wind/wave PSD integral comparison, effect of Floating Feedback control.....	181
Table B.1:	Geometry of Structure	215
Table C.1:	Floating System Geometric Properties	224
Table C.2:	Umbilical Mass Properties.....	227

LIST OF FIGURES

Figure 1.1:	IEA 15 MW RWT and VolturnUS-S Full-scale Design.....	1
Figure 1.2:	FOCAL test campaigns showing the turbine (left), hull (center) and floating turbine (right).....	2
Figure 1.3:	Trends in installed turbine capacity, hub height, and rotor diameter (Musial et al., 2023).....	6
Figure 1.4:	ARPA-e ATLANTIS project areas.....	7
Figure 2.1:	IEA 15MW RWT Performance Plot.....	19
Figure 2.2:	Schematic of the W2 basin and wind machine	21
Figure 2.3:	1:70-scale model of the 15 MW turbine installed in the W2	22
Figure 2.4:	Blade Lift/Drag performance of SD7032 at various Reynolds numbers, Data (Selig, 1995) vs XFOIL	27
Figure 2.5:	Lift/Drag data for OpenFAST rotor optimization process	27
Figure 2.6:	Betz optimal rotor— turbine performance in wind speed = $1.0 \times U_{ms}$	30
Figure 2.7:	Betz optimal rotor— aerodynamic sensitivities computed in wind speed = $1.0 \times U_{ms}$	30
Figure 2.8:	Optimized design – turbine performance with 0.6 chord scale and wind speed = $1.2 \times U_{ms}$	31
Figure 2.9:	Optimized design – aerodynamic sensitivity with 0.6 chord scale and wind speed = $1.2 \times U_{ms}$	32
Figure 2.10:	Scale rotor blade manufacturing showing internal spars (top) and the completed blade (bottom).....	34
Figure 2.11:	Modified profile of SD7032 including added trailing edge thickness	34
Figure 2.12:	Instrumentation (top) and Coordinate systems (bottom). CS1 – at Tower base (not shown), CS2 – at Tower top, CS3 – Blade root, CS4 – Rotor drive shaft.....	36
Figure 2.13:	Wind turbine generator operating regions (Robertson et al., 2023).....	38

Figure 2.14:	ROSCO Control Diagram (Abbas et al., 2021)	38
Figure 2.15:	ROSCO generator control loop.....	40
Figure 2.16:	Preliminary wind survey setup.....	43
Figure 2.17:	Initial wind survey, vertical cut. Power law uses an exponent of 0.11	44
Figure 2.18:	Wind field representations, survey data (left) and horizontally averaged (right)	45
Figure 2.19:	Operating ranges of the IEA Wind 15 MW Reference Turbine	47
Figure 2.20:	Wind Survey for TR1 wind case showing spatial uniformity. X and Y dimensions in model-scale.....	49
Figure 2.21:	Wind dwell measurement locations. Solid line is 100% of blade radius, dashed line is 70%.	51
Figure 2.22:	TR1 Time History and Power Spectral Density Plots.....	52
Figure 2.23:	Measured as-built wind turbine C_t and C_p vs TSR curves	56
Figure 2.24:	Measured ("Exp") vs Simulated ("OpenFAST") turbine thrust (left) and torque (right)	57
Figure 2.25:	Measured ("Exp") vs Simulated ("OpenFAST") turbine thrust (left) and torque (right), including C_d modifications	58
Figure 2.26:	Steady-state rotor thrust (Left) and torque (Right) values (Mendoza et al., 2022)	59
Figure 2.27:	Rated Conditions, derivative of rotor thrust (left) and rotor torque (right) w.r.t changing rotor speed (Mendoza et al., 2022).....	59
Figure 2.28:	Blade pitch schedule for stepped and ramped cases (Mendoza et al., 2022)	60
Figure 2.29:	Rated conditions, rotor thrust (left) and torque (right), response to stepped blade pitch (Mendoza et al., 2022)	60
Figure 2.30:	Rated conditions, rotor thrust (left) and torque (right), response to ramped blade pitch (Mendoza et al., 2022)	61
Figure 2.31:	Rated Conditions, derivative of rotor thrust (left) and rotor torque (right) w.r.t changing blade pitch (Mendoza et al., 2022)	62
Figure 2.32:	ROSCO rotor thrust (top) and derivative of rotor thrust w.r.t wind speed (bottom), response to stepped wind (Mendoza et al., 2022)	63

Figure 2.33:	ROSCO rotor torque (top) and derivative of rotor torque w.r.t wind speed (bottom), response to stepped wind (Mendoza et al., 2022)	65
Figure 2.34:	System response to a large, sustained gust case (Mendoza et al., 2022)	66
Figure 3.1:	Overview of the VolturnUS-S semi-submersible reference hull (Allen et al., 2020)	71
Figure 3.2:	Components of the floating wind system.....	79
Figure 3.3:	Assembled Campaign 2 model in the W2.....	79
Figure 3.4:	Assembled Hull.....	81
Figure 3.5:	FOCAL Hull Cross-Section.....	83
Figure 3.6:	Mooring anchor and fairlead locations	84
Figure 3.7:	View of instrument cable bundle (umbilical) hanging off the hull (platform)	85
Figure 3.8:	Dummy RNA dimensions.....	86
Figure 3.9:	Cutaway Hull Showing Tuned Mass Damper System and Internal Load Sensor.....	87
Figure 3.10:	General Basin Layout for Campaign 2/3 (Model Scale).....	90
Figure 3.11:	Location of the Hull, Tower Base, Tower Top, and Fairlead Coordinate Systems	90
Figure 3.12:	Basin Layout - wave probes and anchor locations.....	92
Figure 3.13:	Instrumentation Overview	94
Figure 3.14:	Internal load cell orientations (viewed from the top).....	95
Figure 3.15:	R1 Time History and Power Spectral Density Plots	98
Figure 3.16:	PN1 Time History and Power Spectral Density Plots.....	98
Figure 3.17:	I1 Time History and Power Spectral Density Plots	99
Figure 3.18:	TMD characterization test setup	102
Figure 3.19:	Natural frequency vs set spring stiffness	106
Figure 3.20:	Repeatability of pink noise wave environment, showing 5 runs with 2,500 repeat time.....	108
Figure 3.21:	Fixed vs Pitch TMD stiffness tuning, effect on platform pitch motion. Inset (a) zoomed into platform pitch frequency.....	109

Figure 3.22:	Fixed vs Pitch TMD stiffness tuning, effect on tower base bending moment. Platform pitch frequency (a) and Tower frequency (b)	110
Figure 3.23:	Fixed vs Tower TMD stiffness tuning, effect on tower base bending moment. Inset (a) zoomed to Tower frequency	111
Figure 3.24:	Effect of damping value on platform pitch, heave, and tower base bending moment for Pitch TMD setting. (a) Pitch near pitch frequency (b) Heave near heave frequency and (c) Tower bending moment near pitch frequency and (d) near tower frequency.	113
Figure 3.25:	Effect of damping value on tower base bending moment for Tower TMD setting. Inset zoomed on tower frequency range.	114
Figure 3.26:	Numerical Validation, Free decay results (Wang et al., 2023a)	117
Figure 3.27:	PSD of pitch motion in wave I4, Pitch TMD locked vs active. a) Experiment and b) WEIS results (Wang et al., 2023a)	119
Figure 3.28:	PSD of tower-base bending moment in wave I4, Tower TMD locked vs active. a) Experiment and b) WEIS results (Wang et al., 2023a).....	120
Figure 4.1:	Above-rated C_p and C_t surfaces	125
Figure 4.2:	Unmodified and baseline C_l (left) and C_d (right) polars	126
Figure 4.3:	Example modified C_l (left) and C_d (right) polars, showing control points and their bounds.....	126
Figure 4.4:	Genetic algorithm Pareto front.....	127
Figure 4.5:	Final C_l (left) and C_d (right) polars compared to baseline	128
Figure 4.6:	C_p vs. TSR comparison of experimental results and baseline and final OpenFAST results at 0 degrees blade pitch	129
Figure 4.7:	ROSCO Floating Feedback Control Loop	130
Figure 4.8:	Simulated ROSCO Performance in Region 3	132
Figure 4.9:	General Basin Layout for Campaign 4	133
Figure 4.10:	FOCAL Scale Model Wind Turbine and Hull	134
Figure 4.11:	Mooring anchor and fairlead locations (not to scale)	137
Figure 4.12:	ROSCO FL feedback filter, magnitude and phase.....	142

Figure 4.13:	Instrumentation employed on the FOCAL hull and turbine	143
Figure 4.14:	W01 wind calibration time history	146
Figure 4.15:	W02 wind calibration time history	146
Figure 4.16:	W03 wind calibration time history	147
Figure 4.17:	E02 wave calibration time history and PSD	148
Figure 4.18:	E11-E15 wave calibration time history and PSD.....	149
Figure 4.19:	E21-E25 wave calibration time history and PSD.....	149
Figure 4.20:	E31 wave calibration time history and PSD	150
Figure 4.21:	Repeats showing inconsistent blade pitch actuation	153
Figure 4.22:	PSD results for fixed TMD and baseline RO turbine control (left) Pitch motion and (right) Tower base bending moment	154
Figure 4.23:	PSD results for Fixed TMD and baseline RO turbine control, (left) Pitch motion and (right) Tower base bending moment	155
Figure 4.24:	PSD results for Fixed, Pitch, and Tower TMD settings, (left) Pitch motion and (right) Tower base bending moment.....	156
Figure 4.25:	Wind Only - Platform and turbine responses.....	157
Figure 4.26:	Blade pitch response with Floating Feedback control	158
Figure 4.27:	Platform pitch response with Floating Feedback control.....	160
Figure 4.28:	Tower base pitch bending moment response with Floating Feedback control	161
Figure 5.1:	Coordinate system for system properties	166
Figure 5.2:	Time history and PSD of U component of wind velocity	168
Figure 5.3:	Time history and PSD of wave elevation	169
Figure 5.4:	Wave-only PSD results	174
Figure 5.5:	Wind-only PSD results	175
Figure 5.6:	Wind/wave with baseline ROSCO (RO) PSD results.....	178

Figure 5.7:	Wind/wave with Floating Feedback (FL) PSD results	179
Figure 5.8:	Rotor speed and rotor torque time history and PSD from experiment.....	184
Figure A.1:	BR1 Time History and Power Spectral Density Plots	209
Figure A.2:	TR1D Time History and Power Spectral Density Plots.....	210
Figure A.3:	TR1G Time History	210
Figure A.4 :	TR1S Time History and Power Spectral Density Plots	211
Figure A.5:	AR1 Time History and Power Spectral Density Plots	211
Figure A.6:	AR2 Time History and Power Spectral Density Plots	212
Figure A.7:	AR2D Time History and Power Spectral Density Plots	212
Figure A.8:	AR2S Time History and Power Spectral Density Plots.....	213
Figure A.9:	CO Time History and Power Spectral Density Plots	213
Figure A.10:	Step Time History	214
Figure B.1:	System Geometry Definitions.....	216
Figure B.2:	Hull Geometry Definitions- Side View	216
Figure B.3:	Hull Geometry Definitions- Top View	2147
Figure B.4:	R2 Time History and Power Spectral Density Plots	218
Figure B.5:	R3 Time History and Power Spectral Density Plots	218
Figure B.6:	R4 Time History and Power Spectral Density Plots	219
Figure B.7:	R5 Time History and Power Spectral Density Plots	219
Figure B.8:	PN2 Time History and Power Spectral Density Plots.....	220
Figure B.9:	I2 Time History and Power Spectral Density Plots	220
Figure B.10:	I3 Time History and Power Spectral Density Plots	221
Figure B.11:	I4S1 Time History and Power Spectral Density Plots	221
Figure B.12:	I4S2 Time History and Power Spectral Density Plots	222

Figure B.13:	I4S3 Time History and Power Spectral Density Plots	222
Figure B.14:	I4S4 Time History and Power Spectral Density Plots	223
Figure B.15:	I5 Time History and Power Spectral Density Plots	223
Figure C.1:	System Geometry Definitions.....	225
Figure C.2:	Hull Geometry Definitions- Side View	225
Figure C.3:	Hull Geometry Definitions- Top View	226
Figure C.4:	System Geometry Definitions- RNA Detail	226
Figure C.5:	System Geometry Definitions- Front View	227

Chapter 1

INTRODUCTION

1.1 Executive Summary

This thesis presents the development and results of the Floating Offshore-wind and Controls Advanced Laboratory (FOCAL) Experiment, which conducted 1:70-scale model testing of the International Energy Agency (IEA) Wind 15 MW Reference Wind Turbine (RWT) and VolturnUS-S semi-submersible platform, see Figure 1.1. FOCAL supported the application of controls co-design (CCD) methods to floating offshore wind turbines (FOWTs) by providing experimental validation data of real-time turbine controls using the Reference OpenSource Controller (ROSCO) and integrating tuned-mass dampers (TMDs) in the hull. Design, construction, and testing of the models was performed in the University of Maine's Alfond Wind/Wave Ocean Engineering Laboratory (W2).

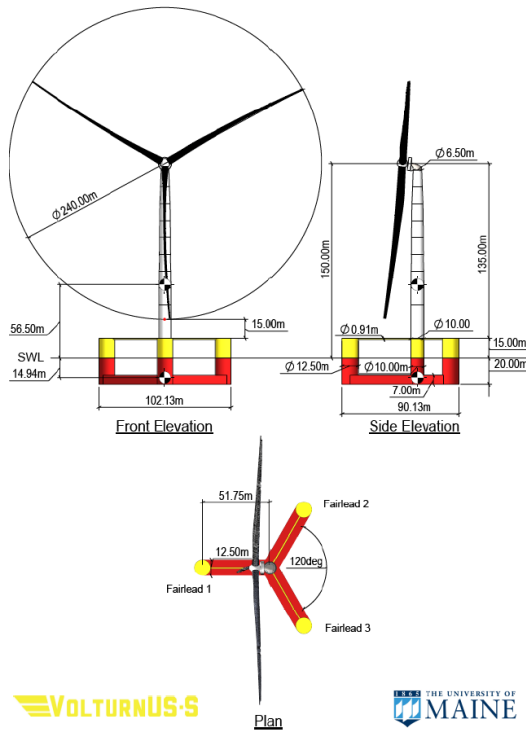


Figure 1.1: IEA 15 MW RWT and VolturnUS-S Full-scale Design

To support the application of CCD to FOWTs, the focus of this research was development and implementation of a scaling methodology to test a realistic wind turbine controller and hull mounted tuned-mass dampers in the scale model test environment. A performance-matched scaling strategy was proposed to match key performance metrics of rotor thrust near rated wind conditions and aerodynamic sensitivities of rotor thrust and torque to changing blade pitch and wind speed. Analysis in OpenFAST was performed to design the scale models, using airfoil geometry optimized for operation in the low Reynolds number environment of the basin test, including wind turbine control using ROSCO, and modeling the TMDs in the hull. Four test campaigns were performed, first characterizing the performance of the turbine and hull separately in wind and wave only environments, respectively. The combined system was then characterized in wind and wave environments, investigating effects of control strategies such as thrust peak shaving, floating feedback, and different TMD target frequencies. An overview of the test campaigns is shown in Figure 1.2. Data were collected and used to validate the OpenFAST models developed by the FOCAL team as well as mid- and high-fidelity simulation tools developed by other ATLANTIS teams.

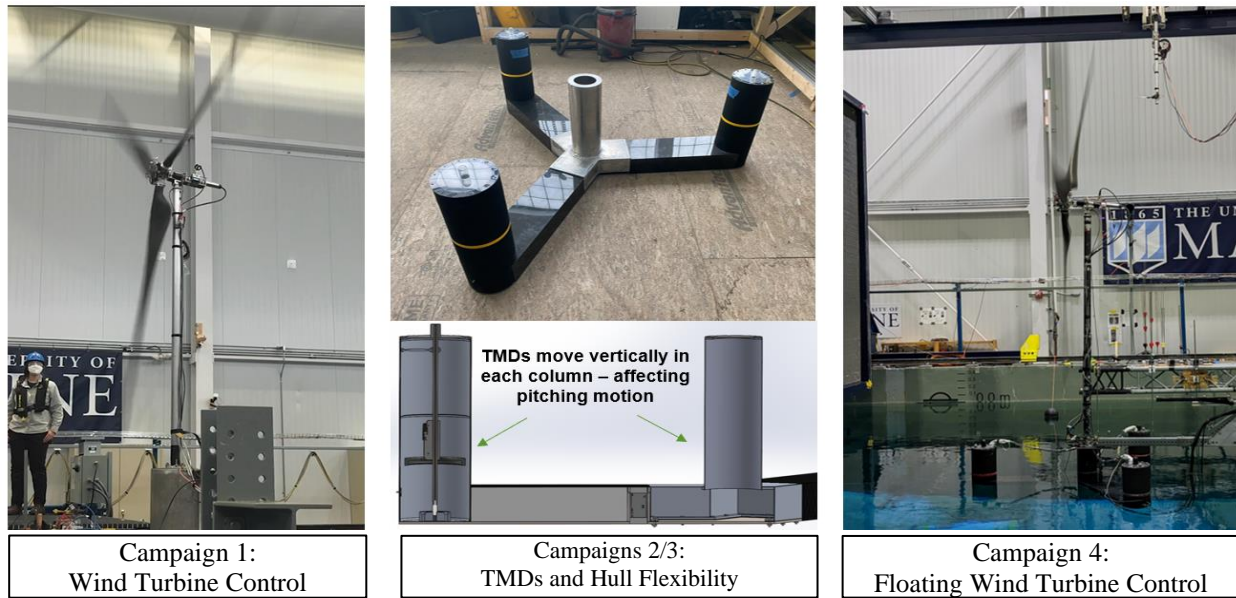


Figure 1.2: FOCAL test campaigns showing the turbine (left), hull (center) and floating turbine (right)

Key outcomes consisted of implementing ROSCO to control the scale model turbine in real-time and investigating the impacts on system behavior. ROSCO Attenuation of platform pitch motion near resonance by 30% with floating feedback control and tower base bending moments in the low frequency regime associated with wind turbulence by 50% due to thrust peak shaving. Successful modeling of the TMDs was demonstrated and their impact effective attenuation of platform pitch motion by 21-47% and tower bending moments by 60% at their respective resonant frequencies, as well as synergistic performance when combined with ROSCO's floating feedback control where a 42% reduction in platform pitch energy was measured. These findings identified opportunities for further optimization of FOWT systems through controls co-design and areas of future work to advance ROSCO and scale model testing of FOWTs with controls. Three datasets were generated and uploaded to the Atmosphere to Electrons portal including time history data, technical reports describing the experimental setup and test articles, and numerical models in Bladed and OpenFAST. Ten publications from the FOCAL team describe the design of the scale model, results of the numerical model validation, and discussion of the experimental results including the effects of ROSCO and TMDs on the performance of the floating wind turbine system. See Section 6.5 for further details.

1.2 Background

The energy capacity of the offshore wind resource in the United States has been thoroughly investigated, with recent assessments from the US Department of Energy's (DOE) Energy Efficiency and Renewable Energy (EERE) Wind and Water Power Program and the National Renewable Energy Laboratory (NREL) estimating 2.8 terawatts of potentially available power (Lopez et al., 2022). In 2011, they published *A National Offshore Wind Strategy: Creating an Offshore Wind Energy Industry in the United States* (Beaudry-Losique et al., 2011), establishing the vision of pursuing offshore wind energy as an integral part of the United States' energy portfolio. In this report, the goals of achieving 10 gigawatts (GW) of offshore wind generation at \$0.10 per kilowatt-hour by 2010 and 54 GW by 2030 were established. It was noted that at the time there were no offshore wind turbines installed in the United States, severely limiting availability of data to support design and development of offshore wind technology. Additionally, when considering the offshore wind resource in the United States, over two-thirds of it exists in deep water (>80m) where conventional fixed-bottom turbines are impractical. This drives the need for advancements in floating offshore wind technology in addition to fixed-bottom solutions to achieve these goals.

Over the past 10+ years, significant progress has been made on floating wind technologies, ranging from simulation and lab-scale experimental work to intermediate-scale demonstration projects consisting of single turbine units in the 1-2 MW range (e.g. Roddier et al., 2010 and Stiesdal, 2009). (Chen, Chen, and Hu, 2020) provide an overview of the major deployments to date. Commercial-scale developments have also taken place, including the world's first floating windfarm the 30 MW Hywind Scotland which began producing electricity in October, 2017 (Hill, 2018). However, most offshore wind commercial development has been focused on fixed-bottom farms. As of 2022, over 50 GW of offshore wind had been deployed globally, with only 0.1 GW of that consisting of floating technologies (The White House, 2022). In March 2021, the Biden-Harris administration in the United States committed to developing 30 GW of offshore wind by 2030 (The White House, 2021). In September 2022, the Floating Offshore Wind

Shot was issued which established the goals of decarbonizing the electric grid by 2035 and updating the 30 GW offshore wind target to include 15 GW of floating offshore wind capacity by 2035 (Department of Energy, 2022). As of 2023, no commercial floating wind farms have been deployed in the United States but many lease areas for offshore wind have been established and sold by the U.S. Department of the Interior's Bureau of Ocean Energy Management (BOEM). In July of 2023, BOEM issued a Draft Environmental Assessment (Bureau of Ocean Energy Management, 2023) as part of its process to establish a Wind Energy Research Lease in the Gulf of Maine for development of commercial offshore wind. With much of this lease area in deep water, floating offshore wind technologies will be essential to developing it.

A common theme throughout the development of offshore wind technology, especially floating offshore wind, is increasing the unit size of the turbine aimed at reducing the project's overall cost of energy. As shown in Figure 1.3, the unit size of turbines from commercial installations has grown steadily, with estimates for future projects in the 17-18 MW range (Lewis, 2023). Unsurprisingly, energy production must be cost-competitive to be pursued at a commercial scale and each successive strategic report continues to identify cost reduction as a critical component of reaching the various offshore wind related deployment goals.

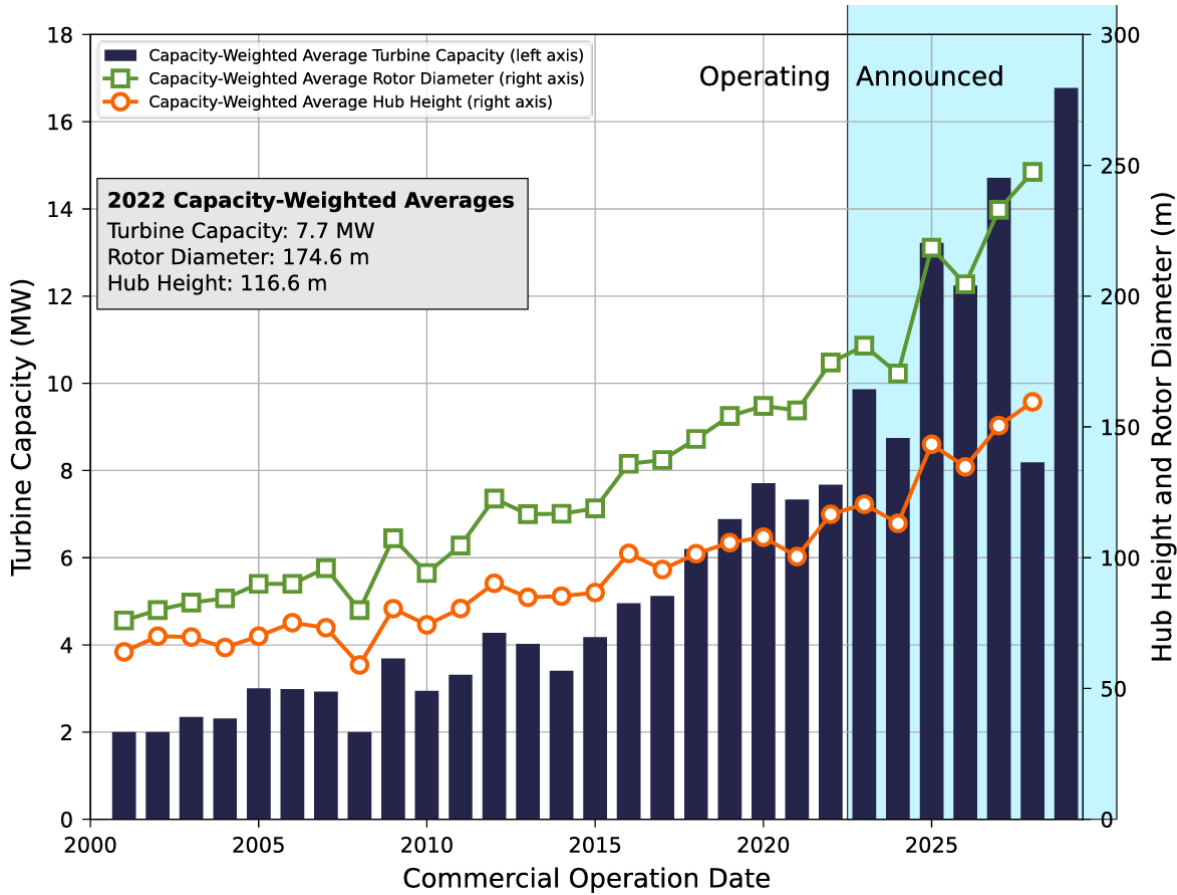


Figure 1.3: Trends in installed turbine capacity, hub height, and rotor diameter (Musial et al., 2023)

However, the size of turbines will not increase indefinitely, and the current industrial standard of 15 MW may represent a trade-off between commercialization or continued upscaling (Shields, 2021). Recent developments in commercial offshore wind development in the United States is applying similar pressure, with most analysts agreeing that achieving 30 GW by 2030 is not feasible and many commercial projects have been halted or cancelled due to cost concerns (Groom, 2023). This highlights the need for continued optimization and pursuit of more economical floating offshore wind turbines continues to drive innovation in platform designs and turbine control systems.

Advances in analysis tools and methods create opportunities to optimize systems and improve the design process. Once such methodology is controls co-design (CCD) (Garcia-Sanz, 2019), by which the impact of controls is considered and leveraged throughout the design stages to optimize the system. In 2019, the

United States Department of Energy's (DOE) Advanced Research Projects Agency–Energy (ARPA-E) funded the Aerodynamic Turbines Lighter and Afloat with Nautical Technologies and Integrated Servo-control (ATLANTIS) research program (ARPA-e, 2019). ATLANTIS focused on applying CCD to the development of innovative and efficient solutions for FOWTs by funding development of numerical tools, experimental data, and novel designs, as shown in Figure 1.4.

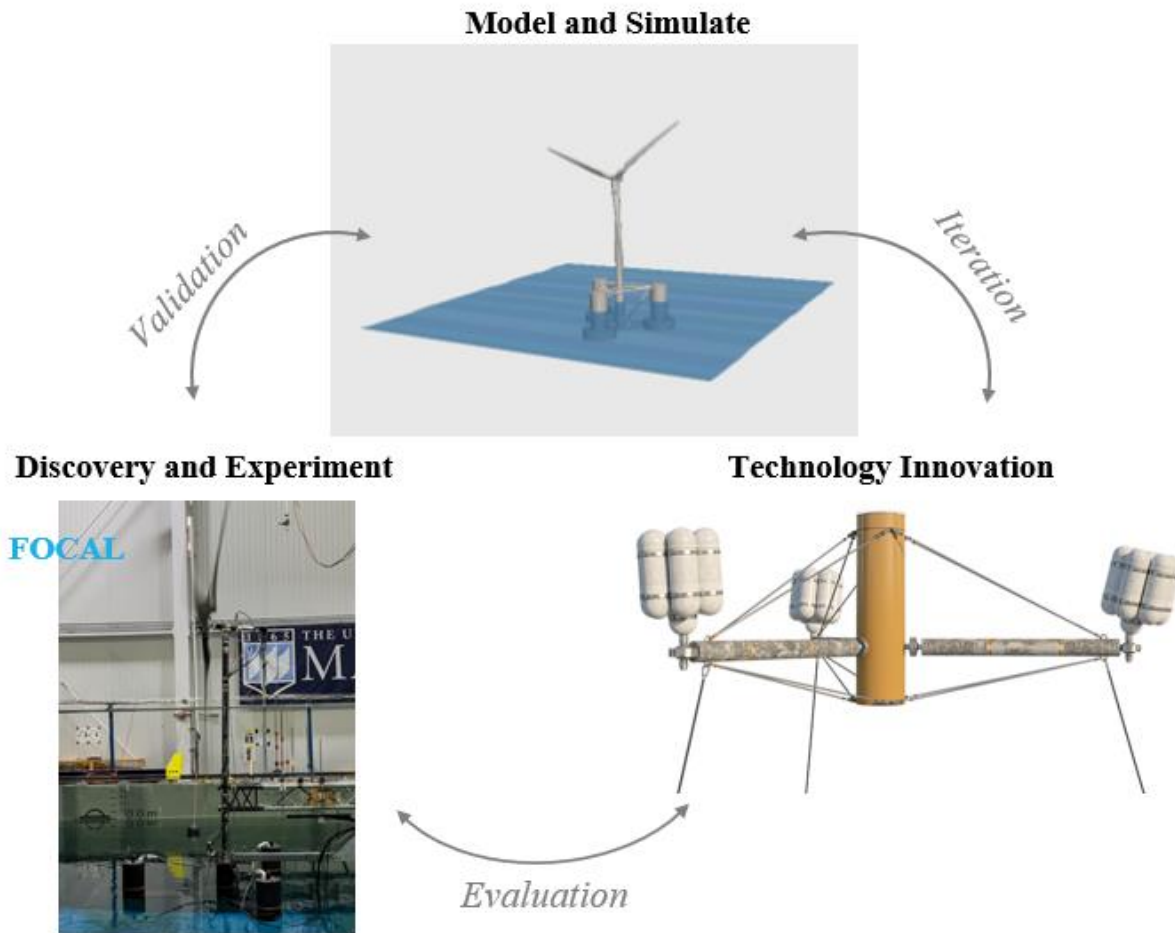


Figure 1.4: ARPA-e ATLANTIS project areas

In response to this call, the University of Maine (UMaine) and the National Renewable Energy Laboratory (NREL) proposed the Floating Offshore-wind and Controls Advanced Laboratory (FOCAL) Experiment. FOCAL aimed to provide experimental data to support validation of CCD tools through testing a 1:70 scale model 15 MW FOWT with real-time turbine control mounted to a semi-submersible

with integrated tuned-mass dampers (TMDs) in the hull. The FOCAL program was awarded and consisted of a series of four model-scale FOWT experimental campaigns conducted in UMaine's Alfond Wind/Wave Ocean Engineering Laboratory (W2). Two cross-collaborative efforts during the project supported validation of various software tools from the ATLANTIS program using data from the first three FOCAL experiments, focusing on the aerodynamic performance of the wind turbine in a fixed-bottom configuration as well as hydrodynamic performance of the floating system with tuned-mass dampers using a flexible tower and fixed mass topside. Data from the four campaigns has been uploaded upon completion of the experimental work and are publicly available with the research community.

1.3 Research Objectives

In developing the FOCAL program to generate publicly available and relevant data, my research objectives focused on the following questions:

- 1) What control methodologies are being considered for CCD of floating offshore wind turbine systems and what is an appropriate open-source FOWT design that is applicable to both research and industry needs?
- 2) What experimental data are needed to validate existing as well as new numerical modeling tools to support their use in CCD of floating wind turbines?
- 3) What scaling methodology and experimental program can provide the needed data considering both wind turbine and hull controls in a scale model wind/wave test campaign?

To effectively utilize a CCD approach, current numerical analysis tools, such as coupled aeroelastic-hydrodynamic software like OpenFAST (Jonkman et al., 2023) and Bladed (DNV-GL, 2023), must be improved to include new turbine and platform controls techniques and hull flexibility, and then validated with experimental data. However, the lack of available offshore wind data, specifically for floating offshore wind, has been a challenging issue for the research community. While more and more data are being collected, either through lab-scale experiments, intermediate-scale offshore deployments, and in

some cases commercial-scale projects, these data are not generally publicly disseminated. When data are available, often turbine and/or platform designs are proprietary, which limits their usefulness in general research. As the cost of performing even a basin scale model test is significant, the goal of providing open datasets on floating turbine systems is a challenging proposition and was one of the guiding objectives of FOCAL.

In this light, I chose to use publicly available designs for the turbine and platform to provide an accessible and applicable dataset for floating offshore wind. As has been done in the DeepCwind (Koo et al., 2014), InnWind (Azcona et al., 2016), and COREWIND (Guanche et al., 2023) programs, I leveraged so-called “reference” designs for the turbine and platform, choosing the recently developed IEA Wind 15 MW Reference Wind Turbine (RWT) (Gaertner et al., 2020), and associated VolturnUS-S (Allen et al., 2020) steel semi-submersible platform. This system was developed to address the need for a reference turbine between 10-20 MW and incorporate industry design paradigms such as a direct-drive generator. It includes an open-source wind turbine controller named the Reference Open-source Controller (ROSCO) and toolbox to implement the controller tuning methodology (Abbas et al., 2022). Both the source code and toolbox are available as repositories on github.com, see (Abbas et al., 2023) and (NREL, 2021). The design process for the IEA 15 MW RWT was similar to other reference turbine designs, such as the NREL 5 MW (Jonkman et al., 2009) and DTU 10 MW (Bak et al., 2013), and included input from researchers and industry experts. Main parameters for these are shown in Table 1.1.

Table 1.1: Main parameters of reference turbines

Parameter	NREL 5 MW	DTU 10 MW	IEA Wind 15 MW
Year Developed	2009	2013	2020
Control	Variable Speed – Collective Pitch	Variable Speed – Collective Pitch	Variable Speed – Collective Pitch
Drive train	Geared	Geared	Direct-drive
Rated Power	5 MW	10 MW	15 MW
Rated Rotor Speed	12.1 rpm	9.6 rpm	7.56 rpm
Rotor Diameter	126 m	178.3 m	240 m
Hub Height	90 m	119 m	150 m
Cut-in, Rated, & Cut-Out Wind Speeds	3, 11.4 & 25 m/s	4, 11.4 & 25 m/s	3, 10.59 & 25 m/s

Use of reference designs has allowed the larger research community to investigate areas of interest in a coordinated fashion by providing representative turbine and platform designs. The most well-known collaboration efforts are the Offshore Code Collaboration (OC3) projects (Jonkman & Musial, 2010), funded under International Energy Agency Wind tasks and led by NREL. This work has focused on validating numerical tools in critical research areas through providing data and leading validation campaigns. Over the years, subsequent phases of the various OC- projects (OC4, OC5, and OC6) have continued to identify and focus on the needs of the research community (e.g. Robertson et al., 2014; Robertson et al., 2017; Wendt, Robertson, & Jonkman, 2019; and Robertson et al., 2020). While most of the work performed in OC3-OC5 has focused on the development of mid-fidelity tools (e.g. FAST/OpenFAST, HAWC2, SIMA, and Bladed), recent work has considered higher fidelity computational fluid dynamics (CFD) tools and validation work is being carried out in the OC6 series (e.g. Wang et al., 2022b and Robertson & Wang, 2021). FOCAL was conceived with a similar mindset as the OC projects and sought to provide scale-model test data to advance numerical tools.

In addition to the use of ROSCO in the OpenFAST modeling of the IEA 15 MW RWT, recent developments in OpenFAST enabled the ability to simulate tuned-mass damper (Randall, 1981) elements, representing an emerging trend to consider additional hull damping mechanisms than traditionally “rigid” systems. While traditionally considered in seismic load mitigation in buildings and fixed-bottom turbines (e.g. Lin et al., 2021), floating concepts have also looked to these damping mechanisms to attenuate unwanted motion. Some designs specify tuned-liquid column dampers (e.g. Yu et al, 2023) while others consider mobile mass elements attached to the platform (e.g. Jahangiri & Sun, 2020; Wang et al., 2020; and Han et al., 2022) or the nacelle (e.g. Zhao et al., 2020). As of OpenFAST v3.0.0 (NREL, 2021), the “Structural Control” module was implemented in ServoDyn based on the work of Lackner & Rotea (2011), allowing for multiple TMDs to be located in the platform, tower, and/or nacelle of a floating wind turbine model. Upon release, there were no test cases associated with this module and no experimental data available for validation (Platt, 2020).

With this in mind, FOCAL was designed as follows:

- 1) Utilize an industry representative and publicly available turbine and platform design
 - Achieved through using the IEA 15 MW RWT and VolturnUS-S reference hull.
- 2) Include representative control methods, specifically for the turbine
 - Achieved by implementing the ROSCO wind turbine controller in real-time and tuning the controller using the ROSCO toolbox
 - Conducted multiple reviews with an External Advisory Board consisting of industry and research experts in the field of wind turbine research
- 3) Incorporate tuned-mass damper elements in the platform
 - TMDs integrated into the platform to address research interest and numerical code developments in OpenFAST enabling use of tuned-mass dampers in simulations
- 4) Measure internal structural loads in hull
 - Load cells in the platform included to address numerical models seeking validation data on internal loads
- 5) Support validation of numerical models developed in OpenFAST and Bladed
 - Achieved through multiple test campaigns to support validation of the various components of the model prior to validation of the fully coupled turbine and platform model

1.4 Scale Model Testing Methodologies

Conducting a scale model test of a floating wind turbine requires proper scaling of the dominant forces present in the system. From a global performance standpoint, the hydrodynamic loading and restoring

forces associated with a floating body can be well represented by following a Froude-scaling approach by which the balance of gravitational and inertial loads acting on the system is maintained. This approach has a long history of utilization and is the dominant scaling methodology for floating offshore oil & gas platforms (Chakrabarti, 1994). However, the performance of a wind turbine is much more sensitive to the balance of viscous and inertial forces, which is represented by the Reynolds number. As it is impossible to match both the Froude and Reynolds number in the same experimental setup, alternative scaling approaches have been considered. Gueydon et al. (2020) discuss the evolution of scaling methods as applied to floating wind turbine systems and categorize the strategies as “full” or “simplified”, depending on if they utilize a scale model wind turbine or an alternative representation to generate the appropriate loading. In order of increasing fidelity, the loading can be represented by a fixed mass, a drag disk, a simple actuator system to represent global loading, or a fully operational wind turbine or actuated system that strives to represent the fully coupled interaction between the turbine, controller, and platform.

Hybrid testing methods, where a component of the system is represented through a hardware-in-the-loop implementation using a characterized numerical model, are gaining popularity. This approach has been used to simulate the response of the turbine through actuators, typically with actuated tendons (Hall, 2016) or fans (Battistella et al., 2018 and Fontanella, 2020), with promising results. An alternate hybrid approach can instead include the hydrodynamic effects of the floating system through an actuated system in conjunction with a wind turbine scale model in a wind field, see (Bayati et al., 2013 and Bayati et al., 2019). A summary of scale-model testing campaigns through 2014 can be found in (Manjock, 2016), and the current state of the art for hybrid testing methods is discussed within the COREWIND project (Facchinetti et al., 2020), which considered multiple ways to model the IEA Wind 15 MW RWT in wind/wave basin tests. The InnWind program (Azcona et al., 2016) performed testing of a 10 MW floating wind turbine on a semisubmersible using a performance-matched turbine and a ducted fan to simulate the thrust force. Bachynski et al. (2016) present hybrid model tests of the NREL 5 MW turbine on a semisubmersible platform at 1:30 Froude scale, and Thys et al. (2018) discuss testing of the DTU 10

MW RWT on a semisubmersible at 1:36 scale. In these campaigns, the turbine was represented by the MARINTEK Real-Time Hybrid Model (ReaTHMTM) method (Sauder, 2016), which used a series of cables connected to the rotor-nacelle assembly to affect 5 degrees of freedom forcing in rotor thrust, tangential force, generator torque, and pitch and yaw bending moments. The system could effectively actuate loads at frequencies up to 2 Hz, covering most frequencies of interest for typical floating wind turbine tests. Fontanella et al. (2020) present testing of the NREL 5 MW turbine on the DeepCwind semisubmersible at 1:50 scale using hardware-in-the-loop and an array of fans to simulate the turbine. Industry standard control strategies using a proportional-integral controller collective blade pitch controller in the above-rated conditions, as well as an individual blade pitch control algorithm, were considered.

An alternative method to represent the scale turbine is through a “performance-matched” methodology, where the rotor is redesigned to produce appropriate Froude-scale quantities (e.g. rotor thrust) in the Froude-scale wind/wave environment of a basin test. This methodology was used by the University of Maine and developed during the model tests performed at the Maritime Institute of the Netherlands (MARIN), see Fowler et al. (2013). The objectives of the performance-matching process generally focus on achieving a steady-state rotor thrust and involves changing the airfoil geometry to respond well in the low Reynolds number environment of a wind/wave basin test and generate reasonable loads. Numerous projects have explored variations of this methodology, summarized by Wen et al. (2019) where they also presented a rotor design for the DTU 10 MW RWT utilizing low Reynolds airfoils and adjusted chord and twist distributions to match rotor thrust near operation points. Recent developments have improved the performance-matched methodology with the goal of enabling testing of realistic wind turbine controllers. Savenije (2017) performed testing utilizing a performance-matched model of the NREL 5MW RWT on the OC4 semi-submersible where three controllers were tested, including tunings for fixed-bottom and floating turbines. Results indicated that a properly designed scale wind turbine could be successfully controlled utilizing industry representative techniques such as a gain-scheduled proportional-integral (PI)

blade pitch controller. Cao et al. (2020) conducted 1:64-scale tests of the DTU 10 MW RWT on a semi-submersible. Generator torque and collective blade pitch controllers were considered, but in above-rated conditions, the pitch angle of each blade was set manually, and an external control loop maintained constant rotor speed. Bredmose et al. (2017) tested the Triple Spar floater with a performance-matched model of the DTU 10 MW RWT at 1:60 scale. Three control strategies were considered, including fixed blade pitch, a standard land-based controller, and a tuned controller designed to address floating system instability (Yu et al., 2017). The platform pitch instability inherent in floating turbine control was demonstrated with the land-based controller, and reductions were realized through retuning the controller. Additional work by Yu et al. (2018) evaluated re-tuning onshore turbine control strategies for floating wind systems through numerical modeling of the TELWIND-5MW-FOWT in Bladed. They showed significant potential for increasing platform stability and reducing system loads with a well-designed turbine controller. Most recently, the IEA Wind 15 MW RWT was tested at 1:70 scale on a version of the VolturnUS-S platform at the Coastal Ocean and Sediment Transport laboratory using real-time hybrid testing to simulate the turbine (Ransley, 2023). Machine learning was used to train a surrogate model using OpenFAST simulations to control a ducted fan in the hardware-in-the-loop system to generate the turbine thrust load. The simulations included a number of simplifications, most notably fixed rotor speed and blade pitch, which implies that effects of turbine controls are not considered.

To model the turbine for FOCAL I utilized a performance-matched methodology to scale the IEA Wind 15 MW RWT, including real-time implementation of the ROSCO turbine controller, in conjunction with a Froude-scale floating platform and corresponding environments. Consideration was given to both the steady-state loads generated by the rotor as well as the aerodynamic sensitivities to changing wind speed, rotor speed, and blade pitch. This was done to investigate the aerodynamic load effects of controller actions in the coupled floating system and evaluate performance of the ROSCO controller in-the-loop with the scale model turbine where it had authority over the blade pitch and generator torque setpoints. As explored in Hmedi et al. (2023), the performance-matched rotor is the preferred methodology to capture

unknown coupling effects between the hydrodynamic and aerodynamic systems of a floating wind turbine system. To date, fully coupled wind/wave experimental results using a performance matched turbine with this fidelity of controls are not available for the IEA Wind 15 MW RWT. As such, a key outcome of my research is to provide this open dataset for use within the ATLANTIS project and for dissemination with the broader research community.

1.5 Outline

This thesis presents my work leading the University of Maine's efforts in the FOCAL Experimental program. As the project manager and lead engineer for the UMaine team, I carried both management as well as technical responsibilities. My management roles consisted of project conceptualization, developing the proposal and test program, reporting to NREL as well as ARPA-e, and managing the testing schedules, budget, and technical deliverables. In addition, my technical contributions focused on the design of the experimental program and test articles to achieve the program objectives as well as conducting the testing with my team of engineers and students in the W2 facility. My specific contributions were:

- Test planning: design of experiments, developing scaling methodology, authoring test plans, engagement with external advisory board, and coordinating test schedule
- Model Design: designing the scale turbine, hull, and tuned-mass damper system; instrumentation design and integration; software development; integrating the real-time turbine controller; programming and modifying the data acquisition system
- System Characterization: tuning controllers, characterizing TMD system, calibrating test environments
- Test Execution: lead test operator and engineer, developing test methods and training of staff; performing tests and collecting data

- Data analysis: performing data analysis; supporting numerical model validation efforts by NREL; performing numerical analysis and model validation

The dissertation is organized into five chapters, covering the extent of my work over the 3.5 year FOCAL program.

Chapter 1 is an introduction, outlining the FOCAL program and its development.

Chapter 2 covers Campaign 1, including the design and construction of the 1:70-scale performance-matched model of the IEA Wind 15 MW RWT, details of the fixed-bottom wind-only test campaign, and a summary of results from the numerical model validation efforts.

Chapter 3 presents results from test Campaigns 2 and 3, which focused on the development of the 1:70-scale model hull, tuned-mass damper design, wave-only testing, and a summary of results.

Chapter 4 considers Campaign 4 testing of the full floating turbine system in combined wind/wave environments and presents the test setup, execution, and summary of results.

Chapter 5 presents work conducted developing the OpenFAST model for Campaign 4 and selected numerical results relating to the performance of the system.

Chapter 6 is the final chapter and presents a summary of significant findings and discussion of some potential impacts of controls co-design on design of offshore wind turbines and future work.

Throughout this thesis, various components have also been published as conference papers, journal papers, or test reports. As co-author on these FOCAL publications, I attempted to identify this content when applicable. Additionally, I was lead author on (Fowler et al., 2023a), which was referred to in Chapter 4, as well as (Fowler et al., 2023b) which provided the content for Chapter 5.

Chapter 2

CAMPAIGN 1: WIND ONLY TURBINE TESTING

2.1 Research Objectives

Chapter 2 presents my work determining the scaling approach, designing the scale model wind turbine, integrating the instrumentation and wind turbine controller, and results from the first of the four FOCAL experimental campaigns. My research objectives for Campaign 1 focused on how to properly design and build the scale model turbine with consideration for implementing ROSCO in real-time. To focus on characterizing the wind turbine, I developed the test plan to consider wind-only testing of the fixed-base turbine and characterization of the turbine's aerodynamic performance in the model-scale test environment of the W2 facility. To design the turbine, I expanded the previously developed turbine performance-matched methodologies (Martin et al., 2014; Fowler et al., 2013; and Fowler et al., 2016) to include active turbine controls and account for the known Reynolds number issues associated with the Froude-scale test environment. The objectives of Campaign 1 included:

- Design and construction of a performance-matched 1:70 scale model of the IEA Wind 15 MW RWT and tower
- Scaling industry-representative turbine control methods for floating wind systems (e.g. peak shaving and collective pitch control), and implementing them in real-time
- Expansion and characterization of the wind generation system in the W2 facility to enable testing the larger 15 MW model scale turbine
- Measuring the steady-state loads and performance of the wind turbine
- Quantifying the turbine dynamic response, including the sensitivity of the rotor thrust and torque to changing blade pitch and wind speed
- Validation of numerical models, specifically the OpenFAST to be uploaded with the dataset

2.2 Methodology

2.2.1 Full-Scale Design

The target turbine for the FOCAL program was the IEA 15 MW RWT. I chose this turbine for a number of reasons, including:

- Most up to date “reference” turbine, presenting a relevant open-source design for the research community
- Newly developed ROSCO wind turbine controller included as an open-source, industry representative controller
- Numerical models provided in a variety of tools, notably OpenFAST
- Reference floating wind turbine system available, including open-source hull and floating turbine controller

The full-scale turbine is a three-bladed upwind design with a rotor diameter of 240m and hub height of 150m. It utilizes a direct-drive generator, following industry trends for large turbines such as GE’s 12+ MW Haliade-X offshore turbine (GE, 2023). Particulars of the turbine design are provided in Table 2.1 below.

Table 2.1: Main parameters of the IEA Wind 15 MW RWT

Parameter	Units	Value
Power Rating	MW	15
Rotor Diameter	m	240
Hub Height	m	150
Number of Blades	-	3
Shaft Tilt Angle	deg	6
Cut-in Wind Speed	m/s	3
Rated Wind Speed	m/s	10.59
Cut-out Wind Speed	m/s	25
Design Tip Speed Ratio	-	9.0
Rated Rotor Speed	rpm	7.56

Detailed information on the rotor performance is hosted on the GitHub repository for the turbine, found at (Barter, 2023). The performance characteristics essential to developing the scale model of the turbine are shown in Figure 2.1. This includes the rotor aerodynamic torque, aerodynamic thrust, blade pitch, and rotor speed as functions of wind speed. These parameters, along with the OpenFAST model of the turbine, were used to define the targets of the performance-matched scale model turbine.

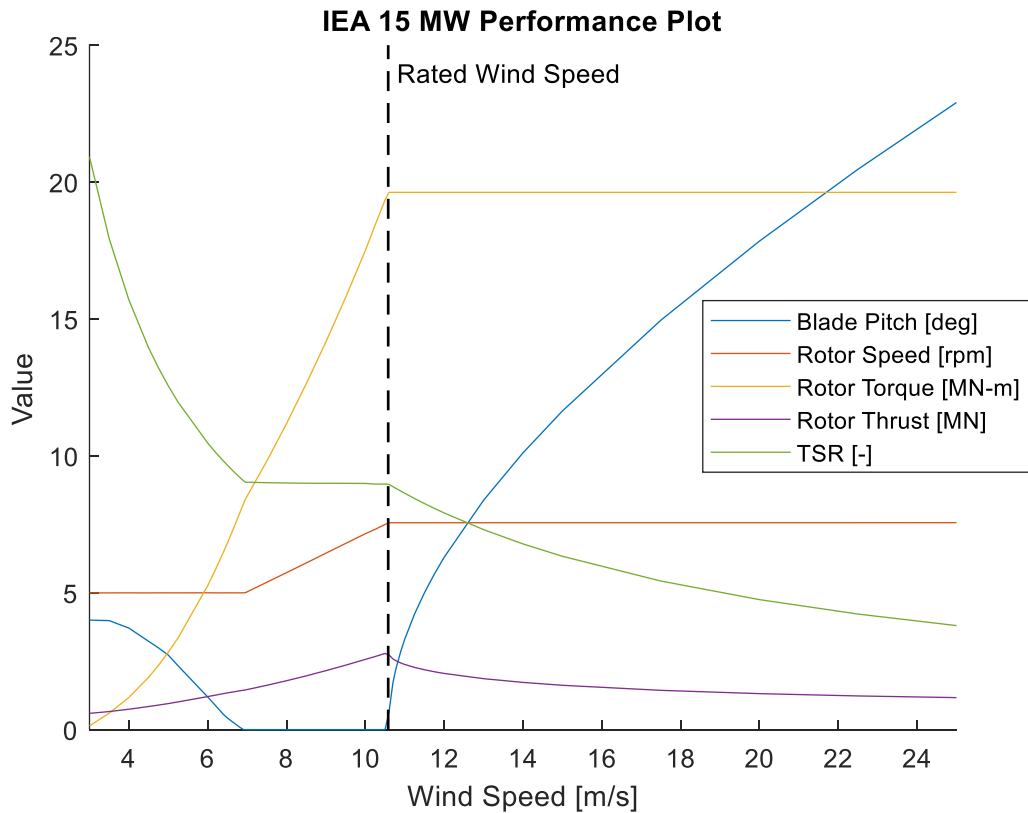


Figure 2.1: IEA 15MW RWT Performance Plot

2.2.2 Scaling Approach

The following section outlines the scaling approach that I implemented for the FOCAL program, which followed Froude-scaling, as is typical of floating offshore wind turbine model testing (Chakrabarti, 1994). Holding Froude number constant ensured that the gravitational and inertial forces were properly scaled, which properly represented the dominant physics for floating structures and provided representative global responses (Olondriz et al., 2016). As discussed in (Kimball et al., 2014), generating appropriate

turbine forces in the Froude-scaled wind environment is challenging as the aerodynamic performance of a wind turbine is sensitive to viscous effects (Glauert, 1983), which are not properly scaled. As discussed in (Gueydon et al., 2020), a variety of solutions to this issue have been proposed, including modifying the test environment, redesigning the turbine for low Reynolds number environments, or using alternative forms of actuators in a hybrid test approach. To create a dataset for validating numerical models and exploring the impact of wind turbine controllers on system responses, it was decided to use a performance-matched turbine to represent the wind turbine. Objectives for this performance-matching was to generate appropriate turbine thrust loading on the system with minimal changes to the Froude-scale environment while also capturing the effects of a realistic turbine controller on the system performance. The additions to the performance-matched methodology that I implemented to enable testing of ROSCO included considering both the rotor thrust and torque as well as their sensitivities to changing blade pitch and wind speed, as discussed in Sections 2.2.4 and 2.2.5.

Froude-scaling dictated the length scale of the model, which was subject to constraints from the physical dimensions of the testing facility. This applied to various aspects of the model test, including the scaled wave environments that could be generated, the extent of the mooring layout, water depth, and the wind generation capabilities, which is often the limiting factor for testing floating wind turbines. In general, these constraints require larger scale ratios to accommodate the increasing size of rotors being considered for floating wind turbines. Previous testing in the W2 facility has demonstrated the ability to test floating 5-10 MW wind turbines at length scales of 1:50 to 1:60, resulting in scaled rotor diameters around 3 m (e.g. Fowler et al., 2017 and Fowler et al., 2016). However, the IEA Wind 15 MW RWT's rotor diameter of 240 m means the scale rotor diameter would be between 4-4.8 m at those scales, exceeding the size of the wind machine test area. As shown in Figure 2.2, the W2's wind machine is an open-jet wind generation source with 32 individual fans and a rectangular outlet width of 7 m and height of 3.5 m.

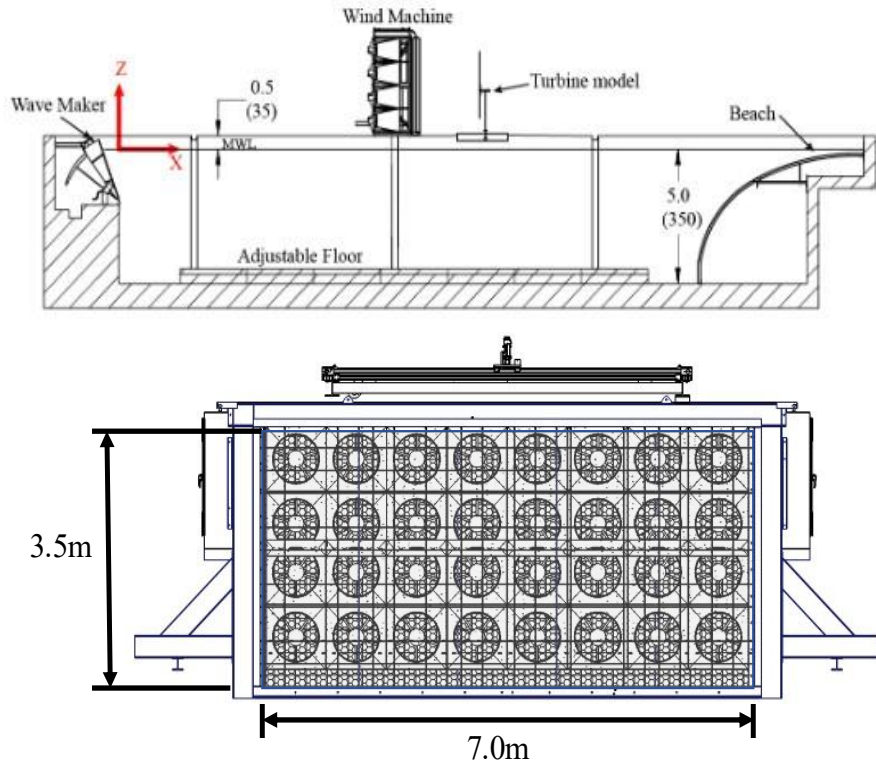


Figure 2.2: Schematic of the W2 basin and wind machine

As discussed in Section 2.3.1, wind speed surveys of the rotor plane identified a maximum rotor diameter of 3.5m to fit within the test area. To maximize the turbine size based on the 3.5 m rotor diameter requirement, the scale ratio of 1:70 was chosen. A higher scale ratio would have resulted in a smaller turbine and made the scale model mass properties difficult to match while a smaller scale ratio would have resulted in a rotor whose swept area put the blade tips outside of the wind machine slipstream. At this scale, the blade tip was 3.6cm from the top or bottom of the wind machine slipstream when the rotor was centered in the test area. While tip vortex interaction with the slipstream was likely at top and bottom, this area was relatively small part of the swept area. The turbine experimental characterization included this interaction effect, and the resulting performance matched parameters were achieved on average. The design of the performance-matched turbine is presented in Section 2.2 and the 1:70-scale turbine is shown in Figure 2.3 as installed in the W2 facility for testing in Campaign 1.

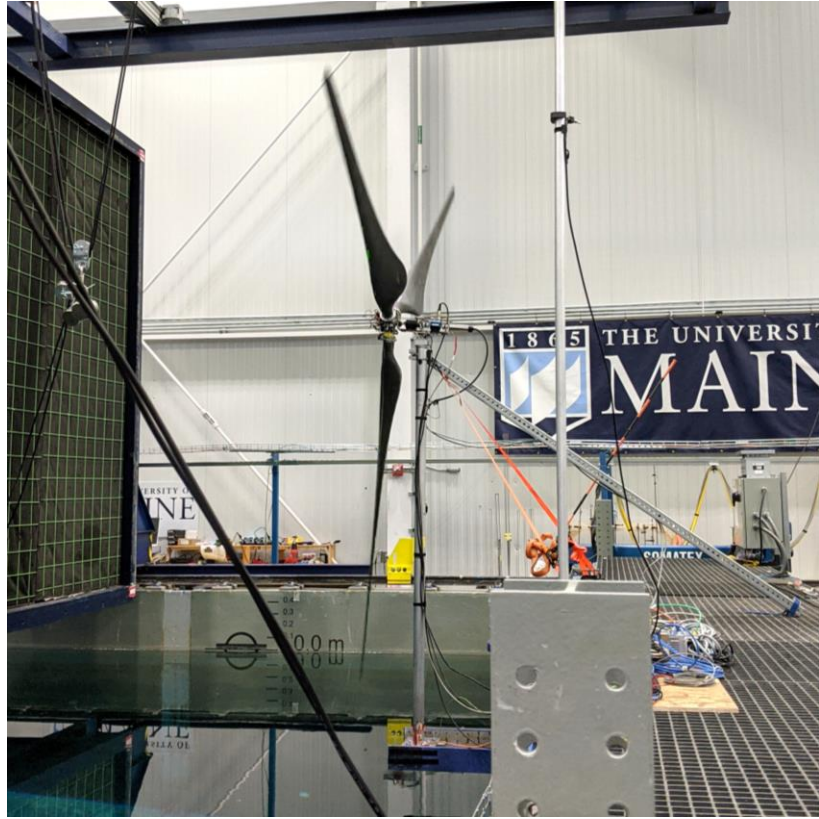


Figure 2.3: 1:70-scale model of the 15 MW turbine installed in the W2

An overview of the Froude scaling approach followed was included with the Test Report, uploaded with the dataset (Robertson, 2023), and is summarized here. The primary scale of the model was defined by the ratio of the full-scale (FS) to model-scale (MS) lengths. The full-scale length L_{FS} was related to the model-scale length L_{MS} through the scaling parameter λ , as shown in Equation 2.1:

$$L_{FS} = \lambda L_{MS}$$

Equation 2.1

As indicated, for this test program, $\lambda = 70$. The scaling of general quantities is provided in Table 2.2 in terms of the scale ratio λ . Data in this document are generally presented at full-scale, unless specified otherwise. To achieve the model values, one needs to divide the full-scale values by the scale factors provided in the table. Conversely, the full-scale values were obtained from the model data by multiplying by the scale factors noted in Table 2.2.

Table 2.2: Scaling parameters for Froude-scale model test campaign

Quantity	Analytic Scale Factor
Scale Factor	λ
Length / Position	λ
Velocity	$\lambda^{0.5}$
Acceleration	1
Angle	1
Angular Velocity	$\lambda^{-0.5}$
Angular Acceleration	λ^{-1}
Time	$\lambda^{0.5}$
Frequency	$\lambda^{-0.5}$
Mass	$\varphi\lambda^3$
Mass Moment of Inertia	$\varphi\lambda^5$
Force	$\varphi\lambda^3$
Moment/Torque	$\varphi\lambda^4$

2.2.3 Water Density Mismatch

An additional scaling factor must be considered related to the density of the water. At model scale, testing was performed using freshwater. However, the full-scale design was for saltwater deployment, which has a 2.5% higher density. In wave tank testing, it is typical to include this density factor in the scaling process, which affects the mass, forces, and inertia. This is indicated by the “phi” factor in Table 2.2, where $\varphi=1.025$. It then follows that even though there is not a density mismatch of the air between model- and full-scale, to keep the balance between wind and wave forces consistent, the target aerodynamic thrust force was decreased by 2.5%.

Following this process, the design parameters for the scale model turbine were determined. As described in Section 2.2.5, a performance-matched turbine was designed to impart the appropriate mean loads to the floating hull, prioritizing the thrust load as that is most significant for global responses. Low-Reynolds-number Selig-Donovan SD7032 airfoils (Broeren, 1996) were used to generate enough lift in the low Reynolds number environment to enable reasonable matching of the target thrust and power curves. Use of this low-Reynolds-number airfoil was informed by recent performance matched turbine testing performed in (Bayati et al., 2016) and addressed some, but not all, of the Reynolds number mismatch found in Froude-scaled test environments. Another consideration was that the rotor blades were designed to be effectively “rigid” at model scale as aeroelastic scaling would be prohibitively complicated and not

directly supportive of the test objectives. The tower was also made to be rigid for Campaign 1 to focus on the turbine performance and loads, but was flexible for subsequent campaigns.

2.2.4 Wind Speed Adjustment

While a performance-matched scaling approach has been used successfully in several experimental campaigns (e.g Goupee et al., 2014 and de Ridder et al., 2014) to generate appropriate scaled thrust loads, the inclusion of active turbine controls in the FOCAL project required that additional factors be considered such as reasonable sensitivities of rotor torque to changes in blade pitch and thrust to changes in wind speed. As shown in (Kimball et al., 2014, the larger sectional drag of the model wind turbine blades limited the ability to match performance by only changing the turbine geometry, even with the use of low-Reynolds airfoils. To help overcome this, the experimental wind speed was increased by roughly 20% to impart more energy in the wind field (see wind speed adjustment factor below) while holding the scaled rotor rotation speed at Froude-scale to ensure the turbine blade-passing frequencies retained their appropriate relationship to other system frequencies (e.g., tower frequencies and rigid-body floater frequencies), which is important to controller design. The wind speed adjustment was also applied to other wind speed parameters, such as turbulence. This was particularly important when looking at the sensitivity of the turbine power and thrust to changes in wind speed. To this end, the target wind speed sensitivities were reduced by the same factor as the increased mean wind speed, ensuring that the effect of the wind speed increase was not “double-counted”. The adjusted wind speed is defined as Equation 2.2:

$$U^* = U_{ms} \times WF$$

Equation 2.2

where U^* is the adjusted wind speed used in the rotor design, U_{ms} is the Froude-scaled wind, and WF is the wind speed adjustment factor. Changing the wind scale factor without modifying the turbine rotational speed resulted in a different tip speed ratio (TSR) for the same operating point, which was taken into account during the design process by lowering the operating TSR target in the controller. Tip speed ratio

is the ratio of the relative velocity of the rotor blade tip due to its rotation divided by the far-field wind velocity, shown in Equation 2.3:

$$TSR = \frac{\omega R}{U_\infty}$$

Equation 2.3

where ω is the rotor rotational speed, R is the rotor radius, and U_∞ is the far-field wind velocity. This change in TSR was incorporated into the rotor design process and did not prevent realizing appropriate force magnitudes, frequencies, and overall control responses.

2.2.5 Model Turbine Design

The focus of Campaign 1 was to quantify the aerodynamic performance of the scale turbine and ensure we could accurately implement floating wind turbine control strategies within the scaled wind/wave basin environment to investigate the effect of the controller on system behavior. Therefore, rigor was taken in ensuring the scaled turbine design retained the appropriate relationships between the control properties and dynamic response. The performance-matching objectives were to match the full-scale turbine in overall thrust (reduced by 2.5%, as discussed earlier), while having power and sensitivities to several key control parameters be reasonably matched. Performance targets were determined from the OpenFAST model of the IEA 15 MW RWT and are summarized in Table 2.3.

Table 2.3: Main particulars of the IEA Wind 15 MW RWT

Quantity	Units	Full-Scale	Model-Scale
Scale Factor	-	1	70
Hub Height	m	150	2.14
Rotor Diameter	m	240	3.43
Individual Blade Mass	kg	68,000	0.19
Hub Mass	kg	190,000	0.54
Nacelle Mass	kg	607,275	1.73
Rotor Nacelle Assembly (w/ 3 blades)	kg	1,001,000	2.85
Shaft Tilt	°	6	6
Rated Rotor Speed	RPM	7.55	63
Wind Speed (Cut-in to Cut-Out)	m/s	3-25	0.4-3.0
Tower Mass	kg	1,263,000	3.59
1st Bending Mode (Fore-Aft or Side-Side)	Hz	0.496	4.15
Blade Pitch Rate	rad/s	+/- 0.0349	0.29
Rated Thrust	N	2.48e6	7.05
Rated Torque	N-m	1.962e7	0.80

Sensitivities of torque and thrust to changing blade pitch and wind speed were obtained through linearization analysis in OpenFAST using the frozen wake assumption and conditions specified in the turbine design. As such, the sensitivities are so-called open-loop responses because the controller action was not included in the linearization. This same process was used to quantify the performance and sensitivities of the design rotor for comparison.

The design of the scale rotor required knowledge of the lift and drag characteristics of the airfoils in the low Reynolds environment of the wind/wave tank. Airfoil performance data are often not available at Reynolds numbers below 100,000 and it was expected that the design Reynolds number of the scaled rotor would be between 30-50,000. There are a number of ways to obtain the required data including numerical tools such as XFOIL, numerical simulations using computational fluid dynamics, or experimentally measured data from airfoil tests. For FOCAL, performance data for the SD7032 airfoil was available at a Reynolds number of 60,000 from (Selig, 1995). While these data were able to be recreated in XFOIL, as shown in Figure 2.4, it was determined that performance data at lower Reynolds numbers were necessary for design of the rotor and thus XFOIL was not used to generate blade polars.

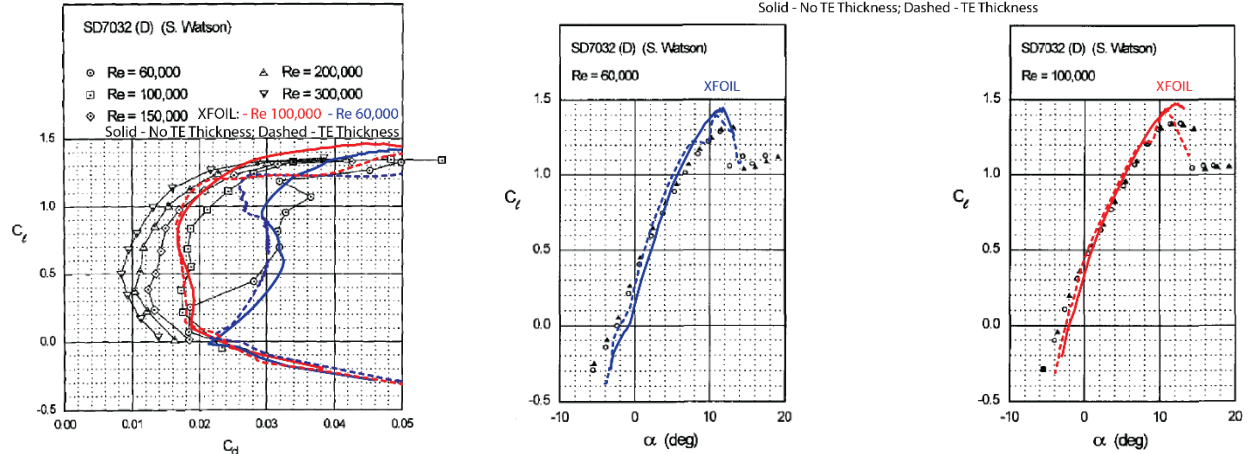


Figure 2.4: Blade Lift/Drag performance of SD7032 at various Reynolds numbers, Data (Selig, 1995) vs XFOIL

To determine lift and drag performance of the SD7032 airfoil at lower Reynolds numbers, data were provided by the LIFES50+ project (Bayati et al., 2016). These data were collected from 2D airfoil tests performed in a wind tunnel at a range of Reynolds numbers from 50,000-200,000. Data from the $Re = 50,000$ runs was considered for FOCAL, as it was closest to the estimated 30,000-40,000 Reynolds number of the test, and smoothed for use in the blade design optimization process to prevent localized phenomena from overly influencing the optimization algorithm. The original and smoothed lift and drag data are shown in Figure 2.5 for a range of angles of attack typical of an operating turbine.

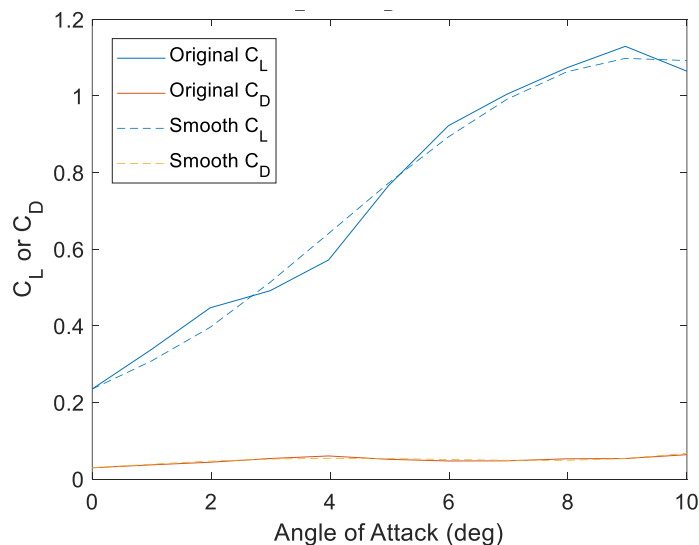


Figure 2.5: Lift/Drag data for OpenFAST rotor optimization process

The initial rotor design process follows the “Betz optimal rotor” as outlined by (Manwell, McGowan, and Rogers, 2002). By making assumptions of no wake rotation, no drag, no tip loss, and an optimal axial induction factor of 1/3, the basic chord and blade twist distribution are defined. The resulting chord, $c(r)$, and blade twist, $\phi(r)$, distribution along the blade are shown in Equation 2.4:

$$\phi = \left(\frac{2}{2\lambda_r} \right), c = \frac{8\pi r \sin \phi}{3BC_l \lambda_r}$$

Equation 2.4

where $\lambda_r = \lambda(r/R)$, r is the radial location, R is the rotor radius, B is the number of blades, and C_l is the lift coefficient. These distributions are further adjusted during the design process to define the blade design.

To assess the rotor design, the following process was carried out:

- The target angle of attack was selected for the blade design. An angle of 6° was selected for the SD7032, as it represented a region of the airfoil performance where high C_l and low C_D were observed and was far enough from the stall region to ensure stable performance, see Figure 2.5.
- Chord and twist distribution were set by the Betz optimal equations, and a chord distribution scale was adjusted. This applied uniformly to the chord distribution over the entire length of the blade.
- Design optimization loop, Above-Rated
 - Evaluate the rotor performance using a blade element method analysis tool and scaled design conditions, including any wind speed scale factor.
 - Calculate sensitivities using a perturbation approach and frozen wake.
 - Discard results with greater than 50% error on rated thrust or power.
 - For designs that pass, determine error as area between target and calculated metric from rated to cut-out wind speed. Total error was calculated as the root-mean-square of the errors on various metrics

- Prioritize thrust matching and $\frac{\partial Power}{\partial Blade Pitch}$ and $\frac{\partial Thrust}{\partial Wind Speed}$.
 - Adjust chord scale and wind scale factor until an optimal design is found.
- Final Design
 - Perform steady analysis in OpenFAST using final rotor design.
 - Perform linearization with frozen wake assumption for sensitivities.

Figure 2.6 shows the blade twist, blade chord, and blade pitch schedule as well as the predicted performance as a function of wind speed for the “Betz optimal” turbine. Note that all results are plotted using “Adjusted Wind Speed/WF” to compare the IEA Wind 15 MW RWT results against the scaled-up model results on the same axis. As shown in Figure 2.6, without wind speed adjustment ($WF = 1.0$), the ability to performance-match both thrust and power was not achieved. The thrust was well matched around the rated wind speed of 10.59 m/s, but significantly less power was produced over all wind speeds. While the performance wasn’t well matched, the sensitivities of thrust and power to changing wind speed and blade pitch was reasonable, as shown in Figure 2.7.

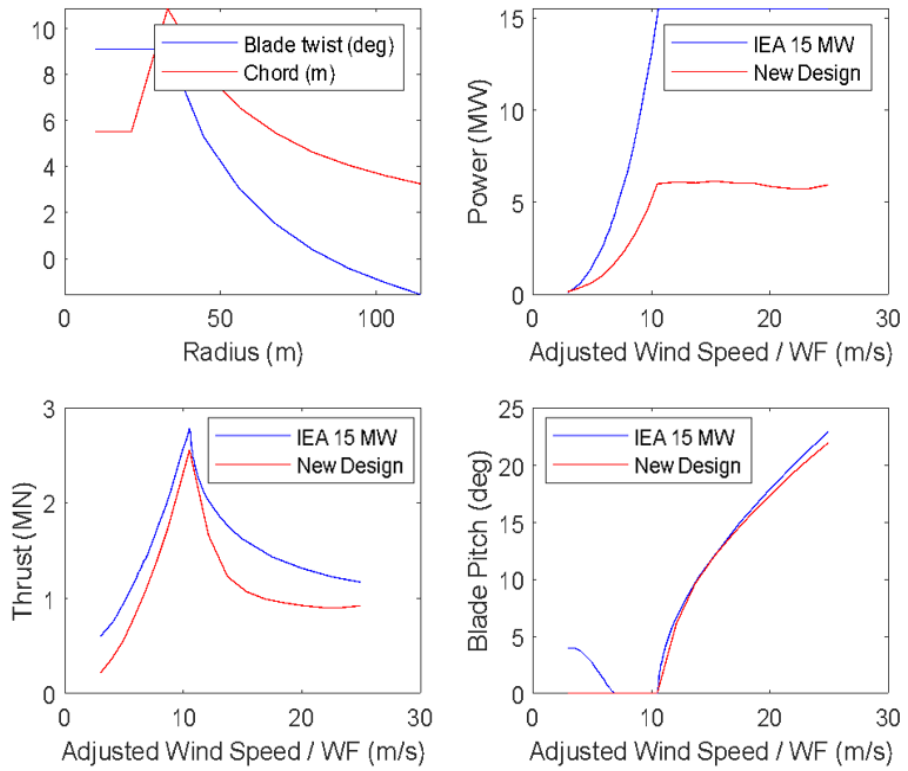


Figure 2.6: Betz optimal rotor—turbine performance in wind speed = $1.0 \times U_{ms}$.

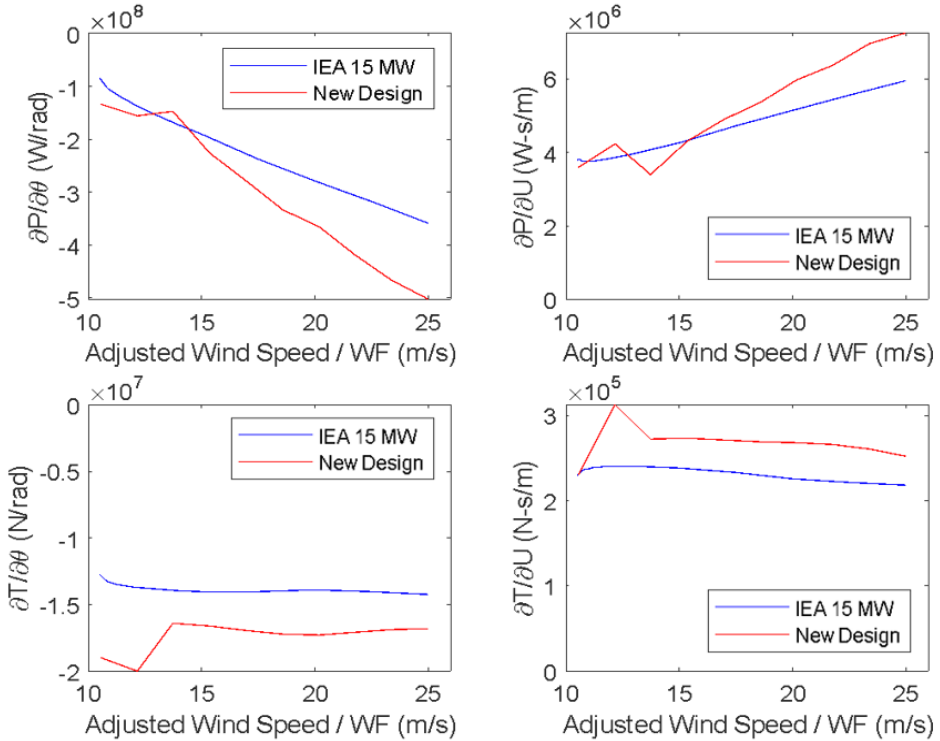


Figure 2.7: Betz optimal rotor— aerodynamic sensitivities computed in wind speed = $1.0 \times U_{ms}$

Figure 2.8 shows results of the optimization process, where the wind speed and chord scale were adjusted. Overall, the use of a higher wind speed along with reduced chord length provided better performance-matching for thrust and power. A good match of all target parameters was found at an increased WF of 1.2 and a 0.6 chord “scale” relative to the baseline blade. There is a better thrust match at the rated wind speed of 10.59 ms^{-1} and above-rated conditions while generating marginally more torque (power) than needed, giving some margin for losses in the as-built design. Note that the thrust curves in Figure 2.8 are based on the Yaw Bearing F_x force from OpenFAST and therefore include the additional thrust component due to the rotor weight at six degrees of tilt of the rotor. Figure 2.9 shows the sensitivities of power and thrust to changes in wind speed and blade pitch. Comparing with the targets, the sensitivities have similar trends and magnitudes which is indicative that a controller tuned using the optimized design should behave in a similar fashion as the baseline.

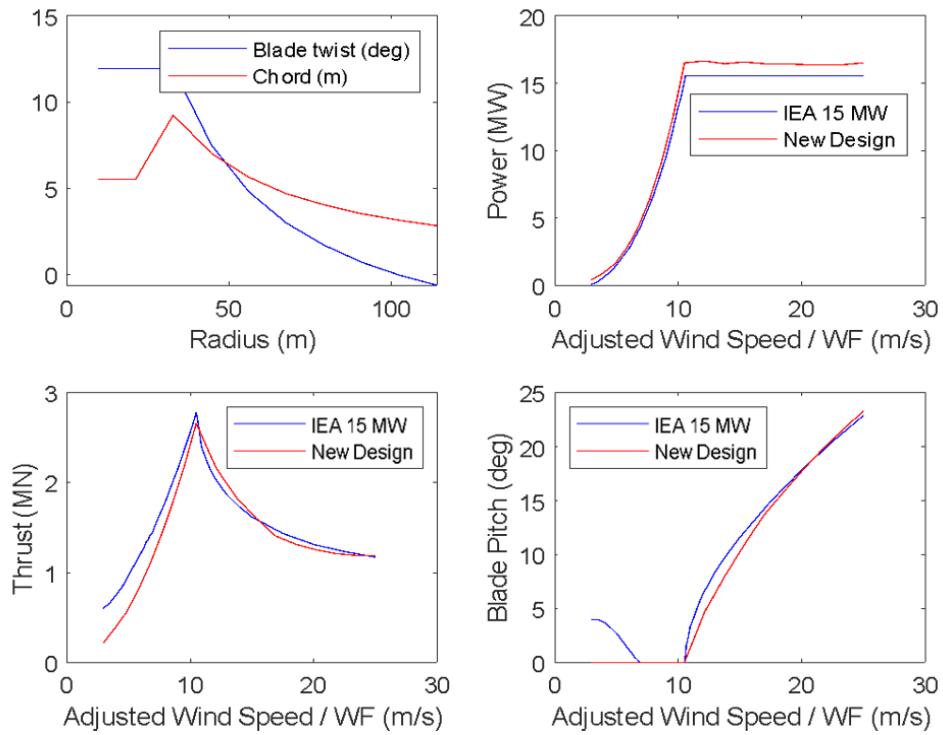


Figure 2.8: Optimized design – turbine performance with 0.6 chord scale and wind speed = $1.2 \times U_{ms}$

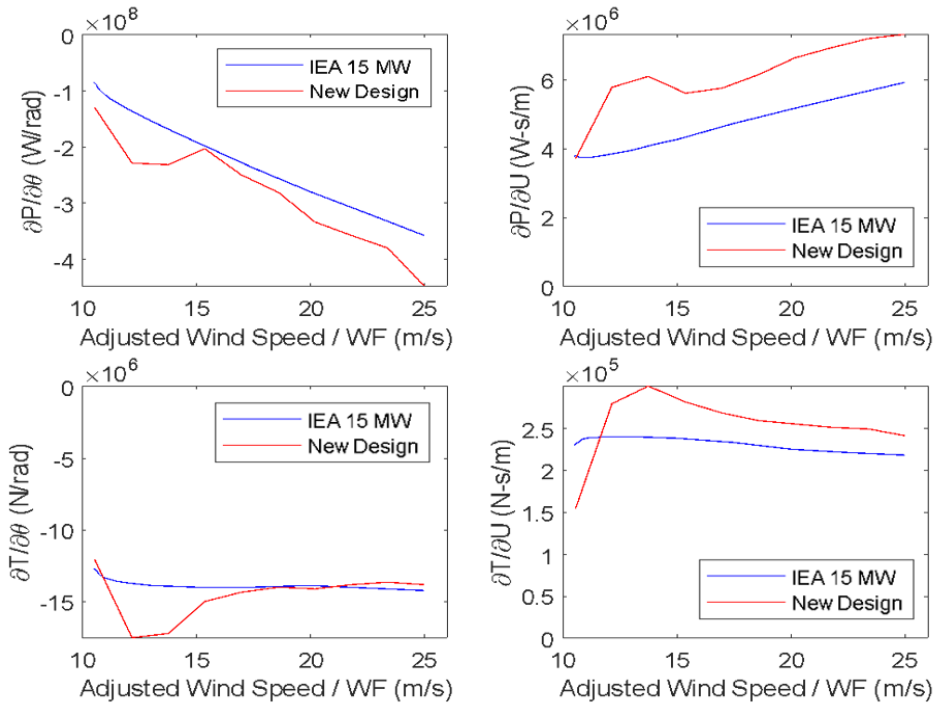


Figure 2.9: Optimized design – aerodynamic sensitivity with 0.6 chord scale and wind speed = $1.2 \times U_{ms}$

2.2.6 Model Rotor and Nacelle Construction

The scale turbine blade geometry was designed using the SD7032 airfoil profile and the optimized blade twist and chord distribution. Profiles were defined at multiple radial stations and imported into SolidWorks to loft the 3D blade geometry. Near the root, surface modeling tools were used to create a transition from the airfoil profile to the cylindrical root to interface with the hub. This geometry was then used to machine a series of molds to be used in the composite layup of the blade shell. The resulting blade properties, including chord, twist, relative thickness, pitch axis, and airfoil information can be found in Table 2.4.

Table 2.4: As-designed distributed blade properties, 1:70 scale

Radial Station	Distance along pitch axis from blade root [m]	Chord [m]	Aerodynamic twist [deg]	Aerodynamic center [% chord]	Relative thickness [%]	Airfoil ID [-]
1	0	0.05490	27.13	50	100	Cyl
2	0.01907	0.05490	27.13	50	100	Cyl
3	0.27839	0.19800	13.42	25	10	SD7032
4	0.33364	0.17409	11.00	25	10	SD7032
5	0.38890	0.15515	9.10	25	10	SD7032
6	0.44415	0.13981	7.58	25	10	SD7032
7	0.49940	0.12716	6.33	25	10	SD7032
8	0.55466	0.11657	5.29	25	10	SD7032
9	0.60991	0.10758	4.41	25	10	SD7032
10	0.66516	0.09986	3.65	25	10	SD7032
11	0.72041	0.09316	3.00	25	10	SD7032
12	0.77567	0.08729	2.43	25	10	SD7032
13	0.83092	0.08211	1.93	25	10	SD7032
14	0.88617	0.07751	1.48	25	10	SD7032
15	0.94143	0.07339	1.08	25	10	SD7032
16	0.99668	0.06969	0.72	25	10	SD7032
17	1.05193	0.06633	0.40	25	10	SD7032
18	1.10718	0.06329	0.10	25	10	SD7032
19	1.16244	0.06051	-0.17	25	10	SD7032
20	1.21769	0.05796	-0.41	25	10	SD7032
21	1.27294	0.05562	-0.64	25	10	SD7032
22	1.32820	0.05346	-0.85	25	10	SD7032
23	1.38345	0.05146	-1.04	25	10	SD7032
24	1.43870	0.04960	-1.22	25	10	SD7032
25	1.49395	0.04788	-1.39	25	10	SD7032
26	1.54921	0.04626	-1.54	25	10	SD7032
27	1.60446	0.04476	-1.69	25	10	SD7032
28	1.65130	0.00498	-1.77	25	10	SD7032

The turbine blade construction consisted of one layer of plain-weave carbon fiber infused with epoxy vinyl ester resin manufactured with a vacuum infusion process using high-density foam molds.



Figure 2.10: Scale rotor blade manufacturing showing internal spars (top) and the completed blade (bottom)

The blades were infused in two parts in a modified butterfly configuration and assembled with two foam spars and a mounting flange using a methacrylate adhesive, as shown in Figure 2.10. This methodology introduced a nominal trailing edge thickness, shown in Figure 2.11. More details on the blade manufacturing process can be found in (Parker, 2022).

To achieve appropriate scaling of the blade weight and sufficient stiffness, the use of low-density, high-strength materials was required. The blades were evaluated for mass, center of gravity, stiffness, and inertia, and final adjustments were made to the mass properties to achieve consistent properties. Average full-scale blade properties are shown in Table 2.5, as are other key turbine characteristics. Due to the high stiffness of the model scale blades, the coning angle for the model was 0° to keep the blades in the rotor plane.

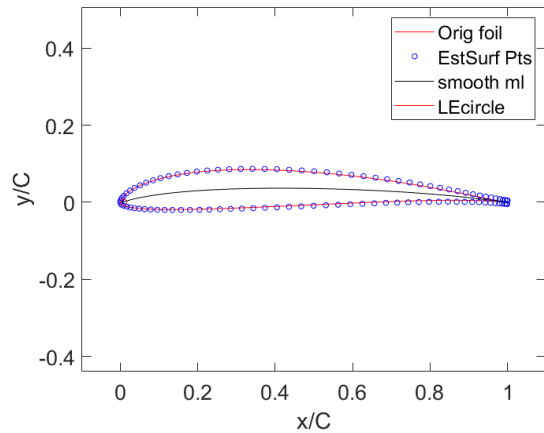


Figure 2.11: Modified profile of SD7032 including added trailing edge thickness

Table 2.5: As-built rotor blade properties

<i>Quantity</i>	<i>Units</i>	<i>Average Value</i>		<i>Source</i>
		<i>Full Scale</i>	<i>Model Scale</i>	
<i>Length</i> ¹	m	1.159E+2	1.655	Measured
<i>Blade Mass</i>	kg	8.081E+4	2.356E-1	Measured
<i>CM Location</i> ¹	m	3.773E+1	5.390E-1	Measured
<i>First Mass Moment of Inertia</i> ¹	kg-m	3.049E+6	1.270E-1	CAD
<i>Second Mass Moment of Inertia</i> ¹	kg-m ²	1.951E+8	1.161E-1	Swing Test

¹w.r.t. root along axis

The model turbine nacelle was fully instrumented to measure turbine performance data, including aerodynamic torque and rotor thrust as shown in Table 2.6. Figure 2.12 shows the model turbine nacelle instrumentation and the coordinate systems used to present results. Data were collected using a National Instruments cRIO real-time platform and etherCAT communication to increase bandwidth with minimal cabling. The nacelle design was optimized to minimize weight while providing sufficient stiffness to support the rotor drivetrain. A servo-motor and gearbox on the back of the nacelle was attached to the driveshaft which connects to an inline shaft torque sensor mounted between two bearings. The torque sensor was attached to a shaft that extended forward to the rotor hub and used to measure the shaft torque. The rotor housed the three individual pitch control motors, encoders, and drives used to actuate the pitch of each blade. An ethernet compatible slip ring was used to communicate with the pitch drives and provide power to the rotating hub. The nacelle was mounted to a six degree-of-freedom load cell located at the tower top and measured reaction forces into the tower, e.g. rotor thrust. Finally, a three degree-of-freedom accelerometer was mounted at the tower top. The scaled turbine was designed to be capable of achieving the desired rotor speed and torque set points, as well as individual blade pitch control with blade pitch rate limits exceeding that of most commercial scale turbine.

Table 2.6: Campaign 1 instrumentation

Component	Measurement	Device	Coordinate System*
Turbine	Individual Blade Pitch	Pitch Motor Encoder	CS3
Turbine	Rotor Speed	Rotor Motor Encoder	CS4
Turbine	Rotor Position (Azimuth)	Rotor Motor Encoder	CS4
Turbine	Rotor Thrust	Tower Top 6DoF	CS2
Turbine	Rotor Torque	Inline torque sensor	CS4
Turbine	Nacelle Acceleration, XYZ	Triaxial Accelerometer	CS2
Environment	Survey Wind Speed and Direction	Ultrasonic anemometer	Global
Environment	Survey Wind Speed and Turbulence	Hotwire Anemometer	Global
Environment	Air Temperature, Pressure, Rel. Humidity	PTU300	N/A
Environment	Upstream Reference Wind Speed, Turbulence Characteristics	Hotfilm anemometer	Global

*Note: coordinate systems are defined in Figure 2.12

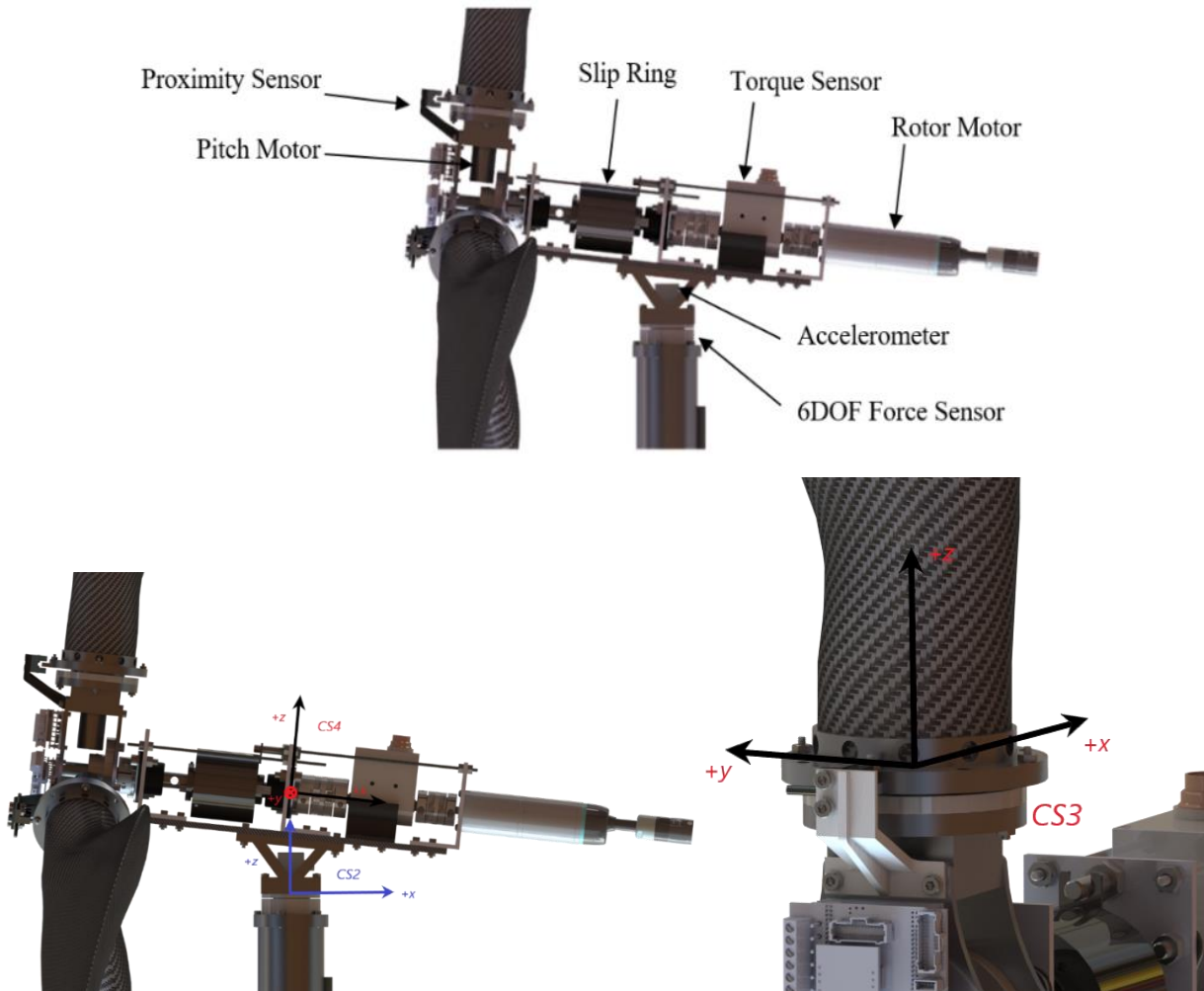


Figure 2.12: Instrumentation (top) and Coordinate systems (bottom). CS1 – at Tower base (not shown), CS2 – at Tower top, CS3 – Blade root, CS4 – Rotor drive shaft

2.2.7 Controller Design

Control of the model-scale turbine was performed in real-time using the NREL-developed Reference Open-Source Controller (ROSCO). This controller was developed separately from FOCAL and a few modifications were made to accommodate running it in real-time in an experimental setup. The ROSCO controller_formulation, compilation, and installation and ROSCO toolbox used for FOCAL are available via [Github](#) (Abbas et al., 2023). ROSCO requires two input files to operate: the primary input file with the desired settings and parameters, and the turbine performance map (power, C_p , thrust, C_t , and torque, C_q , coefficient surfaces as functions of tip-speed ratio and blade pitch). These were prepared based on as-built rotor performance and included with the OpenFAST model developed as part of the project.

The basic control methodology in ROSCO is typical of most commercial wind turbines. In below-rated (Region 2) the controller uses a variable-speed generator torque controller and constant blade pitch to optimize power capture. In rated and above-rated (Region 3) conditions, the controller actuates collective blade pitch to minimize rotor speed error relative to the rated rotor speed setpoint for a constant rotor torque. In addition to these fundamental control strategies, ROSCO implements additional features including a set-point smoother, rotor thrust Peak Shaving, and platform pitch stabilization through a nacelle velocity Floating Feedback loop. The control regions are shown in Figure 2.13, where τ_g is generator torque, β is blade pitch, ω_g is generator speed, R is rotor radius, λ_{opt} is C_p maximizing tip-speed ratio, N_g is gearbox ratio, k_{vs} , k_{pc} are tunable gain factors.

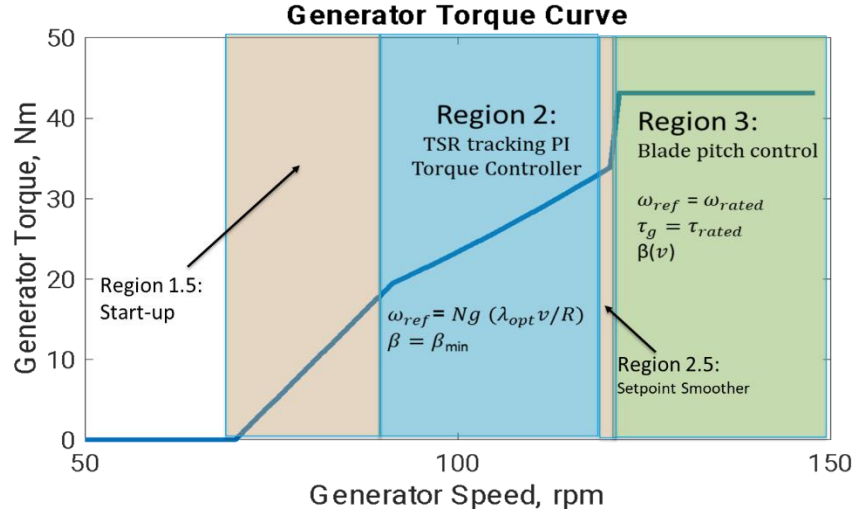


Figure 2.13: Wind turbine generator operating regions (Robertson et al., 2023)

The control diagram for ROSCO is shown in Figure 2.14, where ω_g is generator speed, τ_g is generator torque, β is blade pitch angle, \hat{v} is estimated wind speed, $\Delta\omega$ is controller set point shifting term, β_{float} is the floating feedback gain, \dot{x}_t is the nacelle's fore/aft velocity, β_{min} is the minimum blade pitch angle, and “LPF” stands for low-pass filter.

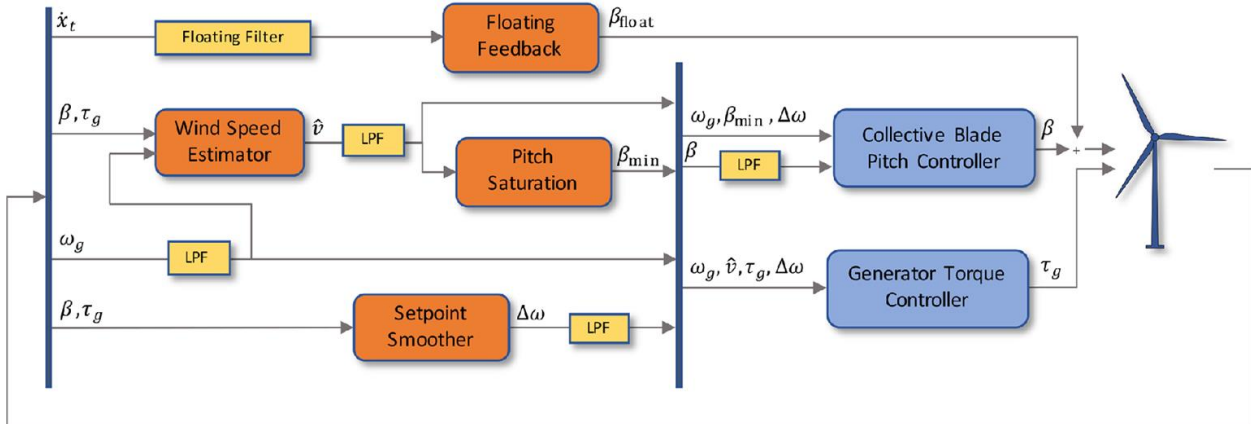


Figure 2.14: ROSCO Control Diagram (Abbas et al., 2021)

The controller designed for FOCAL was tuned using the ROSCO toolbox and as-built performance-matched wind turbine aerodynamics following the procedure described in Abbas et al. (2021). This

process utilized the as-measured steady-state performance data and as-built rotor parameters (diameter, rated speed, and rotor inertia) to create a simplified first-order model of the turbine, shown in Equation 2.5:

$$\dot{\omega}_g = \frac{N_g}{J} (\tau_a - N_g \tau_g)$$

Equation 2.5

where $\dot{\omega}_g$ is the generator rotational acceleration, J is the rotor rotational inertia, N_g is the gearbox ratio, τ_a is the aerodynamic torque and τ_g is the generator torque. The IEA Wind 15 MW RWT is a direct drive turbine, so $N_g=1$. The turbine performance data (C_p) was then used to define the aerodynamic torque in terms of wind speed based on Equation 2.6:

$$\tau_a = \frac{1}{2} \rho A_r \frac{C_p(\lambda, \beta)}{\omega_r} v^3$$

Equation 2.6

where ρ is the density of air, A_r is the rotor swept area, ω_r is the rotor rotational speed, and v is the wind speed. Based on this, the first-order linearized plant model about an operating point can be described as Equation 2.7:

$$d\dot{\omega}_g = A(v_{op}) d\omega_g + B_{\tau_g} d\tau_g + B_\beta(\beta_{op}) d\beta + B_v dv$$

Equation 2.7

where A is parameterized by the operating velocity v_{op} , and B is parameterized by β_{op} (which is subsequently parameterized by v_{op}), and shown in Equation 2.10. B_v is the disturbance input matrix to the system and is set to zero for the calculation of gain scheduling. Next, the generator control loop is shown in Figure 2.15.

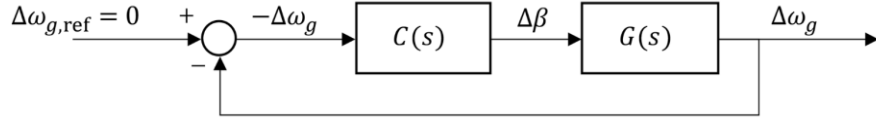


Figure 2.15: ROSCO generator control loop

where $C(s)$ and $G(s)$ are the PI controller and plant transfer functions, respectively. The general form of the PI controller is shown in Equation 2.8:

$$(d\beta) = k_p(d\omega_g) + k_i \int_0^T (d\omega_g) dt$$

Equation 2.8

where k_p and k_i are the proportional and integral gains of the controller, respectively. Combining Equation 2.7 and Equation 2.8 in a negative feedback loop results in the closed-loop transfer function shown in Equation 2.9:

$$H(s) = \frac{d\omega_g(s)}{d\omega_{g,ref}(s)} = \frac{B(k_p(v)s + k_i(v))}{s^2 + (Bk_p(v) - A(v))s + Bk_i(v)}$$

Equation 2.9

where ω_g and $\omega_{g,ref}$ are the generator speed and generator reference speed respectively and B is either B_{τ_g} or B_β (v_{op}) depending if the turbine is in below- or above-rated operation, respectively, as shown in Equation 2.10:

$$\text{Below - Rated Operation: } B = B_{\tau_g} = \frac{-N_g^2}{J}$$

$$\text{Above - Rated Operation: } B = B_\beta(v_{op}) = \frac{N_g}{J} \frac{\partial \tau_a}{\partial \beta} = \frac{N_g}{2J} \rho A_r R v_{op}^2 \frac{1}{\lambda_{op}^2} \left(\frac{\partial C_p}{\partial \beta} \Big|_{\lambda_{op}, \beta_{op}} \lambda_{op} \right)$$

Equation 2.10

The gain calculation was performed using the ROSCO toolbox , with the integral gain (k_i) calculated as shown in Equation 2.11:

$$k_i = \frac{\omega_{DES}^2}{B}$$

Equation 2.11

and the proportional gain (k_p) as shown in Equation 2.12:

$$k_p = \frac{1}{B} (2\zeta_{DES}\omega_{DES} + A(v_{op}))$$

Equation 2.12

where B is either B_{τ_g} or B_β (v_{op}) for below- or above-rated operation and ζ_{des} is the desired damping ratio and ω_{des} is the desired natural frequency of the controller. For Campaign 1, the controller gains were tuned for a desired natural frequency of 0.2 rad/s and damping ratio of 1.0 to achieve a highly damped response to a step change in wind speed. The k_p and k_i values were calculated based on the performance data provided in the C_p , C_t , and C_q surfaces and gain scheduled with respect to wind speed. The IEA 15 MW RWT's rotor inertia was used since the as-built inertia was not available during initial tuning. Subsequent measurements showed that the as-built rotor inertia was roughly twice the target. This resulted in gains that were lower than intended, representing a “soft” tuning of the controller. It was decided to keep this definition consistent throughout all experimental runs and numerical analysis to minimize impact to the validation process.

The ROSCO controller was deployed to a National Instruments cRIO as a compiled dynamically linked Shared Object library (.so). The controller utilizes the Bladed-style DISCON interface and associated DISCON.IN parameter file. The ROSCO simulation ran at full-scale and interfaced with LabVIEW in real-time in the following manner:

- Measured model-scale rotor torque, turbine rotational velocity, blade pitch angle, and current time from the experiment are scaled up to full-scale for input to ROSCO using Froude scaling.
- ROSCO generates setpoints (generator torque and blade pitch) which are sent back to the real-time system. The generator torque and time output by ROSCO is Froude scaled down to model-scale for application in the test.
- This communication occurs at the loop rate of the cRIO, which is 2ms model scale.

The ROSCO control strategies considered in FOCAL are shown in Table 2.7 and are representative of the types of simple control strategies employed by current commercial turbines. The thrust peak-shaving algorithm and platform pitch stabilization were not employed in Campaign 1, but were included in Campaign 4 when the turbine was deployed on a floating platform.

Table 2.7: Controller strategies considered for the IEA Wind 15 MW RWT

Ctrl Method	Operational Case	Actuation	Sensing
ROSCO torque ctrl	Below-rated (BR)	Generator torque (GT)	Rot- or gen-speed (RS or GS)
ROSCO pitch ctrl	Above-rated (AR)	Collective pitch (CP)	RS or GS
ROSCO transition ctrl	Transition region (TR)	CP + GT	RS or GS
Platform pitch stabilization	AR	CP	Tower-top acceleration or motion
Thrust peak-shaving	TR plus near rated (NR)	CP + GT	RS or GS

2.3 Experiment Setup

2.3.1 Initial Wind Surveys

To establish the effective test area of the W2 wind machine, a series of wind surveys were performed to quantify the mean flow characteristics of axial velocity (U-component), turbulence intensity, spatial uniformity, wind shear, and the boundaries of the test area. A shrouded TSI-8455 series hot-film

anemometer was mounted to the 3D traverse and used to measure the flow in the axial (+X) direction.

Sampling was at 32 Hz. The test setup is shown in Figure 2.16.

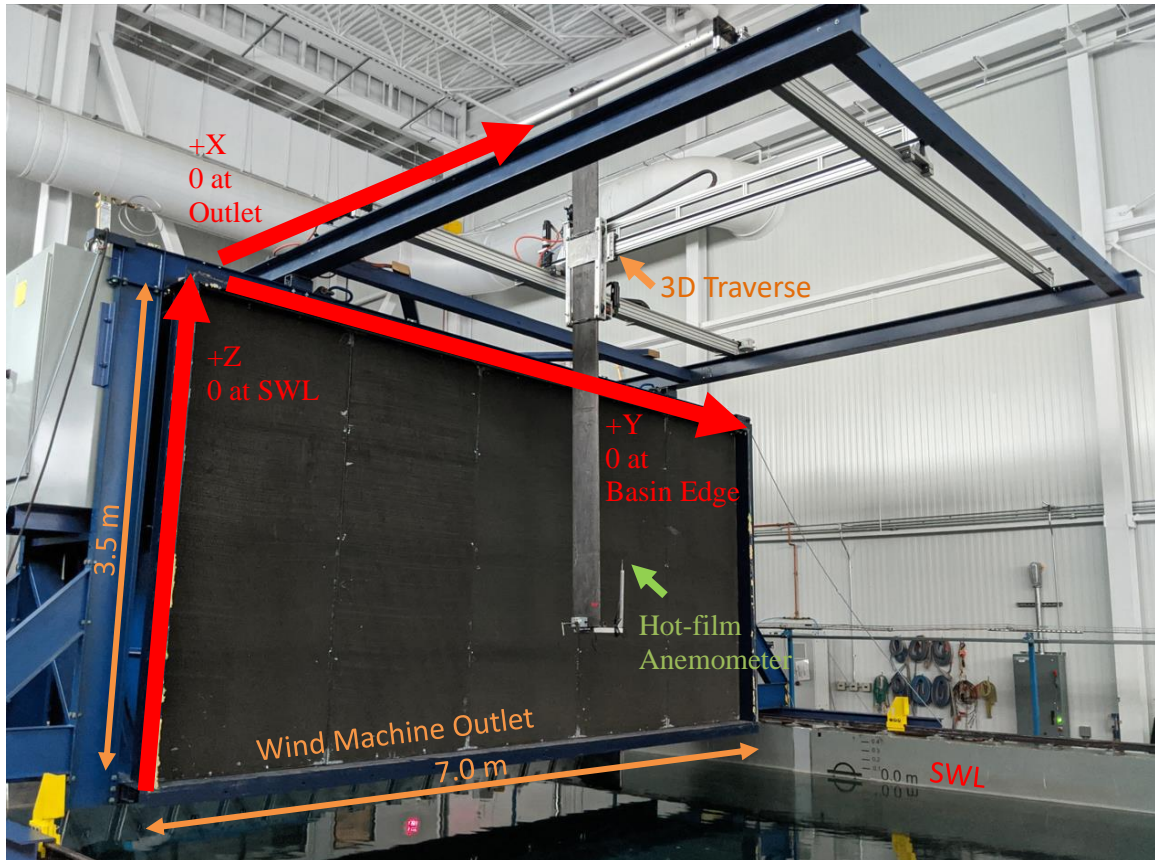


Figure 2.16: Preliminary wind survey setup

Dwell sampling was conducted first, where the probe was located 1 m from the face of the wind machine (model scale), centered in the basin and elevated to the hub height. The wind machine was run at 25%, 50%, and 75% power. These data established the average steady-state wind velocities available to test the turbine and demonstrated that a maximum velocity of 7 m/s was reasonably obtained. This would correlate to a scale ratio of ~18 to scale the cut-out wind speed of 25 m/s, meaning that maximum wind speed was unlikely to be the limiting factor in determining the scale ratio.

Next, vertical cuts of the wind field were performed by slowly moving the anemometer through the wind field along a vertical path, centered at the basin centerline in +Y and located 1 m from the wind machine in +X. Data were captured continuously and used to establish the location of the slip stream and measure wind uniformity over the test area. Data were averaged and fit with a Power Law wind profile with exponent 0.11, as shown in Figure 2.17. The results indicated that the boundaries of the slipstream cause wind speed drop-off at the top and the bottom of the rotor. While this represented a small portion of the overall rotor's swept area, the effect on turbine performance was estimated.

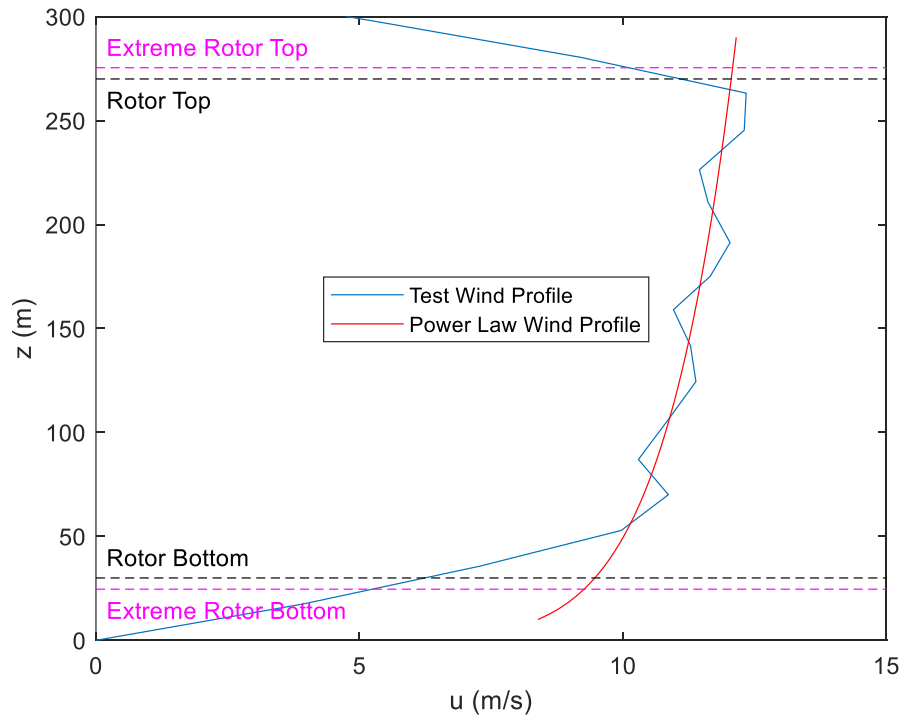


Figure 2.17: Initial wind survey, vertical cut. Power law uses an exponent of 0.11

To quantify the effect, simulations were performed in OpenFAST using the measured wind field. Additional vertical cuts were performed at different Y-locations to quantify the flow over the rotor area. The field was then represented in TurbSIM using a time series input, which required using a horizontally

uniform field, as well as a Power Law fit. The full-field data and the horizontally uniform field are shown in Figure 2.18.

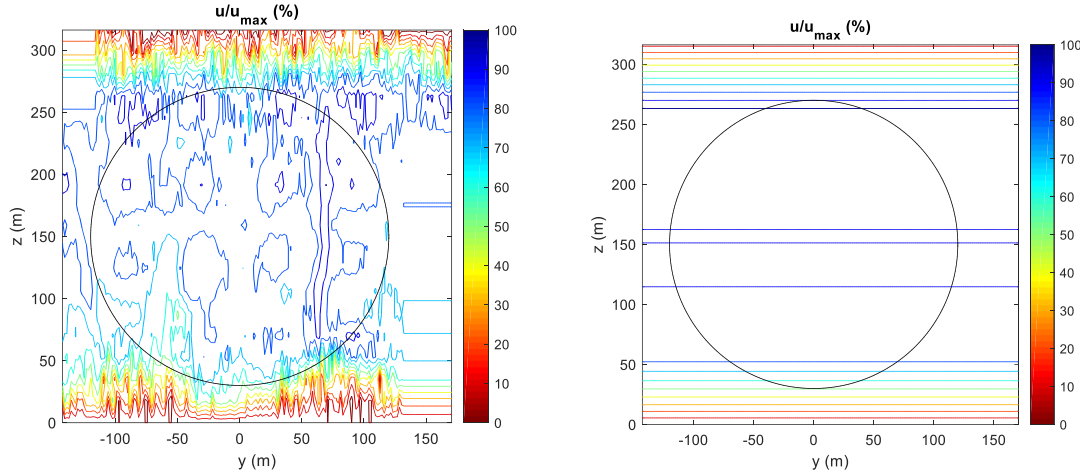


Figure 2.18: Wind field representations, survey data (left) and horizontally averaged (right)

Simulations were then performed in OpenFAST using the reference IEA 15 MW RWT OpenFAST model and the Volturnus-S semi-submersible. Both wind speed representations were simulated, and the platform was both held fixed and also moved up and down sinusoidally 5.4 m in heave to approximate the effect of the floating turbine system moving during wave environments. This was performed to determine if the rotor tip moving up and down within the wind field would have a noticeable effect on rotor performance.

Results from the study are shown in Table 2.8. As shown, representing the wind field using a Power Law or a horizontally averaged representation of the test data has less than 1% change on the mean blade pitch, rotor speed, thrust, or power. Comparing the effect of the heaving platform compared with the fixed, there was small increase in the mean blade pitch setpoint and generally small decreases in rotor speed, thrust, and power. However, the changes on a percent basis were generally less than 1%. Overall, it was concluded that the uniformity of the sampled wind field was adequate for generating appropriate turbine loading and that the wind field could be reasonably implemented in OpenFAST.

Table 2.8. Wind shear sensitivity study, OpenFAST simulation mean responses

Wind Condition	Platform (Fixed / Heave)	Blade Pitch [deg]	Rotor Speed [rpm]	Thrust [kN]	Power [kW]
Power Law	Fixed	4.68	7.14	2,121	14164
Power Law	Heave	4.72	7.15	2,111	14178
% Change, Heave vs Fixed		0.9%	0.1%	-0.5%	0.1%
Test Data	Fixed	4.65	7.22	2,139	14316
Test Data	Heave	4.72	7.21	2,124	14299
% Change, Heave vs Fixed		1.5%	-0.1%	-0.7%	-0.1%

2.3.2 Wind Conditions

The turbine performance testing in Campaign 1 considered the turbine model with a rigid tower affixed to a rigid platform and subject to forcing from various wind environments. The environments were calibrated to be as uniform as possible over the rotor swept area with low levels of turbulence. Calibrated environments were measured using an anemometer survey of the rotor plane and other areas of interest. The calibration survey quantified spatial uniformity using a directional acoustic anemometer to measure wind speed and direction as well as high-resolution hotwires for measuring turbulence. Additional data was collected using dwell-sampling to quantify the time-varying effects and statistics of the wind field. During testing, downwind sampling was conducted to measure certain wake characteristics to measure aerodynamic performance.

The wind environments were based on the operating ranges of the IEA 15 MW RWT, primarily where the controller was most active in Regions 2 and 3, as well as the transition zone between them (Figure 2.19). Lower wind speeds (e.g. Region 1.5) were not considered as they are not key design cases.

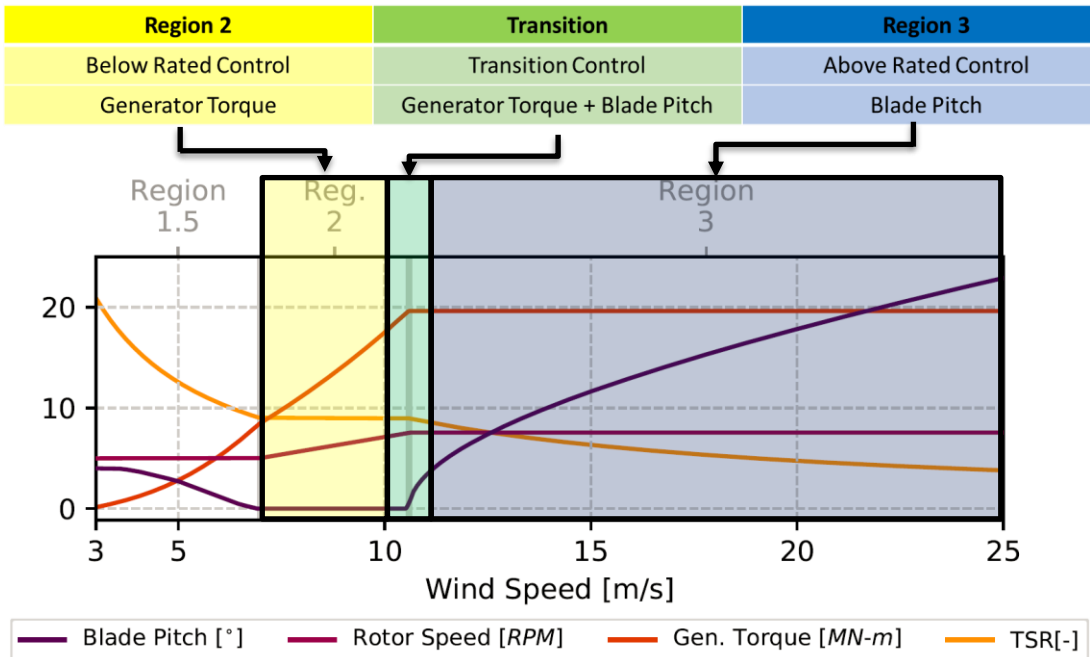


Figure 2.19: Operating ranges of the IEA Wind 15 MW Reference Turbine. Note: These wind speed regions are for the full-scale turbine and don't account for the 21% increased wind used in the

In addition to various wind speeds, several types of environments were considered, as seen in Table 2.9.

Table 2.9: Wind Types

Wind Type	Description	Objectives
Steady	Spatially uniform wind field Constant velocity	Steady-state performance
Dynamic (D)	Spatially uniform wind field Harmonic variation in wind velocity	Mimic relative velocity change due to pitching motion of a floating platform
Spectral (S)	Spatially uniform wind field Spectral distribution of wind velocity	Represent real-world environmental wind conditions (e.g. Kaimal)
Gust (G)	Spatially uniform wind field Linear ramp up / back down of velocity	Mimic wind gust

A complete list of wind environments is outlined in Table 2.10.

Table 2.10: Wind Environments

Wind Case	Operating Region	Wind Type	Wind Speed [m/s] Full Scale
Below Rated 1 (BR1)	Region 2	Steady	9.12
Transition (TR1)	Transition, near Rated	Steady	12.83
TR1D	Transition, near Rated	Dynamic	Same as TR1 Harmonic Variation
TR1G	Transition, near Rated	Gust	Ramp from 8 m/s to 22 m/s
TR1S	Transition, near Rated	Spectral	Same as TR1 Spectral Variation
Above-Rated 1 (AR1)	Region 3	Steady	18.41
Above-Rated 2 (AR2)	Region 3	Steady	23.52
AR2D	Region 3	Dynamic	Same as AR2 Harmonic Variation
AR2S	Region 3	Spectral	Same as AR2 Spectral Variation
Cutout (CO)	Parked Rotor	Steady	27.68
Step	Check controller operation in each operating region	Steady	Steady state set-points from 8-30 m/s (2 m/s steps)

Based on the initial wind surveys, the goal in the basin experiment was to realize as uniform of wind flow as possible over the rotor swept area. The wind speed and turbulence were measured across the rotor plane, with <5% turbulence intensity at hub height and nominal spatial uniformity. Survey transects were performed by continuously sampling data while traversing the probe slowly in the Y direction for a variety of Z elevations and a fixed X location corresponding to the rotor plane. These measurements were compiled to create the survey of the entire rotor plane. An example of the planar wind survey for the TR1 wind case is shown Figure 2.20 where the color map shows the percent deviation from the mean over the rotor swept area.

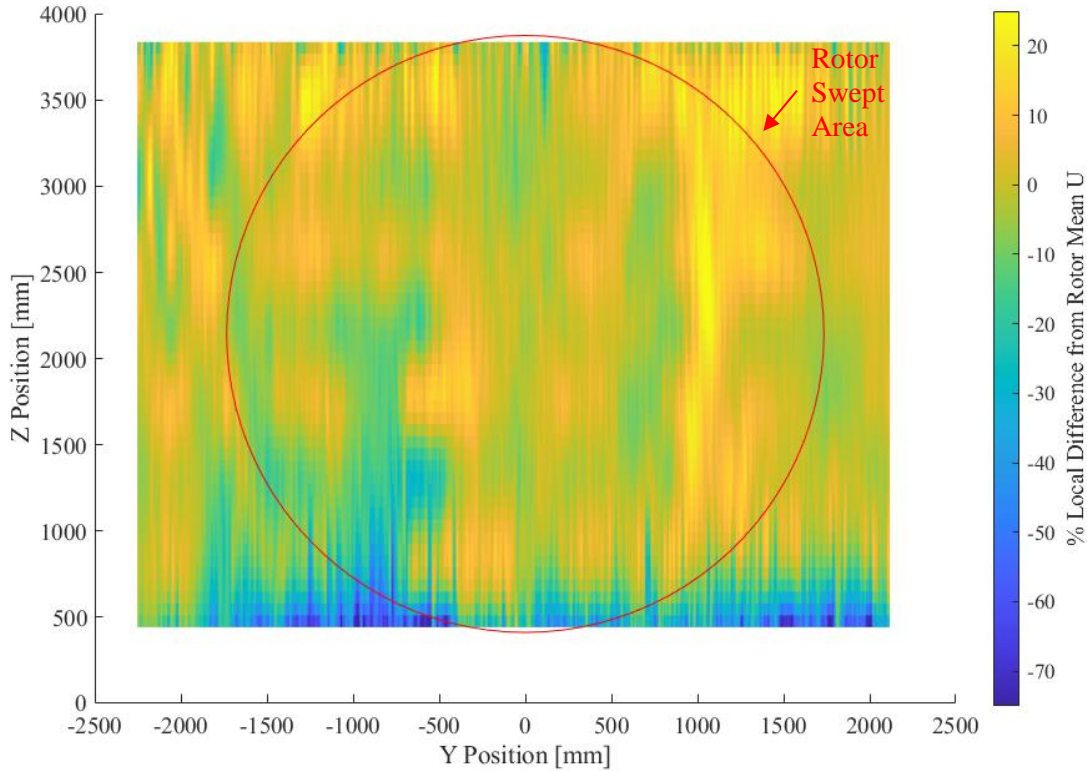


Figure 2.20: Wind Survey for TR1 wind case showing spatial uniformity. X and Y dimensions in model-scale.

Statistics for the steady wind environments are shown in Table 2.11. These values are based on wind surveys where a probe scanned slowly across the wind field. Readings were separated into bins representing about 1 cm/ 0.6 seconds of a transect. Turbulence intensity values were calculated by taking the standard deviation divided by the mean of readings within each bin, then the average turbulence intensity (TI) value was taken as the average of these values representing bins within the rotor area. Coefficient of variance (CoV) was calculated as the standard deviation of bin-mean velocities within the rotor area divided by the overall average velocity. If \mathbf{u}_i represents the set of velocity readings within bin i of n bins and \bar{u}_i represents the mean within that bin, then TI is calculated as Equation 2.13 and CoV as Equation 2.14:

$$TI = \frac{\sum_{i=1}^n \frac{std(\bar{u}_i)}{\bar{u}_i}}{n}$$

Equation 2.13

$$CoV = \frac{std(\bar{u}_{1:n})}{mean(\bar{u}_{1:n})}$$

Equation 2.14

Table 2.11: Wind Survey statistics

Setting	Target*		Avg Speed		TI Avg [%]	CoV Avg [%]
	FS [m/s]	MS [m/s]	FS [m/s]	MS [m/s]		
BR1 Below Rated 1	8.4	1.004	9.117	1.090	4.354	10.380
TR1 Rated	12.71	1.519	12.830	1.534	4.199	10.196
AR1 Above-Rated 1	18	2.151	18.409	2.200	3.782	8.772
R2 Above-Rated 2	24	2.869	23.516	2.811	4.022	9.196
CO Cut-out	30	3.586	27.680	3.308	4.480	9.723

*Note: Targets include the Wind Factor adjustment

2.3.3 Calibrated Environments

Wind calibration dwell measurements were taken at the points outlined in Figure 2.21 for the environments detailed in Table 2.10.

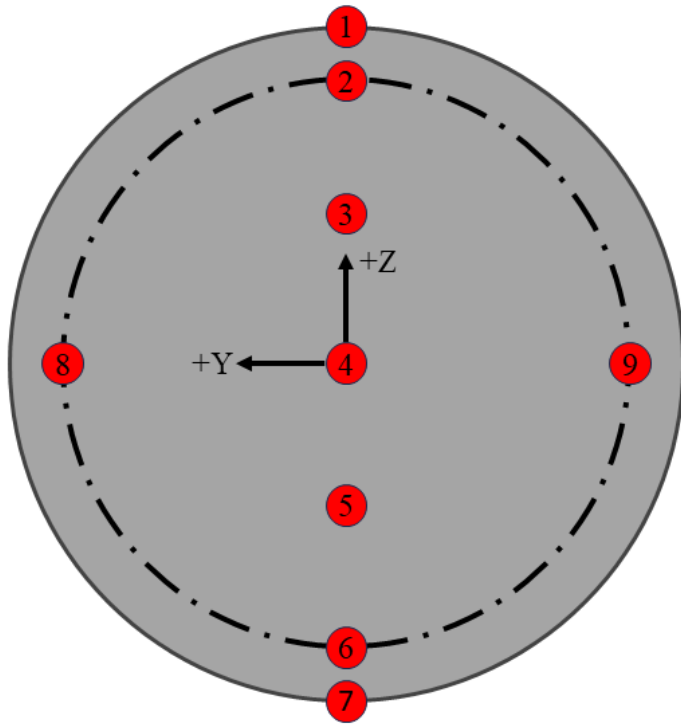


Figure 2.21: Wind dwell measurement locations. Solid line is 100% of blade radius, dashed line is 70%.

The example time series in Figure 2.22 was obtained by averaging the dwells at hub height (points 4, 8, and 9 in Figure 2.21). Data were collected for the entire duration of each environment, including the ramp up period, but a subset was used to compute statistics and frequency distribution, as shown in the associated power spectral density plots with each figure. Plots of all environments are included in Appendix A as Figure A.1 through Figure A.10.

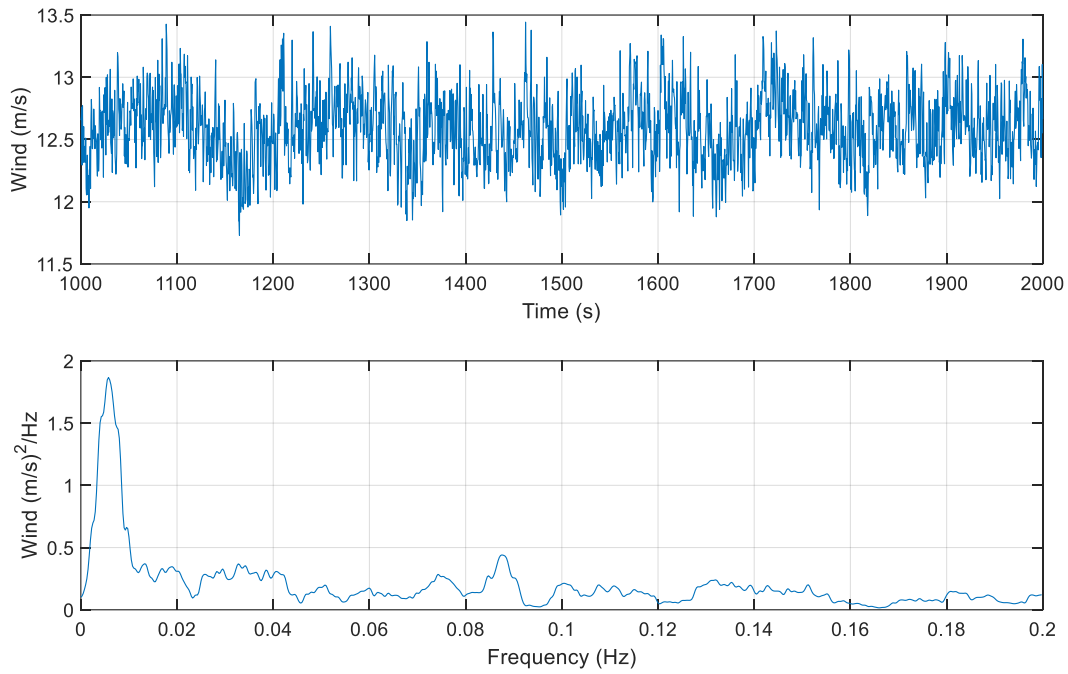


Figure 2.22: TR1 Time History and Power Spectral Density Plots

2.3.4 Test Matrix

A test matrix of wind environments and turbine control parameters is provided in Table 2.12. For each test, the calibrated wind environment setpoints were used and the turbine operation was either manually controlled or under ROSCO control. For the tests utilizing ROSCO, the core features of the controller that were examined include the use of a wind-speed estimator, torque controller, collective blade pitch controller, and a set point smoother (transition controller). These data enabled the calibration of the aerodynamic model and validation of the controller operation in OpenFAST.

Table 2.12: Test Matrix

Test ID	Wind	Duration ¹ [s]	Rotor Control [rpm]	Blade Pitch Control [deg]
A_200-210	TR1	4180	Step 3 to 8	0 to 5 in steps of 0.5
A_211-220	TR1	4180	Step 3 to 8	7 to 25 in steps of 2
A_400-405	AR1	2510	Step 5 to 8	9 to 19 in steps of 2
B_200	TR1	10040	7.56	-2 to 2
B_300	AR1	10040	7.56	10 to 14
B_400	AR2	10040	7.56	15 to 19
D_500	CO	5860	0	-2 to 30
E_200	TR1	10040	7.56	-2 to 2
E_201	TR1	2510	7.56	-1 to 5
E_300	AR1	10040	7.56	10 to 14
E_301	AR1	2510	7.56	10 to 16
E_400	AR2	10040	7.56	15 to 19
E_401	AR2	2510	7.56	15 to 21
G_600	Step	25010	ROSCO	ROSCO
H_104	BR1	3000	ROSCO	ROSCO
I_202	TR1G	2150	ROSCO	ROSCO
I_203	TR1	3000	ROSCO	ROSCO
I_204	TR1S	12000	ROSCO	ROSCO
I_205	TR1D	2500	ROSCO	ROSCO
J_200	TR1	3000	ROSCO	ROSCO, no peak shaver
J_201	TR1G	2150	ROSCO	ROSCO, no peak shaver
J_202	TR1S	12000	ROSCO	ROSCO, no peak shaver
K_300	AR1	3250	ROSCO	ROSCO
K_400	AR2	3350	ROSCO	ROSCO
K_401	AR2D	2850	ROSCO	ROSCO
K_402	AR2S	12000	ROSCO	ROSCO
K_500	CO	3500	ROSCO	ROSCO

¹Test durations are listed at full scale and include rotor spin-up time.

For the C_p/C_t Performance Curves tests (sequence A_###), the turbine was operated in a variety of environments under fixed rotor speed control without ROSCO and subject to rated (TR1) and above-rated (AR1) winds. The turbine RPM was stepped through constant speed setpoints during the steady winds to measure steady-state performance for several different operating TSR values. This was continued for a range of blade pitch angles to collect enough data to compute the turbine power (C_p), thrust (C_t) and torque (C_q) surfaces as a function of TSR and blade pitch. This process was then repeated in the above-

rated wind condition to investigate Reynolds effects and create additional performance curves if needed to retune the controller.

For the Sensitivity Study tests (sequence B_###), the turbine was operated at the rated rotational speed in both rated and above-rated winds and a stepped blade pitch setpoint was imposed that stepped +/- 2° about the estimated steady-state pitch setpoint in increments of 1°. This allowed for calculation of rotor torque and thrust sensitivities with respect to changing blade pitch.

The Parked Performance tests (sequence D_###) utilized a parked turbine and the cut-out wind speed. The blade pitch was then stepped through the range of blade pitches from -2 to 30° to provide turbine drag data for a variety of blade pitch angles.

The Dynamic Performance tests (sequence E_###) were conducted near rated wind speeds and in the above-rated conditions with the turbine operating at the rated rotor speed. The blade pitch setpoint was linearly ramped about the steady-state blade pitch setpoint to quantify the dynamic response of the rotor to changing blade pitch.

Data from the first tests in Sequence A were used to tune the ROSCO controller. This work was performed by the NREL team using the ROSCO toolbox and resulted in the C_p , C_t , and C_q surfaces and DISCON.IN files included in the OpenFAST model. The remaining tests utilized the ROSCO controller and were conducted with ROSCO controlling both the generator torque and blade pitch of the turbine.

Sequence G_600 measured performance of the ROSCO controller using a stepped wind file that stepped the wind from below-rated (~ 8 m/s) to above-rated conditions (~28 m/s). Each step was roughly 1 m/s and was held for 500 s to enable the turbine to reach steady-state operation before moving to the next operating point. These data were used to confirm appropriate operation of ROSCO and the ability of the controller to transition between operating regions autonomously.

Performance of ROSCO was further quantified in various wind conditions with and without the Peak Shaver control method. Sequence H measured performance in below-rated conditions. Sequence I utilized environments near rated wind and considered steady, turbulent, and sinusoidally varying dynamic winds. Sequence J considered rated wind environments without the Peak Shaver and considered steady, gust, and turbulent winds. Sequence K investigated performance in the above-rated region and considered two steady wind environments, one low speed and one high speed, as well as spectral and sinusoidally varying higher speed conditions and finally a cut-out wind speed. In general, the conditions with spectral turbulence were most representative of the wind conditions likely to be used in Campaign 4 when testing the floating system.

2.4 Results and Discussion

As part of the experimental campaign, I led data analysis and examination along with the UMaine team. We processed a dataset to publish as well as share with NREL as part of the FOCAL program's cross-collaboration efforts to validate numerous analysis codes. The National Renewable Energy Laboratory led the numerical model validation efforts and I led the UMaine efforts to process the dataset and interpret the results. Three project participants ran their own numerical models in the collaboration and selected results are shown here. The reader is encouraged to reference the original publication for more detail (Mendoza et al., 2022).

2.4.1 Steady-State Performance and Performance-Matching

The first set of tests performed quantified the steady-state response of the turbine for a variety of prescribed blade pitch and rotor speed set points. The measured steady-state performance of the turbine was used to create performance surfaces for the turbine. Figure 2.23 shows the thrust and power

performance as thrust and power coefficients as functions of tip speed ratio for a variety of blade pitch settings.

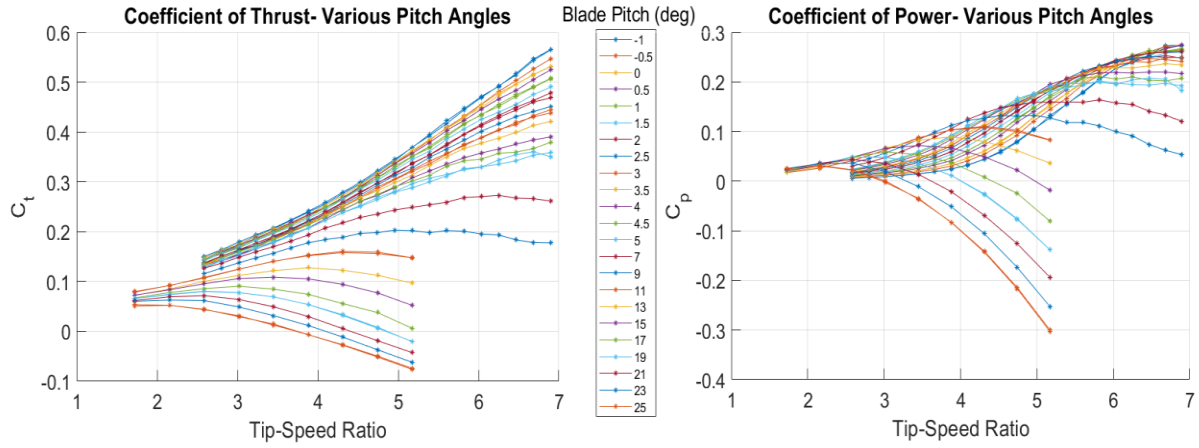


Figure 2.23: Measured as-built wind turbine C_t and C_p vs TSR curves

Once these data were collected, the airfoil polars were tuned to match the measured performance. This was done to account for any discrepancies between the published SD7032 data and the as-built turbine performance data. The process is discussed in Chapter 4 for organizational considerations and summarized here. The process consisted of slightly adjusting the lift and drag characteristics of the airfoil polar to obtain a better match of the steady-state performance between OpenFAST and the experimental data. For Campaign 1, the tuning was performed using data near rated wind speed. The resulting polars were implemented in ROSCO and the OpenFAST model and included with the dataset. As such, the numerical model was optimized for performance matching near rated.

Figure 2.24 shows the measured thrust and torque of the turbine, scaled to full-scale, as compared to numerical predictions of as-built turbine from OpenFAST. As the numerical model was optimized near rated, good performance matching was observed near the rated conditions. However, deviation was observed in above-rated conditions due to increased wind speed affecting the blade section Reynolds

number and altering blade performance. As the wind speed and Reynolds number increased, the rotor became more aerodynamically efficient, generating more lift and less drag. In above-rated conditions, ROSCO was regulating rotor speed through blade pitch and the higher lift resulted in higher rotor torque which caused the controller to feather the blades to compensate. This then resulted in lower rotor thrust values for the same torque target, as shown in the left plot of Figure 2.24.

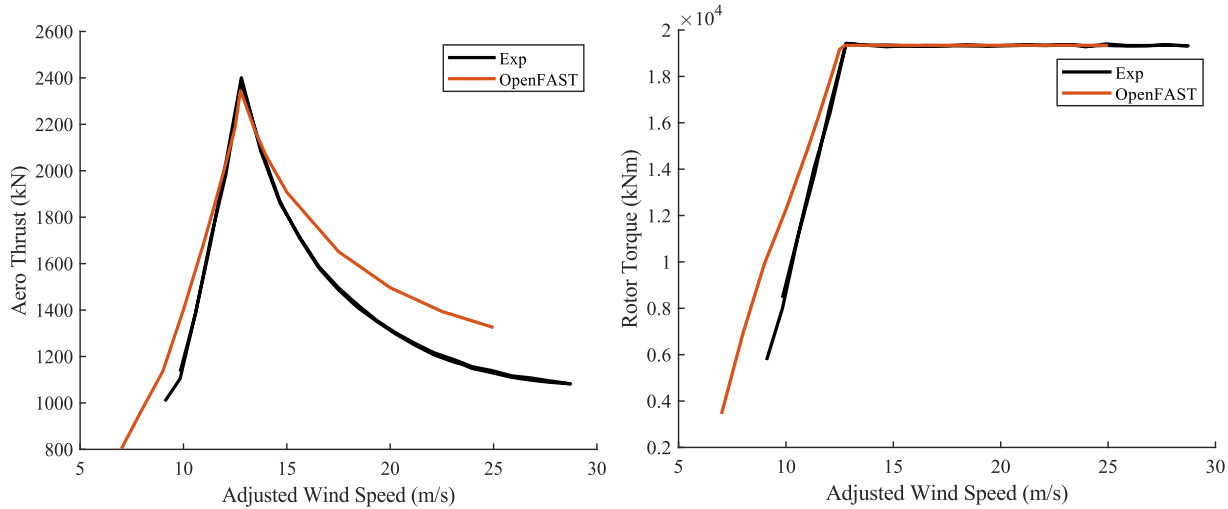


Figure 2.24: Measured ("Exp") vs Simulated ("OpenFAST") turbine thrust (left) and torque (right)

This effect can be approximated by adjusting the drag coefficient of the airfoil in the numerical model. To do this, additional OpenFAST simulations were performed with drag coefficients at 65% and 75% of the baseline values. As shown in Figure 2.25, the results show that as wind speed increases, reducing the drag coefficient in the simulations yields a better thrust match to the experimental values. Near the rated wind speed of 12.71 m/s, the baseline drag coefficient results in reasonable thrust matching while the 75% case matches around 17 m/s and the 65% case around 21 m/s. These results indicate that the Reynolds effects due to changing wind speeds are not negligible. Due to this, after Campaign 1 concluded, another set of polars were generated based on the above-rated performance data measured at higher wind speeds. This was done to create better models for Campaign 4 and is discussed further in Chapter 4.

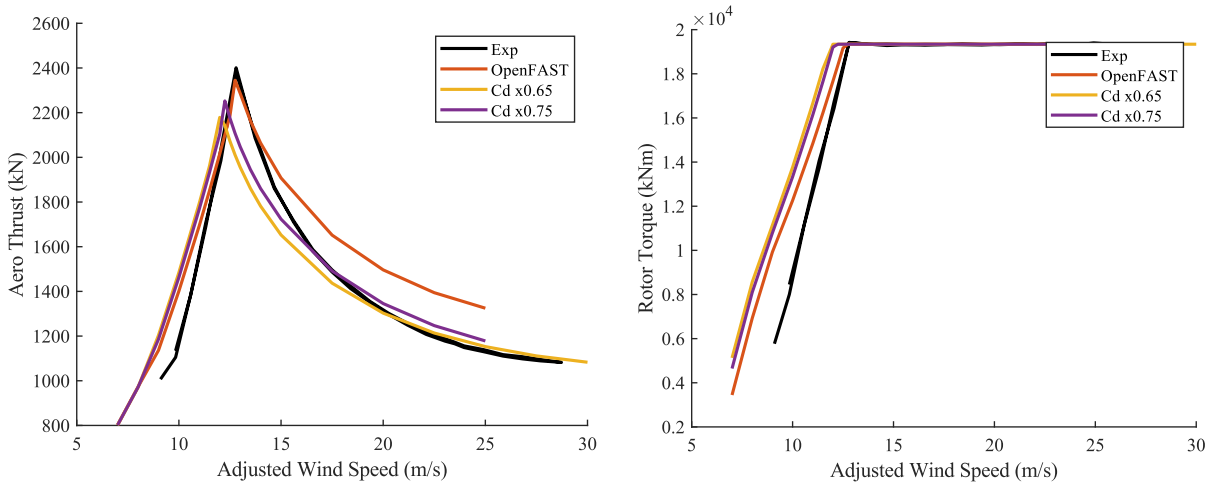


Figure 2.25: Measured ("Exp") vs Simulated ("OpenFAST") turbine thrust (left) and torque (right), including C_d modifications

In addition to tuning ROSCO, these data were also used in the numerical models. The measured performance data was provided to both the numerical models and ROSCO through C_p , C_t , and C_q surfaces as functions of blade pitch and tip-speed ratio. For the tests where blade pitch and wind speed were held constant, the rotor rotational velocity was stepped through a variety of setpoints and the steady-state values were measured. In the validation work, all numerical models showed the ability to reproduce rotor thrust and rotor torque results for the rated condition, as shown in Figure 2.26. The same comparison was also conducted for the tests performed at a blade pitch of 10° and the results were similar.

LC 1.1: Wind speed = 12.83 m/s; Pitch = 0 deg

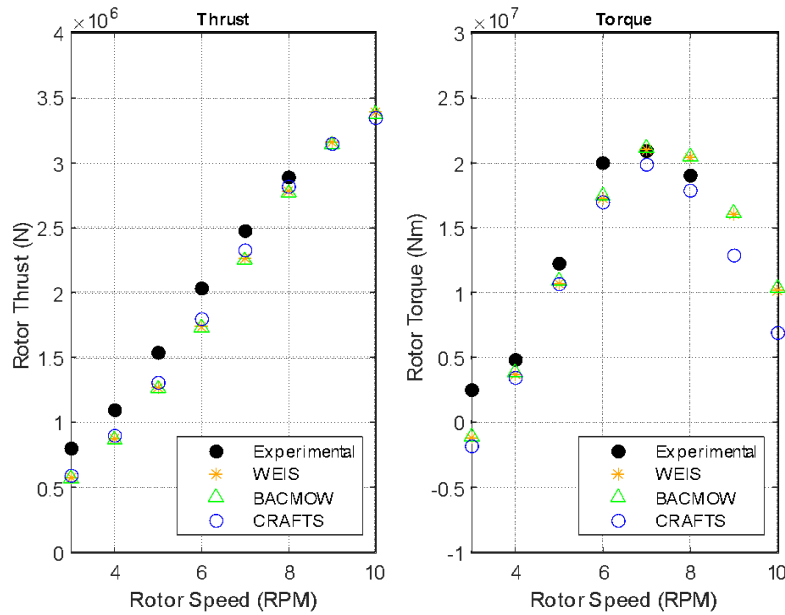


Figure 2.26: Steady-state rotor thrust (Left) and torque (Right) values (Mendoza et al., 2022)

The sensitivity of rotor thrust and rotor torque to changes in rotor speed were also quantified. This was calculated from the experimental data shown in Figure 2.26 through differentiating the data and fitting a 4th order polynomial fit to describe the relationship. As shown in Figure 2.27, the models were able to adequately reproduce this sensitivity for rated conditions.

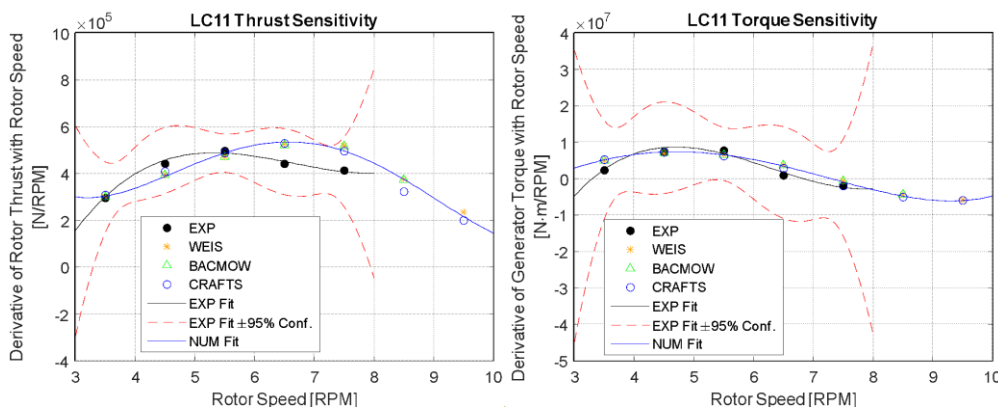


Figure 2.27: Rated Conditions, derivative of rotor thrust (left) and rotor torque (right) w.r.t changing rotor speed (Mendoza et al., 2022)

Tests were also performed where wind and rotor speed were held constant while the blade pitch was stepped and linearly ramped through various setpoints. The blade pitch setpoints are shown in Figure 2.28 and represent perturbations in blade pitch from the nominal rated blade pitch setting.

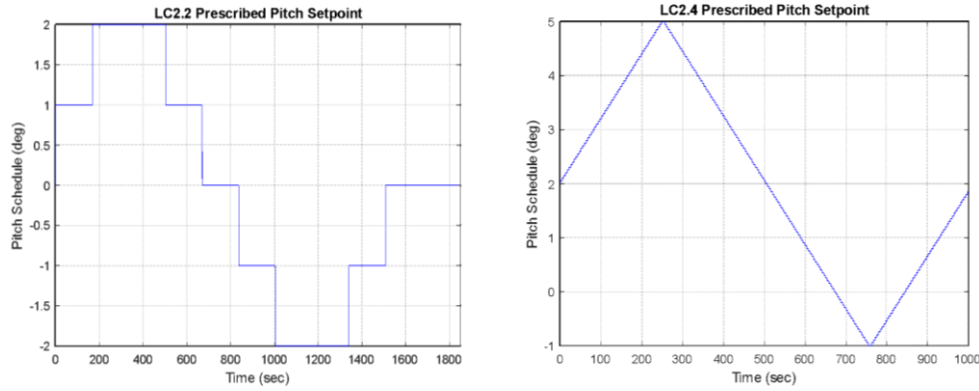


Figure 2.28: Blade pitch schedule for stepped and ramped cases (Mendoza et al., 2022)

Performance data from these tests are shown in Figure 2.29.

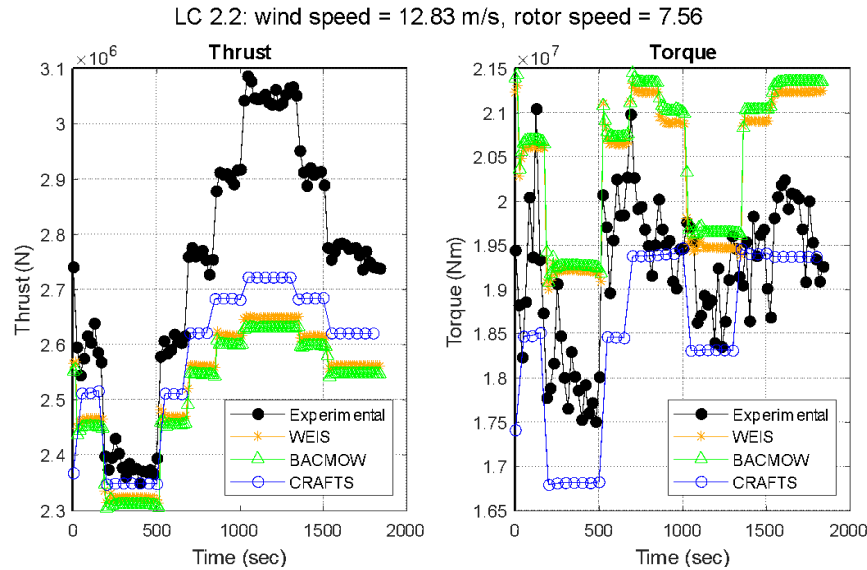


Figure 2.29: Rated conditions, rotor thrust (left) and torque (right), response to stepped blade pitch (Mendoza et al., 2022)

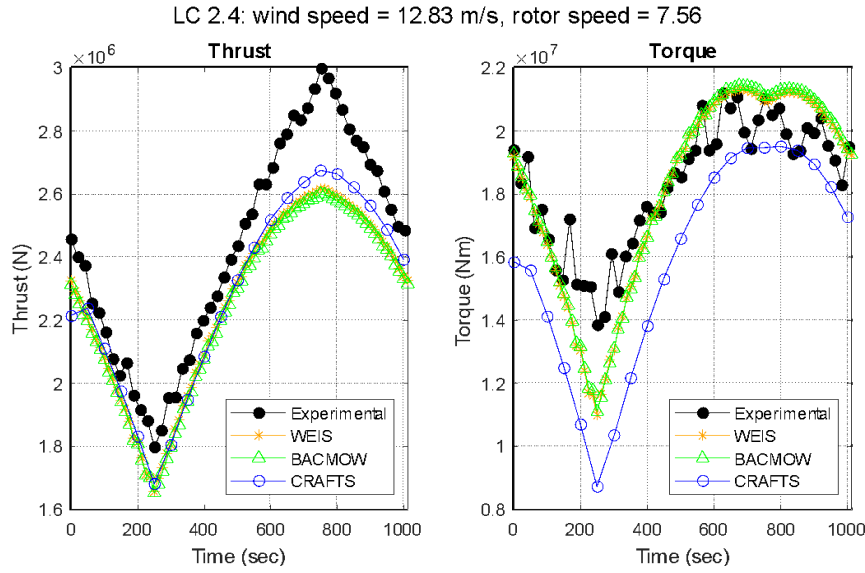


Figure 2.30: Rated conditions, rotor thrust (left) and torque (right), response to ramped blade pitch (Mendoza et al., 2022)

As can be seen, the validation work showed a reasonable match around the rated conditions (0-600s in Figure 2.29 and 0-500s in the Figure 2.30), where the thrust values are $<2.3E+06$ N. After this time there were larger discrepancies the further the blade pitched away from its normal operating range as the angle of attack decreased.

These data were also used to calculate the derivative of rotor torque with respect to blade pitch, which is important in the calculation of the integral gain in the ROSCO Region 3 controller. As can be seen in Figure 2.31, the numerical models predicted similar torque sensitivities with respect to blade pitch, especially near rated blade pitches around 1.5 deg. There was more discrepancy in the sensitivity of thrust to changing blade pitch, which was considered in tuning of the floating feedback loop as discussed in Chapter 4.

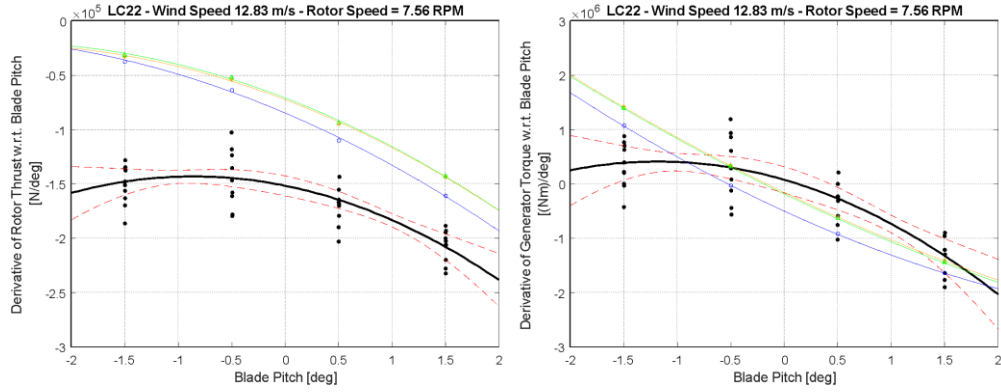


Figure 2.31: Rated Conditions, derivative of rotor thrust (left) and rotor torque (right) w.r.t changing blade pitch (Mendoza et al., 2022)

Values determined for the as-built FOCAL turbine were provided with the data set in the DISCON.IN controller specification files for the rated and above-rated controller tunings and associated C_p , C_t , and C_q surfaces.

2.4.2 Turbine Performance Under ROSCO Control

With the controller tuned, ROSCO control was exercised under a number of dynamic wind cases, including harmonic variation (designed to mimic the pitching motion of the system while floating), spectral turbulence, and extreme gusts. The first set of tests considered a stepped wind speed, ranging from below rated (~8 m/s) to above-rated (~28 m/s) conditions and back down in steps of ~1 m/s. Each wind speed was held for roughly 500 seconds and steady-state conditions were measured from the average response at each step. This was used to evaluate the operating points that ROSCO determined for each wind speed and verify the performance. In the validation work, these data were presented as steady-state operating points. Rotor thrust and its derivative with respect to wind speed are shown in Figure 2.32.

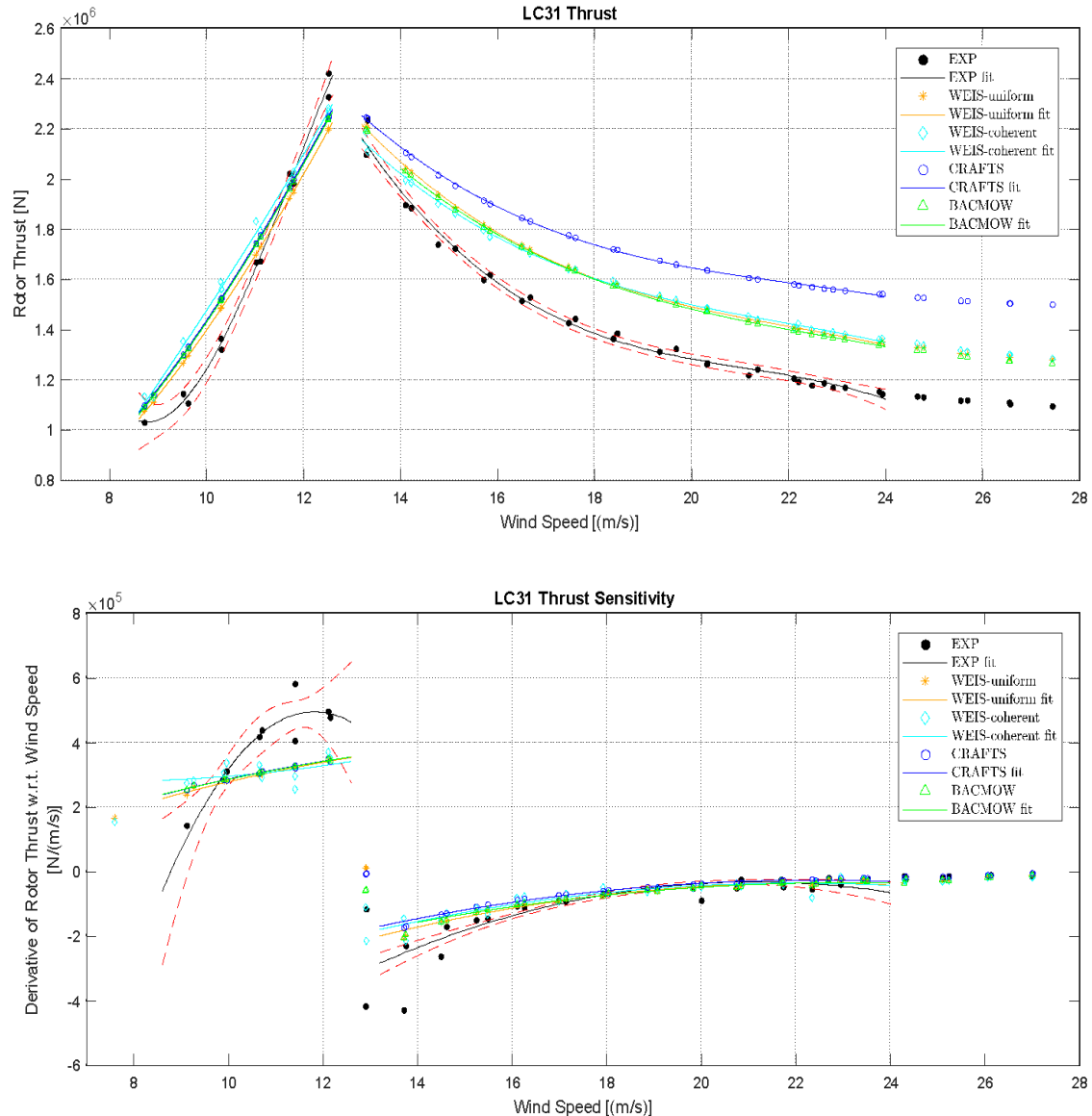


Figure 2.32: ROSCO rotor thrust (top) and derivative of rotor thrust w.r.t wind speed (bottom), response to stepped wind (Mendoza et al., 2022)

As was shown from the open-loop tests, the numerical models matched the mean thrust load near the rated conditions, shown here at the “adjusted wind speed” of 12.8 m/s. In higher wind speeds, the trend was the same where the controller pitched the blades more in the experiment than in the numerical models and the thrust load reduced as wind speed increased. This was also attributed to Reynolds effects, where the relative lift and drag performance of the airfoil changed as wind speed increased and is discussed

more in Chapter 4 when considering the above-rated tuned polars. The derivative of rotor thrust with respect to wind speed was also well represented in the above-rated region. Near rated conditions, the discontinuity between below- and above- rated control schemes represented a more complicated region to model as it incorporated transition between generator torque control and blade pitch control, and the performance match was less accurate.

Rotor torque and its derivative with respect to wind speed are shown in Figure 2.33. As expected, the torque was constant in the above-rated conditions, demonstrating the ability of ROSCO to maintain reasonable rotor behavior through blade pitch actuation. The mean torque values are well matched near rated and through above-rated and the derivative of generator torque to changing wind speed is well matched. This is largely due to the constant rotor torque setpoint. The closed-loop response of the turbine masked the open-loop aerodynamic sensitivity to changing wind speed as the blade pitch was controlled to minimize rotor torque changes as the wind speed changed. In below-rated conditions, the values from the experiment were lower than the numerical models and the derivative of generator torque with respect to wind speed was higher with a similar trend. As the rotor performance and airfoil tunings were prioritized near rated and below-rated conditions were not considered for Campaign 4, discrepancies in below-rated conditions were not explored further.

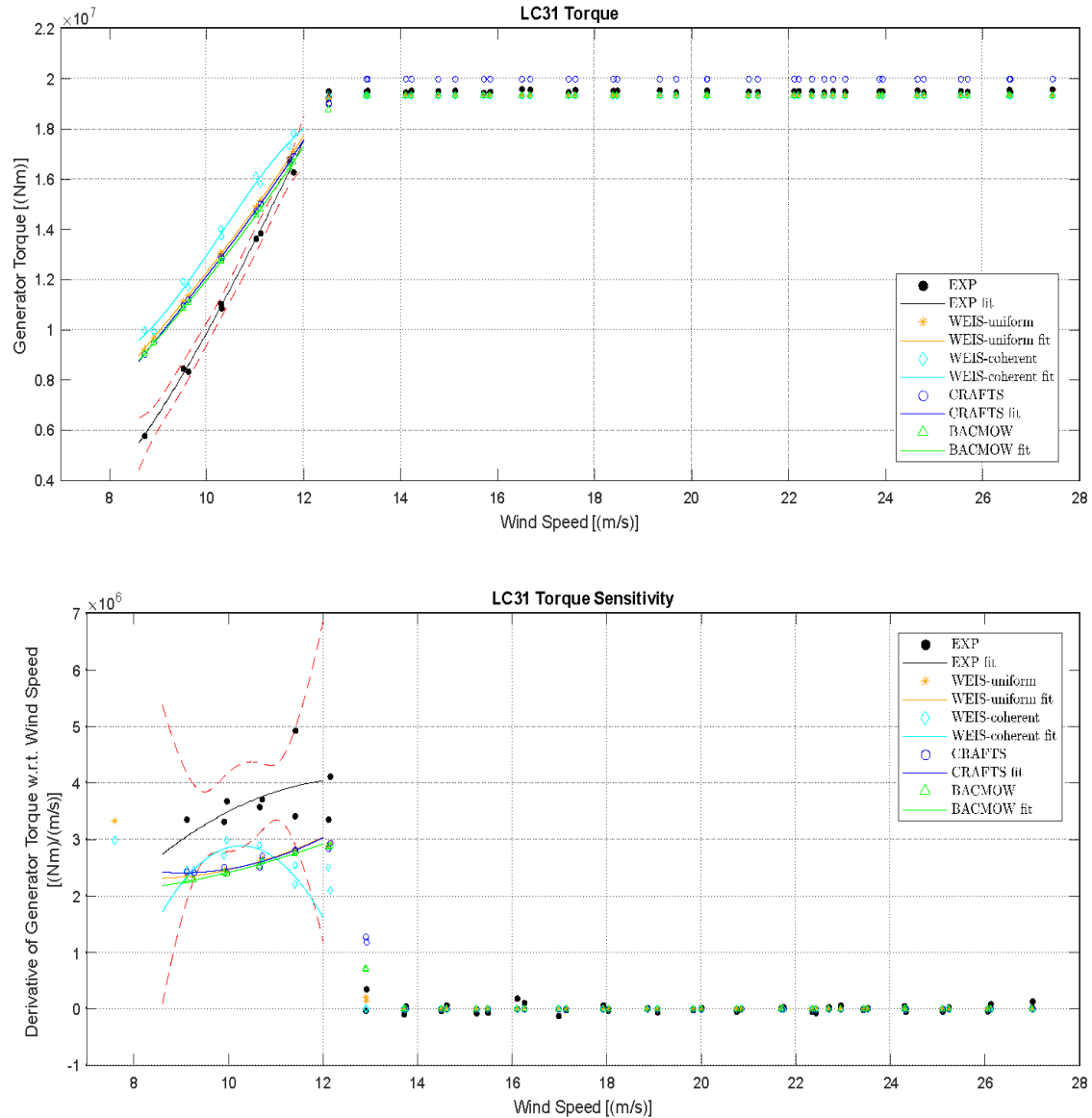


Figure 2.33: ROSCO rotor torque (top) and derivative of rotor torque w.r.t wind speed (bottom), response to stepped wind (Mendoza et al., 2022)

Figure 2.34 shows the control response to a large, sustained gust that carried the turbine from below-rated conditions, through the transition region, and into above-rated conditions, at which point the wind speed was held constant. The plot shows that in the below-rated conditions ROSCO controlled the rotor torque with a constant blade pitch. However, as the wind increased and the turbine moved into above-rated conditions, the blades were pitched to feather to reduce the excess load and maintain rated power. The

turbine then reached a steady-state condition in the above-rated region. The initial overshoot was partially due to the pitch rate limit in ROSCO, as shown in the linear change in blade pitch near 100 s, which determined how fast the turbine is allowed to pitch the blades. Under normal conditions the turbine does not exceed the pitch rate limit; however, increasing this limit for model tests was implemented prior to Campaign 4 to help mitigate excessive loads on the test turbine. This case was explored in the validation campaign and quantities such as rise time, settling time, and overshoot/peak were compared with numerical models.

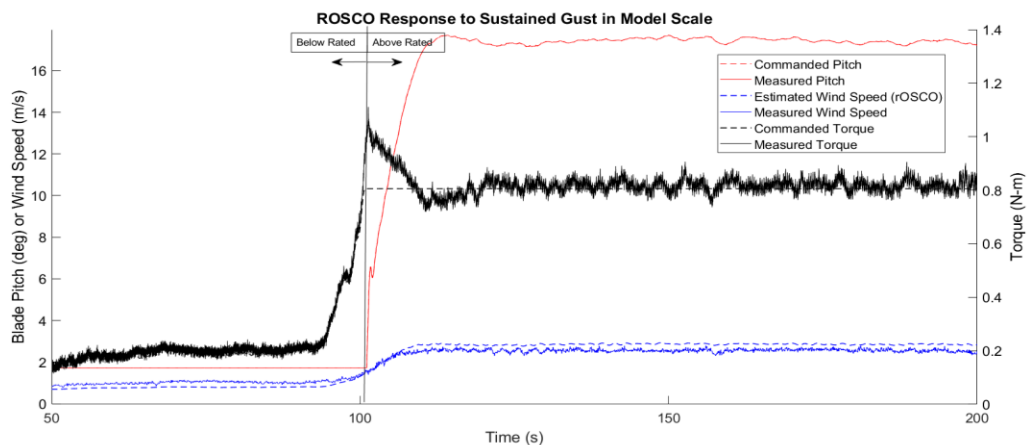


Figure 2.34: System response to a large, sustained gust case (Mendoza et al., 2022)

2.5 Conclusions

Campaign 1 of the FOCAL project successfully commissioned the 1:70-scale turbine and supported the validation of various numerical models.

Key Findings

- The performance-matched rotor methodology was successfully used to design and test a model-scale turbine with realistic turbine controls in a Froude-scale wind/wave basin test

- Steady-state rotor thrust was well matched near rated conditions with reasonable rotor torque to enable a constant generator torque setpoint throughout above-rated conditions
- NREL’s ROSCO controller was run real-time in-the-loop with the model turbine to regulate the turbine using control strategies of generator torque and blade pitch control
- As-built rotor performance was used to successfully tune the ROSCO blade pitch PI controller gains. The sensitivity of rotor torque to changing blade pitch was well scaled and resulted in a reasonable blade pitch schedule for the as-built turbine.
- Various numerical models were validated, including the OpenFAST model used to further inform testing in Campaign 4.

Turbine performance in both steady-state and ROSCO control was determined adequate for subsequent testing in the FOCAL program. No instabilities in the generator torque or blade pitch controller were observed, even when subjecting the turbine to environments well outside expected operating conditions. ROSCO was able to regulate rotor speed in the above-rated conditions through blade pitch actuation and the performance near rated was representative of the scaled performance target thrust and rotor speed.

Some issues were identified during testing that required attention prior to subsequent campaigns. It was noticed that at 1:70-scale, system loads were relatively small and sensitive to disturbances present in the testing. For example, rotor imbalance issues on a single blade introduced 1P excitation that was not representative of a real turbine and blade tip interaction resulted in 3P forcing. These were investigated and improved on prior to the Campaign 4 work through remounting the blade and applying a pitch offset in the controller to address the error as well as modifying the test layout. Other tasks undertaken to prepare the 1:70 scale turbine model and ROSCO control to prepare for Campaign 4 on a floating platform included:

- Tuning the floating feedback control loop. This required as-built system properties, including the system pitch period and operational frequencies
- Tuning above-rated airfoil polars to help address discrepancies with numerical models in above-rated conditions
- Tuning the tower to have appropriate first fore/aft bending frequencies on the floating foundation
- Increasing the blade pitch limits in ROSCO

As indicated, the data was used extensively in a cross-collaboration effort to validate numerical models.

This validation data set and corresponding numerical models are valuable for controls co-design and can be utilized to develop the next-generation technology needed to revolutionize floating offshore wind through optimization and deep cost reductions. All FOCAL data sets, including Campaign 1, are available to the public through the U.S. Department of Energy’s Atmosphere to Electrons Data Access Portal (Robertson, 2023a), including model specifications, controller definitions, and test data.

Chapter 3

CAMPAIGNS 2 AND 3: WAVE ONLY HULL AND TMD TESTING

3.1 Research Objectives

Chapter 3 presents my work designing and testing the model hull, including integration of tuned-mass dampers into the VolturnUS-S design which did not include any active hull elements. The scale model representation of the tuned-mass dampers was developed and built along with the rest of the scale model. Testing was performed back-to-back in two campaigns where Campaign 2 focused on characterization of the hull and TMDs while Campaign 3 considered internal structural loads. These campaigns were conducted simultaneously, generating a combined dataset to validate numerical models that consider dynamic damping elements in the hull as well as structural loads, which are important when looking to optimize structural design. This dataset was used to validate numerical models from a variety of teams, including the OpenFAST model developed by the FOCAL team which modeled the TMDs in the newly developed structural control module. To focus on the performance of the hull in wave-only conditions, the model was tested with a simplified topside where the turbine was represented by a point mass attached to a flexible tower to match the proper inertial properties and Froude-scaled natural frequencies for the system. Load cells in the hull were utilized to measure internal structural loads during the tests and a variety of TMD tunings were explored. The primary objectives for Campaign 2/3 were:

- Develop a hull-based control approach that demonstrates the ability to decrease motion and associated loads in the system, thus showing the potential for light-weighting floating substructures. This included:
 - Developing, and then scaling a control methodology to represent the appropriate system dynamics in the scaled wind/wave facility.

- Implementing vertically mounted passive TMD systems in each hull. The model-scale system consisted of actively controlled TMD devices programmed to simulate the behavior of passive TMD systems at full-scale. This allowed shore side changes to the TMD spring constant and damping coefficient through programming rather than physical reconfiguration of the system. The active control of the TMD was not integrated with ROSCO, but its effects on system dynamics influenced the turbine's response.
- Generate a dataset to validate motion/loads of a floating wind system with and without passive TMD platform control, showing impact of the TMD system under wave loading. This was accomplished by running a series of system identification tests and wave conditions with the varying controller settings.
- Generate a dataset to validate member-level loads for the hull substructure (floating platform hull) under wave loading. Two pontoon legs were instrumented with a 6DoF load cell to collect load data on the pontoon structure in real time during both Campaign 2 and 3, thereby combining the Hull and TMD characterization tests (Campaign 2) and the hull structural load test (Campaign 3).

3.2 Design Methodology

The hull chosen for FOCAL needed to satisfy the requirements of being a publicly available design and capable of supporting the IEA Wind 15 MW RWT. To this end, it was chosen to create a hull based on the reference hull designed by the University of Maine to support the IEA Wind 15 MW RWT. This reference semi-submersible design is termed the VolturnUS-S and is publicly available along with the turbine design. To use for FOCAL, modifications were made to the hull to include TMDs, including moving ballast mass into the TMD to act as actuated mass, but the overall system properties were still

based on the VolturnUS-S target values when possible. The scaled hull design is presented in the Test Report (Robertson, 2023b) for Campaign 2/3 and summarized here.

3.2.1 Full-Scale Design

The VolturnUS-S is a semi-submersible design with three buoyancy columns and a central column, attached to each other via underwater beams. It is a passive, fixed-ballast system, meaning it is designed to be stable without any active hull control devices. Main particulars are presented in Figure 3.1 and Table 3.1.

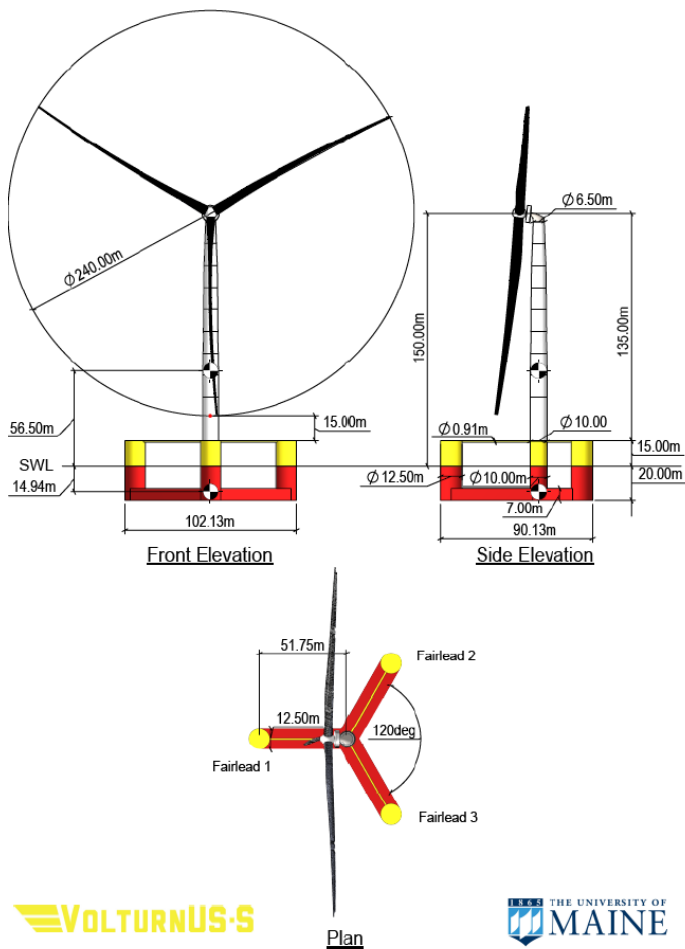


Figure 3.1: Overview of the VolturnUS-S semi-submersible reference hull (Allen et al., 2020)

Table 3.1: Main parameters of the VolturnUS-S reference hull

Parameter	Unit	Value
Rotor Diameter	m	240.00
Keel to hub	m	170.00
Waterline to hub	m	150.00
Keel to Mooring	m	6.00
Draft	m	20.00
Freeboard	m	15.00
Mass		
Hull mass	t	3999
Ballast mass	t	13840
RNA mass	t	991
Tower mass	t	1263
Total mass	t	20093
CG		
CG Hull & Ballast (from keel)	m	5.06
Inertias about CG		
Hull & Ballast only - Ixx, Iyy (pitch, roll)	kg-m ²	1.251E+10
Hull & Ballast only - Izz (yaw)	kg-m ²	2.367E+10

3.2.2 Scaling Methodology

The Froude scaling approach that was followed to design the hull follows that outlined in Chapter 1 using the same scale ratio of $\lambda=70$ and density factor of $\varphi=1.025$.

3.2.3 Turbine Scaling Methodology

For FOCAL Campaign 1, a model-scale turbine that closely matched the IEA Wind 15 MW RWT in overall thrust and power was developed. Since Campaign 2/3 are focused on the floating platform, a stand-in dummy mass with similar mass and CG properties to the Campaign 1 rotor-nacelle assembly was employed. The measured properties are presented in Section 3.3.7.

3.2.4 TMD Design

To provide validation data for numerical models and support design optimization of floating offshore wind systems, the TMD design used for FOCAL needed to be representative of concepts being considered for floating offshore turbines and capable of being represented in design tools. As of OpenFAST v3.0.0, a Structural Control (StC) module has been developed and included in ServoDyn to allow modeling of tuned mass dampers in the system. To satisfy the test objectives of Campaign 2 and attenuate platform motion, tuned mass dampers were designed into each outer buoyancy column and act vertically. This orientation allowed for attenuation of heave motion through synchronous motion of all actuators as well as pitch or roll mitigation through coupled motion. This arrangement was modeled in OpenFAST by defining the inertial properties, line of action, and stiffness and damping characteristics of each element.

Integrating the TMD system into the VolturnUS-S design presented challenges, most notably that the semi-submersible platform was already designed to be stable with fixed ballast and therefore didn't present a compelling dynamic environment suitable for TMDs. To create a workable solution, the TMD design aimed to mobilize some of the fixed ballast mass in the TMD system while maintaining favorable overall dynamics and stability through reasonable mass distribution and center of gravity. Initial design work was performed in OpenFAST, prior to it having the ability to model structural control elements. As such, a simple spring-mass-damper physics model was created and coupled with OpenFAST to include the effects of passive TMD elements through reaction forces at the system center of gravity. This initial study helped inform the design envelope of allowable mass, stiffness, and damper values to generate favorable responses of key system frequencies.

Intuition indicated that there was a direct relationship between the amount of mass in a TMD and the influence it can have on system response. Therefore, it followed that maximizing the mobile mass in a TMD would yield the most favorable design. However, due to the vertical line of action of the TMD,

mobilizing more mass also effectively increased the system center of gravity. This was especially true when trying to retrofit ballast mass as the TMD mass as ballast was located low in the structure. Therefore, the trade-off between dynamic and static stability was considered when designing the TMD. For a semi-submersible design using tuned liquid column dampers, favorable results were seen by mobilizing 2% of the system mass (Coudurier, 2015) and Stewart & Lackner (2014) suggest that 1-2% of the structural mass is typical of civil engineering projects.

Physical size constraints also played a role. The TMD system was intended to be installed inside the outer buoyancy columns and therefore, the motion of the TMD was required to remain inside the hull. While hull penetrations could have been considered, it was deemed impractical for implementation in a scale model test and presented challenges with water intrusion and additional hydrodynamic considerations. Hence, the stiffness and damping of the system were required to provide the correct frequency of response for the TMD as well as reasonable excursion amplitudes. Since the motion was not biased towards the positive or negative direction, the mass was designed to rest at the mid-height of the column at equilibrium to maximize the motion amplitude available.

As discussed earlier, this TMD arrangement most directly influenced platform heave, pitch, and roll motion. For optimization, platform pitch and heave motion were the primary targets of the TMD system and key performance metrics used in the design study were heave and pitch motion, as well as the related responses of tower base fore/aft bending moment and nacelle fore/aft acceleration. Other degrees of freedom were not considered as impactful to system design as they don't typically combine with the loads from the turbine.

Initial design work determined that TMD masses of 686-1,715 MT per leg were possible without adversely affecting overall system stability, representing 3-9% of the total system mass. Frequencies of interest to target were the platform pitch mode, wave energy frequency, and tower first fore/aft bending

mode. These frequency targets, along with the mass ranges, defined the allowable TMD stiffness values.

Finally, a range of damping ratios were chosen, ranging from 0.05 to 0.5, to explore the design space.

Analysis was performed in OpenFAST using the IEA Wind 15 MW RWT and VolturnUS-S models with the added TMD physics. The wind/wave environments used are shown in Table 3.2 and are typical of design load cases (DLC) corresponding to an operating case (DLC 1.2) and a 50-year return period sea (DLC 6.1), as defined in (American Bureau of Shipping, 2020).

Table 3.2: TMD design wave environment definitions

Environment	Wind		Waves		Freq	Zeta
	U [m/s]	Hs [m]	Tp [s]	[rad/s]	[-]	
DLC 1.2	12.0	1.16	7.25	0.2 – 2	0.05 – 0.5	
DLC 6.1	58.7	10.7	14.2	0.2 - 2	0.05 – 0.5	

Results from the design study indicated that a modest reduction in platform pitch motion was possible in the operational case through targeted TMD action and the effect was significantly more noticeable in the larger wave environment of DLC 6.1. Results are shown in Table 3.3 and Table 3.4 for the most impactful mass and damping ratio combinations and there was no single configuration that resulted in improved performance for all metrics. When considering platform pitch motion, the target frequency for DLC 1.2 when the turbine was operational was 0.20 rad/s, while for the parked turbine in DLC 6.1 it was 0.23 rad/s. This was due to the aerodynamic effect of the turbine which changed the platform pitch period and is further discussed in Chapter 4. In DLC 1.2 conditions, reductions in the standard deviation of 1-3% were shown for masses of 686 MT and 1,715 MT respectively. Similarly, standard deviation of nacelle fore/aft acceleration decreased 5-10% and tower base fore/aft bending moment 1-3% for the same TMD mass values. In DLC 6.1 conditions, the responses were much more noticeably affected, and the damping ratios were 0.1 for the 686 MT mass and 0.2 for the 1,715 MT mass. It was noted that the smaller mass experienced more TMD motion than desired with a range of 22.4 m as opposed to the design target of 21 m. Reductions in standard deviation of 22-29% were shown in platform pitch, and 12-13% in tower base

bending moment. Interestingly, the nacelle fore/aft acceleration was less attenuated, showing a reduction of 1% or increase of 3% for the 686 and 1,715 MT mass respectively.

Responses at tower frequencies also showed promise. While TMDs tuned to these higher frequencies had little effect on overall system motion, changing platform pitch standard deviation and maximums less than 2%, the effect on nacelle fore/aft acceleration and tower base bending moment was significant. In DLC 1.2 conditions, the standard deviation of fore/aft nacelle acceleration was reduced 12-19% for the standard tower and maximum values by 19-28%. Tower base bending was also reduced, with the standard deviation reducing 2-4% and maximum value 1-2% respectively.

Table 3.3: TMD Effects on Global Performance, Load Case DLC 1.2

Load Case DLC 1.2	Baseline Standard Deviation			Baseline Maximum						
	RNA Acc_x [m/s ²]	TwrBot My [N-m]	Ptfm Pitch [deg]	RNA Acc_x [m/s ²]	TwrBot My [N-m]	Ptfm Pitch [deg]				
	0.141	5.07E+07	0.684	0.525	4.03E+08	4.69				
TMD Properties			Change Over Baseline %			TMD Motion				
m [MT]	ω [rad/s]	ζ [-]	RNA Acc_x [%]	TwrBot My [%]	Ptfm Pitch [%]	RNA Acc_x [%]	TwrBot My [%]	Ptfm Pitch [%]	Range [m]	V _{max} [m/s]
686	0.20	0.2	-5.54	-1.53	-1.24	-4.17	1.59	2.60	13.2	1.20
1,715	0.20	0.2	-9.86	-3.22	-2.98	-16.70	4.40	5.28	12.3	1.10
686	2.03	0.1	-12.60	-2.40	-0.58	-19.40	-1.32	-0.02	6.9	1.00
1,715	1.70	0.1	-18.50	-3.88	-1.12	-27.60	-1.96	-0.04	6.9	0.91

Table 3.4: TMD Effects on Global Performance, Load Case DLC 6.1

Load Case DLC 6.1	Baseline Standard Deviation			Baseline Maximum						
	RNA Acc_x [m/s ²]	TwrBot My [N-m]	Ptfm Pitch [deg]	RNA Acc_x [m/s ²]	TwrBot My [N-m]	Ptfm Pitch [deg]				
	0.484	1.27E+08	1.78	1.35	5.14E+08	6.98				
TMD Properties			Change Over Baseline %			TMD Motion				
m [MT]	ω [rad/s]	ζ [-]	RNA Acc_x [%]	TwrBot My [%]	Ptfm Pitch [%]	RNA Acc_x [%]	TwrBot My [%]	Ptfm Pitch [%]	Range [m]	V _{max} [m/s]
686	0.23	0.1	-0.79	-12.20	-22.20	13.80	-12.30	-6.64	22.5	2.79
1,715	0.23	0.2	3.42	-12.60	-28.70	24.70	-13.30	-24.20	12.8	1.50
686	0.45	0.1	1.81	1.04	0.85	-0.13	-0.44	1.99	23.5	5.52
1,715	0.45	0.1	11.70	6.37	1.44	23.70	-1.00	2.78	21.5	5.14

Based on these results, it was determined to consider TMD designs tuned to the platform pitch frequency and the tower 1st fore/aft mode. A mass of 686 MT for each TMD was selected to have minimal detrimental effect to the overall system CG and stability, while still providing enough mass to be effective. The optimal damping ratios for the 686 MT mass were either 0.2 for the DLC 1.2 cases or 0.1 for the DLC 6.1 cases. As the range of motion in the DLC 6.1 case exceeded the desired 21 m, a value of 0.2 for the damping ratio was chosen to initially tune the TMD system. The design targets for the TMD system were now defined.

3.3 Model Design

The scale model was designed with the following objectives in mind:

- Match the target geometry, mass, CG, and moment of inertia properties
- Interface with and support the rotor tower and topside
- House a vertically actuated mass in each outer buoyancy column
- Utilize on-board instrumentation to improve signal quality and reduce umbilical cable requirements
- Integrate load measurements into the bottom pontoon beams to measure internal structural loads

The following sections present the design and as-built properties the main components of the floating hull system; namely the hull structure, TMD, tower, nacelle, mooring, and instrumentation system. The main component arrangement is shown in Figure 3.2 and the model installed in the basin is shown in Figure 3.3.

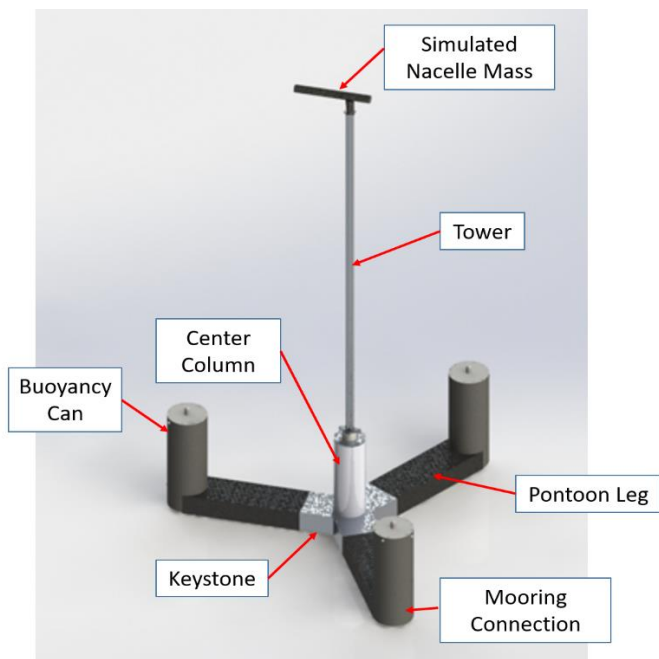


Figure 3.2: Components of the floating wind system

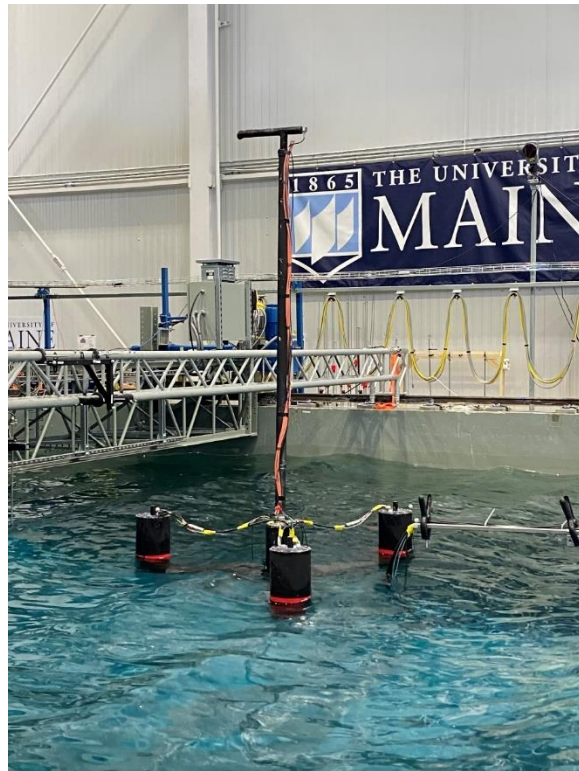


Figure 3.3: Assembled Campaign 2 model in the W2

3.3.1 System Overview

As-built properties for the assembled system are provided in Table 3.5. Measured, and in some cases, derived values are provided for the overall CG x-offset, overall CG y-offset, and model inertia about the y-axis. Derived values for some parameters were determined using the OpenFAST model and measured equilibrium position/orientation of the system. The moment of inertia about the y-axis was set to match the observed pitch period and based on the assumption that the hull is axisymmetric. All properties are representative of the system with the umbilical wires attached. Testing without the umbilical was conducted in Campaign 4, which utilized a similar cable umbilical, to quantify the effect of the bundle, see Chapter 4.

Table 3.5: As-Built System Structural Properties – including hull, tower, dummy RNA (locations relative to centerline of structure at bottom – keel, full-scale)

Property	Unit	As-Built	Value Origin
Total mass of model	kg	2.012E+07	Measured
Overall CG height from keel	m	17.36	Measured
Overall CG x offset keel	m	0.29 -0.04	Measured Derived
Overall CG y offset keel	m	0.53 0.12	Measured Derived
Overall model inertia about x axis	kg-m ²	4.72E+10	Measured
Overall model inertia about y axis	kg-m ²	4.26E+10 4.72E+10	Measured Derived
Overall model inertia about z axis	kg-m ²	Not measured	-

Additional information is included in Appendix B, including system geometries given in Table B.1 and components identified in Figure B.1 through Figure B.3.

3.3.2 Hull Design

In the full-scale design, there is significant ballast mass located in the bottom of the structure, providing stability by lowering the CG. As discussed in Section 3.2.4, a portion of this ballast mass was utilized to

create the 686 MT moving mass elements in the TMDs. To keep the system dynamics similar to the reference hull, the scale-model hull was therefore designed to maintain a similar overall CG with respect to the full-scale when the TMD masses were at their equilibrium position (halfway up the buoyancy column).

The bottom beams of the hull were sized to the appropriate Froude-scale dimensions and used a steel baseplate and adhered foam blocks to create the desired shape and a carbon fiber outer skin for protection. The keystone and central column were an integrated piece with a removable bottom plate. The main instrumentation of the hull was arranged to reside inside the keel, affixed to this plate, to obtain the proper mass distribution in the hull. All wiring was routed through the hollow central column and passed to the outer columns above the waterline. The outer columns of the hull were also hollow to allow installation of the TMD system. The outer walls of the hull were rigid to preserve the proper outer geometry. The assembled hull is shown in Figure 3.4, including the internal components of the instrumentation system, TMD, and associated wiring.

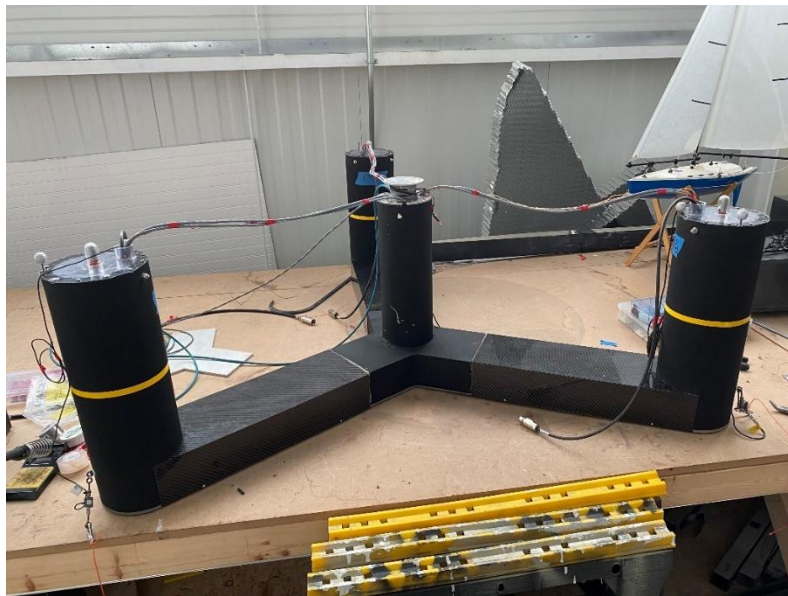


Figure 3.4: Assembled Hull

3.3.3 Hull Properties

Properties for the hull are given in Table 3.6. These values were derived based on the measured properties of the overall system, RNA, and tower. The CG x-offset, CG y-offset, and pitch inertia were set to be consistent with the derived values in Table 3.5 and tuned to match the equilibrium conditions of the model. The given properties represent the hull with the TMDs installed and fixed in their nominal position and include the umbilical cable.

Table 3.6: Hull Properties

Parameter	As-Built (full-scale)	Value Origin
Mass (kg)	1.843E+07	Derived
Vertical Center of Gravity from keel (m)	5.30	Derived
CG x offset	0.25	Derived
CG y offset	0.13	Derived
Pitch Inertia about hull CG (kg^*m^2)	1.29E+10	Derived
Roll Inertia about hull CG (kg^*m^2)	1.29E+10	Derived
Yaw Inertia about hull CG (kg^*m^2)	1.52E+10	Derived
Displaced volume (m^3)	20,173	Derived
Center of buoyancy below SWL (m)	-13.71	Derived
Buoyancy force in undisplaced position ($\rho g V_0$) (N)	1.973E+08	Derived
Hydrostatic restoring in heave ($C_{33}^{\text{Hydrostatic}}$) (N/m)	4.352E+06	WAMIT
Hydrostatic restoring in roll ($C_{44}^{\text{Hydrostatic}}$) (N-m/rad)	2.134E+09	WAMIT
Hydrostatic restoring in pitch ($C_{55}^{\text{Hydrostatic}}$) (N-m/rad)	2.134E+09	WAMIT

3.3.4 Internal Load Measurement

The FOCAL hull was outfitted with three internal load cells, one in each leg (Figure 3.5). The construction of the bottom beam in this way introduced a certain amount of flexibility, which was quantified and provided with the dataset to enable modeling the hull flexibility of these sections.

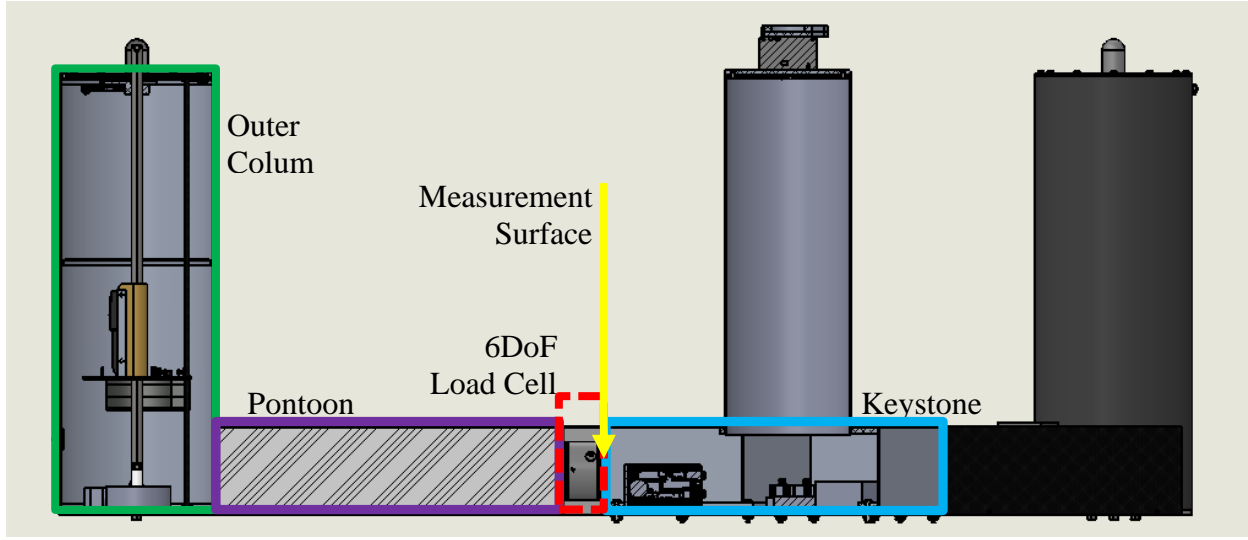


Figure 3.5: FOCAL Hull Cross-Section

3.3.5 Tower Properties

The tower was a hollow aluminum tube fixed on the bottom to a 6DoF force gauge and bolted on the top to the dummy RNA. The tower and connections contribute to the topside flexibility and are important to the overall system dynamics and load transfer. Table 3.7 provides the relevant properties needed to model the system.

Table 3.7: Tower Properties

Property	Units	Value	Value Origin
Elevation to tower base (platform top) above keel	m	38.34	Measured
Elevation to tower top (yaw bearing) above keel	m	161.89	Measured
Tower inner diameter	m	3.36	Measured
Tower outer diameter	m	3.57	Measured
		4,830	Froude-scaled Aluminum 6061
E (Young's modulus)	GPa	3,408	Derived to match cantilever frequency
		1,456	Derived to match floating frequency
G (shear modulus)	GPa	1,281	Froude-scaled Aluminum 6061
Tower mass	kg	336,140	Measured
Tower + wiring mass	kg	4.789E+05	Measured
CG location above keel along centerline (tower + wiring)	m	100.39	Derived from tower + RNA measurement

3.3.6 Mooring Properties

The full-scale mooring system consisted of three catenary chains, one extending radially from each outer buoyancy column. For this campaign, the catenary chain was replaced with a horizontally mounted linear spring mooring. The mooring layout for the model test can be seen in Figure 3.6, with the locations of the attachment points given in Table 3.8.

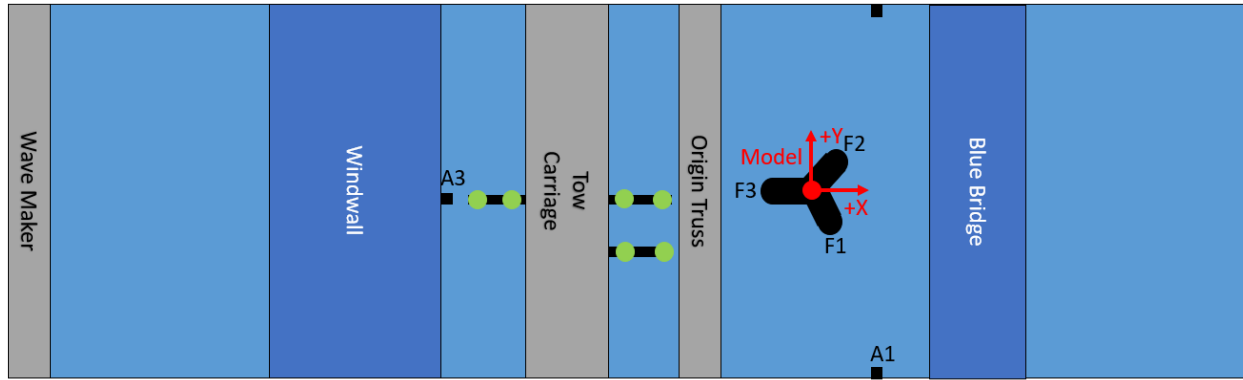


Figure 3.6: Mooring anchor and fairlead locations

Table 3.8: Fairlead and anchor locations

Label	Description	X Position [m]	Y Position [m]	Z Position* [m]
Origin	Model Center	0.0	0.0	0.0
A1	Anchor Point 1	179.8	-293.5	-14.0
A2	Anchor Point 2	180.1	321.9	-14.0
A3	Anchor Point 3	-423.8	13.1	-12.6
F1	Fairlead 1	29.8	-51.5	-14.36
F2	Fairlead 2	29.1	51.5	-14.36
F3	Fairlead 3	-59.4	0.0	-14.36

*Measured from Nominal stillwater level (Table B.1)

The moorings were fishing lines attached to spring elements, and thus can be modeled as linear springs (see Table 3.9). The mooring lines were taut and nearly horizontal, with the spring stiffnesses set to approximate the overall surge stiffness of the VolturnUS-S catenary mooring system under rated wind

load conditions. The small diameter of the fishing wire resulted in minimal wave excitation to the line, which was ignored for the validation campaign.

In addition to the mooring lines, a wiring umbilical related to the measurement sensors also hung off the structure, attached to the aft of the model at the centerline as shown in Figure 3.7. The surge and heave stiffnesses of this bundle are included in Table 3.9.

Table 3.9: Stiffness properties of the mooring lines

Parameter	Pretension (N)	Stiffness (N/m)
Mooring 1 (A1-F1)	3.77E+06	1.261E+05
Mooring 2 (A2-F2)	3.05E+06	1.231E+05
Mooring 3 (A3-F3)	2.76E+06	1.255E+05
Umbilical, Surge	-	1.108E+04
Umbilical, Heave	-	1.644E+04

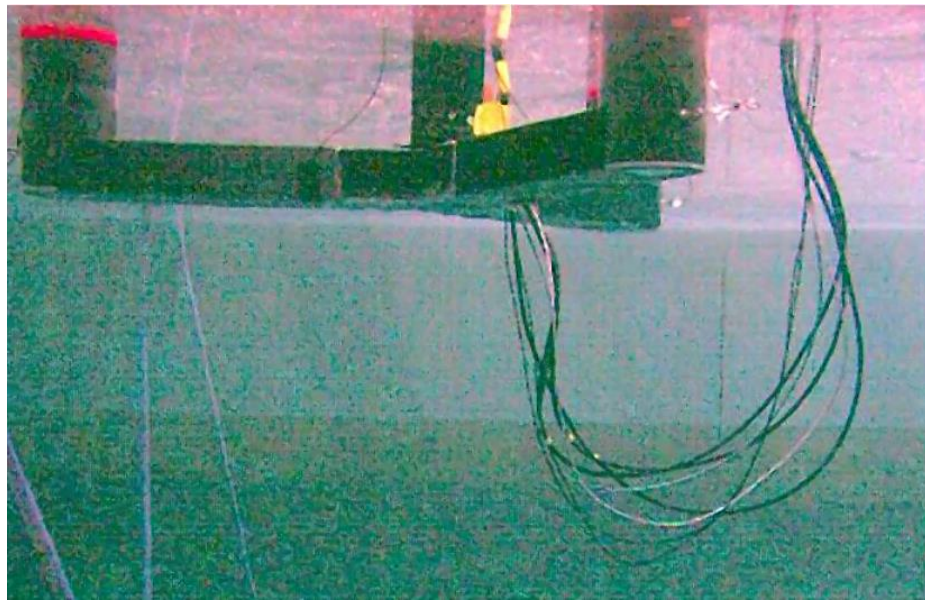


Figure 3.7: View of instrument cable bundle (umbilical) hanging off the hull (platform)

3.3.7 RNA Properties

A lumped mass was used in this experimental campaign in place of the RNA, with matching properties to obtain similar global dynamic characteristics. The moment of inertia of the RNA was small compared to the rest of system and not included. Mass properties of the RNA are shown in Table 3.10 and dimensions are shown in Table 3.11 and Figure 3.8.

Table 3.10: Dummy RNA properties

Property	Unit	As-Built	Value Origin
Mass of RNA	kg	1.205E+06	Measured
CG Height from Keel	m	168.93	Measured
CG x-offset	m	-4.54	Measured

Table 3.11: Dummy RNA dimensions

Dimension	Symbol	Units	Measurement	Value Origin
Dummy RNA Height	Rh	m	7.73	Measured
Dummy RNA Length	Rl	m	23.34	Measured
Dummy RNA Tail Length	Rt	m	5.50	Measured
Dummy RNA Rod Diameter (Typical)	Rd	m	2.67	Measured

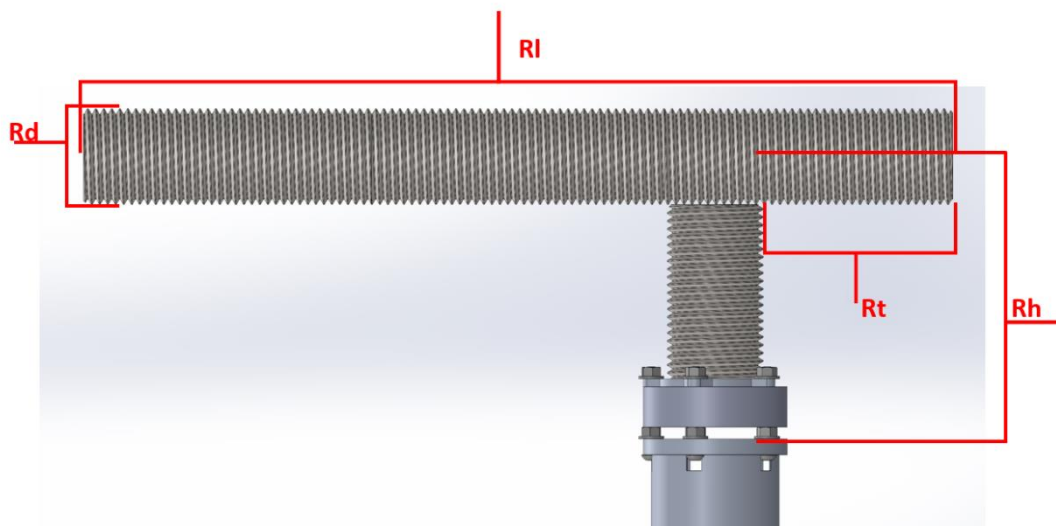


Figure 3.8: Dummy RNA dimensions

3.3.8 TMD Structural Design

The design requirements for the scale model TMD were as follows:

- Total Actuated Mass = 686,000 kg
- Maximum Stroke = +/- 10.5 m
- Static Position = 10.5 m from bottom (centered in 0.3 m travel)
- Spring Constant = 9,800 to 4,900,000 N/m
- Damping Coefficient = 81,993 to 204,982 N-s/m

The entire assembly also needed to be mounted inside the radial buoyancy columns, maintain smooth travel during platform motion (especially pitch/roll motion), and be able to simulate a variety of spring constant and damping coefficients to target different frequency ranges. To this end, a linear actuation system based on LinMot linear motors was designed using a fixed slider rod mounted to the hull via a 1DoF load cell and the motor attached to a mass so that the moving system mass was 686,000 kg. The assembled TMD unit is shown in Figure 3.9 and identical assemblies were used in each outer column.

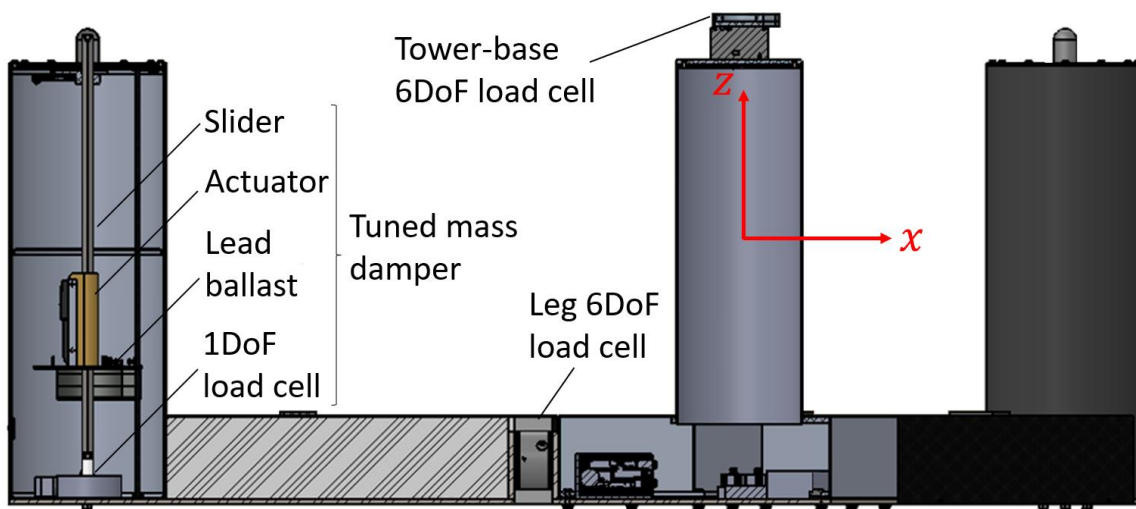


Figure 3.9: Cutaway Hull Showing Tuned Mass Damper System and Internal Load Sensor

A force-feedback controller was utilized to control the motion of the actuated mass such that the response mimicked the behavior of the full-scale passive tuned mass damper with the desired mass, stiffness, and damping characteristics. As designed, the reaction forces measured by the 1DoF load cell were used to close the force feedback loop and used in conjunction with the measured mass's velocity and acceleration to control each TMD independently. Considering the reaction force measured by the load cell and the force balance on the actuated mass, the dynamic system followed Equation 3.1:

$$F_{load\ cell} = m_{dynamic}\ddot{x} + m_{total}g = F_{spring} + F_{motor}$$

Equation 3.1

where $F_{load\ cell}$ was the reading from the 1DoF load cell, $m_{dynamic}$ was the mass of the moving ballast, m_{total} was the mass of the entire assembly mounted to the 1DoF load cell, x represented the position of the actuator (with the dot indicating a time derivative), g was the acceleration due to gravity, F_{spring} was the force of the external spring and F_{motor} was the force of the LinMot actuator acting on the mass. Note, while the acceleration of the stationary rod influences the setpoint, it is an order of magnitude less than the effect of the moving mass. This relationship was then used to control the motion of the TMD where the controller matched the force setpoint to balance the reading of the load cell as shown in Equation 3.2:

$$F_{load\ cell} = F_{setpoint} \rightarrow F_{load\ cell} - F_{setpoint} = 0$$

Equation 3.2

where $F_{setpoint}$ represented the desired reaction force calculated from the full-scale passive TMD system, modeled as the spring-mass-damper system shown in Equation 3.3:

$$m\ddot{x} + c\dot{x} + kx = F$$

Equation 3.3

Where x represented motion of the moving mass, m was the mass value, c was the desired TMD damping value, k was the desired TMD stiffness value, and F was the resulting reaction force. As the inertial

component of the force ($m\ddot{x}$) is also present in the scale model, the force setpoint was then represented as Equation 3.4:

$$c\dot{x} + kx = F_{setpoint}$$

Equation 3.4

This form of the setpoint force now enabled the control of the mass in force-feedback control, where the setpoint force was determined based on the desired stiffness and damping properties of the TMD system being modeled and the controller actuated the mass to match the load cell reading to the setpoint. This control loop was implemented independently for each TMD using the LinMot force-feedback controller on their respective motor drives with gains tuned according to manufacturer best practices. Further details on the characterization of the system are provided in Section 3.7.3.

3.4 Experimental Setup

3.4.1 Orientation and Coordinate Systems

The basin global coordinates and general layout are shown in Figure 3.10. This global coordinate system is used to report, for example, the location of the model in the wave basin. Figure 3.10 also indicates the nominal location of the floating platform for Campaigns 2 and 3. The relevant notations in terms of platform local coordinates and motion definitions are provided in Figure 3.11 and coordinate systems are in Table 3.12. Turbine load measurements will be recorded in the local coordinate system (unless otherwise noted), where the origin is as shown in Figure 3.11.

With reference to Figure 3.10, the wind and waves propagated from left to right in this image. With a 0° heading, the wind and waves traveled in the $+x$ direction with respect to the global and local coordinate systems. $+z$ is up, and the y -direction follows the right-hand rule.

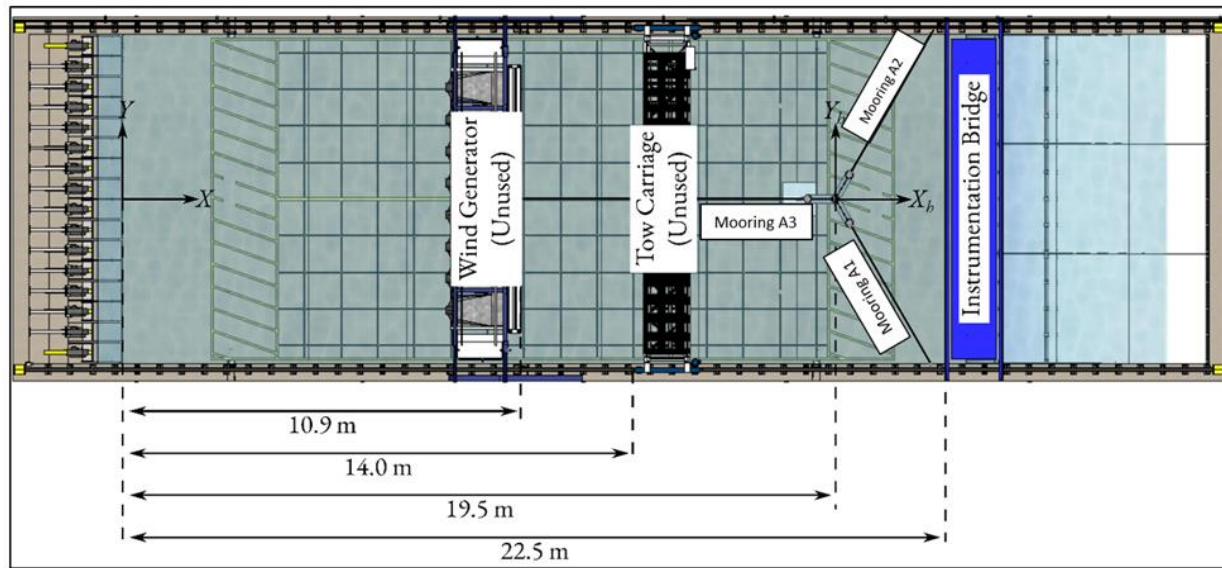


Figure 3.10: General Basin Layout for Campaign 2/3 (Model Scale)

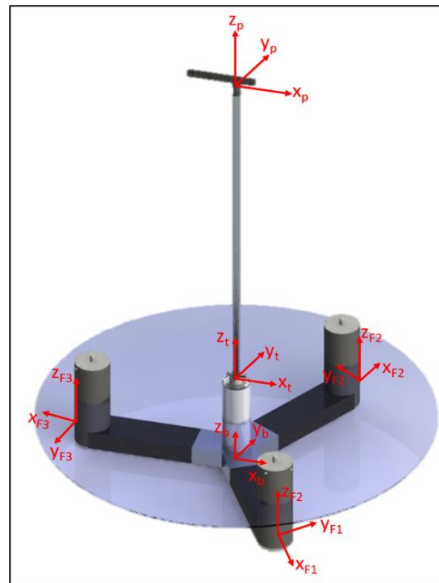


Figure 3.11: Location of the Hull, Tower Base, Tower Top, and Fairlead Coordinate Systems

Table 3.12: Axis Definitions (x,y,z locations relative to bottom of keel center)

Coord. System	Definition	Orientation	Origin X [m]	Origin Y [m]	Origin Z [m]
O	Still Water Line	+X in wave direction	0	0	20
B	Keel Center	+X in wave direction	0	0	0
T	Tower Base 6DoF	+X in wave direction	0	0	37.88*
P	Tower Top	+X in wave direction	0	0	161.89
F1	Column 1 Fairlead	Along mooring line 1	29.8	-51.5	5.64
F2	Column 2 Fairlead	Along mooring line 2	29.1	51.5	5.64
F3	Column 3 Fairlead	Along mooring line 3	-59.4	0.0	5.64

*This is the location of the tower-bottom sensor. The sensor is 0.46 m below the tower base location.

3.4.2 Wave Measurement Locations

Waves were calibrated using an array of wave probes, shown in Figure 3.12 at coordinates defined in Table 3.13. The probes R1-R6 represented “reference probes”, which were a capacitive style probe situated in the basin to provide a measurement of the incoming wave at multiple stations in the basin to assess the development of the wave and calculate reflection. They were installed during calibration and left in place during the test campaign. The probes C1-C3 were the “calibration probes”, which collected data at the intended deployment location of the model. Data from these probes were used to calibrate the wave environments, where gains in the wave maker controller were iterated until the desired environment was measured. These probes were removed once the environments were calibrated and the model was installed in their place.

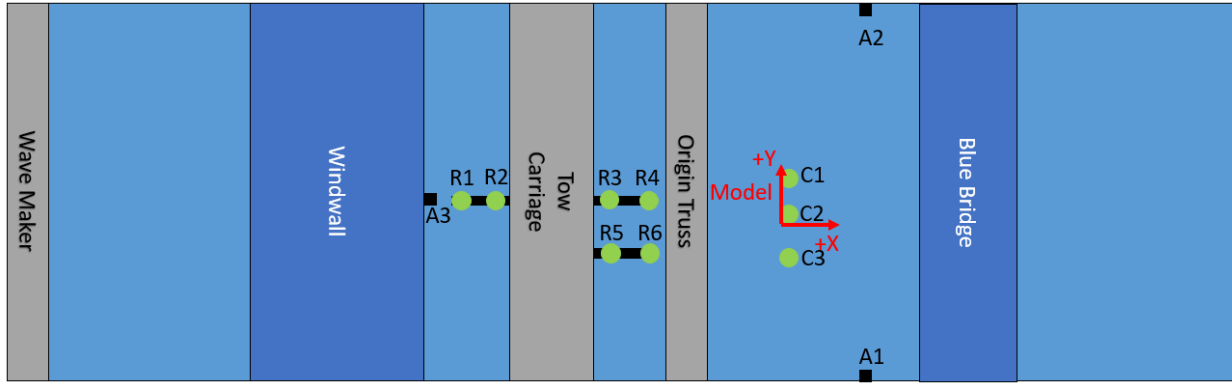


Figure 3.12: Basin Layout - wave probes and anchor locations.

Table 3.13: Location of wave probes and anchors (relative to O coordinate system; Full Scale)

Label	Description	File ID	X Position [m]	Y Position [m]
Model Origin	Model Origin	N/A	0.00	0.00
C1	Calibration Probe	Element 1	-0.28	51.38
C2	Calibration Probe	Element 2	4.97	30.17
C3	Calibration Probe	Element 3	4.69	-13.09
R1	Reference Probe	AI3	-297.78	90.02
R2	Reference Probe	AI2	-269.22	84.35
R3	Reference Probe	AI1	-152.95	74.34
R4	Reference Probe	AI0	-120.47	73.85
R5	Reference Probe	AI4	-150.29	-114.8
R6	Reference Probe	AI5	-116.83	-113.89

3.4.3 Tuned Mass Dampers

Tuned-mass dampers were placed in each of the offset columns to provide damping to the system motion.

Each of the three TMDs had a mass of 686,000 kg at full scale, which was accounted for in the hull properties. The spring stiffness of the TMDs were tuned to focus on either the pitch or the first tower-bending natural frequencies, and the damping was set to produce a 20% damping ratio, as discussed in Section 0. They were also held fixed in one location for baseline conditions.

Three TMD conditions were tested in the campaign:

- **Fixed:** TMD masses were held in place at their nominal position (see Table 3.15).
- **Pitch TMD:** TMD response was tuned to the platform pitch resonance frequency of the entire floating turbine system.
- **Tower TMD:** TMD response was tuned to the first tower-bending frequency in the fore/aft direction with the entire system floating and the RNA attached.

Settings for each TMD condition are outlined in Table 3.14, based on the results of the characterization described in Section 3.7.3. TMD center of mass information is presented in Table 3.15.

Table 3.14: Tuned Mass Damper Settings

Target Frequency	Mass [kg]	Stiffness [N/m]	Damping [N-s/m]
Fixed	686,000	inf	--
Pitch	686,000	31,482	58,783
Tower	686,000	4,624,376	712,441

Table 3.15: Tuned Mass Damper CG locations

Position	CG Z* Location [m]
Nominal	12.97
Negative Stop Position	2.47
Positive Stop Position	23.47

*Distance from Keel

3.5 Instrumentation and Data Acquisition

3.5.1 Instrumentation

An overview of the sensors used in this campaign is given in Figure 3.13, and a table of devices used is provided in Table 3.16.

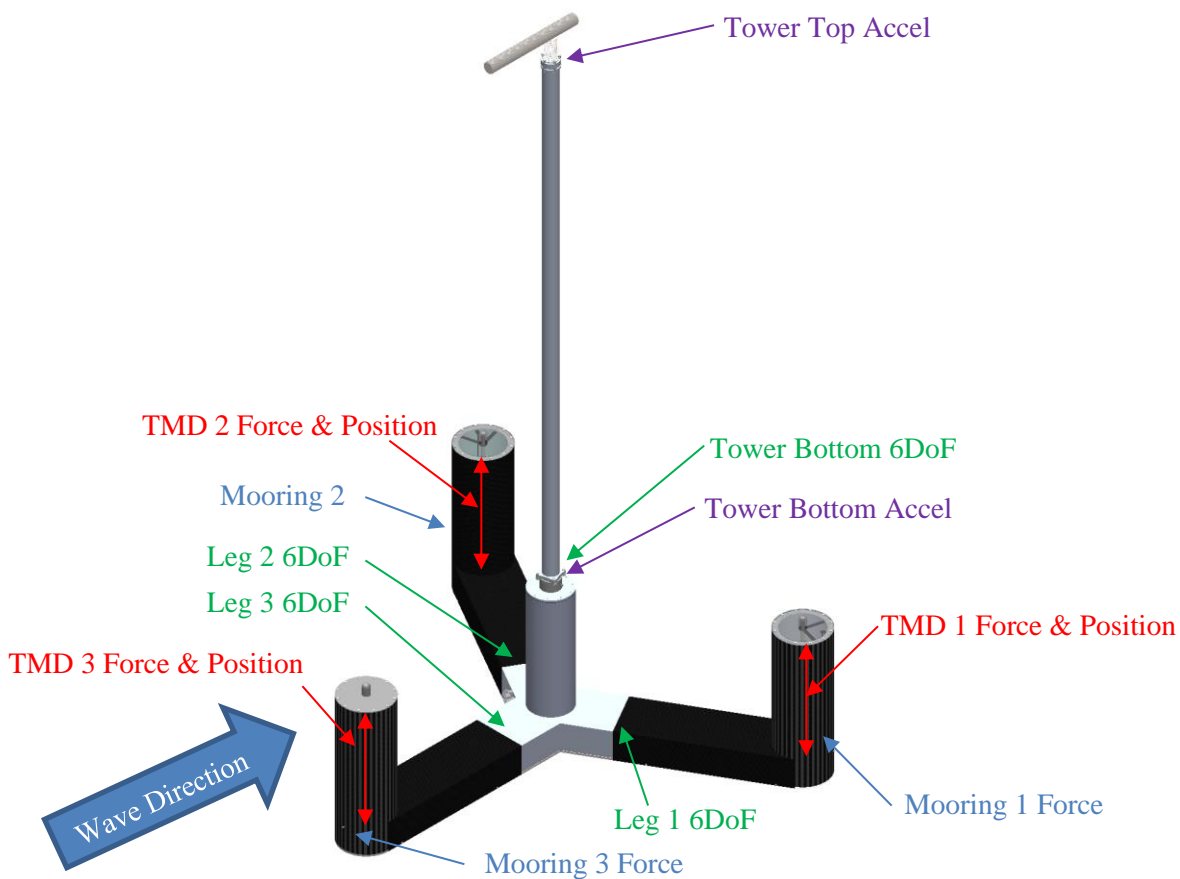


Figure 3.13: Instrumentation Overview

Table 3.16: Instruments List

Description	Instrument	Quantity
TMD load cell	Interface 2420	3
TMD actuator	LinMot PS02-23Sx80F-HP-K	3
TMD drive	LinMot C1250-DS-XC-0S-000	3
Pontoon internal 6DoF load cell	ATI Mini58 IP68	3
Tower base 6DoF load cell	ATI Mini58 IP68	1
Tower top/base accelerometer (X, Y, Z)	PCB Piezotronics 3713F112G	2
Port/starboard mooring load cell	Interface WMC-22N	2
Bow mooring load cell	Interface WMC-45N	1
Analog input	Beckhoff EP3174-0002	2
EtherCAT junction	Beckhoff EP9128-0021	1
Signal conditioner	ATI 9105-ECATOEM	5
Load cell amplifier	Tacuna EMBSGB200	6
cRIO	cRIO-9036	1

Coordinate systems for the readings of the pontoon 6DoF internal load cells are given in Figure 3.14. The load cell interface location is described in Table B.1. During testing, the internal load cell in leg 1 was damaged and found to be giving faulty readings. It was excluded from any results or analysis.

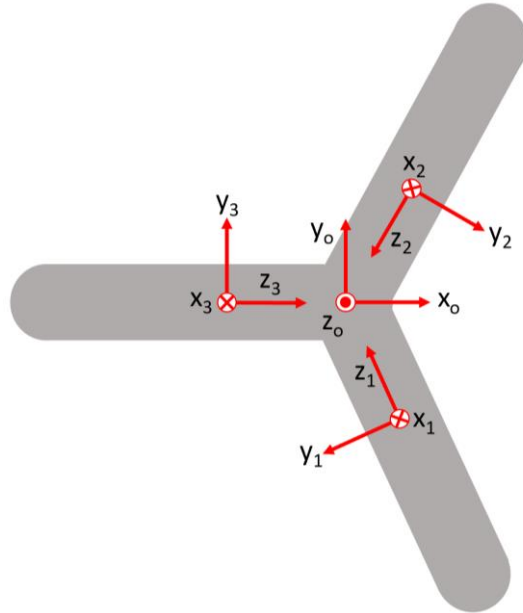


Figure 3.14: Internal load cell orientations (viewed from the top)

3.5.2 Sample Rates

Platform motion data from Qualisys was captured at 100 Hz model scale. All other data was recorded at 200 Hz model scale.

3.6 Test Program

3.6.1 Wind Conditions

Campaign 2/3 was a wave-only test campaign, so there were no wind environments.

3.6.2 Wave Conditions

A variety of wave conditions were used in the experimental campaign. Specifications for these waves are given in the following tables at full scale. Pink noise waves, specified in Table 3.17, were used to evaluate the response of the system over a broad range of frequencies. Note that the frequency range of the pink noise environment encompasses the platform pitch period of 0.034 s, meaning that direct wave forcing of this resonant mode was expected.

Table 3.17: Pink noise wave properties

Wave ID	H _s [m]	Frequency Range [Hz]
PN1	8.1	0.02 – 0.10
PN2	10.34	0.03 – 0.09

This test campaign used regular waves to verify the system's response to first-order wave loads. These waves are outlined in Table 3.18.

Table 3.18: Regular wave case properties

Wave ID	H [m]	T [s]
R1	10.85	12.8
R2	10.85	13.5
R3	10.85	14.2
R4	10.85	14.9
R5	10.85	15.6

Five JONSWAP spectra irregular wave cases were examined: an operational sea state (I1), 1-year extreme sea states corresponding to 4 m/s (full scale) and rated wind conditions (I2 and I3, respectively), the 50-year sea state (I4), and the 500-year extreme sea state (I5). Four seeds of the I4 wave environment (different time histories with the same overall statistics), designated I4S1 - I4S4, were generated to assess

the dependence of measurements on individual wave time histories. Specifications for these environments are given in Table 3.19.

Table 3.19: Irregular wave case properties

Wave ID	H _s [m]	T _p [s]	γ [-]
I1	3.1	8.96	1.80
I2	6.3	11.46	2.75
I3	8.1	12.8	2.75
I4	10.89	14.2	2.75
I5	12.54	14.97	2.75

Environmental properties for the test basin are given in Table 3.20.

Table 3.20: Water Properties

Property	Units	Value
Water depth	m	350
Water density	kg/m ³	997.2

3.6.3 Calibrated Environments

The wave time histories in Figure 3.15 to Figure 3.17 were recorded using the central calibration wave probe “C2”, located as described in Table 3.13. Additional plots are included in Appendix B as Figure B.4 through Figure B.15.

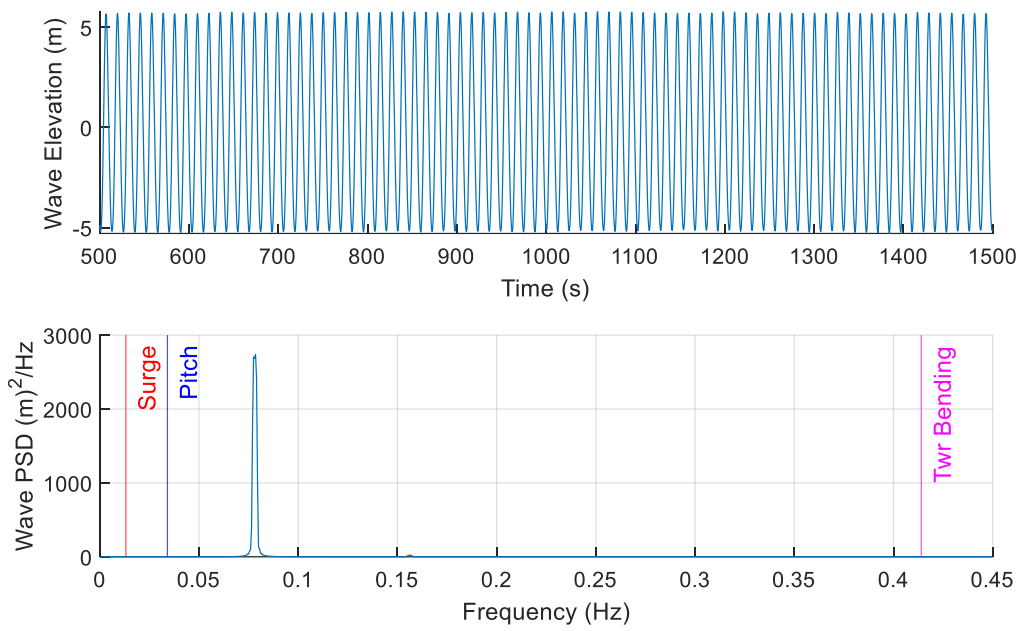


Figure 3.15: R1 Time History and Power Spectral Density Plots

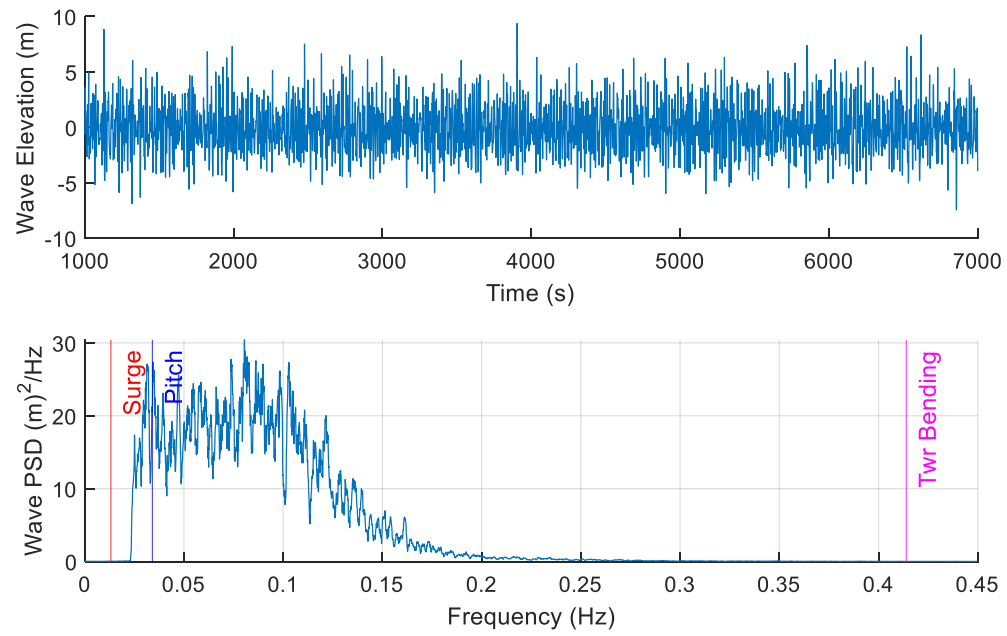


Figure 3.16: PN1 Time History and Power Spectral Density Plots

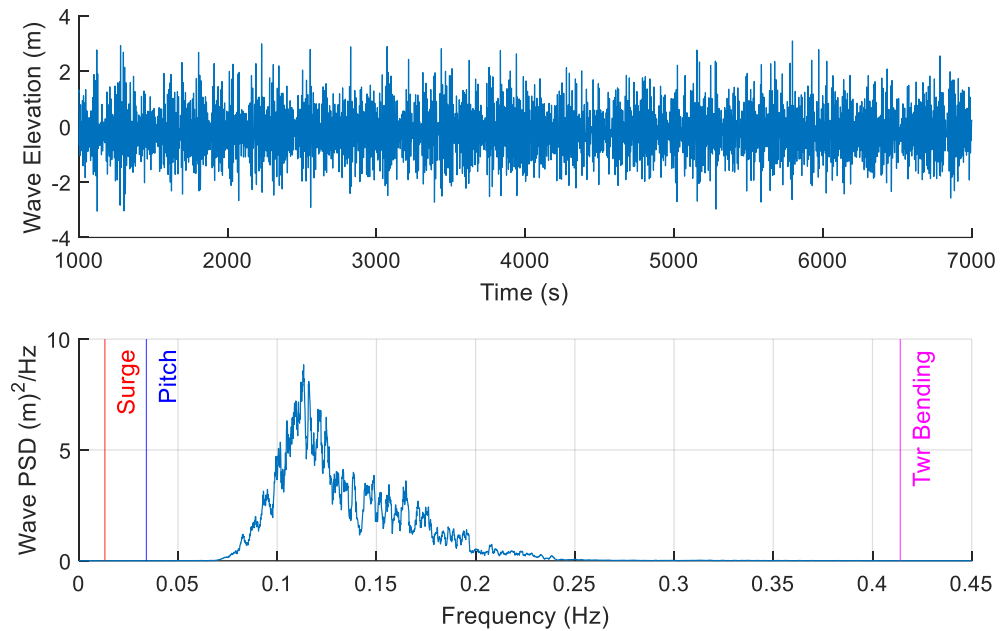


Figure 3.17: II Time History and Power Spectral Density Plots

3.6.4 Test Matrices

A test matrix of system ID tests is provided in Table 3.21. The TMD was fixed for all these cases. Free decay tests were run by manually offsetting the model in the specified degree of freedom, then releasing and allowing the system to return to rest. Hammer tests were run by striking the tower top with the system either resting on supports beneath the outer columns (simply supported) or floating. For hydrostatic stiffness tests, a known force (heave) or moment (pitch) was applied to the model, and the displacement recorded. Mooring offset tests were run by displacing the model in surge and sway, and recording the amount of force in each mooring line to determine the stiffness. To calculate the umbilical surge stiffness, the “shore” side of the umbilical was displaced a known distance, and the change in the net force on the rest of the model moorings was recorded. For heave, the “shore” end of the umbilical was displaced vertically, and the force on the model was calculated using its heave displacement and the stiffness from the hydrostatics test.

Table 3.21: System ID Test Matrix

Test Type	Description	Repeats
Free Decay	Surge, Sway, Heave, Roll, Pitch, and Yaw	6
Tower Hammer Tests	Simply Supported Hull: Fore/Aft and Side/Side	4
	Floating Hull: Fore/Aft and Side/Side	4
Hydrostatic Stiffness	Heave and Pitch	2
Mooring Offsets	Surge and Sway Displacement, with Umbilical Cable	3
	Surge and Sway Displacement, without Umbilical Cable	3

Wave tests are outlined in Table 3.22, with ‘TMD Target’ corresponding to the settings in Table 3.14.

Table 3.22: Active Wave Test Matrix

Wave ID	Duration [s]	Repeats for TMD Target		
		Fixed	Pitch	Tower
Regular Waves				
R1	2500	1	2	
R2	2500	1		
R3	2500	1		
R4	2500	1		
R5	2500	1		
Pink Noise				
PN1	15000	3	1	1
PN2	15000	2		1
Irregular Waves				
I1	9800	1		1
I2	9700	3	1	1
I3	10000	3	1	1
I4S1	10000	3	2	1
I4S2	10000	1	1	
I4S3	10000	1	1	
I4S4	10000		1	
I5	10000	1		

3.7 System Characterization

Prior to performing the wave tests of the hull, a series of characterization tests were performed. These quantified the system properties such as natural frequencies, tower bending frequencies, and hydrostatic stiffnesses.

3.7.1 System Natural Frequencies

Free decay periods were measured from free decay tests of the floating hull conducted with all mooring lines and the cable umbilical connected. The model was moved in each degree of freedom, held steady, and then released. The resulting motion was measured, and the free decay periods calculated as listed in Table 3.23.

Table 3.23: As-Built System Free-Decay Properties

	Surge	Sway	Heave	Roll	Pitch	Yaw
Measured Period [sec]	75.95	79.99	21.39	29.77	29.33	48.75
Frequency [Hz]	0.0132	0.0125	0.0468	0.0336	0.0341	0.0205

3.7.2 Tower Frequency

The tower natural frequency was measured by striking the tower top with a hammer under several conditions and measuring the resulting frequency. Due to questions about how best to model the tower, multiple test cases were considered with different boundary conditions. In the ‘floating’ case, the entire system was floating in the basin and tethered using the mooring lines and cable umbilical. For the ‘simply supported’ case, the tower, RNA, and associated wiring were mounted to the hull, which was resting on supports beneath the outer columns. The ‘cantilever tower’ case was a test where the RNA, tower, and associated wiring were mounted to a rigid surface. ‘Cantilever tower + 6DoF’ was similar, but with the

tower-bottom 6DoF sensor mounted between the tower bottom and the rigid mounting surface. Average full scale natural frequencies from these tests are given in Table 3.24.

Table 3.24: Tower Natural Frequencies

Test Condition	Average Natural Frequency (Hz)
Floating, Fore-Aft	0.414
Floating, Side-Side	0.421
Simply supported, Fore-Aft	0.273
Simply supported, Side-Side	0.275
Cantilever Tower, Fore-Aft	0.391
Cantilever Tower + 6DoF, Fore-Aft	0.351

3.7.3 TMD Characterization

The dynamic performance of the TMD control system was characterized through a System Identification (SID) style experiment (e.g. Bacelli et al., 2017). The TMDs were mounted inside the hull and the hull was set on a frame outside the wave basin, as shown in Figure 3.18. Each TMD was characterized and tuned individually.



Figure 3.18: TMD characterization test setup

The methodology of the SID test was to apply a known excitation to the TMD and measure the response to compute the transfer function. A broadband “external force” was synthetically added to the force-control system as a disturbance force, simulating the effect of the platform moving. The controller responded dynamically and the response was measured. The experiment was run multiple times, for a range of stiffness values from 9,800-4,900,000 N/m and damping values of 81,993 – 204,982 N-s/m to characterize the range of natural frequency and damping coefficients needed for subsequent testing. Each TMD was characterized independently.

Determination of the system transfer function was completed in MATLAB for each TMD and combination of stiffness and damping values. First, fast Fourier transforms of the TMD setpoint force and position were computed. As discussed earlier, the TMD system was treated as a spring-mass-damper system, modeled in Equation 3.5.

$$m\ddot{x} + c\dot{x} + kx = F$$

Equation 3.5

Where x represented motion of the moving mass, m was the mass value, c was the damping value, k was the stiffness value, and F was the applied force.

In the Laplace domain, the transfer function of this system could be written as shown in Equation 3.6.

$$H(s) = \frac{x}{F} = \frac{1}{ms^2 + cs + k}$$

Equation 3.6

This equation was then represented in the general form shown in Equation 3.7 and the *ttest* function was invoked in MATLAB for a standard spring-mass-damper system with two poles and no zeros:

$$H(s) = \frac{1}{ms^2 + cs + k} = \frac{1/m}{s^2 + \frac{c}{m}s + \frac{k}{m}} = \frac{\alpha}{s^2 + 2\zeta\omega_0s + \omega_0^2}$$

Equation 3.7

Where m was the mass, c was the damping value, k was the stiffness, ω_0 was the natural frequency, and ζ was the damping ratio. Finally, the dynamic system properties of natural frequency, spring constant, mass, and damping coefficient were extracted by comparing the transfer function forms shown in Equation 3.7.

Trials were conducted for each combination of k and c , and the results are shown in Table 3.25 where each row represents one experimental run for a specific stiffness (k in N/m) and damping value (c in N-s/m). The n column represents the force amplitude in Newtons applied to scale the excitation input and was adjusted to ensure reasonable range of motion during the tests. The remaining columns are the natural frequencies (f in Hz) and damping ratio (ζ) for the three TMDs as computed from the SID method.

Table 3.25: TMD characterization data

k	c	n	f1	ζ_1	f2	ζ_2	f3	ζ_3
[N/m]	[N-s/m]	[N]	[Hz]	[-]	[Hz]	[-]	[Hz]	[-]
9800	81993	686000	2.594	0.730	3.096	0.750	2.259	0.690
19600	81993	686000	2.845	0.650	3.179	0.660	2.594	0.550
29400	81993	686000	3.096	0.610	3.514	0.640	2.845	0.460
39200	81993	686000	3.263	0.560	3.765	0.610	3.096	0.450
49000	81993	686000	3.514	0.530	3.932	0.540	3.347	0.370
98000	81993	686000	4.434	0.420	4.853	0.410	4.351	0.290
245000	81993	686000	6.442	0.280	6.777	0.250	6.359	0.180
490000	81993	686000	8.701	0.240	9.203	0.170	8.785	0.130
490000	81993	1372000	8.952	0.150	9.120	0.130	8.869	0.110
735000	81993	686000	10.458	0.220	10.793	0.100	10.542	0.110
980000	81993	686000	11.713	0.210	12.299	0.100	12.048	0.100
2450000	81993	686000	16.984	0.230	17.821	0.110	17.235	0.110
2450000	81993	1372000	17.988	0.130	18.574	0.080	18.323	0.070
2450000	81993	2058000	18.574	0.100	18.992	0.070	18.741	0.060
4900000	81993	686000	22.673	0.370	23.343	0.170	21.084	0.150
4900000	81993	1372000	24.514	0.210	25.936	0.130	23.426	0.090
4900000	81993	2058000	24.932	0.160	26.187	0.100	24.514	0.080
9800	122989	686000	2.510	0.850	3.012	0.830	2.259	0.790
19600	122989	686000	2.761	0.760	3.096	0.720	2.510	0.640
29400	122989	686000	3.012	0.680	3.096	0.650	2.845	0.540
39200	122989	686000	3.263	0.660	3.765	0.710	3.096	0.550
49000	122989	686000	3.430	0.620	3.932	0.630	3.347	0.460
98000	122989	686000	4.434	0.470	4.853	0.460	4.351	0.350
245000	122989	686000	6.359	0.330	6.777	0.300	6.359	0.230
490000	122989	686000	8.701	0.290	9.203	0.210	8.701	0.170
735000	122989	686000	10.375	0.260	10.793	0.140	10.458	0.150
980000	122989	686000	11.713	0.240	12.215	0.130	11.964	0.130
2450000	122989	686000	16.901	0.250	17.905	0.120	17.235	0.120
4900000	122989	686000	23.259	0.410	23.677	0.180	21.000	0.160
9800	204982	686000	2.510	1.070	3.096	1.030	2.259	1.000
19600	204982	686000	2.761	0.970	3.347	0.950	2.510	0.890
29400	204982	686000	3.012	0.880	3.514	0.900	2.845	0.770
39200	204982	686000	3.263	0.820	3.765	0.830	3.096	0.730
49000	204982	686000	3.514	0.780	3.932	0.790	3.347	0.650
98000	204982	686000	4.434	0.610	4.769	0.610	4.351	0.500
245000	204982	686000	6.359	0.450	6.777	0.400	6.359	0.330
490000	204982	686000	8.618	0.400	9.203	0.280	8.701	0.250
735000	204982	686000	10.291	0.330	10.709	0.200	10.375	0.210
980000	204982	686000	11.630	0.310	12.132	0.190	11.797	0.190
2450000	204982	686000	16.901	0.300	17.821	0.150	17.068	0.150
4900000	204982	686000	22.841	0.420	23.761	0.200	21.167	0.190

Figure 3.19, shows the natural frequency (characterized by the SID) as a function of set spring stiffness (k in N/m) for varying damping coefficient values (c in N-s/m). The trendline equations given were fit to all data points for a given TMD and were used for calculating setpoint values for a targeted frequency in Table 3.26. At this stage, target frequencies considered were the platform pitch mode, the platform heave mode, the wave energy peak period, and the tower first fore/aft bending mode.

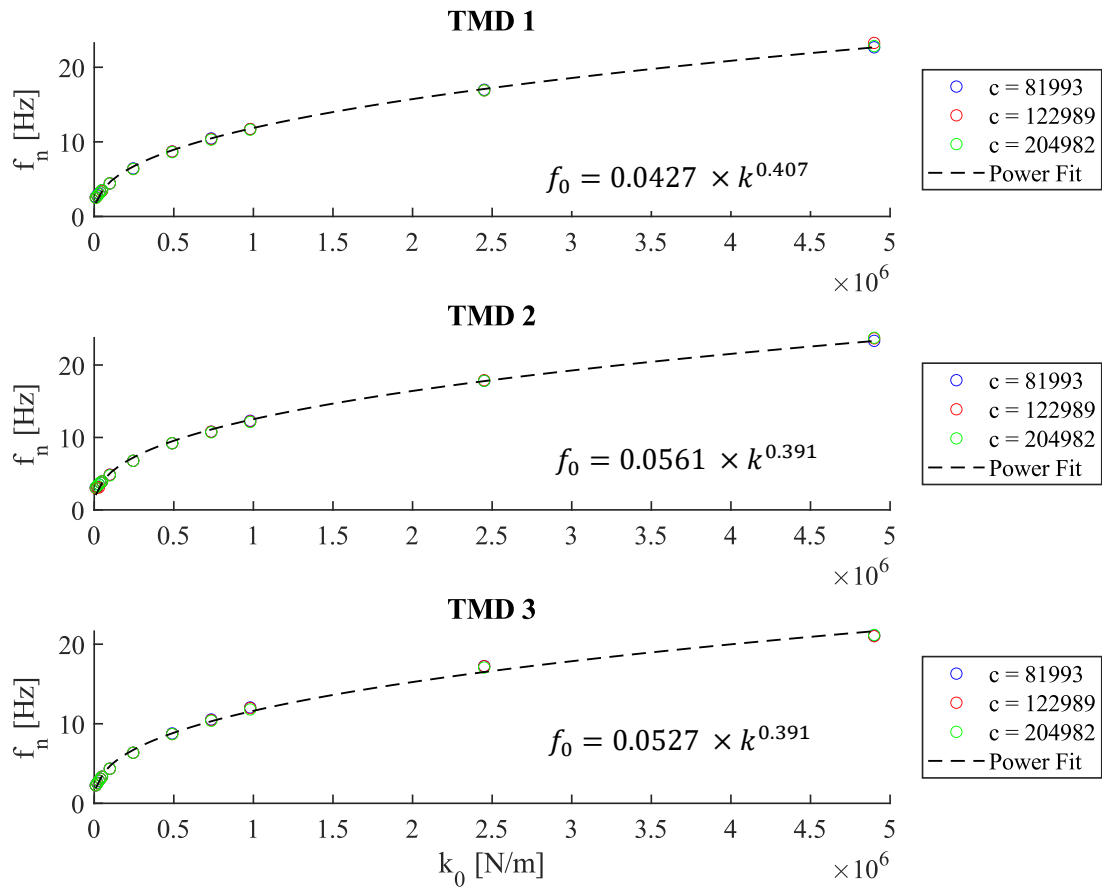


Figure 3.19: Natural frequency vs set spring stiffness

Table 3.26: Full and model scale target frequencies and corresponding spring stiffness setpoint required to achieve that frequency.

Frequency Target	Period [s]		Frequency [Hz]		k_0 [N/m]
	FULL	MODEL	FULL	MODEL	
Pitch	29.33	3.506	0.034	0.28	~19,500
Heave	21.39	2.557	0.047	0.39	~44,100
“Wave Effect”	8.20	0.980	0.122	1.02	~400,000
Tower	2.42	0.289	0.414	3.46	~8,575,000

The initial characterization identified baseline stiffness values for each target TMD frequency, designated as k_0 in Table 3.26. The next step was to deploy the hull in the basin and measure the response in the water for these baseline stiffness values. To determine sensitivity to the stiffness setting, each target frequency was tested using a range of stiffness values representing +/- 5% and +/-10% of the baseline value ($k=k_0$, $1.05\times k_0$, $1.10\times k_0$, $0.95\times k_0$, and $0.90\times k_0$) as well as a “fixed” case where the TMDs were held in place using a fixed position control. For all dynamic cases, the damping ratio was set at $\zeta=0.2$ by using Equation 3.8 to calculate the appropriate damping value, where m was equal to 686,000 kg and k was equal to k_0 for each target frequency.

$$\zeta = \frac{c}{2\sqrt{km}}$$

Equation 3.8

Excitation was provided by running a pink noise wave with 0.030 – 0.18 Hz excitation, 15,000 s duration, and 2,500 s repeat time. The wave environment is shown in Figure 3.20 and demonstrated good repeatability over the repeat times, allowing for multiple settings to be investigated per run.

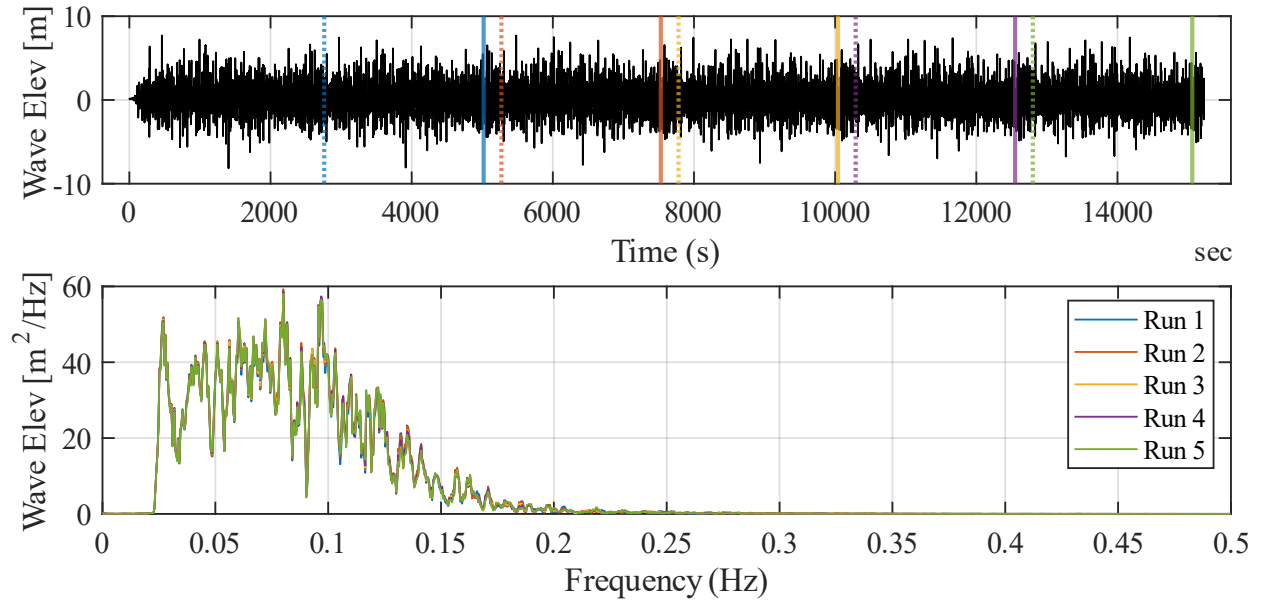


Figure 3.20: Repeatability of pink noise wave environment, showing 5 runs with 2,500 repeat time

During these tests, the full system instrumentation system was used to collect response data. Data were post-processed by analyzing each repeat individually and evaluating key metrics of tower base bending moment and platform heave and pitch motion. Figure 3.21 shows the platform pitch response for the pitch tuned TMD frequencies as well as the fixed case.

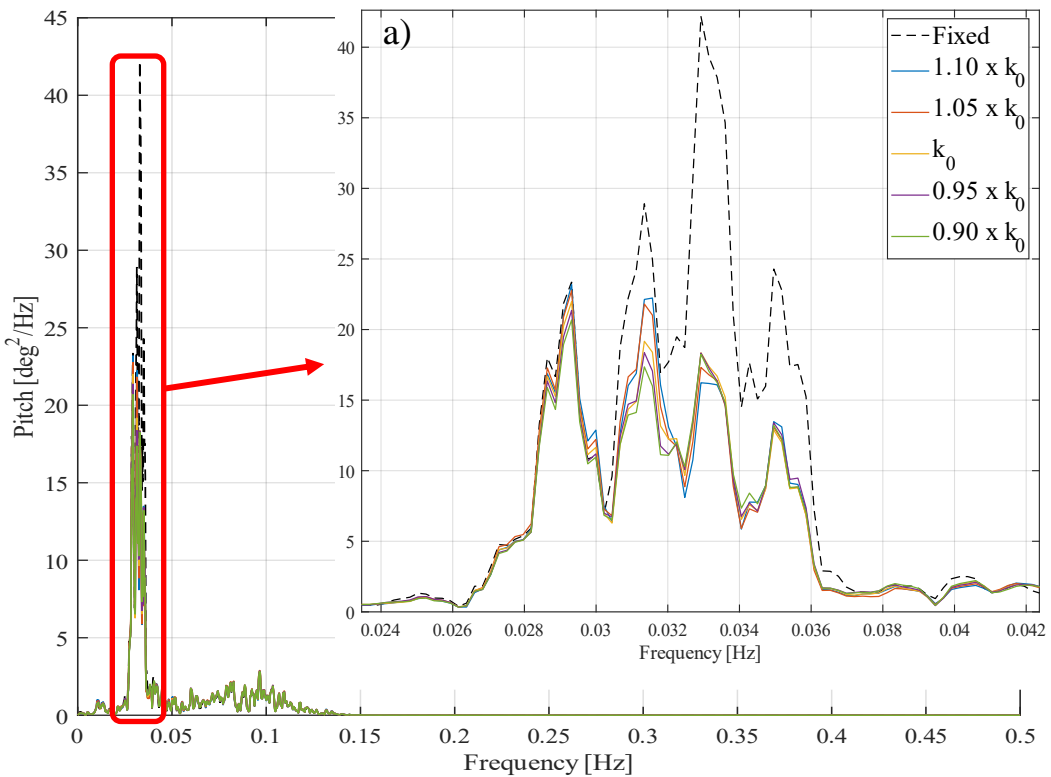


Figure 3.21: Fixed vs Pitch TMD stiffness tuning, effect on platform pitch motion. Inset (a) zoomed into platform pitch frequency.

As shown in Figure 3.21, while there was a noticeable decrease in platform pitch motion near the platform pitch frequency of 0.034 Hz for all active cases as compared with the fixed case, there was not a significant difference between the different stiffness values tested. The effect was similar for the tower base bending moment as shown in Figure 3.22. There was reduction in energy near the pitch natural frequency with the Pitch TMD active relative to the fixed TMD, but there was little difference between the various TMD stiffness settings. Additionally, there was a shift in the apparent tower bending frequency, shown by the response shifting to a higher frequency than the fixed TMD case near 0.41 Hz. As indicated in Section 3.3.5, the tower boundary conditions are important to the tower bending frequency and the observed frequency change is likely due to the change in platform dynamic stiffness with the TMD active.

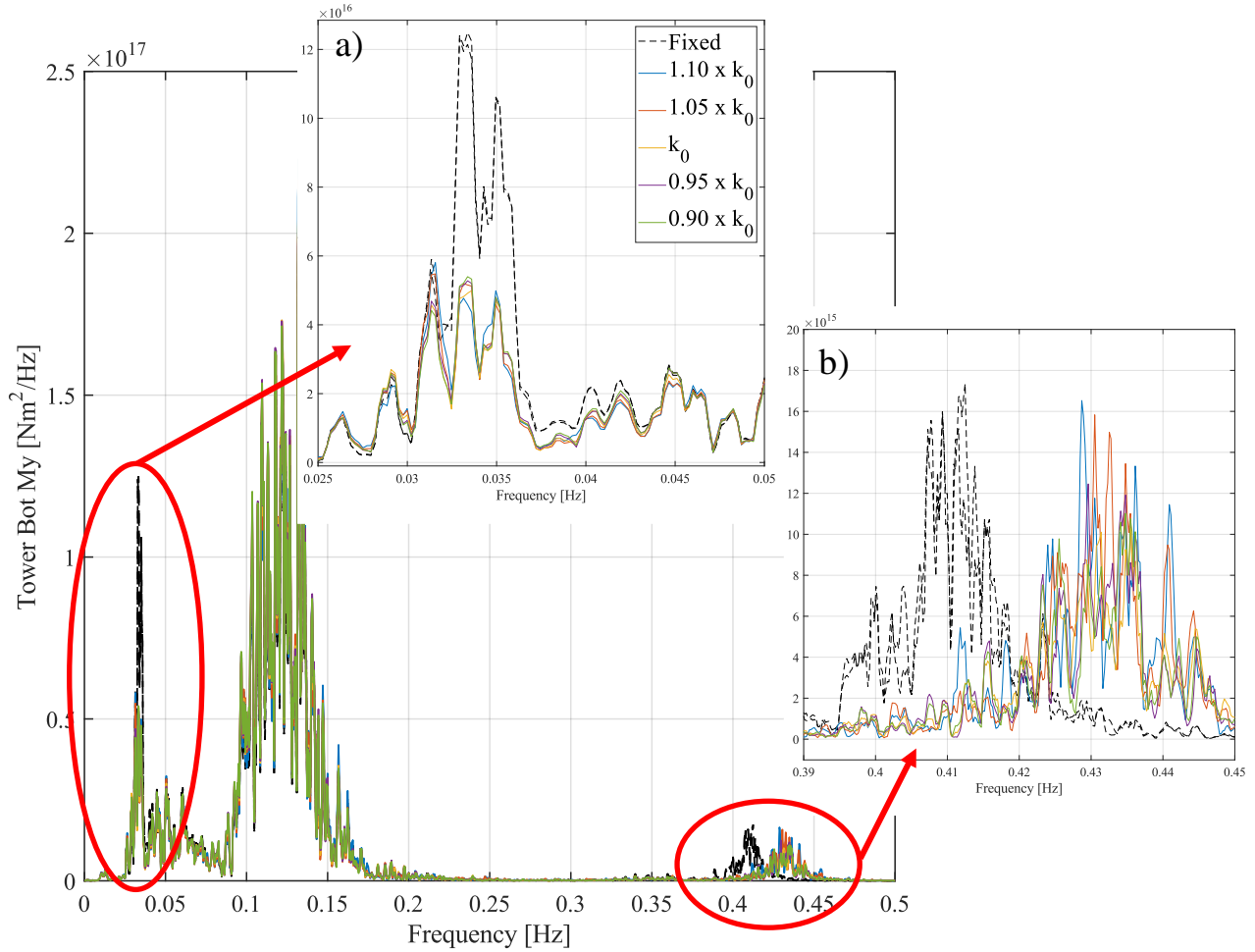


Figure 3.22: Fixed vs Pitch TMD stiffness tuning, effect on tower base bending moment. Platform pitch frequency (a) and Tower frequency (b)

With regards to the Pitch TMD tuning, these results indicated that the effectiveness of the TMD was relatively insensitive to the +/- 5 to 10% change in stiffness values tested.

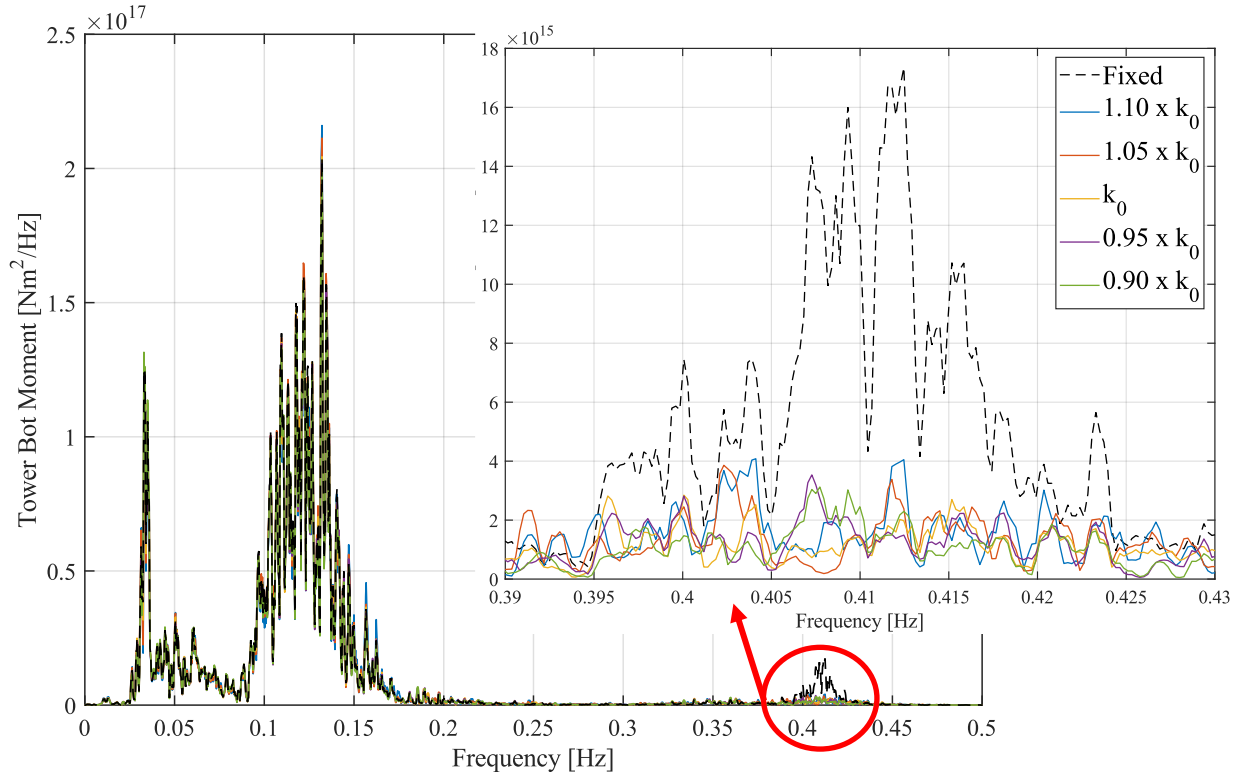


Figure 3.23: Fixed vs Tower TMD stiffness tuning, effect on tower base bending moment. Inset (a) zoomed to Tower frequency

In Figure 3.23, the tower bottom bending moment results are shown for the tower frequency TMD. Like the Pitch TMD, there was a significant reduction in response when the TMDs were active relative to the fixed case but little variation between the various stiffness values chosen. As such, the baseline stiffness value k_0 was chosen to define the stiffness setting for each target frequency. Testing of the “wave” frequency TMD showed that it was not effective in mitigating any targeted response, and—in some cases—worsened the response. Therefore, there was not any perceived benefit to continuing to focus on this TMD setting further. Furthermore, the heave frequency TMD either performed similarly to, or worse than, the pitch targeted one; as such, this TMD setting was also not considered further. The settings chosen for the pitch frequency and tower frequency TMDs are given in Table 3.27.

Table 3.27: FOCAL TMD Initial Setpoint Values

Target Freq	TMD 1		TMD 2		TMD 3	
	k [N/m]	c [N-s/m]	k [N/m]	c [N-s/m]	k [N/m]	c [N-s/m]
Pitch	2.205E+04	4.920E+04	1.764E+04	4.510E+04	2.156E+04	4.920E+04
Tower	8.614E+06	9.716E+05	8.183E+06	9.470E+05	9.075E+06	9.962E+05

Once the stiffness values had been defined, the optimal damping ratios were determined using a similar parameter sweep methodology. For the Pitch TMD and Tower TMD stiffness values, a range of damping values were applied representing damping ratios of 10, 20, 30, 50, and 100%. From benchtop tuning of the active TMD system it was identified that the TMD was unable to realize damping ratios less than 10% without instability, likely due to the inherent damping in the wiring that required the control loop to impose negative damping on the system to overcome. Each stiffness and damping ratio were then tested by subjecting the floating system to the same pink noise wave-only excitation test in the basin as used in the stiffness characterization. Performance was measured and the results were processed to investigate platform pitch and heave motion and tower base fore/aft bending response.

Figure 3.24 shows the results from the Pitch TMD. The “Fixed” case is shown in black, while the various damping ratios are shown in the color traces. Looking at Pitch and Heave motion, the 20% case showed the most favorable response with attenuation at the resonant modes of 0.034 Hz and 0.047 Hz for Pitch and Heave motion respectively. Considering tower base bending moment, while the majority of the response was in the wave energy region, the response in these frequencies appeared insensitive to the amount of damping. When comparing the response at the tower fore/aft bending mode frequency of 0.414 Hz, 20% case demonstrated some attenuation relative to the fixed case. Therefore, the 20% damping ratio was chosen for the Pitch TMD.

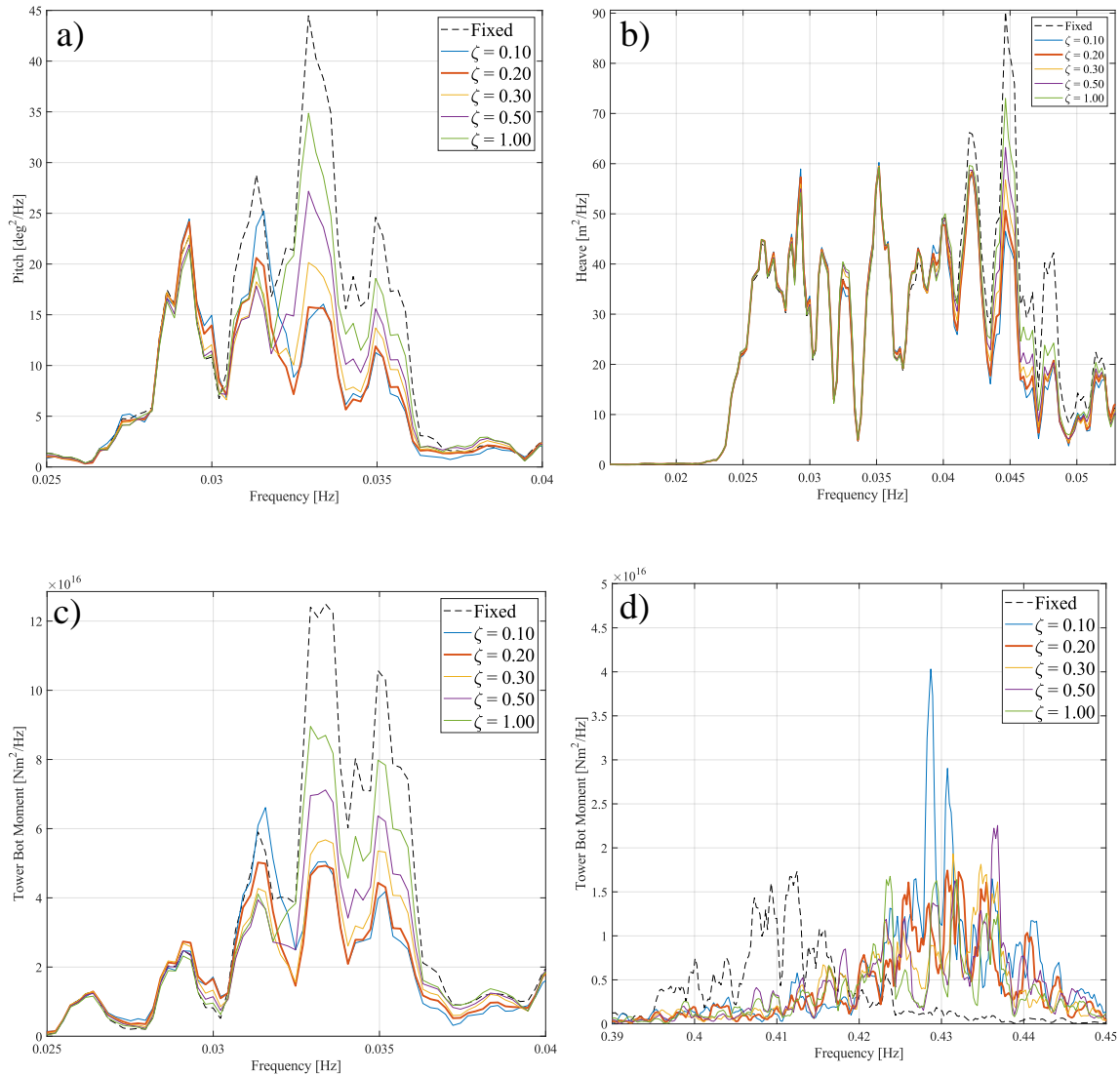


Figure 3.24: Effect of damping value on platform pitch, heave, and tower base bending moment for Pitch TMD setting. (a) Pitch near pitch frequency (b) Heave near heave frequency and (c) Tower bending moment near pitch frequency and (d) near tower frequency.

The process was repeated for the Tower TMD and the results are shown in Figure 3.25 for the tower base bending response. As shown previously, the majority of the response was in the linear wave forcing region. Considering the response near the tower natural frequency of 0.41 Hz, the 10% and 20% damping

ratio showed the most reduction in tower base bending moment. However, vibrations were observed with 10% damping so 20% was chosen as the setpoint chosen for the Tower TMD.

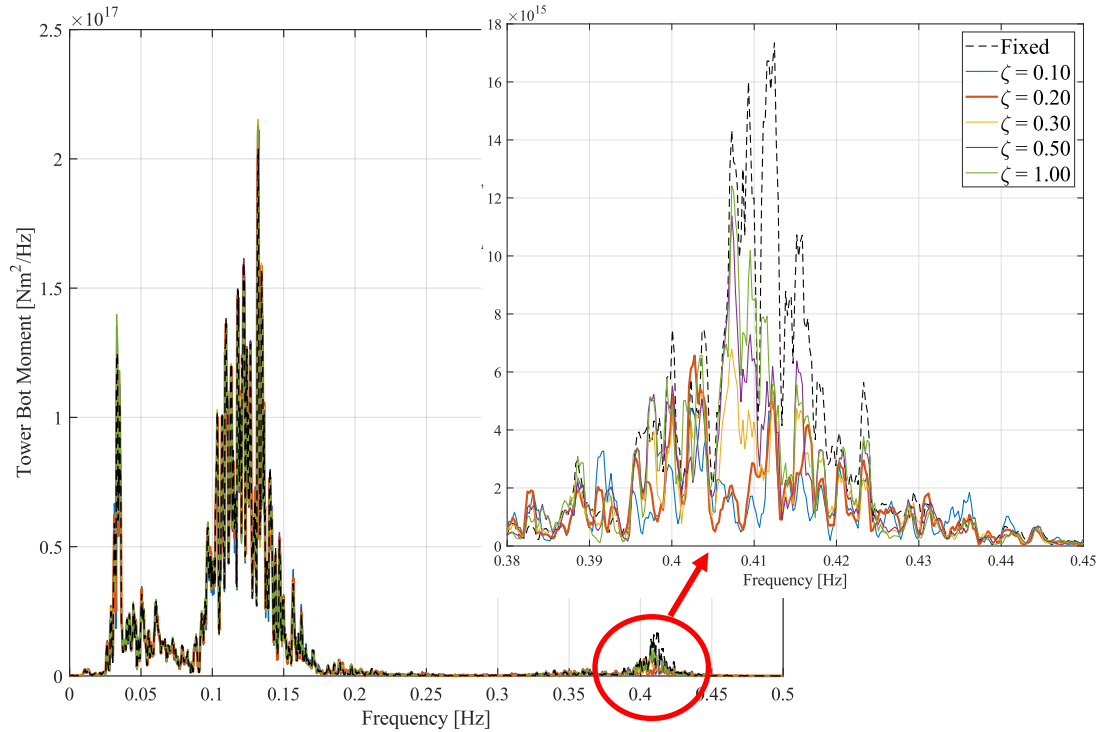


Figure 3.25: Effect of damping value on tower base bending moment for Tower TMD setting. Inset zoomed on tower frequency range.

3.8 Results

Similar to Campaign 1, the results from Campaign 2 were used in a cross-collaboration project to validate various numerical models from four participants. This process was led by NREL with support from UMaine on data processing and investigation of phenomena. The results of this study have been published (Wang et al., 2023a) and key results are summarized here. The reader is encouraged to consult the published paper for more information.

3.8.1 System Characterization

Data from the test campaigns were used to develop the floating hull numerical model, including the geometry, mass, center of gravity, moments of inertia, hull stiffness, tower, mooring, and hydrodynamic damping. The hull geometry, mass, center of gravity and moments of inertia were directly measured during the test campaign. The mooring stiffness values were determined from force-displacement tests of the model where the model was moved in either the surge or sway direction and the resulting mooring tensions were measured. Additionally, the hull flexibility was determined as discussed in the Test Report and the results provided to the modeling teams although all teams modeled the hull as a rigid body.

Modeling of the flexible tower required an appropriate beam model of the tower structure in addition to accounting for compliance of the tower bottom connection to the hull and load cell. While the methodology for accounting for this was left up to the modelers, good results were obtained by all models by tuning the tower stiffness to obtain the correct fundamental bending frequencies of the tower based on results from the hammer tests.

While different codes modeled the hydrodynamic damping in different ways, the methodology followed by the Wind Energy with integrated Servo-control (WEIS) team, using a model based on OpenFAST, is described here as it pertains to the OpenFAST model included with the FOCAL dataset. The OpenFAST model used potential flow results from first- and second- order analysis in WAMIT (Lee & Newman, 2006), therefore contributions from hydrodynamic viscous drag were included through additional linear and quadratic drag coefficients. Baseline coefficients from the VolturnUS-S model were tuned to match the free decay results using the P-Q methodology presented in (Wang et al., 2022a). In this manner, the effective linear and quadratic damping coefficients were characterized in terms of the linear damping ratio, ζ , and the P and Q parameters which are linked to the linear and quadratic damping coefficients, B_1 and B_2 , as shown in Equation 3.9:

$$B_1 = \frac{2k}{\pi\omega} P, B_2 = \frac{3k}{4\omega^2} Q,$$

Equation 3.9

where k and ω are the stiffness and angular frequency of the specific degree of freedom corresponding to the free-decay being analyzed. The P-Q method did not account for pitch-surge coupling and it was noted that additional tuning would likely improve results. All of the numerical models tuned damping based on results from the free decays and none refined these tunings based on the wave environments being considered.

As described in the validation paper, each numerical model reproduced the system natural frequencies well as shown in Figure 3.26. This was critical to assessing the performance of the tuned-mass dampers as they target system frequencies, namely the pitch and tower fore/aft bending mode frequencies, and therefore the same TMD stiffness and damping values could be used by all participants.

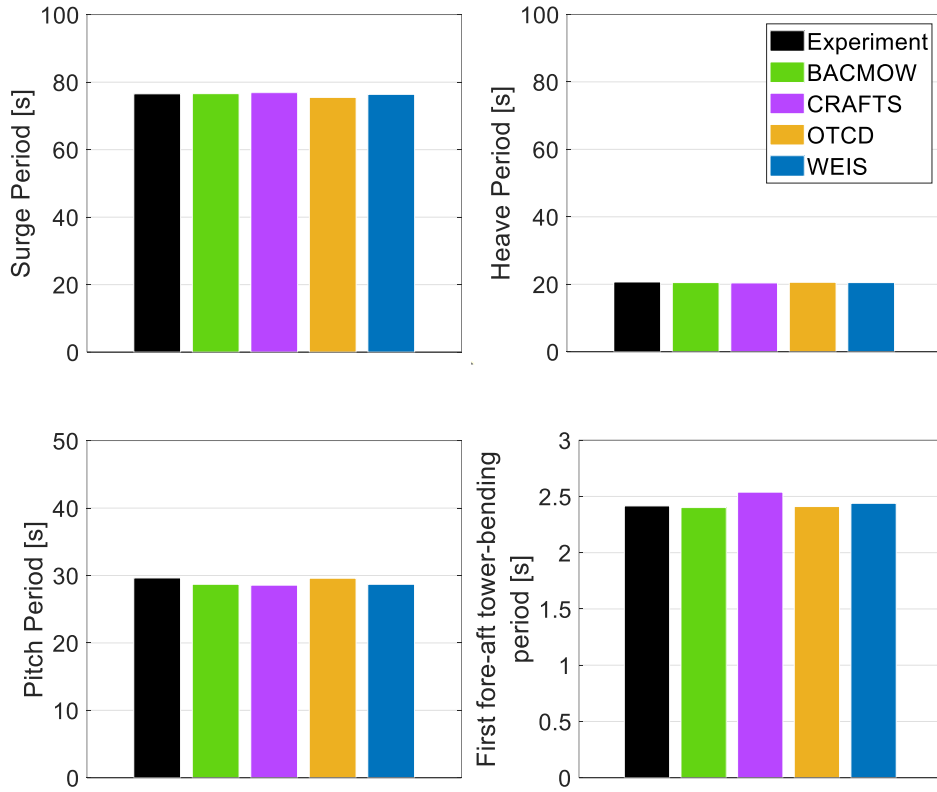


Figure 3.26: Numerical Validation, Free decay results (Wang et al., 2023a)

3.8.2 Load Cases

Three load cases were considered in the validation study corresponding to the I2, I4, and PN1 wave cases as described earlier in the Wave Environments section. I2 and I4 represent 1-year and 50-year return period wave cases respectively, and PN1 is a broadband pink noise wave case. The two TMD target frequencies considered were the Pitch frequency and Tower fore-aft frequency, referred to as Pitch TMD and Tower TMD. Additionally, the cases were run with the TMD locked at its neutral position, referred to as Fixed TMD. The load case definitions are shown in Table 3.28.

Table 3.28: List of load cases (LCs) from (Wang et al., 2023a)

Wave Condition	TMDs locked	TMDs tuned to platform pitch resonance	TMDs tuned to the first fore-aft tower-bending resonance
I4	LC 3.2	LC 3.5	LC 3.8
PN1	LC 3.3	LC 3.6	LC 3.9
I2	LC 3.10	LC 3.11	LC 3.12

For the Pitch TMD, the effect was assessed by comparing the response of the Pitch TMD with those of the Fixed TMD. The effectiveness of each TMD was assessed by analyzing the PSD of responses, specifically platform pitch motion and tower base fore/aft bending moment. For the I4 condition, integrating the PSD of the pitch response in the frequency range of 0.017 to 0.062 Hz shows reductions in pitch energy of 21% while an integration over the entire frequency range only shows a reduction of 1%. However, when considering the effect of the Pitch TMD in the I2 and PN1 environments, the reduction in pitch energy in the pitch frequency range is roughly 47% or 30% respectively, while the overall reduction in variance is roughly 20%. All numerical models also showed reductions in pitch energy when considering the Pitch TMDs, but generally estimated significantly more attenuation than was measured in the experiment. It was also observed that the pitch response in the Fixed TMD case was over-represented by all numerical models and it was proposed that improved modeling of the viscous drag load, especially on the large rectangular pontoons of the VolturnUS-S design, would better capture the low frequency pitch response. Results for the WEIS model as compared with the experiment is shown in Figure 3.27. It can be seen that WEIS overpredicts the pitch response near resonance in both the fixed and active TMD cases, but shows a similar effect of the TMD when considering the attenuation at the resonant frequency.

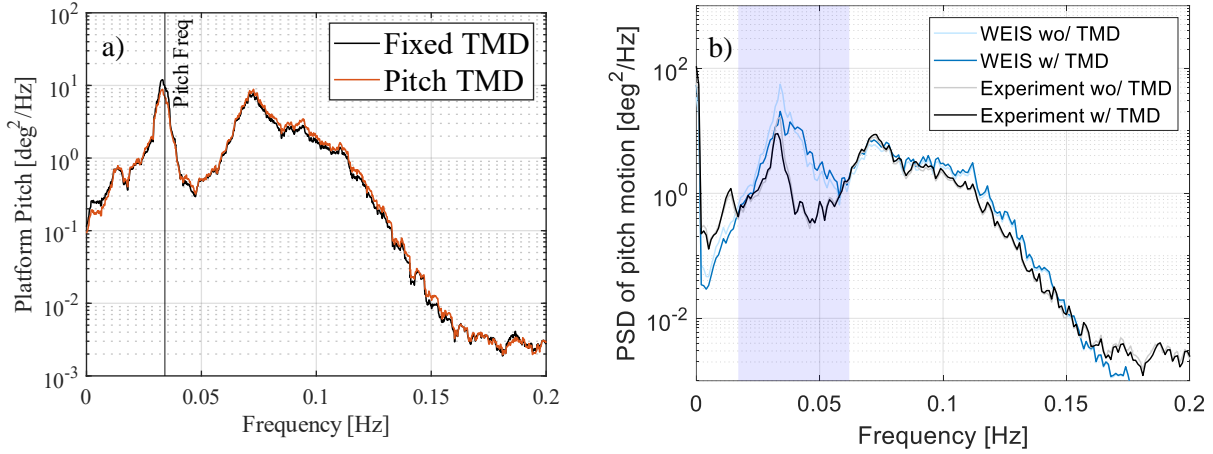


Figure 3.27: PSD of pitch motion in wave I4, Pitch TMD locked vs active. a) Experiment and b) WEIS results (Wang et al., 2023a)

For the Tower TMD, a significantly higher stiffness was used in the TMD to target the tower fore/aft bending mode. The PSD integral range of 0.32 to 0.48 Hz was used to capture the response around the tower fore/aft frequency of 0.414 Hz. Comparing these integrals, the experiment and all models showed roughly 60% reduction in tower base bending moment in the range of 0.32 to 0.48 Hz for all wave environments. Conversely, while the experiment also showed a reduction in tower base bending over the entire frequency range, most numerical models did not. Results comparing the WEIS model with experimental data are shown in Figure 3.28. In the experiment there was a strong resonant response in the fixed TMD case near the 1st fore-aft tower bending mode which was strongly attenuated when the Tower TMD was active. This was also demonstrated in the numerical model, however the magnitude of the tower-base bending moment was underpredicted by the WEIS model near resonance. The relative change in response for both the experiment and numerical models was consistent, with each showing roughly 60% reduction in tower-base bending load near the resonant frequency.

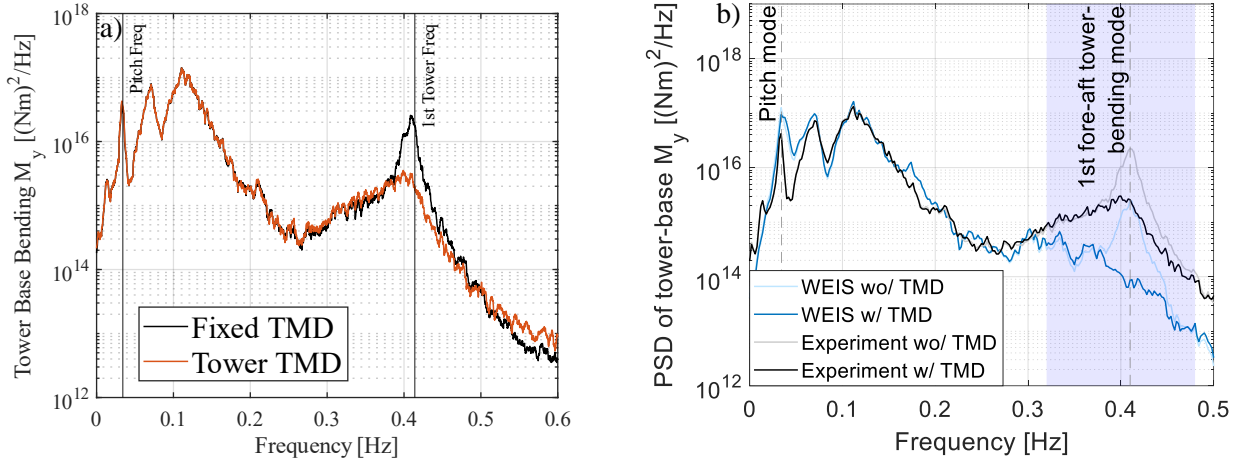


Figure 3.28: PSD of tower-base bending moment in wave I4, Tower TMD locked vs active. a) Experiment and b) WEIS results (Wang et al., 2023a)

3.8.3 Internal Load Measurements

Results from the internal load cells was collected during the various tests performed in the campaign consisting of 6DoF measurements in each pontoon leg. While these data were checked for consistency, they have not been used to validate numerical models or further considered by the team at this time. They are, however, included in the dataset and available to the wider research community when considering the effects of platform flexibility and measuring internal hull loads which is an area currently lacking robust datasets.

3.9 Conclusions

Campaign 2 and Campaign 3 successfully characterized the properties of the floating hull system and TMD performance for the FOCAL experimental program. The dynamics of the TMD system were verified and their ability to operate in the scale-model environment at the desired frequency and damping setpoints was demonstrated. Results from the testing were used to validate numerical models, including the OpenFAST model with TMD control. Data from the campaign were used to tune the hydrodynamic

coefficients, tower stiffness values, and mooring definition. Overall the numerical models were able to reproduce free decay results and showed similar trends to the experiment when considering the effects of the TMDs in mitigating resonant platform pitch motion and tower base bending moments near their respective natural frequencies.

Key Findings

- The scale-model representation of the TMD system simulated the response of a full-scale passive TMD system, including various frequency and damping setpoints, and a fixed case.
- The Pitch TMD was effective in reducing platform pitch motion near resonance by 21-47%, depending on the wave environment with most reduction seen in the I2-Rated case.
 - Pitch TMD slightly increased platform pitch motion in the wave energy region
- The Tower TMD was effective in reducing tower base bending loads near resonance by 60% in all wave conditions.
- The effect of the umbilical cable was significant and specific tests in Campaign 4 were included to further quantify the effect. Additional surge and (minor) heave stiffness terms were added to the hydrostatic model.
- Internal load measurements in the pontoon legs were collected.
- Numerical Modeling
 - Numerical models showed good agreement for matching system free decay responses and the qualitative effects of the TMDs were reproduced
 - Improved representation of viscous effects on the hull would likely improve capturing low frequency resonant motion (e.g. surge and pitch motion). Viscous elements with depth dependent drag coefficients are suggested to implement.
 - The tower and hull connection introduced non-negligible compliance in the model that was well accounted for by a finite-stiffness element located at the interface.

Chapter 4

CAMPAIGN 4: FLOATING TURBINE WIND/WAVE TESTING

4.1 Research Objectives

Chapter 4 presents the results from Campaign 4, including the work performed after Campaigns 1-3 to prepare for the coupled wind/wave testing of the floating wind turbine system. The model for Campaign 4 consisted of the turbine from Campaign 1 mounted to the hull from Campaign 2/3 using a new flexible tower tuned to the appropriate stiffness to achieve the correct fore/aft bending frequency in floating conditions. The basin setup, including moorings and test environments, were based on those from Campaigns 1-3. The work completed between Campaigns 1-3 included:

- Calculating an additional set of airfoil polars based on above-rated turbine performance data. This sought to address the Reynolds number sensitivities identified in the above-rated region. As such, two ROSCO tunings were considered in Campaign 4, with one tuned for “Rated” conditions and one tuned for “Above-Rated” conditions.
- Rebuilding and retuning the TMD system. Improvements were made to the wiring to reduce mechanical damping. This helped improve the stability of the force-feedback system at low stiffness and damping settings for the Pitch TMD tuning.
- Tuning floating feedback gain in ROSCO. With the hull characteristics determined, the floating feedback loop of ROSCO was tuned using the ROSCO Toolbox. This allowed testing of the floating feedback control loop in Campaign 4.

4.2 Airfoil Performance Tuning

As discussed in Chapter 2, the airfoil polars were initially based on published data for the SD7032 airfoil. These polars were used for the initial ROSCO tuning and updated once performance data from the as-

built turbine was collected. Tuning was performed for data collected at both rated and above-rated wind speeds to determine the Reynolds effect due to the increased wind speed. The tuning process was as follows:

4.2.1 Power And Thrust Coefficient Determination

As described in Chapter 2, steady-state operational data for the turbine were collected for a variety of blade pitch and turbine rotor speed setpoints, at a total of three steady wind speeds. These data were used to create a map of power, thrust, and torque coefficients as a function of tip-speed ratio. The wind speeds tested were 12.8, 14.7, and 18.4 m/s, representing rated and two above-rated setpoints. Tests were conducted where the collective blade pitch was set to the specified angle, and then rotor speed was stepped through various speeds. Each turbine speed was held constant until the turbine reached steady state prior to stepping to the next setpoint to cycle through a range of TSR values. The power, thrust, and torque coefficients are ratios of the amount of power, thrust, and torque, respectively, generated by the rotor relative to the theoretical amount available in the wind passing through the rotor's swept area and are calculated as follows (Jamieson, 2011).

The power coefficient is the ratio of the mechanical power generated by the turbine divided by the available power in the wind. The mechanical power was calculated using the torque values recorded from the turbine and the relationship shown in Equation 4.1:

$$P_{mechanical} = Q\omega$$

Equation 4.1

where Q was torque and ω was the rotor angular velocity. The power in the wind was calculated using Equation 4.2:

$$P_{wind} = \frac{1}{2} \rho U_{\infty}^3 A$$

Equation 4.2

where ρ was air density, U_{∞} was far-field wind speed, and A was the swept area of the rotor. The performance coefficient was then calculated using Equation 4.3:

$$C_p = \frac{P_{mechanical}}{P_{wind}} = \frac{Q\omega}{\frac{1}{2} \rho U_{\infty}^3 A}$$

Equation 4.3

The thrust coefficient is the ratio of the thrust generated by the turbine relative to the thrust available in the wind. The thrust available in the wind was calculated as Equation 4.4:

$$T_{wind} = \frac{1}{2} \rho U_{\infty}^2 A$$

Equation 4.4

and the thrust on the turbine was recorded using a load cell. The thrust coefficient was then calculated using Equation 4.5:

$$C_t = \frac{T_{mechanical}}{T_{wind}} = \frac{T_{mechanical}}{\frac{1}{2} \rho U_{\infty}^2 A}$$

Equation 4.5

The torque coefficient can be calculated from the performance coefficient using the Equation 4.6:

$$C_q = \frac{C_p}{TSR} = \frac{Q\omega}{\frac{1}{2} \rho U_{\infty}^3 A} * \frac{U_{\infty}}{\omega R} = \frac{Q}{\frac{1}{2} \rho U_{\infty}^2 A R}$$

Equation 4.6

where TSR was the tip-speed ratio (shown in Equation 2.3 from Chapter 2) and R is the rotor radius.

The determined power and thrust coefficients were then gridded onto a surface referenced to blade pitch and TSR. Performance data were collected around the turbine's expected operating blade pitch and TSR values. The ‘rated’ performance map drew from data taken at the rated wind speed. Data at higher blade pitch angles and lower TSRs were collected at higher wind speeds and the ‘above-rated’ performance map was created by filling in data collected at lower wind speeds for the lower blade pitch angles. Therefore, values far outside the turbine’s expected operating range (e.g. low pitch angle at low TSR or high pitch angles at high TSR) are not likely to be referenced by the tuning process. A spline fit was used to fill in remaining gaps in the surface, with a minimum allowable value of zero. The ‘above-rated’ C_p and C_t surfaces are shown in Figure 4.1.

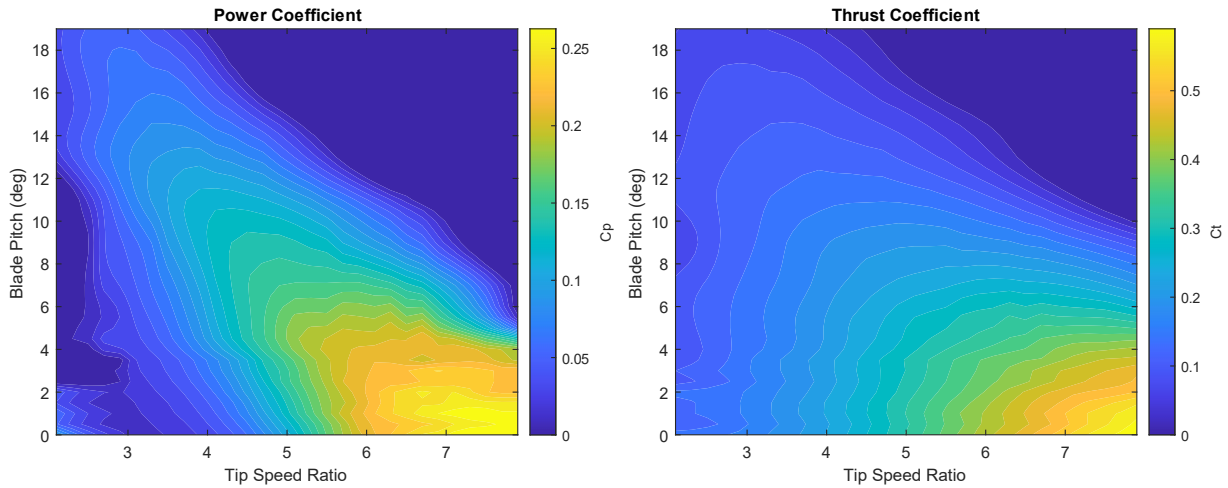


Figure 4.1: Above-rated C_p and C_t surfaces

4.2.2 Tuning Lift and Drag Polars

To determine the lift and drag polars of the as-built FOCAL turbine blades, an initial set of polars for the SD7032 airfoil (“Unmodified”) was smoothed to produce a set of baseline polars (“Baseline”). This was done to prevent the optimization process finding very narrow, local solutions that may not be reproducible in the basin. The polars are shown in Figure 4.2.

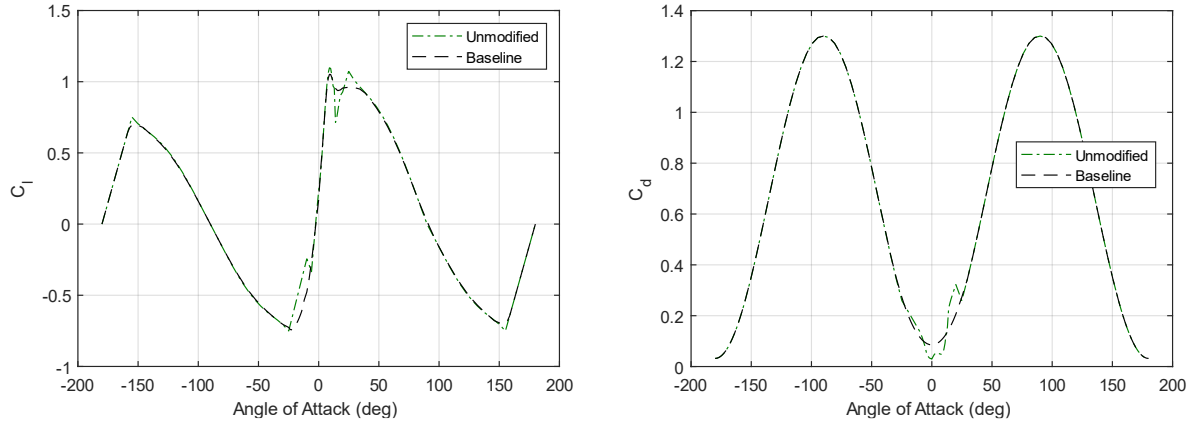


Figure 4.2: Unmodified and baseline C_l (left) and C_d (right) polars

A set of “control points” was established at several angles of attack: -23, 0, 9, 13, 16, 20, and 25 degrees for C_l and 0, 9, and 25 degrees for C_d . These control points spanned the range of expected blade pitch angles and were adjusted up and down individually within defined bounds to modify the polars. Variations from the baseline polars were interpolated linearly between each control point. “Stationary points” were set at ± 90 degrees, to control the blend into the first and last control points. An example set of modified polars is shown in Figure 4.3.

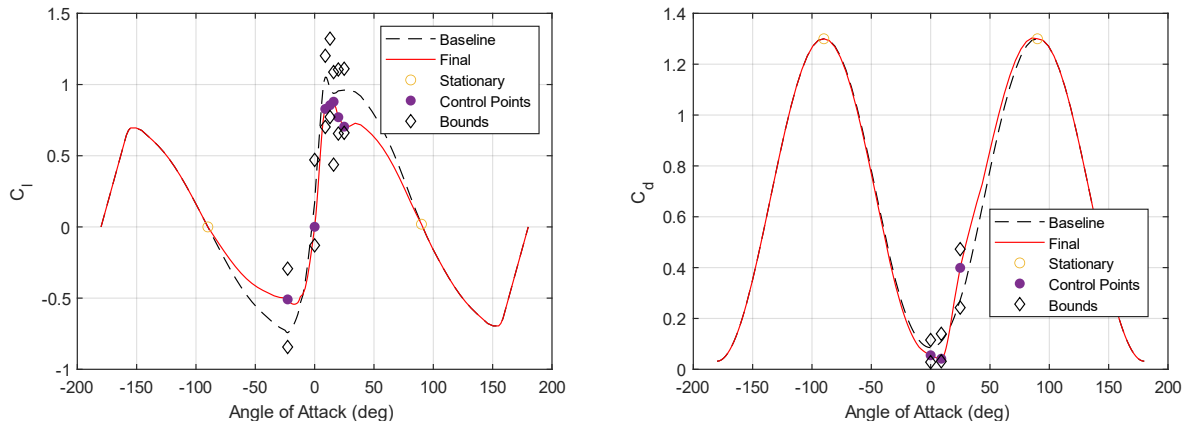


Figure 4.3: Example modified C_l (left) and C_d (right) polars, showing control points and their bounds

To determine the settings of the control points that best reflected the performance of the as-built turbine, a multi-objective genetic algorithm was used (e.g. Deb, 2004). The genetic algorithm selected values for each of the control points within their bounds and then ran OpenFAST simulations at several blade pitch angles at rated rotor speed. Since OpenFAST doesn't inherently account for Reynolds effects in the airfoil performance, running at different rotor speeds was not necessary. For the rated tuning, 0, 5, and 15 degrees of blade pitch were used. For above-rated, 9, 11, and 17 degrees were used. Wind speed in these simulations slowly ramped so that a range of TSR values were covered. C_p and C_t values were extracted at various TSRs and compared with the experimental data. The mean error between the OpenFAST and experimental C_p and C_t values was then calculated for each of the three blade pitch angles, normalized by the maximum experimental value at each blade pitch angle. These normalized errors for the different blade pitch angles were then averaged to produce two cost metrics for the genetic algorithm, one for C_p and one for C_t .

The genetic algorithm was run for 100 generations with a population of 100 individuals. A Pareto front, shown in Figure 4.4, shows the performance of the individuals of the final generation for the rated wind speed case.

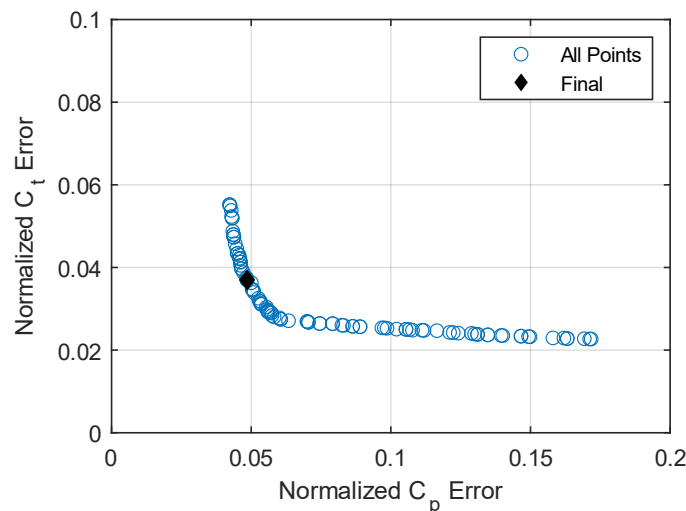


Figure 4.4: Genetic algorithm Pareto front

Of these, a “final” individual was chosen that minimized Equation 4.7:

$$err = \sqrt{(err_{C_p})^2 + (err_{C_t})^2}$$

Equation 4.7

where err_{C_p} and err_{C_t} are the two cost metrics for the genetic algorithm. The final polars for the rated and above-rated tunings are shown in Figure 4.5.

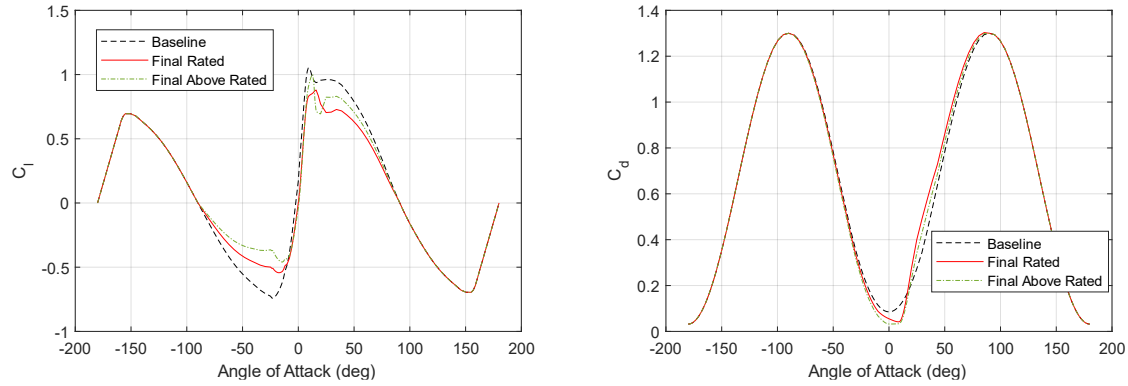


Figure 4.5: Final C_l (left) and C_d (right) polars compared to baseline

An example comparison of the how the baseline and final rated polars match the experimental C_p results at 0 degrees of blade pitch are shown in Figure 4.6. These polars were then used in Campaign 4 in the ROSCO toolbox to create the “rated” and “above-rated” tunings for ROSCO.

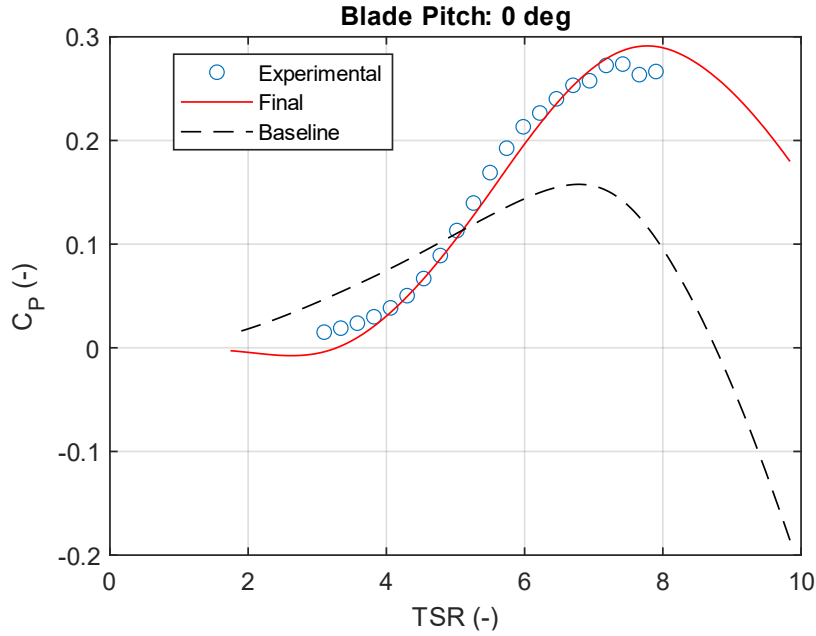


Figure 4.6: C_p vs. TSR comparison of experimental results and baseline and final OpenFAST results at 0 degrees blade pitch

4.3 TMD Tuning

It was noticed during Campaign 2/3 that the performance of the TMD was subject to repeatability issues where the mechanical function of the TMD, wire routing, and equilibrium springs would sometimes inhibit free motion of the actuated mass. In such cases, the force feedback controller of the TMD would be unable to implement the appropriate motion of the mass as the total reaction force of the TMD was no longer exclusively felt by the 1DoF load cell. When the wiring would entangle with the equilibrium springs, they would act as an additional external spring whose effect was unaccounted for in the control system and therefore produce erroneous behavior. To fix this, an alternative cable routing was employed which prevented the wires from entangling with the springs. However, this changed the effective spring constant of the system and thus the TMD calibration process described in Section 0 had to be performed again to determine the appropriate TMD setpoint mapping. This did not change the frequency or damping targets, just the internal setpoints needed to achieve the targets with the actuated mass system.

4.4 ROSCO Floating Feedback Control Tuning

As mentioned in Chapter 2, the floating feedback control loop of ROSCO was unable to be tested in the fixed base configuration of Campaign 1. Additionally, the as-built hull characteristics were required to tune the gain of the floating feedback loop, which acts in a “parallel compensation” method (Van Der Veen, 2012 and Abbas et al., 2023) as shown in Figure 4.7.

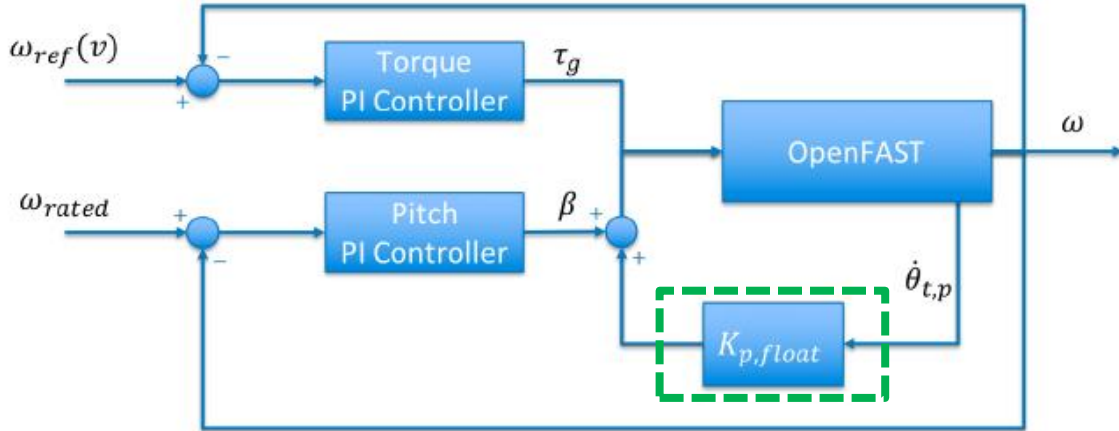


Figure 4.7: ROSCO Floating Feedback Control Loop

With the hull characteristics determined, most specifically the platform pitch natural period and tower fore/aft bending modes, the gain of the floating feedback controller was tuned. This was done in the ROSCO toolbox using the methodology outlined in (Abbas et al., 2021). The goal of this additional control term was to provide a correction to the blade pitch setpoint to account for the change in relative wind speed experienced by the rotor due to platform pitch motion. It was based on feedback from the nacelle fore/aft or pitch rotational acceleration and acted in parallel with the blade pitch PI controller in ROSCO to correct the blade pitch setpoint and reduced the need to detune the blade pitch controller gains due to the negative-damping issue identified by (Larsen & Hanson, 2007).

To implement the floating feedback control, real-time nacelle acceleration data from the scale model needed to be provided to ROSCO. This was initially attempted using a tri-axial accelerometer located in the nacelle to directly provide the fore/aft acceleration. However, the accelerometer used also measured the acceleration due to gravity. Thus, when the platform would pitch from vertical, contributions to the measured acceleration from gravity would be added to the measured signal. It was not possible to filter the signal sufficiently to completely remove this phenomenon without imposing detrimental phase-lag. As such, we instead used an inertial measurement unit (IMU) mounted to the hull, which measured pitch velocity directly, to provide the needed input to ROSCO. ROSCO was then modified to accept this data stream and perform the appropriate differentiation and filtering to generate the needed nacelle rotational acceleration signal. The effect of this feedback loop was demonstrated in OpenFAST. Results in Figure 4.8 compare the response with the feedback term OFF (thin lines) and ON (thick lines) and show effective attenuation of the high-frequency oscillations in rotor thrust and platform pitch due to a step wind input.

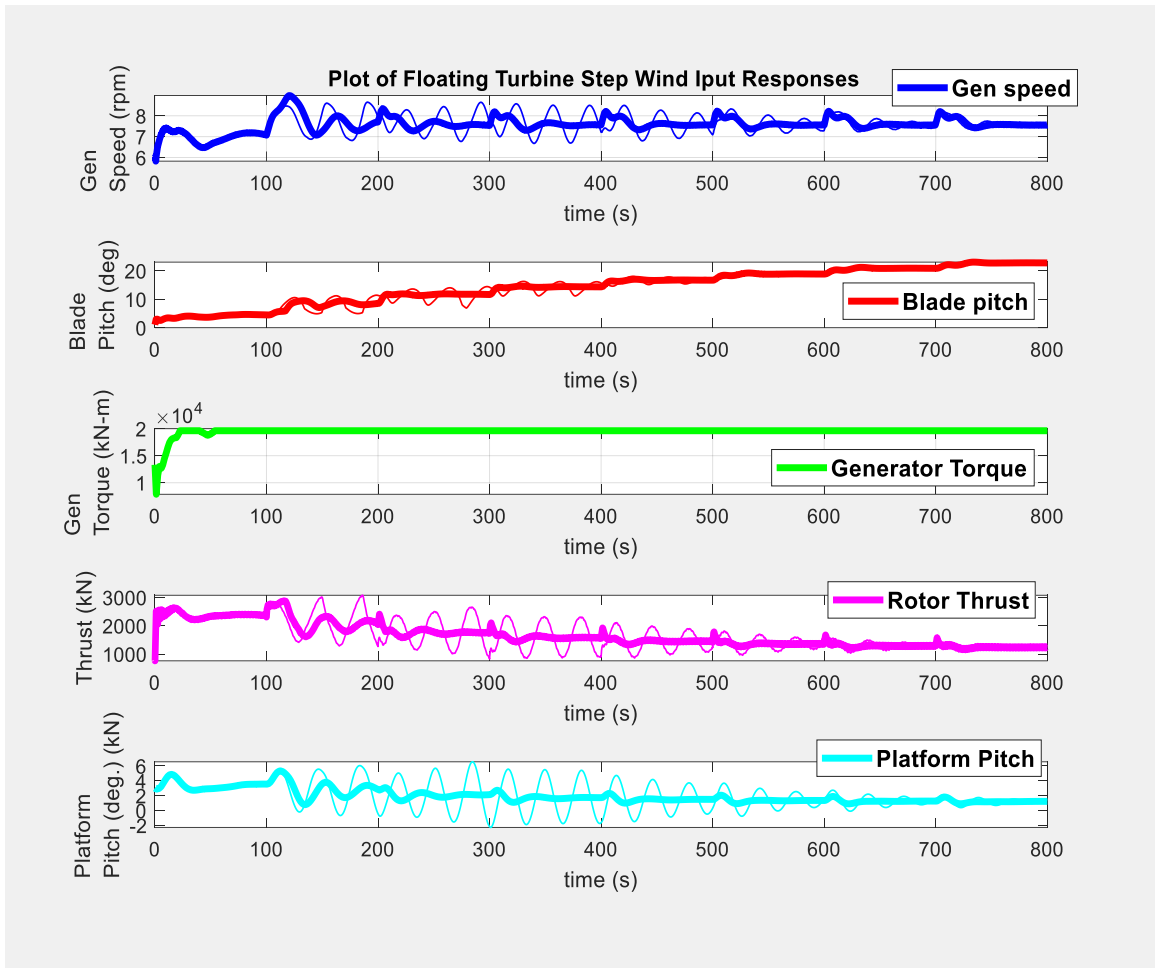


Figure 4.8: Simulated ROSCO Performance in Region 3

4.5 Experimental Setup

As discussed previously, the experimental setup for Campaign 4 involved attaching the operational turbine to the platform using a flexible tower and perform testing with the same wind/wave conditions developed from Campaigns 1-3. The model was installed in the basin where the turbine was tested in Campaign 1 to maintain similar wind flow conditions. This layout is shown in Figure 4.9.

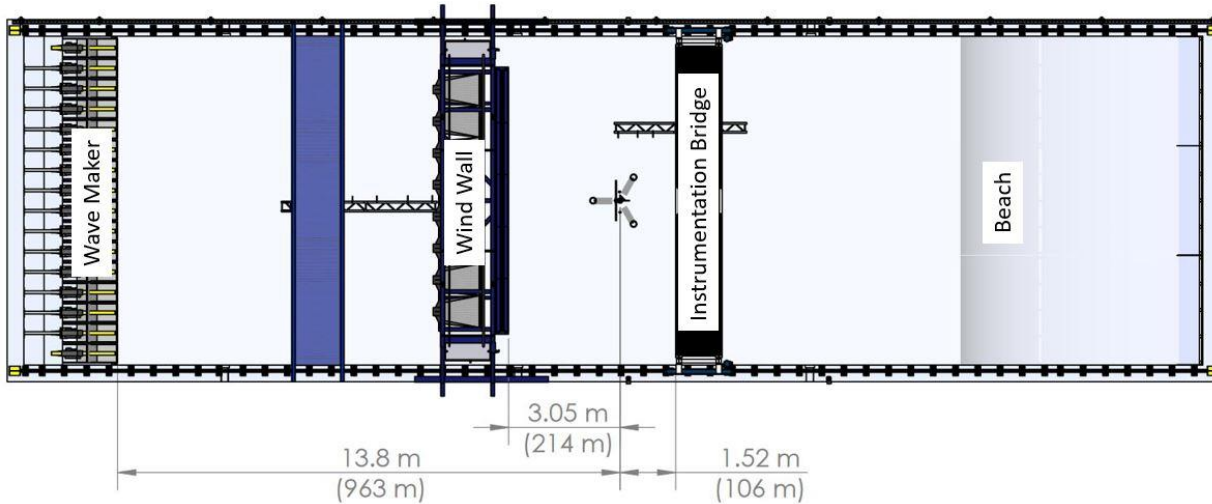


Figure 4.9: General Basin Layout for Campaign 4

The as-built system properties were measured and the test report (Robertson, 2023c) provides the relevant properties of the floating wind system needed to develop a simulation model. This information is summarized here and provided at full-scale using a 1:70 ratio. These data are provided in an effort to provide a cohesive description of the as-built floating turbine system as there were slight changes in overall system properties due to modifications needed to assemble the turbine onto the platform. An overview photo of the FOCAL system is shown in Figure 4.10.

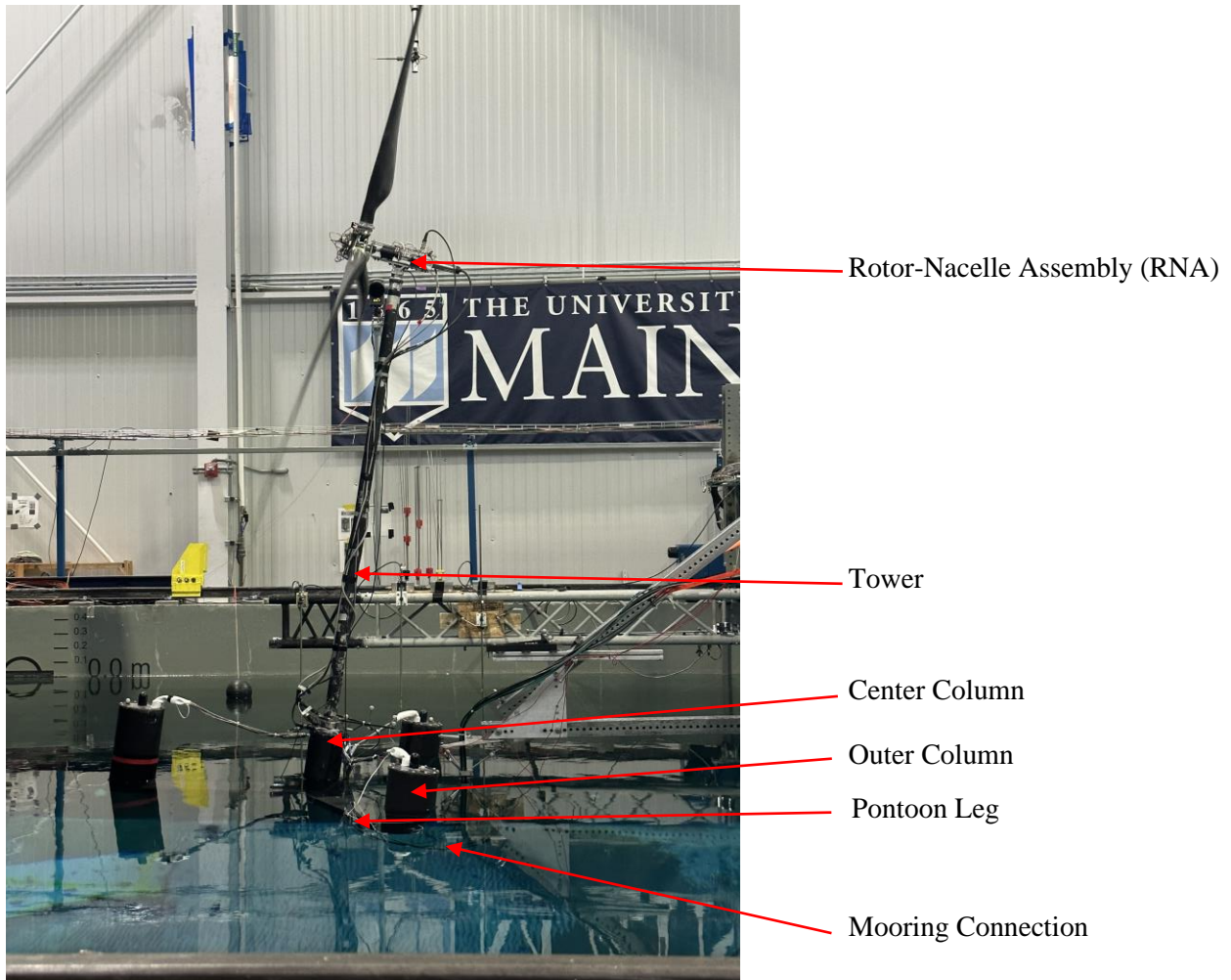


Figure 4.10: FOCAL Scale Model Wind Turbine and Hull

Table 4.1 describes the properties of the assembled system. Center of gravity locations are given relative to the centerline of the model at the bottom (keel). Inertia values are given about the system center of gravity.

Table 4.1: As-Built System Structural Properties

Property	Unit	Value (Sans Umbilical)	Value (With Umbilical)
Total Mass of Model	kg	20,494,250	20,734,350
Overall CG height from keel	m	19.39	19.08
Overall CG x offset keel	m	-0.08	0.24
Overall CG y offset keel	m	-0.53	-0.53
Overall I_{xx} (Roll Inertia) about CG	$\text{kg}\cdot\text{m}^2$	4.919E+10	4.937E+10
Overall I_{yy} (Pitch Inertia) about CG	$\text{kg}\cdot\text{m}^2$	4.936E+10	4.972E+10
Overall I_{zz} (Yaw Inertia) about CG	$\text{kg}\cdot\text{m}^2$	Not Measured	Not Measured

Free decay results for various system configurations are shown in Table 4.2.

Table 4.2: As-Built System Free Decay Periods

Degree of Freedom	Period (s) Sans Umbilical Fixed TMD	Period (s) With Umbilical Fixed TMD	Period (s) With Umbilical Pitch-Tuned TMD	Period (s) With Umbilical Tower-Tuned TMD
Surge	82.56	80.79	-	-
Sway	-	79.56	-	-
Heave	20.98	21.16	-	-
Roll	-	31.09	-	-
Pitch	31.00	30.79	31.23	30.94
Yaw	-	50.94	-	-

Additional properties of the floating system are included in Appendix C where geometric quantities are listed in Table C.1 and system layout and coordinate systems are identified in Figure C.1 through Figure C.5. Buoyancy characteristics for the system are given in Table 4.3.

Table 4.3: Floating System Buoyancy Characteristics

Property	Units	Value (Sans Umbilical)	Value (With Umbilical)
Draft (Keel to SWL)	m	20.09	20.66
Displaced volume	m^3	20,551.8	20,792.6
Center of buoyancy from keel	m	6.27	6.43
Buoyancy force in undisplaced position ($\rho g V_0$)	N	2.010E+08	2.033E+08

4.5.1 Hull Properties

Properties for the hull are given in Table 4.4. The given properties represent the hull with the TMDs installed and fixed in their nominal position, but without the umbilical cable attached.

Table 4.4: Hull Properties

Property	Units	Value
Mass	kg	1.866E+07
Vertical Center of Gravity from keel	m	6.94
CG x offset	m	0.08
CG y offset	m	-0.60
I_{xx} Roll Inertia about hull CG	kg-m ²	1.353E+10
I_{yy} Pitch Inertia about hull CG	kg-m ²	1.402E+10
I_{zz} Yaw Inertia about hull CG	kg-m ²	1.52E+10
Hydrostatic restoring in heave ($C_{33}^{Hydrostatic}$) ¹	N/m	4.352E+06
Hydrostatic restoring in roll ($C_{44}^{Hydrostatic}$) ¹	N-m/rad	2.134E+09
Hydrostatic restoring in pitch ($C_{55}^{Hydrostatic}$) ¹	N-m/rad	2.134E+09

¹From WAMIT model of VolturnUS-S

4.5.2 Tuned Mass Damper Properties

As before, the TMDs were placed in each of the offset columns to provide damping to the system motion. Each TMD had a mass of 686,000 kg at full scale, which was accounted for in the hull properties. The spring stiffness of the TMDs were tuned to focus on either the platform pitch or the tower fore/aft bending natural frequencies, and the damping was set to produce a 20% damping ratio. They were also tested in a fixed configuration and held at their neutral position to establish “baseline” performance.

Three TMD conditions were tested in the campaign:

- **Fixed:** TMD masses were held in place at their nominal position (see Table 4.6).
- **Pitch TMD:** TMD response was tuned to the Rigid Body Pitch Frequency of the entire floating turbine system.

- **Tower TMD:** TMD response was tuned to the 1st Tower Bending Frequency in the fore/aft direction with the entire system floating and the RNA attached

Settings for each TMD condition are in Table 3.14 and center of mass is presented in Table 4.6.

Table 4.5: Tuned Mass Damper Settings

File Code	Target Frequency	Mass [kg]	Stiffness [N/m]	Damping [Ns/m]
D01	N/A (TMDs fixed)	686,000	inf	--
D02	Pitch	686,000	31,482	58,783
D03	Tower	686,000	4,624,376	712,441

Table 4.6: Tuned Mass Damper CG locations

Position	CG Z* Location [m]
Nominal	12.97
Negative Stop Position	2.47
Positive Stop Position	23.47

*Distance from Keel

4.5.3 Mooring Properties

The mooring layout for the model test can be seen in Figure 3.6, with the locations of the attachment points given in Table 3.8.

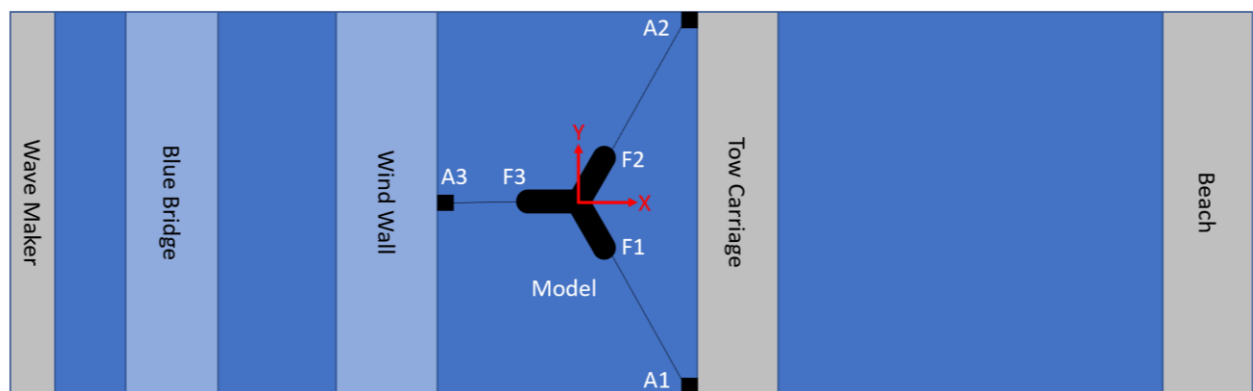


Figure 4.11: Mooring anchor and fairlead locations (not to scale)

Table 4.7: Fairlead and anchor locations

Label	Description	X Position [m]	Y Position [m]	Z Position* [m]
Origin	Model Center	0.0	0.0	0.0
A1	Anchor Point 1	179.55	-305.69	-13.44
A2	Anchor Point 2	175.91	303.66	-13.58
A3	Anchor Point 3	-186.97	2.94	-14.98
F1	Fairlead 1	29.8	-51.5	-14.36
F2	Fairlead 2	29.1	51.5	-14.36
F3	Fairlead 3	-59.4	0.0	-14.36

*Based on Nominal Still Water Line (Table 4.3)

As before, the moorings were fishing lines attached to spring elements with spring stiffnesses set to approximate the overall surge stiffness of the VolturnUS-S catenary mooring system under rated wind load conditions. In addition to the mooring lines, a bundle of wiring related to the measurement sensors also hung off the structure, as can be seen in Figure 3.7. The surge and heave stiffnesses of this umbilical cable were characterized with force/displacement tests and included in Table 3.9.

Table 4.8: Stiffness properties of the mooring lines

Line	Pretension [N]	Stiffness [N/m]
Mooring 1 (A1-F1)	3.31E+06	1.26E+05
Mooring 2 (A2-F2)	3.24E+06	1.27E+05
Mooring 3 (A3-F3)	3.41E+06	1.23E+05
Umbilical, Surge	-	6.86E+03
Umbilical, Heave	-	6.22E+04

Mass properties for the umbilical are included in Table C.2 in Appendix C.

4.5.4 Tower Properties

The tower was a hollow aluminum tube fixed on the bottom to a 6DoF force gauge and bolted on the top to a 6DoF force gauge on the bottom of the RNA. Table 4.9, below, provides the relevant properties needed to model the tower and a drawing of the tower and its flanges is provided in the Test Report.

Table 4.9: Tower Properties

Property	Units	Value
Elevation to tower base (platform top) above keel	m	38.34
Elevation to tower top (yaw bearing) above keel	m	161.89
Tower inner diameter	m	3.36
Tower outer diameter	m	3.57
E (Young Modulus) – scaled 6061 Aluminum property	GPa	4,830
E (Young Modulus) – derived to match floating frequency	GPa	1,456
G (Shear Modulus) – scaled 6061 Aluminum property	GPa	1,281
Tower mass	kg	3.361E+05
Tower + wiring mass	kg	6.414E+05
Vertical center of gravity from keel (Tower + Wiring)	m	102.78
CG x offset (Tower + Wiring)	m	3.31
CG y offset (Tower + Wiring)	m	0.49
I_{xx} Roll Inertia about tower+wiring CG	kg-m ²	9.368E+08
I_{yy} Pitch Inertia about tower+wiring CG	kg-m ²	9.203E+08

The tower natural frequency was measured by striking the tower top with a hammer under several conditions. In the ‘floating’ case, the entire system was floating in the basin with the umbilical cables attached and tethered using the mooring lines. For the ‘simply supported’ case, the tower, RNA, and associated wiring were mounted to the hull, which was resting on a level floor outside the tank. Average full scale natural frequencies from these tests are given in Table 4.10.

Table 4.10: Tower Natural Frequencies

Test Condition	Average Natural Frequency [Hz]
Simply Supported, Fixed TMD: Fore-Aft, Side-Side	0.261, 0.281
Floating, Fixed TMD: Fore-Aft, Side-Side	0.406, 0.423
Floating, Pitch TMD: Fore-Aft, Side-Side	0.424, 0.433
Turbine, Rated Operation 1P and 3P	0.126, 0.378

It is important to note that a numerical model using the scaled Aluminum material properties from Table 4.9 will result in a higher tower frequency than those listed in Table 4.10. This is due to compliance in the tower bottom load cell and the hull. To compensate, a derived Young's modulus of 1,456 GPa can be used to achieve the correct floating tower frequency.

4.5.5 RNA Properties

The turbine used in this campaign was identical to the one used in Campaign 1, with a rated rotor speed of 7.56 rpm. Mass properties for the RNA and its components are given in Table 4.11. Inertia values are given about the center of gravity of the individual component. There is no CG y-offset for any of the components.

Table 4.11: RNA Mass Properties

Component	Mass [kg]	CG_z-offset from keel [m]	CG_x-offset [m]	I _{xx} about local CG [kg·m ²]	I _{yy} about local CG [kg·m ²]
Blades (total)	242,633	169.74	-10.86	6.712E+08*	3.356E+08*
Hub	442,573	169.72	-10.71		
Nacelle	479,960	167.73	4.38	1.580E+06	3.430E+07
Tower-Top 6DoF	31,899	162.55	0.00	-	-
RNA Total	1,197,065	168.74	-4.40	6.751E+08	3.723E+08

*Rotor combined inertia expressed along rotor shaft axis (6° incline) about the combined CG of -10.76 in X and 169.73 in Z

The nacelle yaw inertia (I_{zz}) about its center of gravity was 3.33E+07 kg·m² and the hub inertia about the rotor axis was 7.34E+06 kg·m². Note that this value was included in the combined I_{xx} value for the hub and blades.

4.6 Turbine Controller

As in Campaign 1, control of the turbine was accomplished through a real-time implementation of ROSCO, run at 120 Hz (1,000 Hz model-scale) on the cRIO-9047 real-time system utilizing the Bladed-

style DISCON.IN input file. Two tunings were performed, depending on if the turbine was at rated or above-rated conditions, as shown in Table 4.12. The main control loops of the “ROSCO Baseline” (RO) controller are the Collective Blade Pitch Controller and the Generator Torque Controller. For Campaign 4, only rated and above-rated conditions were considered. In these conditions, the baseline controller used a constant generator torque setpoint and a proportional-integral controller to regulate rotor speed through collective blade pitch actuation. Additionally, the “Floating Feedback” (FL), “Pitch Saturation” (PS), and “Setpoint Smoother” (SS) control strategies were toggled on/off through the DISCON.IN input file. This experiment implemented the SS for all tests and selectively activated the FL and PS control loops to assess their impact on system performance. A summary of control methodologies for Campaign 4 is provided in Table 4.12.

Table 4.12: Controller strategies for FOCAL Campaign 4

File Code	Control Method	ROSCO Tuning	Actuation	Sensing
T00	N/A	N/A	N/A	Idle turbine
T01	ROSCO Rated	Rated	Collective pitch & Generator torque	Rotor speed, Generator torque
T03	ROSCO + PS	Rated	Collective pitch & Generator torque	Rotor speed, Generator torque
T05	ROSCO Above-Rated	Above-Rated	Collective pitch & Generator torque	Rotor speed, Generator torque
T06	ROSCO + FL	Above-Rated	Collective pitch & Generator torque	Rotor speed & Nacelle acceleration from IMU

4.6.1 Floating Feedback

The FL control loop was used to decouple platform motion and generator speed variation. In Campaign 4, this feedback loop was considered with the above-rated wind and wave conditions. It used the platform pitch rotational velocity and a tuned control loop gain to calculate a blade pitch correction to the baseline blade pitch setpoint. The nacelle pitch velocity signal was filtered with a first-order high-pass filter and a

second-order low-pass filter based on the input settings in the DISCON.IN file. The default settings were used for these filters with the high-pass frequency set to 0.0016 Hz and the low-pass frequency set to 0.034 Hz to include the system pitch natural frequency. A Bode plot of the filter is shown in Figure 4.12.

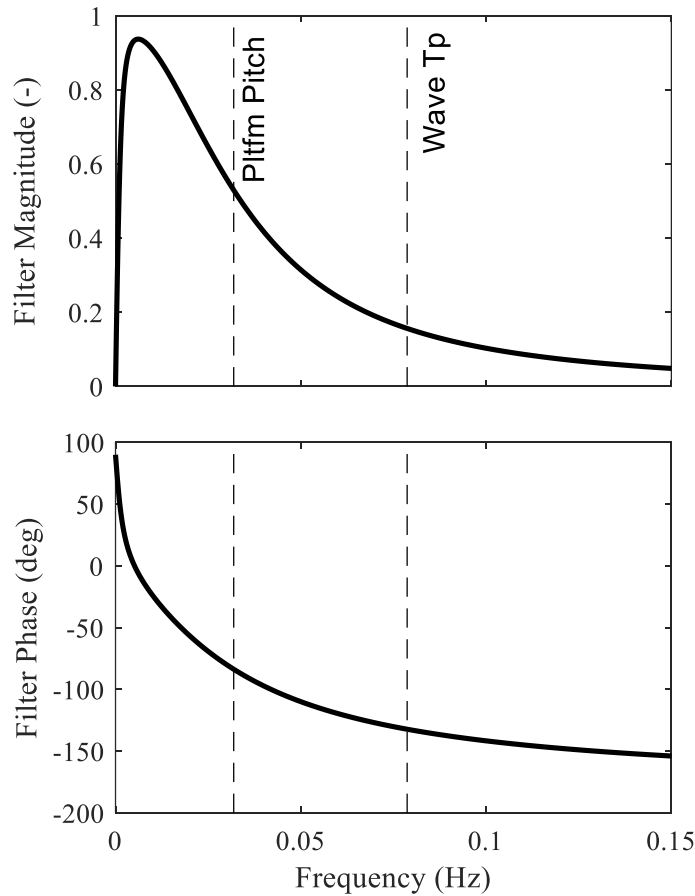


Figure 4.12: ROSCO FL feedback filter, magnitude and phase

4.6.2 Peak Shaving

Rotor thrust is typically at a maximum at near-rated wind speeds and plays a large role in the tower base loads experienced by the system. Peak shaving is a control strategy that reduces these loads by imposing a minimum blade pitch angle scheduled by wind speed. It was considered in Campaign 4 and selectively enabled to assess the effect. The default maximum allowable thrust load of 80% thrust at rated was set,

which defined the minimum blade pitch schedule based on the thrust coefficient (C_t) for a given wind speed.

4.7 Instrumentation and Data Acquisition

The turbine and floating platform were fully instrumented, and all data are recorded with a National Instruments cRIO-9047 data acquisition system. Data were collected at 120 Hz (1,000 Hz model-scale) and recorded to file at 24 Hz (200 Hz model-scale). Additionally, a Qualisys motion capture system tracked reflective markers on the hull to resolve 6DoF motion of the hull. This system recorded data at 12 Hz (100 Hz model-scale). An overview of the system and primary instrumentation is shown in Figure 4.13, and a listing of sensor models used during Campaign 4 is shown in Table 4.13.

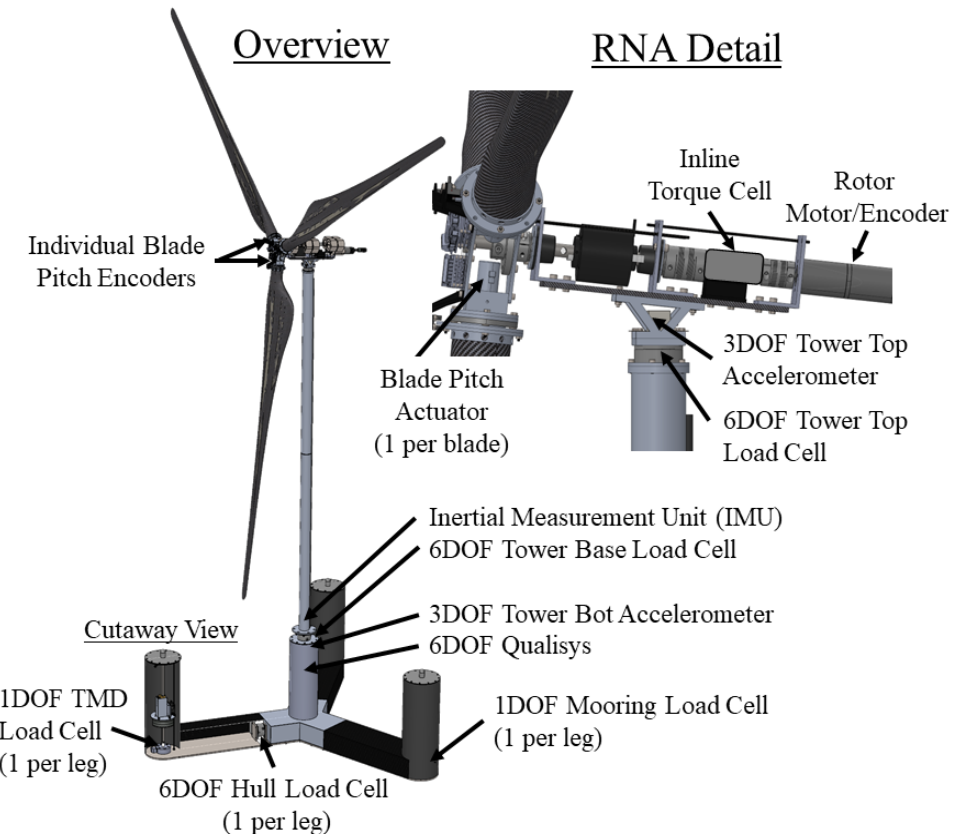


Figure 4.13: Instrumentation employed on the FOCAL hull and turbine

Table 4.13: Instrumentation list

Description	Instrument	Quantity
TMD load cell	Interface 2420	3
TMD actuator	LinMot PS02-23Sx80F-HP-K	3
TMD drive	LinMot C1250-DS-XC-0S-000	1
Pontoon internal 6DoF load cell	ATI Mini58 IP68	3
Tower Base 6DoF load cell	ATI Mini58 IP68	1
Tower Top 6DoF load cell	ATI Mini45	1
Tower Top/Base Accelerometer (X, Y, Z)	PCB Piezotronics 3713F112G	2
Port/Starboard mooring load cell	Interface WMC-22N	2
Bow mooring load cell	Interface WMC-45N	1
Rotor Drive	Accelnet BEL-090-14	1
Analog Input	Beckhoff EP3174-0002	2
EtherCAT Junction	Beckhoff EP9128-0021	1
Signal Conditioner	ATI 9105-ECATOEM	5
Load Cell Amplifier	Tacuna EMBSGB200	6
DC Power Converter	CUI Inc. PQAE50-D48-S24-T	1
Leak Sensor	Grove Water Sensor	4
cRIO	cRIO-9047	1

4.7.1 A Note on Rotor Thrust

It is important to note that while rotor aerodynamic thrust was not measured directly, it was calculated from the tower top 6DoF force sensor located between the tower top and the nacelle, see Figure 4.13. In this configuration, this sensor measured all reaction loads from the nacelle. To calculate the rotor thrust force, the effect of gravity and nacelle inertial forces were removed from the signal in post-processing using the values measured by the tower top accelerometer, the RNA mass, and the platform pitch inclination angle.

4.7.2 Internal Load Cells

Internal load cells in the pontoons were included and the coordinate systems for the readings of the pontoon 6DoF internal load cells are given in Figure 3.14. The load cell interface location was the same as Campaign 2, as shown in Figure 3.14. The load cell in leg 1 was found to be faulty from Campaign 2/3 and was unable to be repaired, therefore its readings have been excluded from the results.

4.8 Test Program

4.8.1 Wind Conditions

Three wind environments were tested during Campaign 4; a gust case with sudden ramps between below-rated and near-rated operating conditions (W01, mean wind speeds of 10.10 and 12.90 m/s), a turbulent wind environment at near-rated conditions (W02, mean wind speed 12.76 m/s), and a turbulent wind with an above-rated mean wind speed (W03, mean wind speed 24.05 m/s).

Table 4.14: Wind environments

Wind ID	Mean Wind Speed [m/s]	Type
W01	10.10 and 12.90	Linear gust and hold, repeat
W02	12.76	Turbulent, near rated wind speed
W03	24.05	Turbulent, at above-rated wind speed

Wind calibration dwell measurements of these environments were taken at the hub center, and at hub height at a roughly one meter (model scale) lateral offset. To compensate for nonuniformity in the wind field, provided wind calibration data is the result of averaging data from these two probes, and then multiplying the resultant time series by a constant to reflect a rotor-average wind speed determined by a wind survey. The processed wind calibration time series are shown in Figure 4.14 to Figure 4.16. Power spectral density plots for W02 and W03 use data from 2000-12800 seconds (three hours).

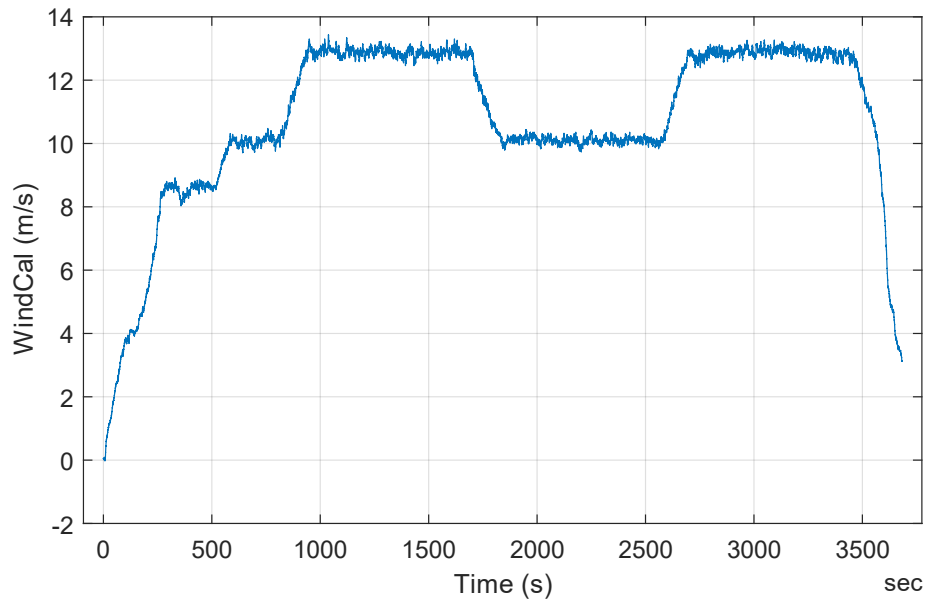


Figure 4.14: W01 wind calibration time history

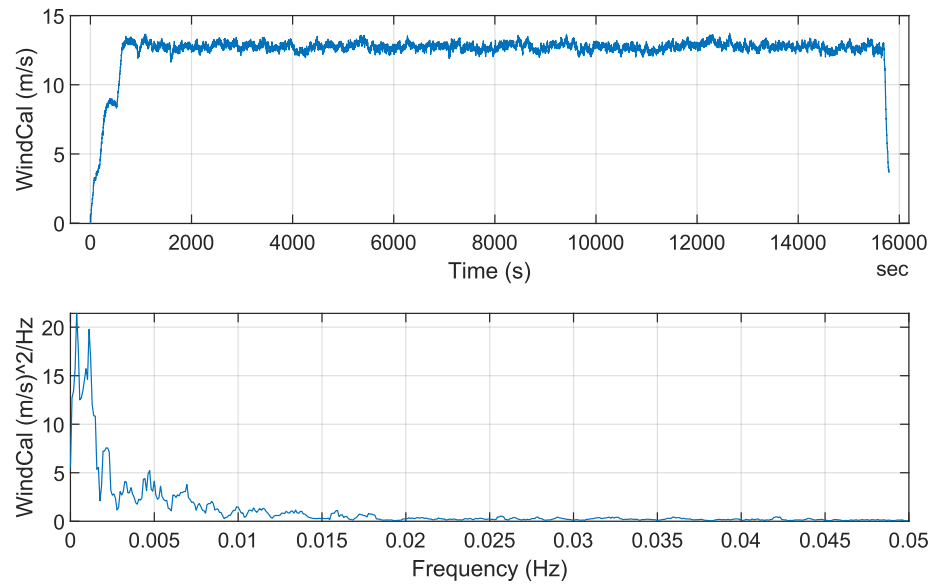


Figure 4.15: W02 wind calibration time history

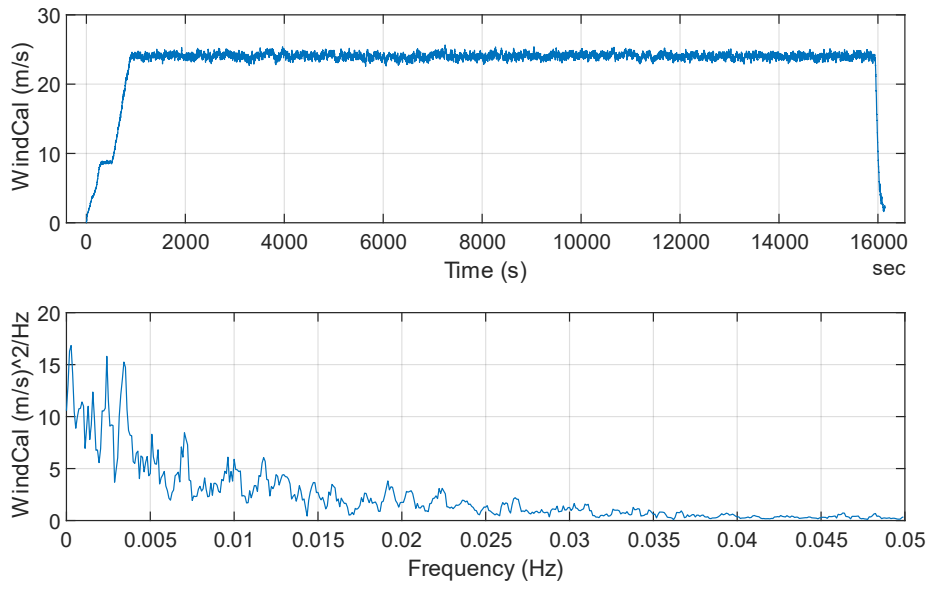


Figure 4.16: W03 wind calibration time history

4.8.2 Wave Conditions

A variety of wave conditions were used in the experimental campaign. Specifications for these waves are given in the following tables at full scale. A pink noise wave environment, specified in Table 4.15, was used to evaluate the response of the system over a broad range of frequencies.

Table 4.15: Pink noise wave properties

Wave ID	H _s [m]	Frequency Range [Hz]
E30	8.1	0.02 – 0.10

A regular wave, the properties of which are given in Table 4.16, was used to verify the system's response to first-order wave loads.

Table 4.16: Regular wave case properties

Wave ID	H _s [m]	T _p [s]
E02	10.85	13.5

Two JONSWAP spectra irregular wave cases were examined: an operational sea state (E11-E15) and 1-year extreme sea states corresponding to rated wind conditions (E21-E25). Five seeds of each wave environment (different time histories with the same overall statistics) were generated to assess the dependence of measurements on individual wave time histories. Specifications for these environments are given in Table 4.17.

Table 4.17: Irregular wave case properties

Wave ID	H_s [m]	T_p [s]	γ [-]
E11-E15	3.1	8.96	1.80
E21-E25	8.1	12.8	2.75

The following Figure 4.17 through Figure 4.20 show wave elevation time series captured with a calibration probe at the model location. Power spectral density plots denote the natural surge, pitch, and floating tower frequencies for the system with a fixed TMD and the umbilical connected. PSDs were taken from $t=1000-1600$ seconds for E02, and from $t=2000-8000$ seconds for all other environments.

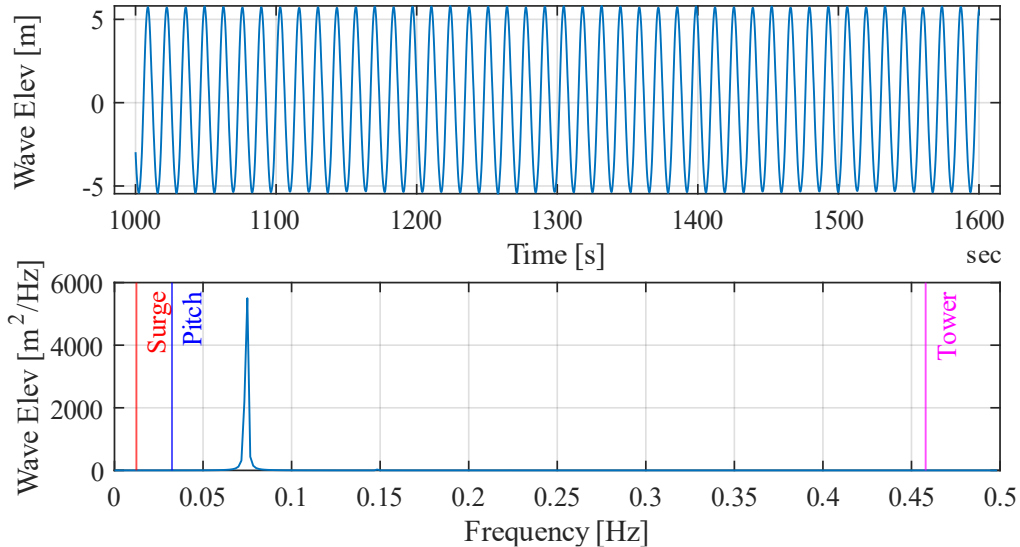


Figure 4.17: E02 wave calibration time history and PSD

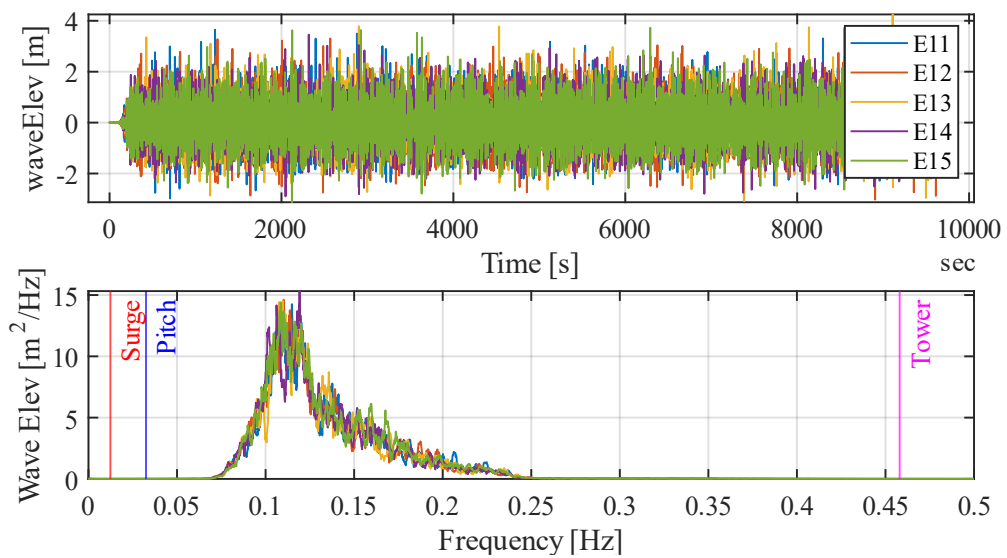


Figure 4.18: E11-E15 wave calibration time history and PSD

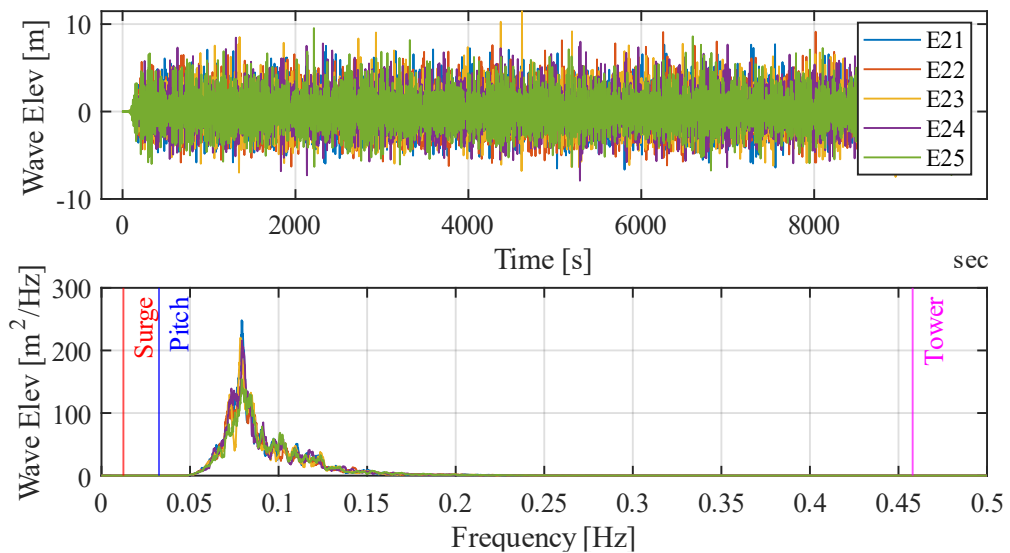


Figure 4.19: E21-E25 wave calibration time history and PSD

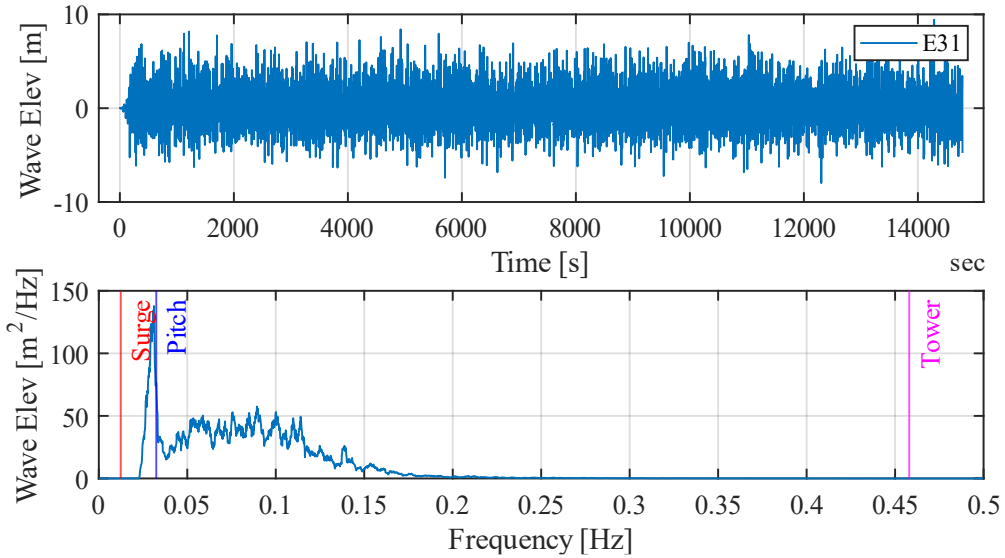


Figure 4.20: E31 wave calibration time history and PSD

4.8.3 Test Matrices

A matrix of system ID tests is provided in Table 4.18. Free decay tests were run by manually offsetting the model in the specified degree of freedom, then releasing and allowing the system to return to rest. Hammer tests were run by striking the tower top with the system either resting on a concrete floor (simply supported) or floating. For hydrostatic stiffness tests, a known force (heave) or moment (pitch) was applied to the model, and the displacement recorded. Mooring offset tests were run by displacing the model in surge and sway, and recording the amount of force in each mooring line to determine the stiffness.

In Table 4.18 through Table 4.20, codes are used to denote the test configuration. For the mooring code, “M00” denotes a test run without any mooring lines attached to the model. For “M02”, the lines are attached (though this does not indicate the status of the umbilical, which is specified separately). Tuned mass damper configuration (“D##”) follows the settings outlined in Table 4.5, and the turbine controller

("T##") codes are outlined in Table 4.12. Codes for the wind (W##") environments are specified in Table 4.14 and wave ("E##") environments are specified in Table 4.15 through Table 4.17.

Table 4.18: System ID Test Matrix

Test	Description	Configurations	Repeats
FD##	Free Decay: Surge, Sway, Heave, Roll, Yaw	M02D00T00 (No Umbilical) M02D01T00	4 4
FD02	Pitch Free Decay	M02D00T00 (No Umbilical) M02D01T00 M02D01T05_E00W03 M02D01T06_E00W03 M02D02T00 M02D02T05_E00W03 M02D02T06_E00W03 M02D03T00 M02D03T05_E00W03 M02D03T06_E00W03	4 4 1 1 4 1 1 4 1 4
HB##	Hammer Test, Simply Supported	M00D01T00	3
HF##	Hammer Test, Floating	M00D01T00 M00D02T00	3 3
SH##	Hydrostatic Pitch, Heave	M00D00T00 (No Umbilical) M00D01T00	2 2
SO##	Static Offset: Surge, Sway +	M02D00T00 (No Umbilical) M02D01T00	2 2

For the active wave/wind environments, testing was conducted with and without the umbilical. The matrix of tests conducted without the umbilical is shown in Table 4.19, and the with-umbilical matrix is presented in Table 4.20.

Table 4.19: "No-Umbilical" Test Matrix

Environment	Repeats
E02W00	1
E11W00	2
E12W00	1
E13W00	1
E14W00	1
E15W00	1
E21W00	4
E22W00	1
E23W00	1
E24W00	1
E25W00	1
E30W00	2

Table 4.20: “With-Umbilical” Test Matrix

Turbine Controller	D01 (Fixed TMD) Environment	Repeats	D02 (Pitch-tuned TMD) Environment	Repeats	D03 (Tower-tuned TMD) Environment	Repeats
T00	E02W00	1				
	E11W00	5				
	E12W00	1				
	E13W00	1				
	E14W00	1	E02W00	1	E02W00	1
	E15W00	1	E11W00	1	E11W00	1
	E21W00	5	E21W00	1	E21W00	1
	E22W00	1	E30W00	1	E30W00	1
	E23W00	1				
	E24W00	1				
T01	E25W00	1				
	E30W00	5				
	E00W01	1				
	E00W02	1				
	E02W01	1				
	E11W02	4				
	E12W02	1	E30W02	1		
	E13W02	1				
	E14W02	1				
	E15W02	1				
T03	E30W02	1				
	E00W01	1	E11W02	4	E11W02	1
	E02W01	1	E12W02	1	E12W02	1
	E30W02	1	E15W02	1	E13W02	1
			E30W02	5	E14W02	1
T05	E30W02				E30W02	5
	E00W03	1				
	E02W03	1				
	E21W03	5				
	E22W03	1	E02W03	1	E02W03	1
	E23W03	1	E21W03	1		
	E24W03	1				
T06	E25W03	1				
	E02W03	1	E02W03	1	E02W03	1
	E21W03	1	E21W03	5	E21W03	1
					E22W03	1
					E24W03	1
					E25W03	1

As an important note regarding Table 4.20, it was noticed during post-processing that the repeatability characteristics of the wind field caused slight differences in ROSCO’s wind speed estimate for some runs at rated wind (W02). Because of the characteristics of the blade pitch controller at this transition region,

runs with the slightly lower wind estimate saw much less blade pitch actuation. Runs without sufficient blade pitch actuation were removed from consideration, an example is shown in Figure 4.21.

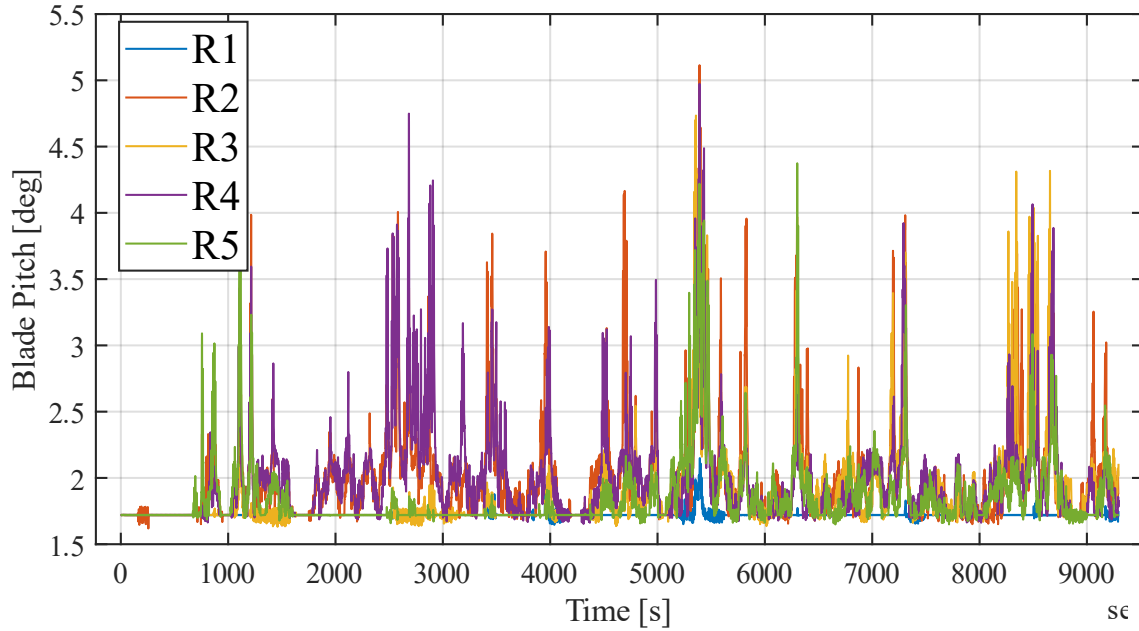


Figure 4.21: Repeats showing inconsistent blade pitch actuation

4.9 Results

This section presents results from my analysis as well as various studies performed by the FOCAL team. An overview of the experimental results was performed by me and presented here. Performance of the wind turbine controls was also performed by me and published in (Fowler et al., 2023a). This early analysis prioritized the behavior in the above-rated conditions with fixed TMDs. A more detailed analysis of all test conditions was performed by Wang et al (2023b), which is currently under review for publication, and the reader is encouraged to review that publication for additional information once published. Conclusions drawn from their work are included here for context and cited when referenced.

4.9.1 Baseline – No Load Mitigation

To understand the effects of the various load mitigation strategies tests, first results with fixed TMDs and the baseline RO controller are presented. Results for the DLC 1.2 case are shown in Figure 4.22 for wave only, wind only, and wind + wave environments. As shown in Figure 4.22a, the platform pitch response was largest for the wind+wave case and dominated by low frequency wind forcing, represented by the similar response below 0.012 Hz between the wind only and wind+wave cases, and a significant contribution around the platform pitch natural frequency. The tower base bending moment is shown in Figure 4.22b, and the dominant response was in the wave energy region. As discussed earlier, while 3P excitation is expected for a 3-bladed turbine there was additional response due to the interaction of the rotor blades with the wind slipstream.

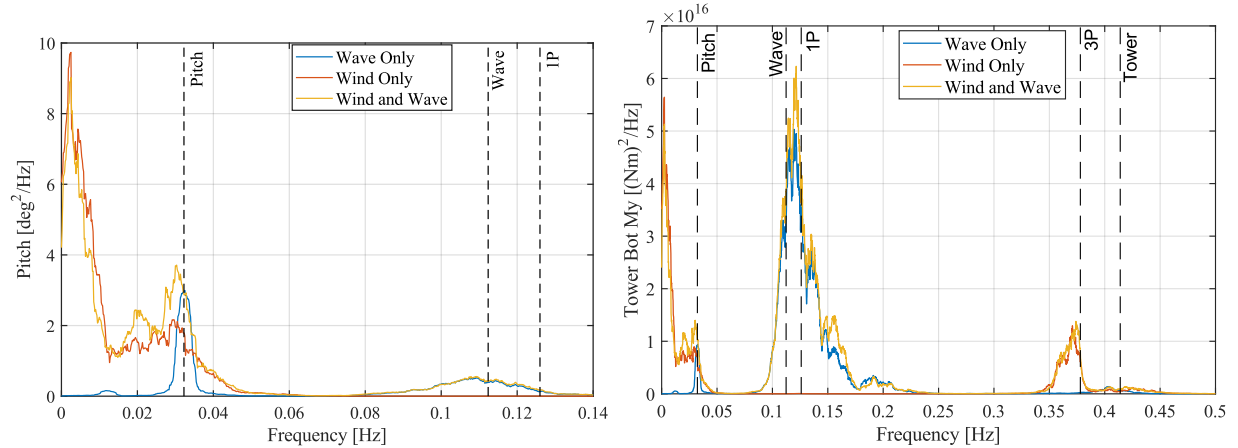


Figure 4.22: PSD results for fixed TMD and baseline RO turbine control (left) Pitch motion and (right) Tower base bending moment

When considering the larger sea state of DLC 1.6, the wave forcing becomes more significant relative to the wind components. Comparing the wave only, wind only, and wind+wave results in Figure 4.28a, the platform pitch response at the wave forcing frequency is comparable to the response around the pitch natural frequency. There is also an apparent shift in platform pitch natural frequency when the wind is

present. This is due to the effect of the operational turbine and implications on system performance are discussed further in Section 5.3.3. Additionally, the 3P forcing is much more pronounced for the DLC 1.6 case. In this environment, the wind speed is faster, but the rotor thrust is lower due to the blade pitch feathering. These two factors would lead to stronger interaction with the top of the slipstream boundary as the mean pitch offset of the system reduces from over 8 deg for DLC 1.2 to approximately 5 deg for DLC 1.6 (Wang et al., 2023b).

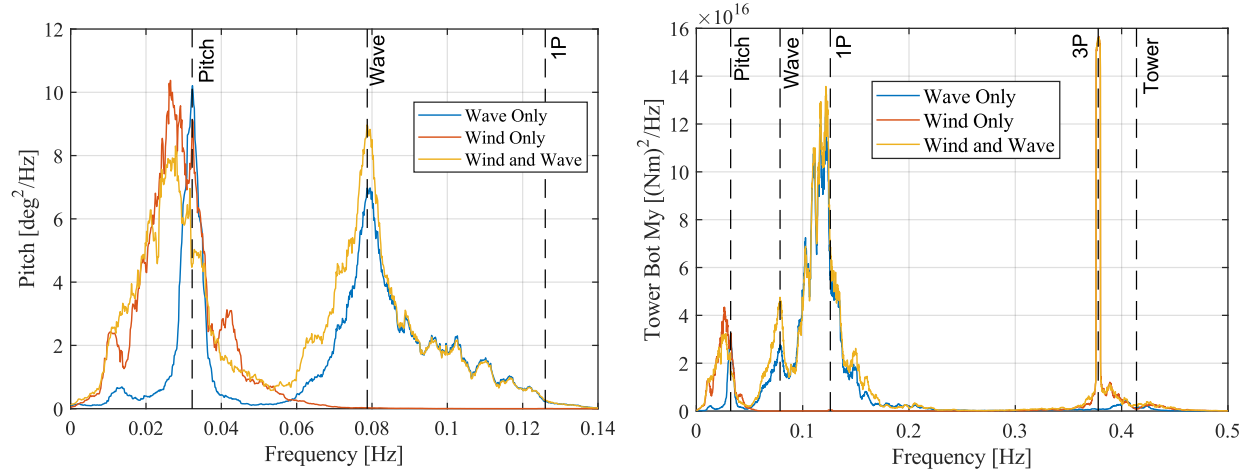


Figure 4.23: PSD results for Fixed TMD and baseline RO turbine control, (left) Pitch motion and (right) Tower base bending moment

4.9.2 Wave Only - Effect of TMDs

The effects of the TMDs in wave only tests are presented next. Both the Pitch and Tower TMD settings in wave only conditions from the severe sea state of DLC 1.6 are considered. Considering the pitch response shown on the left of Figure 4.24, the effect of the Pitch TMD shows reduction in response at the platform pitch resonant frequency while increased motion in the wave energy region. The effect on the tower base moment, shown in the right of Figure 4.24, is that the Pitch TMD shifts the tower resonant mode to a higher frequency due to modifying the boundary condition at the base of the cantilever tower.

The Tower TMD had little effect on the pitch motion of the system, having a similar response to the Fixed TMD over all frequencies. However, there was significant attenuation of the tower base bending moment at the resonant frequency. These effects were quantified in the work of Wang et al. (2023b) through integrating the PSD between frequency bounds corresponding to regions of interest. This calculation showed a 29% reduction in pitch response at the resonant mode for the Pitch TMD and an increase in the wave frequency region of 11%. It also reduced the tower base bending moment by 30% at the pitch resonant mode while the Tower TMD reduced the tower base bending response near the tower frequency by 26%.

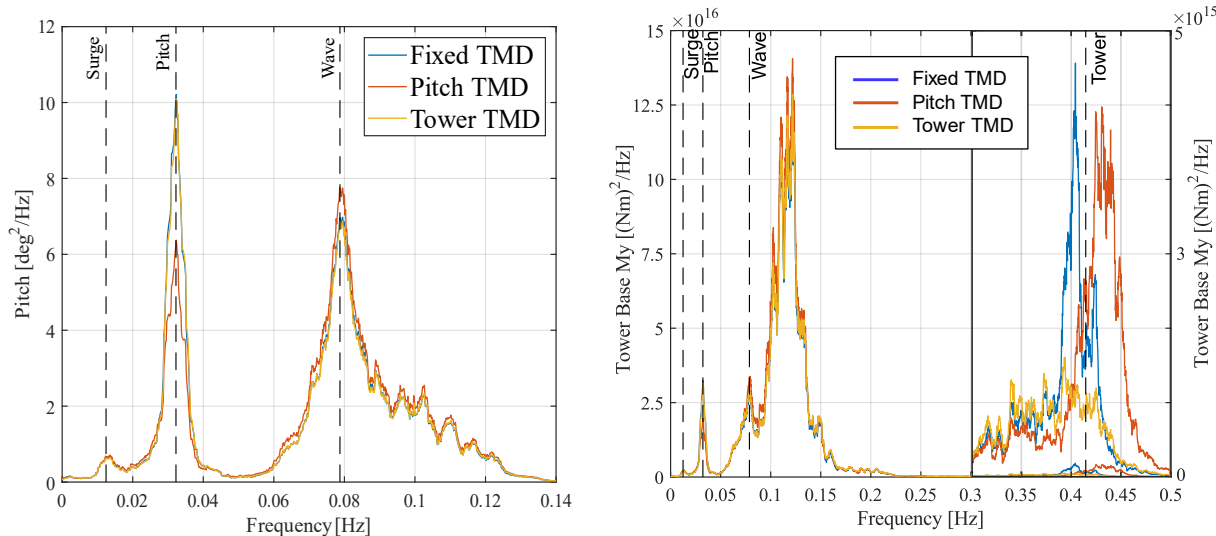


Figure 4.24: PSD results for Fixed, Pitch, and Tower TMD settings, (left) Pitch motion and (right) Tower base bending moment

4.9.3 Wind Only

The aerodynamic performance of the wind turbine in fixed-bottom conditions with no waves was studied in Campaign 1 (Mendoza et al., 2022) and the remainder of these results are adapted from Fowler et al. (2023a). In Campaign 4, the turbine was mounted to the floating platform and the system was subject to

wind-only excitation. Results for the above-rated wind case are shown in Figure 4.25 and Table 4.21. In above-rated conditions, the rotor torque set point was the rated torque value of 1.87E+07 Nm, and ROSCO used collective blade pitch control to regulate rotor speed to the rated rotor speed of 0.126 Hz. Results show that the rotor torque and speed were well regulated, with a coefficient of variation of 3.0% and 1.6%, respectively. Blade pitch actuation corresponded to the energy in the wind energy frequencies and had a COV of 1.7%. Note that rotor thrust, rotor speed, and rotor torque results here have been low-pass-filtered at 0.25 Hz using a third-order Butterworth filter to remove a 3P (0.38 Hz) excitation effect due to boundary effects of the wind field impacting the tip of each blade.

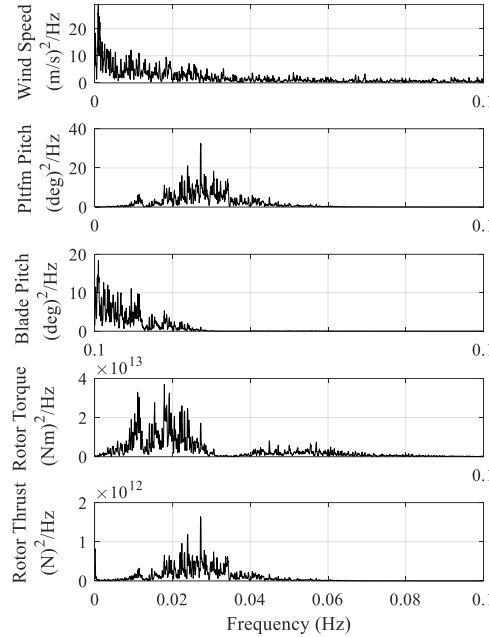


Figure 4.25: Wind Only - Platform and turbine responses

Table 4.21: Measured values - Wind only

Channel	Unit	Mean	Range	COV
Platform Pitch	[deg]	5.2	2.7	8.2%
Blade Pitch	[deg]	17.1	2.1	1.7%
Rotor Torque	[N-m]	1.87E+07	4.28E+06	3.0%
Rotor Speed	[Hz]	0.126	0.016	1.6%
Rotor Thrust	[N]	1.07E+06	6.79E+05	9.2%

4.9.4 Wind/Wave – DLC 1.6

The next cases considered are an irregular sea state with the same above-rated wind condition. The wind/wave case was run five times with the baseline RO controller to establish repeatability of the test setup, wind/wave environments, and controller response. Statistics for the repeat RO cases were taken as the average of statistics computed from each individual run.

Under RO control, the blade pitch response was predominantly in the wind turbulence frequency range, and the rotor speed and rotor torque were well regulated with a COV of 1.9% and 3.8%, respectively. These results were similar to the wind-only case, indicating that the baseline controller was relatively insensitive to platform motion due to hydrodynamic forcing. With the floating feedback enabled, as shown in Figure 4.26, there was an increase in blade pitch actuation in the lower frequencies near the platform pitch natural frequency and extending into the wave energy region, starting to trail off after the wave peak frequency of 0.079 Hz. The range increased by 24.8%, and comparing integrals of the PSD from 0 to 0.2 Hz, indicates that there was 23% more energy when the FL controller was active.

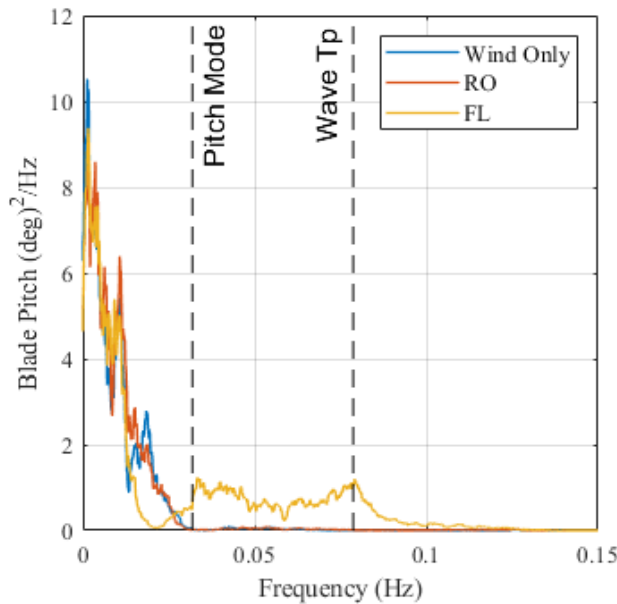


Figure 4.26: Blade pitch response with Floating Feedback control

For the wind-only and RO cases, the platform pitch motion around the natural frequency was similar, indicating that the interaction of the wind and baseline RO controller excited the resonant platform pitch behavior in the absence of waves. When the floating feedback was enabled, the platform pitch response showed a significant decrease around the system pitch frequency and increased motion at frequencies between 0.03 Hz and 0.08 Hz relative to the RO controller. The increased motion was due to the ROSCO controller with the FL loop not having any information regarding the wave frequency and elevation, so it was unable to attenuate response at the wave frequency. The Bode plot of the filter shown in Figure 4.12 demonstrates that the filter magnitude at the platform pitch period was 0.6 and decreased to 0.2 at the wave peak period while the phase decreased from -85 deg at the platform pitch frequency to -130 deg by 0.079 Hz. This shows that while the magnitude of the feedback signal was being more strongly attenuated as the frequency increased, the phase was also becoming less effective for platform pitch control.

Additionally, as shown in Figure 4.26, there was considerable platform pitch motion between 0.05 and 0.08 Hz, which corresponded to relatively strong feedback signals being considered by ROSCO. The tuning of the high- and low-pass filters affected how ROSCO behaved and future work could consider additional tuning of this filter to identify optimal settings. For the settings considered in FOCAL, comparing integrals of the power-spectral density of platform pitch show that the energy present from 0 to 0.05 Hz was 33% lower with the FL controller than the RO baseline, and was 8% lower when considering all frequencies.

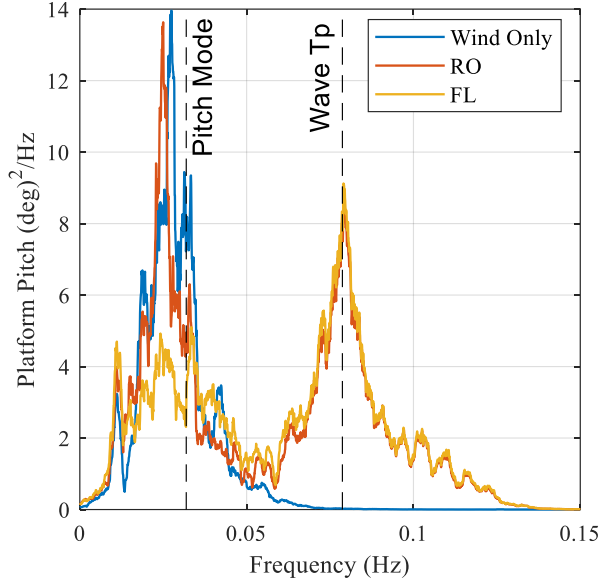


Figure 4.27: Platform pitch response with Floating Feedback control

A comparison of statistics for key metrics is shown in Table 4.22.

Table 4.22: Comparison of statistics for key metrics

Channel	Wind Only			RO Controller			FL Controller			RO vs FL - % Diff		
	Avg	Rng	SD	Avg	Rng	SD	Avg	Rng	SD	Avg	Rng	SD
Surge [m]	8.7	5.1	0.74	9.6	12.0	1.61	9.9	12.2	1.59	2.7	1.2	-1.7
Pitch [deg]	5.2	2.7	0.42	5.2	4.6	0.59	5.2	4.1	0.57	0.6	-11.3	-3.9
Bld Pitch [deg]	17.1	2.1	0.30	17.1	2.0	0.31	17.0	2.5	0.36	-0.4	24.8	13.7
Rotor Speed [Hz]	0.126	0.016	0.002	0.126	0.016	0.002	0.126	0.016	0.002	0.0	-7.2	1.3
Rotor Tq [MN-m]	18.7	4.3	0.57	18.7	4.5	0.63	18.7	5.1	0.65	0.0	13.3	2.9
Thrust [MN]	1.07	0.68	0.10	1.16	1.87	0.25	1.15	1.95	0.26	-1.6	4.1	1.0
TowerBot My [MN-m]	371.7	286.4	41.3	374.1	490.3	70.5	375.8	481.4	68.3	0.5	-1.8	-3.1

Considering the tower base pitch moment, the wind-only and baseline RO controller showed similar results below 0.05 Hz, corresponding to the platform natural pitch period as shown in Figure 4.28. When the FL controller was used, there was a significant reduction in tower base pitch moment around the platform pitch period of 0.0319 Hz while the higher frequency response in the wave energy region and

above were the same. Comparing integrals of the power-spectral density of tower base pitch moment shows that the energy present from 0 to 0.05 Hz was 40% lower with the FL controller than the RO baseline and was 7% lower when considering all frequencies.

Statistics for each of the five runs of the baseline controller were computed and then averaged for comparison with other runs. It is notable that the range of the blade pitch and rotor torque increased by 24.8% and 13.3%, respectively, when the FL controller was used, corresponding to the increased blade pitch action. This increased blade pitch actuation resulted in a reduction in range of platform pitch by 11.3% and tower base pitch moment by 1.8%.

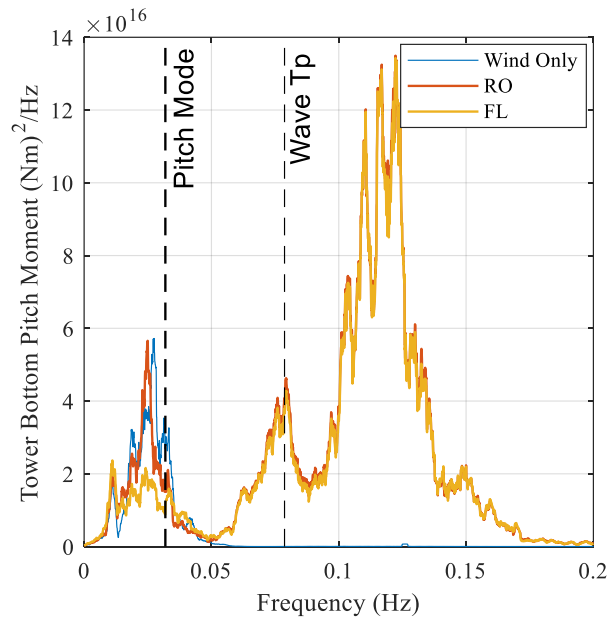


Figure 4.28: Tower base pitch bending moment response with Floating Feedback control

4.9.5 Combined Effect of ROSCO and TMDs

The effects of TMDs as well as system performance near rated were thoroughly explored by Wang et al. (2023b) as part of the FOCAL project, but are not published at the time of this writing. Summarized

results from their work are that the Peak Shaving routine was effective in reducing the platform pitch response in the low frequency range corresponding to the wind turbulence regime, with a 50% reduction in the PSD integral metric. Considering the TMD effects, the Pitch TMD increased the response near the pitch resonant mode. This was possibly because the platform pitch period shifted away from the tuned TMD frequency and TMDs tend to amplify responses near their tuned frequency (Randall, 1981). The Pitch TMD was synergistic with the Floating Feedback FL controller, showing a 42% reduction in the pitch PSD where the FL controller showed a reduction of 29% with the Fixed TMDs.

4.10 Conclusions

Results from 1:70-scale model wind/wave testing for the IEA Wind 15 MW RWT on a VolturnUS-S inspired semi-submersible floating platform are presented. The ROSCO controller was implemented on a real-time data acquisition and control system. Results from above-rated conditions are presented, showing the influence of the baseline blade pitch controller as well as a platform pitch floating feedback control loop, which demonstrated in the experiment a reduction in overall platform pitch motion and tower base bending loads, particularly near the platform pitch natural period.

The baseline ROSCO controller demonstrated the ability to regulate rotor torque and rotor speed in above-rated conditions through collective blade pitch actuation. The blade pitch response was primarily in the wind-energy frequency range, showing that the controller was responding to the turbulent changes of the wind field. It was observed that platform pitch motion was excited similarly in both wind-only and wind/wave environments with the baseline RO controller.

When the floating feedback control loop was enabled, the blade pitch controller took into account the platform pitch rotational motion, and the blade pitch command showed significant activity around the platform pitch natural frequency as well as in the lower frequencies of the wave energy region. As there was significant platform pitch motion in these regions, this was consistent with the filtering of the platform

pitch motion feedback signal, which passed through motion at the system pitch natural frequency and began to attenuate the response at frequencies in the lower wave energy region. This blade pitch actuation resulted in a significant reduction in platform pitch motion around the platform pitch natural frequency as well as reductions in tower base bending moment and rotor thrust. While there was a moderate increase in platform pitch motion at the lower frequencies of the wave energy region, the system responses were largely unaffected in the wave energy region and the FL controller showed an overall reduction in platform pitch motion and tower bottom pitch moment.

Tests with the peak shaving control enabled showed a reduction in platform pitch motion and tower base bending moments at the low frequency ranges associated with wind turbulence. It was observed that the relatively low wind turbulence level relative to the wave environment limited the overall impact.

Regarding the effects of the TMDs, Wang et al. (2023b) analyzed the effect of the TMDs and ROSCO in DLC 1.2 operational conditions with near-rated wind and DLC 1.6 with above-rated wind and a severe sea state. Conclusions from their published paper are summarized here and the reader is encouraged to consult the publication for detailed results. Overall, the TMDs were effective at attenuating motion and loads at their tuned frequencies. In wave only environments, the Pitch TMD reduced the platform pitch motion and tower base bending loads near the platform pitch resonant frequency while slightly amplifying at other frequencies. When tested in conjunction with ROSCO, the Pitch TMD tended to amplify motion since the platform pitch frequency was lowered due to the operating turbine. This tuning sensitivity to target frequencies provides motivation to consider active tuning adjustments for offshore designs. When floating feedback was enabled, the Pitch TMD was synergistic with ROSCO and helped reduce platform pitch motion and loads. Overall, the Tower TMD reduced tower base loads at the tower resonant frequency with minimal effect at other frequencies.

Chapter 5

CAMPAIGN 4 OPENFAST SIMULATIONS

The content of this chapter is from my journal paper (Fowler et al., 2023b) and has been slightly edited for readability.

This paper considers the performance of the floating wind turbine system and presents a comparison of my OpenFAST simulation results against experimental data for above-rated conditions, including the effects of the floating feedback control loop in ROSCO. FAST, and subsequently OpenFAST, has a long history of open-source development and has been validated with numerous experimental campaigns (e.g. Robertson et al., 2014; Robertson et al., 2017; Wendt, Robertson, and Jonkman, 2019). With the recent development of structural control elements to represent the tuned-mass damper elements, as well as ROSCO, OpenFAST was used extensively in the FOCAL program to design the scale rotor, implement and tune ROSCO, and conduct model validation efforts of aerodynamic performance from Campaign 1, hydrodynamic performance from Campaigns 2 and 3, and the fully floating model from Campaign 4. This paper is organized with the OpenFAST methodology and experimental setup in Section 5.1. Section 5.2 presents results from the simulation and comparisons with the experiment. Significant findings are discussed in Section 5.3, and conclusions are presented in Section 5.4.

5.1 Materials and Methods

The goal of the FOCAL project was to generate validation data for analysis codes; the project team has iteratively developed an OpenFAST model over the course of the FOCAL project. This model is included in the dataset and shared with the research community as a starting point for representing the FOCAL system. Data from Campaign 1 defined the aerodynamic characteristics of the as-built rotor, as discussed in (Mendoza et al., 2022) and Chapter 2. Results from Campaign 2/3 were used to define the hull mode

and tuned-mass damper representation, as described in (Wang et al., 2023) and Chapter 3. The subject of this paper is the Campaign 4 model I developed, described in Chapter 4, which combines the turbine topside and the floating platform into a fully coupled model. It was created by combining the Campaign 1 and Campaign 2/3 OpenFAST models, with modifications to represent as-built component mass/inertia values and configuration changes, such as adjusting tower flexibility and replacing the dummy mass with an operational turbine. The turbine model was also updated to include the additional airfoil tunings performed based on the above-rated performance data.

5.1.1 Model Description

Control of the turbine in both the experiment and the OpenFAST model was achieved through ROSCO. As explained in (Wang et al., 2023), ROSCO was implemented in real time for the experiment where data from the laboratory were scaled from model scale to full scale and passed to the full-scale ROSCO using the appropriately scaled time step. This means that, effectively, the same ROSCO control algorithm was used for both the experiment and the full-scale simulation, with the exception of the time step. The basin loop time was effectively 0.001 s model scale, which corresponded to 0.008 s full scale, while the integration time step for the OpenFAST analysis was 0.025 s.

Section on airfoil tuning removed, see Sections 2.2.5 and 4.2.

The main parameters of the model are published with the data set and summarized in Table 5.1. Note that all data are presented at full scale, following Froude-scaling relationships.

Table 5.1: Floating turbine system properties for OpenFAST model

Property	Unit	Value
Total System Properties (XYZ₁ Coordinate System *)		
Mass	kg	2.073×10^7
Center of gravity (CG)–Height from keel	m	19.1
CG–X offset	m	0.2
CG–Y offset	m	-0.5
I _{xx} (Roll Inertia) about system CG	kg·m ²	4.937×10^{10}
I _{yy} (Pitch Inertia) about system CG	kg·m ²	4.972×10^{10}
Hull Properties (XYZ₂ Coordinate System *)		
Mass	kg	1.866×10^7
CG–Height from Keel	m	6.9
CG–X Offset	m	0.1
CG–Y Offset	m	-0.6
I _{xx} (Roll Inertia) about hull CG	kg·m ²	1.353×10^{10}
I _{yy} (Pitch Inertia) about hull CG	kg·m ²	1.402×10^{10}
I _{zz} (Yaw Inertia) about hull CG	kg·m ²	1.52×10^{10}
Rotor Nacelle Assembly Properties (XYZ₃ Coordinate System *)		
Mass	kg	1.197×10^6
CG–Height from keel	m	168.7
CG–X Offset	m	-4.4
I _{xx} (Roll Inertia) about RNA CG	kg·m ²	6.751×10^8
I _{yy} (Pitch Inertia) about RNA CG	kg·m ²	3.723×10^8

* Coordinate systems are defined in Figure 5.1.

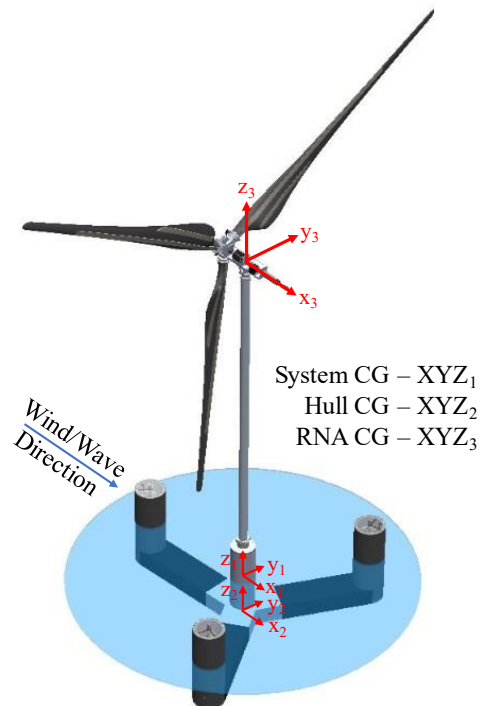


Figure 5.1: Coordinate system for system properties

The tuned-mass damper elements are represented in the OpenFAST model but are not considered in this comparison. They are modeled with stiff springs in the OpenFAST model, and comparisons are made to experiment conditions where the TMDs were similarly fixed in place.

5.1.2 Wind Environment

This study considers one of the three wind environments that were run in the experimental campaign: a turbulent wind environment (designated W03) at an above-rated mean wind speed of 24.05 m/s. Wind calibration dwell measurements of this environment were taken without the model in the basin and using one anemometer that was located at the hub center, one placed at hub height but offset laterally by 70 m, which is roughly 60% of the rotor radius, and one that was offset laterally and downwind. Additionally, a survey of the rotor plane was carried out and used to determine the averaged mean wind speed and uniformity of the rotor. To represent both the correct wind turbulence and rotor averaged mean velocity, the wind time history for the OpenFAST model is created by scaling the dwell time history to match the mean of the rotor averaged survey by multiplying the time series by the appropriate factor. This time history is then implemented as a spatially uniform unsteady wind in the OpenFAST model. Wind calibration time series are shown in Figure 5.2, while the power spectral density plot uses data from 2000 to 9500 s for consistency with the analysis in this section.

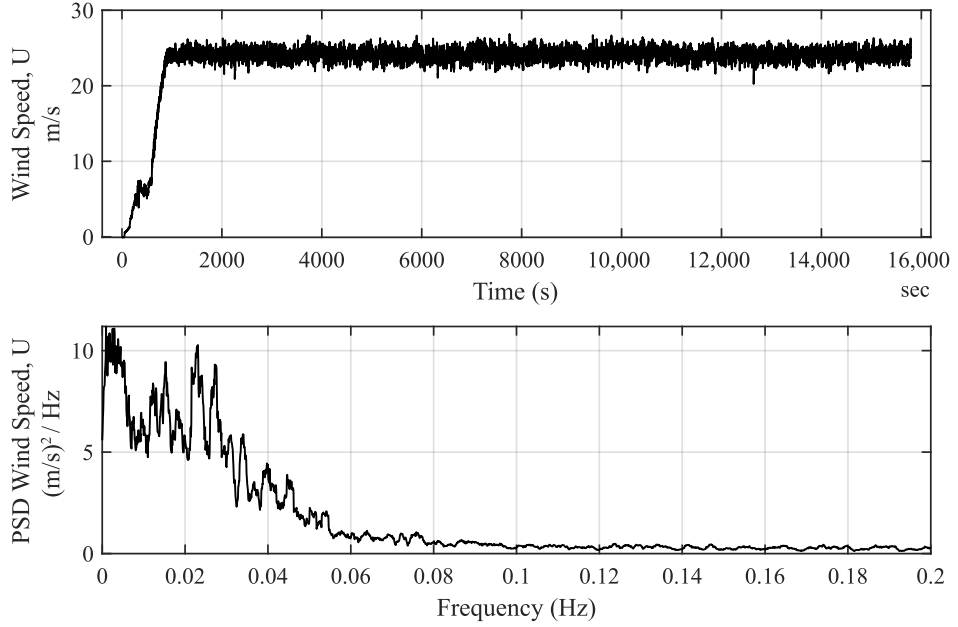


Figure 5.2: Time history and PSD of U component of wind velocity

5.1.3 Wave Environment

In the experiment, a JONSWAP spectrum irregular wave definition was considered for a 1-year extreme sea state corresponding to rated wind conditions. Five realizations of this environment were created that had different time histories but the same statistics, identified as E21–E25. Five repeats of the E21 wave environment were run in the experiment to assess repeatability, and this wave environment is what is considered in the OpenFAST model. Specifications for this environment are given in Table 5.2.

Table 5.2: Wave environment parameters

Wave ID	Significant Wave Height, H_s [m]	Peak Period, T_p [s]	γ [-]
E21–E25	8.1	12.8	2.75

In the experiment, waves were calibrated by running each wave in the wave tank without the model installed. Wave time history data were collected from an array of probes that were located where the model would be installed. Data from these runs were used to create the time history wave environment for

the OpenFAST model. Figure 5.3 shows the wave elevation time series and PSD plot where the PSD is calculated using data from 2000 to 9500 s for consistency.

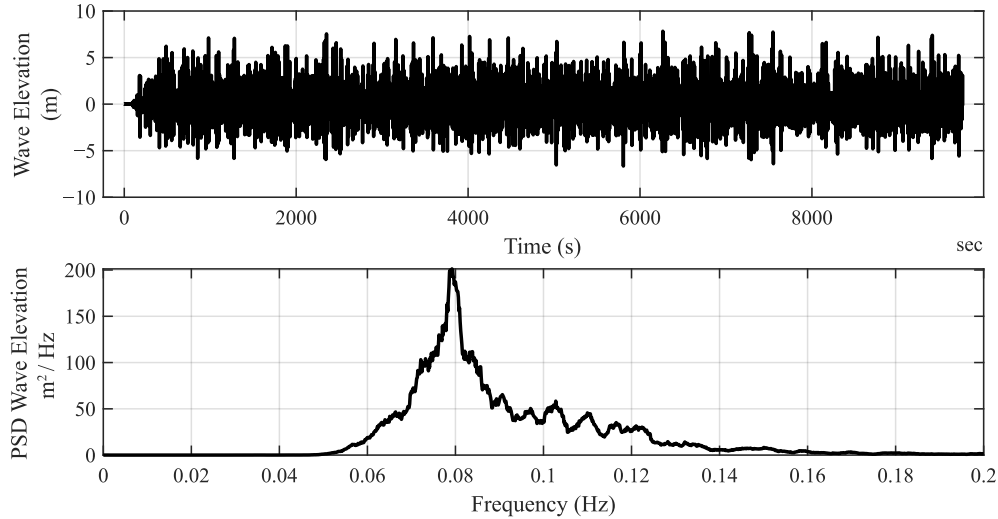


Figure 5.3: Time history and PSD of wave elevation

5.1.4 Mooring

The mooring system for the experiment consisted of three lines, each extending radially from the outer columns and spaced 120° apart. These lines were nominally horizontal and mounted to anchors near the same elevation as the fairlead. Each line was stiff monofilament in line with a linear spring. The stiffness of each line was determined such that the surge restoring force of the mooring system was equivalent to the VolturnUS-S catenary chain mooring system in the mean displaced position due to rated thrust load on the turbine. There was also a restoring effect due to the umbilical cable, which acted as an additional soft mooring line. This effect was quantified by performing offset tests in the surge and sway direction, both with and without the umbilical cable attached, and results with the umbilical cable attached are shown in Table 5.3.

Table 5.3: Linearized mooring stiffnesses

Degree of Freedom	Experiment	OpenFAST
Surge [$\text{N}\cdot\text{m}^{-1}$]	217,863	211,420
Sway [$\text{N}\cdot\text{m}^{-1}$]	224,008	221,232

The mooring system was modeled in OpenFAST using three lines with properties shown in Table 5.4.

Note, Line3 is the lead line while Line 1 and Line 2 are the port and starboard lines, respectively. The three lines had the same nominal stiffness, but the bow line was shorter in the experiment. The umbilical cable's effect is included as additional linear surge and heave stiffness terms.

Table 5.4: Mooring model parameters

Line ID	Line Location	EA [N]	Unstretched Length [m]	Number of Segments [-]
1	Port	33,862,500	268.75	15
2	Starboard	33,816,290	266.27	15
3	Bow (Lead Line)	12,285,240	99.88	15

5.1.5 Instrumentation

The turbine model was instrumented to measure turbine performance, global dynamics, mooring loads, and internal loading, as presented in Section 4.7. Table 5.5 describes the OpenFAST data channels and their corresponding data channels from the experiment. In the experiment and the simulation, ROSCO was run at full scale, and all comparisons are completed using full-scale values (including time).

Table 5.5: Instrumentation and data channel list

Channel	Experiment Source	OpenFAST Channel	Notes
Platform Surge	Qualisys 6DoF Motion	PtfmSurge	Rigid body motion
Platform Pitch	Qualisys 6DoF Motion	PtfmPitch	Rigid body motion
Rotor Torque	Inline Torque Sensor	RotTorq	Low-speed shaft torque
Rotor Speed	Rotor Encoder	RotSpeed	1:1 Gearbox
Blade Pitch	Blade Pitch Encoder	BldPitch1	Collective blade pitch
Tower Base Moment	6DoF Load Cell	TwrBsMyt	Pitch moment
Mooring Fairlead Tension	1DoF Inline Load Cell	FAIRTEN3	Lead line tension

5.2 Results

5.2.1 Free Decay

Free-decay tests of the model were performed in its floating configuration with moorings attached, both with and without the umbilical cable. This was performed to quantify the effect of the umbilical cable on the model. For this comparison, only the cases with the umbilical cable attached are considered. The additional linear stiffness terms are then computed for surge and heave to match the free-decay period and were small compared with the mooring restoring and hydrostatic stiffness terms, respectively. The additional linear and quadratic damping values computed are shown in Table 5.6 and are consistent with the P-Q method outlined in (Wang et al., 2022a).

Table 5.6: Additional linear stiffness, linear damping, and quadratic damping terms

Degree of Freedom		Linear Stiffness	Linear Damping	Quadratic Damping
Surge	[N/m or N/(m/s) or N/(m/s) ²]	6.9×10^3	1.6×10^5	1.0×10^6
Sway	[N/m or N/(m/s) or N/(m/s) ²]	N/A	1.6×10^5	1.0×10^6
Heave	[N/m or N/(m/s) or N/(m/s) ²]	3.2×10^4	0.0	6.6×10^6
Roll	[N·m/rad or N·m/(rad/s) ²]	N/A	2.7×10^8	7.2×10^{10}
Pitch	[N·m/rad or N·m/(rad/s) ²]	N/A	2.7×10^8	7.2×10^{10}
Yaw	[N·m/rad or N·m/(rad/s) ²]	N/A	0.0	7.2×10^{10}

The resulting natural periods are shown in Table 5.7.

Table 5.7: Natural periods for experiment and simulation

Degree of Freedom	Period* [s]	Experiment Frequency [Hz]	OpenFAST Period * [s]	OpenFAST Frequency [Hz]
Surge	80.8	0.0124	79.2	0.0126
Sway	79.6	0.0126	78.1	0.0128
Heave	21.2	0.0473	20.6	0.0486
Roll	31.1	0.0322	30.1	0.0333
Pitch	30.8	0.0325	30.0	0.0333
Yaw	50.94	0.0196	46.05	0.0217

* Periods are from free-decay tests performed in still water with no wind and do not include the aerodynamic effects of an operating turbine in wind.

5.2.2 Above-Rated Conditions

The test environment considered is a turbulent wind at an above-rated wind speed and an irregular sea state, referred to as W03 and E21, respectively. In the experiment, wave condition E21 was performed five times to determine repeatability and estimate measurement uncertainty. This comparison uses average statistics from these five runs to compare with the OpenFAST simulation. In the experiment, the tests performed included wind-only, wave-only, and then combined wind/wave loading. These cases are also simulated in OpenFAST to compare the wind-only, wave-only, and coupled loading in the model. Results are generally compared in context with different frequency regions, namely those dominated by wind turbulence, system resonance responses, and wave energy. These regions are summarized in Table 5.8 and follow those used by Wang et al. (2023). Results from higher frequencies are not shown in spectral plots to focus on where ROSCO is most active but are still considered in calculating statistics. To remove startup transients and compare results, power spectral results and statistics are presented for the time subset of 2000 to 9500 s with the mean value removed. The equilibrium values of the system in still water with no wind applied are also removed prior to computing statistics; therefore, the results can be interpreted as the deviation from the still water equilibrium condition.

Table 5.8: Key frequency ranges for PSD analysis

Frequency Range [Hz]	Dominant Forcing or Response
0.0005–0.0120	Wind Turbulence
0.0120–0.0500	Platform Pitch Response
0.0550–0.2500	Wave Energy

5.2.3 Wave Only

The wave-only condition is simulated using the wave elevation time history data collected from the calibration of the wave environments during the experiment (OpenFAST option WaveMod = 5). The simulation is run for 9754 s and analysis is performed from 2000 to 9500 s to remove startup transients

and provide consistent comparison. During these cases, the turbine is parked with the blade pitch at 0°. Second-order wave kinematics are not computed, but sum- and difference-frequency loading is computed from the second-order WAMIT [33] quadratic transfer functions (0.12s and 0.12d files, respectively). There is no current or inclusion of Morison-type elements, and the additional damping is included through the linear and quadratic damping matrices, as discussed in Section 5.2.1.

Key metrics are considered in the frequency domain, shown as PSD results in Figure 5.4, where “Exp, R#” refers to experimental results from the five repeated runs (R1 to R5), and “OF” refers to OpenFAST results. Statistics are presented in Table 5.9, where results for the experiment are the average of each statistic over all repeated runs, and OpenFAST results are statistics for the single simulation. The wave-only results show that the hydrodynamic forcing on the model is well accounted for. Because the turbine is parked, comparison of turbine operation is not discussed here. Mean, range, and standard deviation (SD) of platform surge and pitch motion, as well as tower base pitch bending moment and lead fairlead tension compare favorably. The experiment exhibits more surge motion at the surge natural frequency of 0.0124 Hz while platform pitch motion is well represented, both in the wave forcing region as well as at the platform pitch natural frequency of 0.0325 Hz. Discussion of this is provided in Section 5.3. Fairlead tension follows the same trend as the surge, with a good match on mean values and larger variation at the surge natural frequency in the experiment.

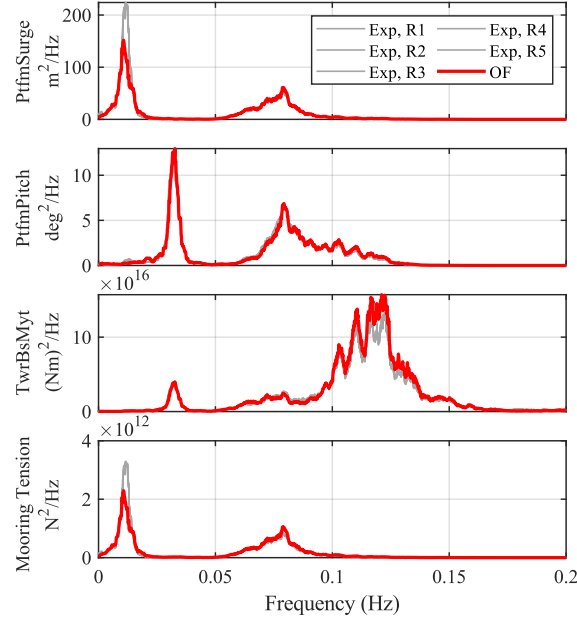


Figure 5.4: Wave-only PSD results

Table 5.9: Wave-only statistics

Channel	Unit	Experiment, Average			OpenFAST		
		Mean	Range	SD	Mean	Range	SD
Pltfm Surge	m	0.6	11.7	1.45	0.6	11.6	1.39
Pltfm Pitch	deg	0.0	3.6	0.46	0.0	3.3	0.46
TowerBsMyt	N·m × 10 ⁸	-0.01	5.46	0.66	-0.01	5.22	0.70
Lead Fairlead	N × 10 ⁶	0.07	1.48	0.18	0.07	1.54	0.18

5.2.4 Wind Only

The wind-only condition is simulated using time history wind data from the calibration of the wind environment for the experiment. The wind is represented as a spatially uniform and unsteady wind field, with uniform directionality and no swirl. The rotor is operational during the wind conditions and under the baseline ROSCO control. The wind speed is slowly ramped up from 0 m/s to the above-rated condition, as shown in Figure 5.5, and ROSCO is utilized to control the rotor torque and blade pitch of the turbine to regulate operation. The simulation is run for 15,794 s and analysis is conducted from 2000 to 9500 s to remove startup transients and provide consistent comparison.

Results from the wind-only condition show good agreement of mean values for key metrics, as shown in Table 5.10. For global motion, there is a larger mean platform surge and pitch in the experiment. Figure 5.5 shows that the dynamic motion near the surge natural frequency is well matched; however, platform pitch response near the platform pitch natural frequency is larger for the OpenFAST model.

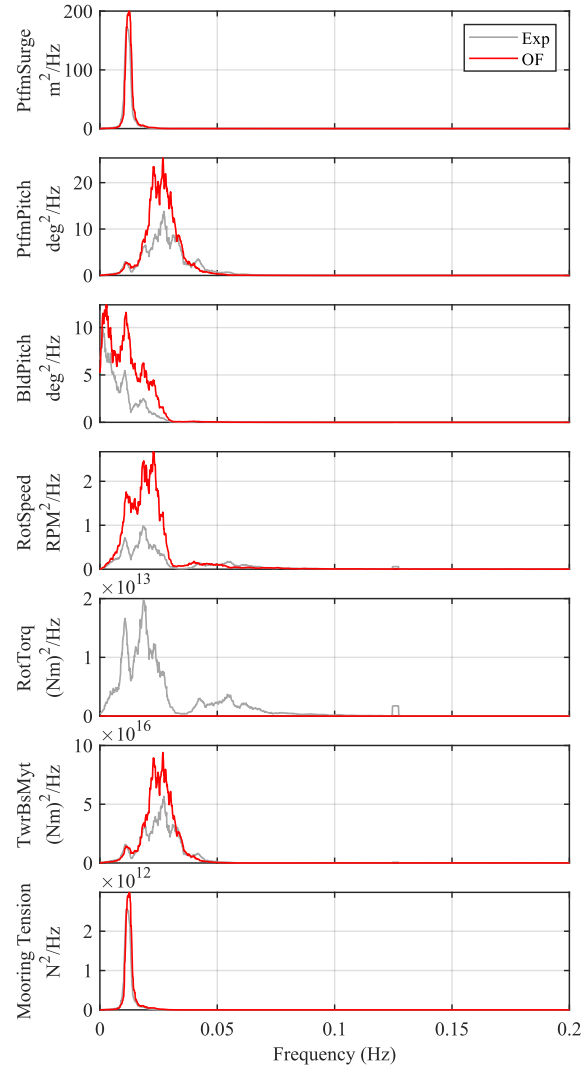


Figure 5.5: Wind-only PSD results

Mean blade pitch is well matched while there is a larger range and standard deviation in the OpenFAST model and more energy in the blade pitch actuation, rotor speed, platform pitch, and tower base bending

moment in the frequency range between 0.0 and 0.05 Hz, corresponding to wind turbulence and platform pitch. While mean rotor torque agrees between the experiment and OpenFAST, there is no rotor torque variation in the OpenFAST simulation, as ROSCO utilizes constant generator torque in the above-rated region. In contrast, the experiment utilized a proportional-integral controller on the scale turbine motor torque to track the constant rotor torque set point from ROSCO. The implications of this are further explored in Section 5.3. Lastly, the mooring response agrees well in both mean value and dynamic response.

Table 5.10: Wind-only statistics

Channel	Unit	Experiment, Average			OpenFAST		
		Mean	Range	SD	Mean	Range	SD
Pltfm Surge	m	8.8	4.9	0.76	7.0	4.9	0.82
Pltfm Pitch	deg	5.2	2.7	0.44	4.3	4.2	0.55
Blade Pitch	deg	17.1	1.9	0.31	17.0	3.2	0.43
Rotor Speed	RPM	7.46	1.1	0.13	7.56	1.5	0.20
Rotor Torque	N·m × 10 ⁶	18.67	5.93	0.68	18.67	0.00	0.00
TowerBsMyt	N·m × 10 ⁸	3.72	2.86	0.42	3.12	2.82	0.37
Lead Fairlead	N × 10 ⁶	0.78	0.61	0.10	0.78	0.61	0.10

5.2.5 Combined Wind and Wave

5.2.5.1 Baseline ROSCO

Combined wind and wave results were simulated for the E21 wave condition with the corresponding W03 wind condition. The simulation was run for 9754 s based on the length of the wave time history. The wind was ramped up from 0 ms⁻¹ with the turbine operational under the baseline ROSCO's control, referred to as "RO." Analysis was performed from 2000 to 9500 s to remove startup transients. Results of the OpenFAST simulation are compared with the average of the five experimental cases that were performed.

Results from the combined cases show similar trends as the wind-only and wave-only cases. With regard to mean values, the experiment exhibits larger platform surge and pitch motion, and OpenFAST continues to underpredict surge motion at the natural frequency, as shown in Table 5.11.

Table 5.11: Wind/wave statistics with baseline ROSCO (RO)

Channel	Unit	Experiment, Average			OpenFAST		
		Mean	Range	SD	Mean	Range	SD
Pltfm Surge	m	9.7	12.0	1.61	7.5	9.2	1.33
Pltfm Pitch	deg	5.2	4.6	0.59	4.3	4.7	0.67
Blade Pitch	deg	17.1	2.0	0.32	17.0	3.1	0.44
Rotor Speed	RPM	7.46	1.3	0.15	7.56	1.7	0.21
Rotor Torque	$N \cdot m \times 10^6$	18.67	6.05	0.72	18.67	0.00	0.00
TowerBsMyt	$N \cdot m \times 10^8$	3.74	6.04	0.79	3.11	5.54	0.74
Lead Fairlead	$N \times 10^6$	1.07	1.51	0.20	0.84	1.24	0.17

Differences in rotor performance exhibit the same trends as in the wind-only case. The mean blade pitch is matched, while the OpenFAST simulation has more blade pitch and rotor speed variation below 0.05 Hz, and more platform pitch motion and tower base bending around the platform pitch frequency, as shown in Figure 5.6. Results in the wave energy range from 0.055 Hz to 0.25 Hz generally agree well, with the experiment showing slightly more platform pitch motion and tower base bending around the wave peak frequency of 0.078 Hz. The double-peaked response in tower base loading for semisubmersibles is well documented (Kimball et al., 2012) and the difference seen here at the wave peak frequency is likely due to the additional pitch motion seen in the experiment at these frequencies. The dominant contributions to the tower base bending moment at the higher frequencies are well represented by both. Mooring tensions follow the trend of surge motion, where the experiment has larger mean value and more energy at the surge resonant frequency.

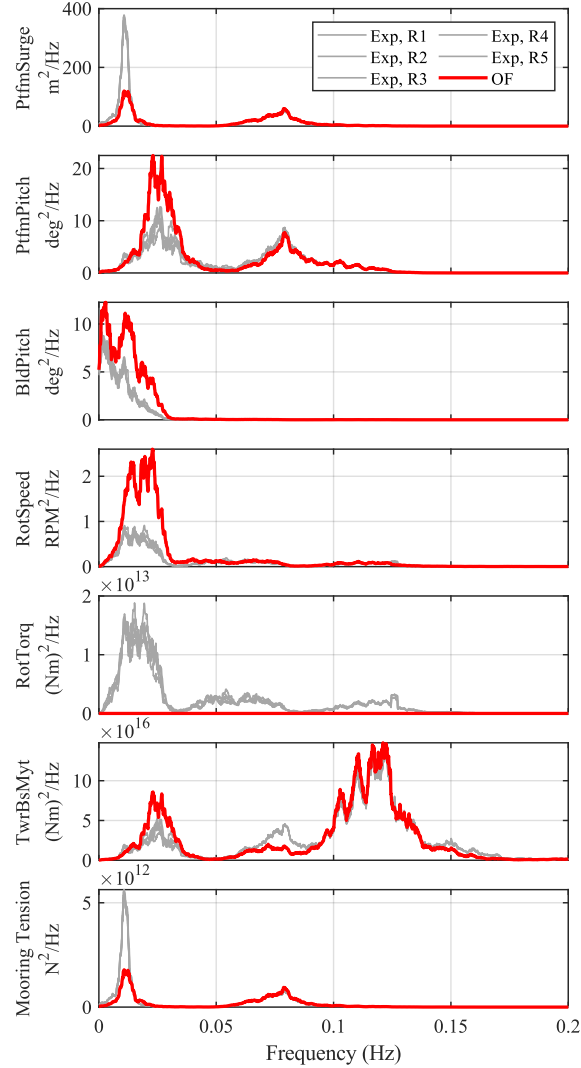


Figure 5.6: Wind/wave with baseline ROSCO (RO) PSD results

5.2.5.2 ROSCO with Floating Feedback

This wind/wave case was also run using the floating feedback control option in ROSCO, designated as “FL” in Figure 5.7. For this case, floating feedback was enabled for platform pitch rotational velocity (OpenFAST DISCON option Fl_Mode = 2). In the experiment, the platform pitch rotational velocity was provided to ROSCO at the Froude-scaled time step of the basin real-time controller, whereas in OpenFAST, it is computed internally. The remaining ROSCO parameters were identical between the

experiment and OpenFAST ROSCO implementation. The simulation was run for 9754 s with analysis performed for 2000 to 9500 s. To quantify the effect of the floating feedback control, results are presented comparing the experimental results with and without feedback as well as comparing OpenFAST with and without feedback.

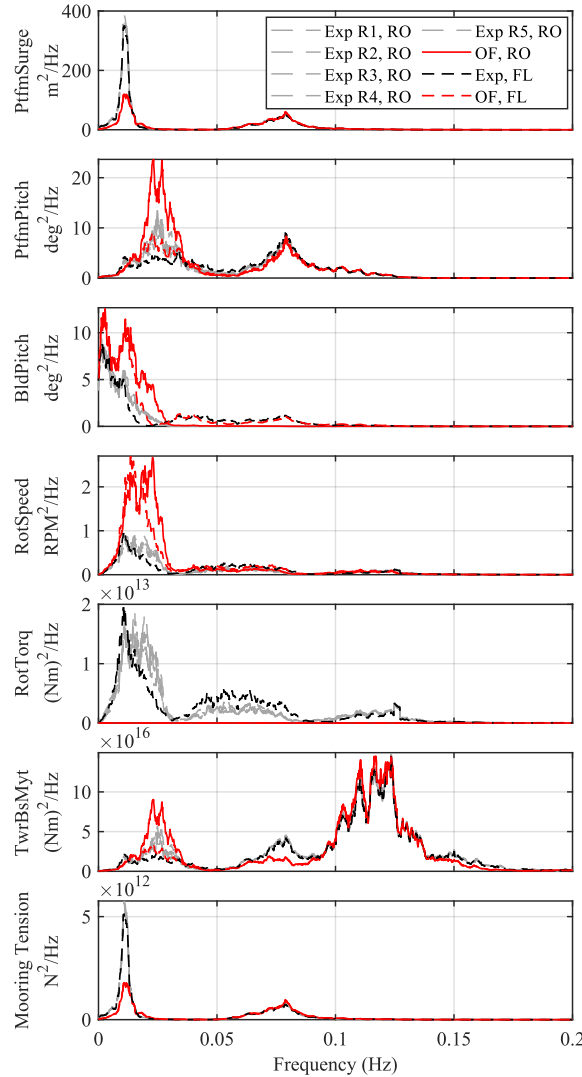


Figure 5.7: Wind/wave with Floating Feedback (FL) PSD results

Table 5.12 shows percent differences calculated such that positive values indicate an increase in the metric for the FL case and negative values are a decrease in the metric. The results show that mean values

for key metrics are largely unaffected by the floating feedback control loop in both the experiment and OpenFAST. Surge and mooring dynamic responses are similarly unaffected; however, noticeable changes in the dynamic performance for other metrics are observed. Platform pitch and tower base moment range and SD decreased in both the experiment and OpenFAST, while overall blade pitch actuation increased. Rotor torque variation also increased for the experiment while OpenFAST maintained a constant rotor torque, as identified in Section 5.2.4.

Table 5.12: Wind/wave statistics comparison, effect of Floating Feedback control

Channel	Experiment, % Difference			OpenFAST, % Difference		
	Mean	Range	SD	Mean	Range	SD
Pltfm Surge	3%	1%	-2%	0%	1%	0%
Pltfm Pitch	0%	-12%	-4%	0%	-13%	-15%
Blade Pitch	0%	22%	13%	0%	6%	0%
Rotor Speed	0%	-1%	2%	0%	-6%	-6%
Rotor Torque	0%	7%	4%	0%	0%	0%
TowerBsMyt	0%	-8%	-2%	0%	-2%	-5%
Lead Fairlead	3%	1%	-2%	0%	-1%	0%

Examining these parameters in the frequency domain, Table 5.13 compares integrals of various metrics over frequency ranges corresponding to wind energy, platform pitch motion, and wave frequency, and values are computed such that positive values indicate an increase in the metric for the floating feedback control. The effect of the floating feedback can be clearly seen in the platform pitch frequency range of 0.012–0.05 Hz, where there is a decrease in platform pitch, rotor speed, and tower base moment, as shown in Table 13 and Figure 10. In this range, there was a 59% reduction in platform pitch energy and a 61% decrease in tower base moment in the OpenFAST model. In the experiment, there were 32% and 38% decreases in pitch motion and tower base bending, respectively. Further investigating the blade pitch response in Figure 5.7, there is a clear reduction in blade pitch actuation between 0.012 and 0.023 Hz for both the experiment and OpenFAST, whereas, above this frequency, there is additional energy that only exists when floating feedback is enabled. The increased blade pitch actuation at these higher frequencies is in the wave energy range and is an undesired effect due to limitation in filtering the floating feedback

signal, as discussed in Section 5.3. This effect is shown in both the experiment as well as the OpenFAST model.

Table 5.13: Wind/wave PSD integral comparison, effect of Floating Feedback control

Channel	Experiment			OpenFAST		
	Wind Freq *	Pitch Freq *	Wave Freq *	Wind Freq *	Pitch Freq *	Wave Freq *
Pltfm Surge	-5%	-1%	-2%	3%	0%	-1%
Pltfm Pitch	20%	-32%	7%	12%	-59%	9%
Blade Pitch	-1%	6%	182%	2%	-35%	183%
Rotor Speed	18%	-26%	26%	16%	-25%	17%
Rotor Torque	28%	-23%	25%	N/A	N/A	N/A
TowerBsMyt	23%	-38%	-3%	14%	-61%	-1%
Lead Fairlead	-6%	-2%	-2%	3%	-1%	0%

* Frequency ranges for PSD integrals shown in Table 8.

5.3 Discussion

5.3.1 Surge Resonant Response

In the wave-only condition, the experiment exhibits more surge motion at the surge natural frequency of 0.0124 Hz. The presented OpenFAST model does not include drag elements and, therefore, does not consider excitation due to viscous effects. This underprediction of surge resonant response is consistent with prior work, including work validating FAST with basin data, (e.g. Robertson et al., 2017 and Coulling et al., 2013). Gueydon et al. (2014) found the effects of second-order difference frequency wave forcing to be significant on the surge resonant response of the OC4 semisubmersible. Subsequent work to capture this response more accurately includes high-fidelity computational fluid dynamics as well as specific improvements to mid-fidelity codes, such as OpenFAST, to better represent the viscous loading on the floating platform. Kvitem et al. (2018) showed that quadratic drag coefficients tuned from free-decay tests underpredicted the surge resonant response, while better agreement was obtained when calibrating drag coefficients from irregular wave test data. Berthelsen et al. (2016) tuned drag coefficients from free-decay tests, and then further tuned the values in the splash zone to better match irregular wave

test data. Pegalajar and Bredmose (2019) presented an operational modal analysis methodology for tuning drag coefficient from irregular sea state test data and observed that the coefficients generally increased with sea state severity. Wang et al. (2022a) discussed tuning drag coefficients from CFD analysis and also demonstrated an improved response in OpenFAST through tuning a depth dependent drag coefficient and implementing vertical wave stretching in (2022b). It is suggested that including viscous drag elements and tuning the drag coefficients, as well as including wave stretching, be carried out to better represent the viscous effects on the floating platform.

Moving to the wind-only condition, the response at resonance agrees well, whereas the mean surge response was larger in the experiment. The turbulent wind environment has energy in the low-frequency range that could directly excite surge resonant motion; therefore, differences in the realized wind time history could affect the response. In the wind/wave condition, the surge resonant response in the experiment was greater than that of the wave-only and wind-only responses. In contrast, in the OpenFAST model, the response in the wind/wave condition exhibits less motion than either the wave-only or wind-only conditions. As Coulling et al. (2013) discuss, the surge resonant response is highly dependent on damping, so it is possible that the low-frequency aerodynamic damping forces are not well matched between the experiment and OpenFAST when the turbine is moving due to the wave environment. Further work to investigate the magnitude and phasing of the aerodynamic loads relative to the viscous loading on the platform is suggested to further explore this phenomenon.

5.3.2 Effect of ROSCO Above-Rated Torque Control

Differences in the blade pitch response can be partially explained by investigating the operation of the ROSCO torque controller in this above-rated wind region. In OpenFAST, the rotor torque was constant at the rated torque value, whereas in the experiment, the turbine motor's proportional-integral control loop attempted to maintain that constant torque set point.

As can be seen in the rotor torque signal in Figure 5.7, the experiment exhibited torque variation in the low-frequency region corresponding to the wind energy range, while OpenFAST maintains a constant torque. As shown in Figure 5.8, the rotor speed and rotor torque were highly correlated when the torque variation was directly in phase with the rotor speed and acted to oppose rotor acceleration, essentially serving as additional rotor speed regulation in the experiment. The larger blade pitch actuation in the OpenFAST model is therefore expected since ROSCO regulates rotor speed in the above-rated region through collective blade pitch, and the additional rotor speed regulation in the experiment was not captured in the OpenFAST model. This larger blade pitch actuation leads to increased platform pitch and tower base bending around the pitch natural frequency and contributes to the discrepancy noted here. Additional factors, such as repeatability in turbulence of the wind around these frequencies and uncertainties in the aerodynamic and hydrodynamic modeling, could also play a role. The additional rotor speed variation in the OpenFAST model is likely due to the inability of ROSCO to perform the same rotor speed regulation as the experiment through blade pitch action alone. It was identified that ROSCO was tuned using a lighter than as-built rotor inertia, so the gains of the blade pitch controller are likely not as aggressive as they could be.

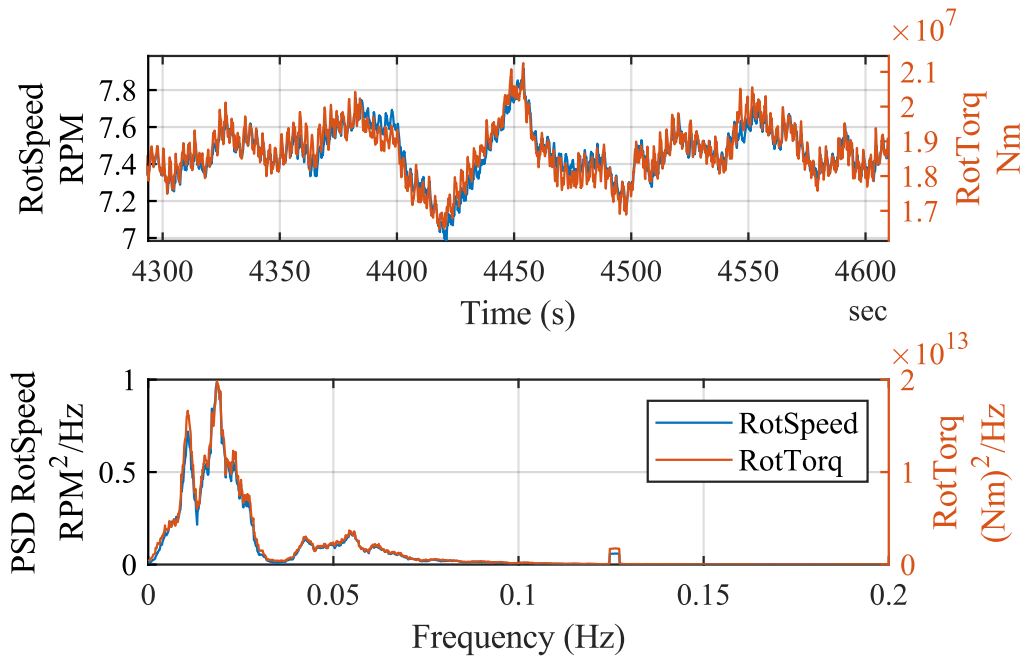


Figure 5.8: Rotor speed and rotor torque time history and PSD from experiment

Further examining the blade pitch difference, we consider the relationship between rotor torque and blade pitch in this operating condition and seek to estimate how much additional blade pitch actuation would be expected in OpenFAST to apply the rotor torque variation from the experiment. The OpenFAST model shows an additional 1.3° of pitch actuation range, which can be taken as a rough indication of the additional blade pitch actuation required. The experiment showed a rotor torque variation range of $5.9 \times 10^6 \text{ N}\cdot\text{m}$, which represents the rotor torque variation that does not exist in OpenFAST. The estimated gradient of the C_p surface at this operating condition with respect to blade pitch ($\partial C_p / \partial \theta$) is -0.013, which means that effecting $5.9 \times 10^6 \text{ N}\cdot\text{m}$ would require a change in blade pitch of 0.9° . Therefore, a significant amount of the additional blade pitch actuation in the OpenFAST model may be due to not representing the generator torque variation, and a more representative rotor torque model in ROSCO could better match the experimental results.

The additional blade pitch actuation in the OpenFAST model also has an effect on the platform dynamics, especially in platform pitch, as blade pitch variation will impart thrust force variation at the nacelle.

Assuming the 0.9° blade pitch variation identified previously, using the gradient of the C_t surface with respect to blade pitch yields a variation in thrust force of 46% of the standard deviation of rotor thrust for this condition. Since this forcing is near the platform pitch resonant frequency, the effect on platform pitch is amplified. Therefore, it is not surprising that the OpenFAST model exhibits additional platform pitch motion, as well as tower base bending motion, around the platform pitch resonant frequency. While not further quantified here, future work on the FOCAL project is considering including rotor generator models in ROSCO that can represent the as-built motor behavior and invite further investigation.

5.3.3 Performance of Floating Feedback Control Loop

The effect of the floating feedback controller was demonstrated in both the experiment and the OpenFAST model. Significant reductions in platform pitch motion and tower base bending loads were obtained around the platform pitch natural frequency, with more reduction seen in the OpenFAST model. This is partly due to the difference in blade pitch actuation caused by the constant generator torque, as described earlier, where adjustments to the blade pitch control would intuitively have a larger effect in OpenFAST, where the blade pitch controller is the only active control parameter in the above-rated region. In the experiment, the rotor speed stabilization effect due to the torque variation was still present during the floating feedback test and was similarly unaccounted for in OpenFAST. Additionally, the reduced blade pitch actuation in the experiment resulted in less platform pitch motion, which generated fewer feedback signals for the floating feedback control loop and reduced their effect.

It was also identified that retuning the filter settings to account for the shift in platform pitch angle due to the effects of the operating turbine may improve the response by more successfully filtering out the unwanted responses in higher frequency ranges. The platform pitch frequency can shift 10–15% lower

due to the effects of wind (Goupee, Kimball, & Dagher, 2017 and Souza & Bachynski, 2019), which would affect the low-pass portion of the filter. In ROSCO, the combination of a first-order high-pass and a second-order low-pass filter is designed to isolate the response around the platform pitch natural frequency. The resulting filter is a compromise between removing unwanted feedback signals from the higher wave energy range while minimizing phase lag. Figure 4.12 shows the magnitude and phase of the combined filter. As shown, around the platform pitch natural frequency, the phase shift is -60 to -80 deg. As the frequency increases, the phase shift becomes more significant, causing the feedback loop to start increasing platform pitch motion at higher frequencies. The floating feedback loop is most effective around the platform pitch natural frequency, where the blade pitch correction is properly phased with the relative velocity change due to the platform pitch motion. As such, further analysis of the sensitivity of filter settings to performance of the floating feedback work is being considered.

5.4 Conclusions

The FOCAL Campaign 4 floating wind turbine experiment was simulated in OpenFAST, and results from the above-rated wind condition with the TMDs locked out were considered. Wind-only, wave-only, and combined wind/wave cases were simulated, and the effects of the ROSCO controller with and without floating feedback were investigated. Comparison of key performance metrics from the wave-only condition showed good agreement in mean values for platform surge and pitch as well as tower base bending moment and mooring tension. The OpenFAST model underpredicted the resonant surge response at the surge natural frequency due to lack of viscous excitation. Results from the wind-only case showed good agreement in platform surge and mooring tension, while the OpenFAST model predicted more blade pitch actuation than the experiment. This was partially attributed to the additional rotor speed attenuation in the experiment due to generator torque variation. ROSCO utilized a constant torque set point in the above-rated condition, which provided the torque set point for the scale model turbine. It was suggested that the rotor torque variation in the experiment, which was due to drivetrain dynamics, contributed to

rotor speed regulation that was not represented in OpenFAST, resulting in larger blade pitch dynamics, rotor speed variation, and additional platform pitch and tower base moment in the simulation. In the wind/wave case, OpenFAST further underpredicted the surge resonant response, likely due to differences in aerodynamic damping and viscous effects. The constant generator torque effects from the wind-only case also applied to the wind/wave case, and the additional blade pitch dynamics resulted in similar trends, where the OpenFAST model showed larger rotor speed variation, platform pitch motion, and tower base bending moment. The effects of the floating feedback control loop were evident in both the experiment and OpenFAST, where the energy in the platform pitch motion near resonance was reduced by 32%, and the tower base bending moments reduced by 38% in the experiment, and by 59% and 61%, respectively, for OpenFAST. Both the experiment and OpenFAST showed significant reduction in blade pitch activity near the platform resonant frequency while increasing at higher frequencies. This additional blade pitch activity in the wave energy region, in combination with the filter phase lag, started to detrimentally affect the performance of the system, and larger platform pitch motion and tower base bending moments were seen in both the experiment and OpenFAST.

Chapter 6

CONCLUSIONS AND FUTURE WORK

6.1 Summary

This thesis presents my work leading the UMaine efforts on the FOCAL Experimental Program. It included conceptualization and planning of the FOCAL test campaigns, numerical modeling of the rotor and floating turbine system, hardware/instrumentation design, construction of the test articles, programming the controllers, and executing the model testing in the W2 facility. I also oversaw data processing and creation of the datasets to disseminate, report writing, and supported numerical model validation.

In Chapter 2, I present the work I performed designing the scaled wind turbine utilizing an improved performance-matched design methodology. This approach was based on previous work designing and testing Froude-scale model turbines and included improvements related to testing a realistic wind turbine controller in the Froude-scale environment. My design considered the sensitivities of rotor torque to changing blade pitch and rotor thrust to changing wind speed in the scaling process to yield a more representative turbine response for the controller to respond to. This involved numerical simulation work, rotor design optimization, instrumentation integration, and programming of the controller. I supervised efforts of a graduate student, Amber Parker, on the detail design of the turbine hardware and provided design specifications, conceptual guidance, and in many cases assisted in the hands-on design and construction of the unit. I also performed detailed characterization of the facility's wind generation capabilities to inform design of the rotor and test program. Commissioning of the turbine was led by me, with support from Amber and Dr. Spinneken, and demonstrated the ability to run ROSCO in real-time using data from the model turbine. It was shown that the scale rotor was able to produce properly scaled

thrust loads and the measured turbine performance was used to successfully tune the gains in the ROSCO PI blade pitch controller. The tuned controller was successful in regulating rotor speed in rated and above-rated conditions. I then used this controller to carry out the Campaign 1 testing, which included running the facility, operating the turbine, and collecting the data for the wind-only testing. Upon completion, I oversaw data processing to quality check the data, disseminated results and reports to NREL and the sponsor, and supported numerical model validation efforts led by NREL.

In Chapter 3, I discuss my work on designing the floating hull, including instrumentation and the tuned-mass damper system, and performing the wave-only testing in Campaigns 2 and 3. I provided the conceptual design of the tuned-mass damper system and supervised the efforts of Mitchell York, a graduate student, on the preliminary design, sizing, and construction of the assemblies. I then performed the system characterization, with support from Mitchell and Dr. Spinneken, and integrated them into the hull. We identified that the most effective frequencies to target were the platform pitch frequency and the tower's first fore/aft bending frequency to attenuate the responses of platform pitch motion and tower base bending moment respectively. We ran broadband excitation tests and determined the optimal damping settings to employ throughout testing. I oversaw the basin staff in the detailed design and construction of the hull, including interfacing with the tuned-mass dampers and instrumentation system. Once complete, I commissioned the hull and performed testing of the model in the wave-only environments of Campaign 2 and 3. As before, I oversaw data processing and quality control, disseminated results and reports to NREL and the sponsor, and supported numerical model validation efforts.

In Chapter 4, I present the work performed to prepare the turbine and hull models for testing in the combined wind/wave conditions of Campaign 4. I worked with NREL to re-tune ROSCO to account for the as-built performance of the wind turbine as measured in Campaign 1. This involved utilizing the ROSCO Toolbox to tune both a “Rated” and “Above-Rated” set of gains. Additionally, the as-built

properties were used to tune the Floating Feedback controller. I performed modifications to the controller to provide the real-time platform pitch motion data from the model hull to ROSCO and enable the use of the Floating Feedback control loop. I also oversaw efforts to re-tune the OpenFAST aerodynamic models to better model the “Rated” and “Above-Rated” performance of the rotor. I assembled the turbine model with the hull and commissioned the integrated system, including demonstrating that ROSCO could run in real-time along with the TMDs. As before, I performed the wind/wave model testing in the basin, operated the turbine, collected data, and oversaw data processing. I worked with the FOCAL team to evaluate the data and presented conclusions about the effect of the various load mitigation methods employed.

Chapter 5 presents my work simulating the Campaign 4 system in OpenFAST. I built upon the various model validation efforts from the FOCAL team on Campaigns 1-3 and simulated the above-rated wind tests with a focus on the ROSCO control features of Peak Shaving and Floating Feedback. My results indicated that the effects of the ROSCO control features were well represented in the numerical model, including the attenuation of rotor thrust variations corresponding to low frequency wind turbulence with the Peak Shaver and reducing the negative pitch damping due to the operational rotor through Floating Feedback. Some improvements to the model were suggested, including additional tuning of the Floating Feedback filters, adding viscous elements in the hull to represent the viscous excitation and damping effects on the platform, and including a generator torque model in ROSCO to simulate the generator torque variation exhibited by the model-scale turbine.

6.2 Significant Findings

The FOCAL program was successfully completed in December 2022 with the conclusion of the final test campaign. While numerical modeling, data processing, and collaborative research efforts continued, there

were a number of significant contributions that this program and the resulting data have made to the floating offshore wind research community.

- 1) Performance-matched methodology successfully applied to a 15 MW turbine and hull
 - Thrust matching demonstrated at rated operation using modest (~20%) increased wind speed
 - The thrust matching was not as accurate as the wind speed increased in the above-rated region. This effect was at least partly due to Reynolds effects on the rotor and was captured by the OpenFAST model through modified airfoil definitions, allowing for validation work to be pursued using the dataset.
 - Sufficient torque matching to utilize a realistic above-rated turbine controller
 - Sensitivities of thrust and torque to changing blade pitch and wind/rotor speed well scaled, enabling tuning of wind turbine controller
 - Phenomena such as shifting platform pitch period due to aerodynamic effects of the rotor and negative pitch damping due to the turbine controller were exhibited in the experiment
 - OpenFAST model was validated, using as-built model properties and tuned airfoil definitions. Simulations were able to reproduce steady-state behavior near design operating points, dynamic responses to changing wind speeds and blade pitch settings, and aerodynamic sensitivities important for the operation of a realistic wind turbine controller
- 2) ROSCO controller implemented in real-time in a 1:70 Froude-scale basin test
 - Rotor speed was well regulated in above-rated conditions using blade pitch PI control
 - COV of 2% for most wind/wave cases
 - ROSCO toolbox was able to tune the controller using measured as-built rotor aerodynamic performance data

- Floating feedback controller worked well to reduce floater motion near the pitch natural frequency
 - 30% reduction in platform pitch energy around platform pitch frequency
 - Peak Shaving was effective in reducing peak thrust near rated wind speed due to wind turbulence
 - 50% reduced energy in platform pitch response in wind frequency region
 - Real-time turbine control was implemented on industry standard hardware, demonstrating sufficient data sample rates and actuator speed and precision for generator torque and blade pitch control at model scale
- 3) Effective tuned-mass dampers were integrated into the floating hull and simulated at model scale using a linearly-actuated mass system
- Hardware-in-the-loop approach adequately modeled passive TMD behavior
 - Targeting the platform pitch frequency and tower first fore/aft bending frequency were most effective
 - The Pitch TMD was effective in reducing platform pitch motion near resonance by 21-47%, depending on the wave environment, with most reduction seen in the I2-Rated case.
 - Reduction of 47% seen in I2-Rated and 30% for PN1-Pink Noise environments
 - Reduction of 21% was shown in Campaign 2/3 and 29% in Campaign 4 for a similar severe wave environment
 - Pitch TMD slightly increased platform pitch response in the wave energy region
 - The Tower TMD was effective in reducing tower base bending loads near resonance by 60% in all wave conditions.
 - Pitch TMD strategy was synergistic with the Floating Feedback controller

- 42% reduction in platform pitch response when used together as opposed to 29% when used independently
- 4) Publicly available dataset and OpenFAST models
- First publicly available experimental dataset on the IEA Wind 15 MW RWT and VolturnUS-S hull
 - Multiple campaigns were run to provide validation data for the turbine performance on a fixed base in wind-only conditions, the hull in wave-only conditions, and the fully assembled system in combined wind/wave environments.
 - Validated OpenFAST models provided for the as-built turbine and hull
 - TMDs modeled in OpenFAST's newly developed Structural Control module
 - Tuned ROSCO controller and as-built rotor performance data included with dataset

6.3 Challenges

While the test campaign was a success, it highlighted a number of challenges present when scale model testing floating wind turbines, particularly with regards to implementing realistic turbine and platform controls. These were generally well quantified within the experiment and able to inform subsequent numerical modeling efforts. However, they do represent areas where future work could make improvements.

- 1) 1:70-scale limitations for model building, challenging as turbine sizes increase to 15+ MW
- Weight restrictions made blade manufacturing and RNA mass/inertia challenging. The as-built blades were heavier than desired, which was due to reinforcements required to achieve sufficient stiffness. This led to the rotor rotational inertia being too large, and added to the overall overweighting of the rotor and RNA.

- Umbilical effects were significant, especially with actuated TMD system. These were quantified with specific tests, but were non-representative of the full-scale system.
- Control forces were small (<1N and <0.5 Nm), which made tuning the primary control loops challenging and the feedback sensitive to noise and vibration in the system.
- Rotor blade tip interaction with wind stream boundary produced 3P excitation, which was worse under smaller steady-state pitch angles indicating the interaction was with the top of the slipstream.

2) Reynolds effects apparent within range of turbine operating wind speeds

- Blade pitch PI control k_i and k_p gains were wind speed scheduled, but OpenFAST airfoil polars were not
- Required different controller tunings for different wind speeds in above-rated region
- Low wind turbulence relative to large wave environments limited the impact of the ROSCO's Peak Shaving routine. However, large turbulence may have introduced unwanted Reynolds effects if the wind velocity change was significant.

3) As-built performance made tuning controllers and comparing results between campaigns challenging

- The operating wind turbine altered the platform pitch resonant frequency, impacting both the performance of the Pitch TMD and ROSCO's filtering.
- The modifications required on the turbine blades changed the rotor inertia, impacting the ROSCO gain tuning.

4) Drivetrain models in ROSCO were limited

- ROSCO used a constant torque model for the generator torque control in above-rated conditions.
- Observations from the experiment were that the model turbine's drivetrain dynamics, particularly drag due to the gearbox, were sufficiently large that it influenced the rotor acceleration and impacted the blade pitch schedule determined by ROSCO.

6.4 Impact and Future Work

Results from the FOCAL program identify areas where design optimization through controls co-design may prove beneficial. The effects of the wind turbine control through ROSCO and the TMD system were demonstrated acting independently and simultaneously in a variety of wind only, wave only, and wind/wave environments. This provided a rich dataset to understand the impact each control system had on global behavior and identify potential areas where coupled interaction could lead to design improvements.

Test cases using ROSCO exhibited some of the phenomena associated with floating wind turbine controllers, such as changing the platform pitch natural frequency and additional pitch motion due to negative platform pitch damping caused by the blade pitch controller. When considering the additional control strategies in ROSCO, platform pitch motion could be significantly attenuated at the resonant frequency through use of the floating feedback loop. Additionally, platform pitch motion due to wind turbulence was greatly reduced through use of the peak shaving algorithm. Reducing platform pitch motion has a direct effect on system loads, specifically tower base bending moments which have significant contributions from the weight of the RNA when offset due to platform pitch/roll motion. Considering these responses in a CCD process, using ROSCO to attenuate platform pitch resonant motion could reduce design loads, allowing for optimizing the tower and structure. It also allows flexibility when placing the platform pitch frequency in the design space.

The TMD system considered two configurations, one targeting the platform pitch frequency and one targeting the tower's first fore/aft bending frequency. For the Pitch TMD, attenuation of platform pitch motion at the resonant frequency was demonstrated in wave only environments while pitch motion was amplified at other frequencies. However, when the wind turbine was operational under baseline ROSCO control, the Pitch TMD amplified pitch motion. This may be because of the turbine's effect on the platform pitch period, resulting in a sub-optimal TMD tuning. When ROSCO's floating feedback control was enabled, the Pitch TMD had a synergistic effect and the platform pitch response was reduced more than either strategy operating on their own. This demonstrates that these control methodologies can greatly reduce resonant platform pitch motion, providing insight into how to incorporate them into a CCD process. It also suggests that active tuning of a TMD system may be required for optimal designs, allowing for adjustment of target frequencies and damping based on environmental conditions.

Future work relating to the FOCAL program are focused on improving scale model testing capabilities of the W2 facility as well as numerical modeling and validation using the dataset. Improvements in wind generation and characterization of the W2 facility will address the wind jet boundary layer effects present when testing the large rotor, as well as improve characterization of the wind field. My own numerical modeling and validation efforts will continue where Chapter 5 left off, and some possible avenues of investigation are:

- 1) Utilize Reynolds dependent airfoil definitions in OpenFAST
 - Utilizing polars for different airfoil performance based on velocity would enable the Reynolds effect to be captured in a single OpenFAST model.
 - A unified model would also incorporate these effects into the rotor design process, where OpenFAST was used to model the open-loop performance of the rotor during optimization
- 2) Additional tuning of ROSCO's filters and control loops

- ROSCO's Floating Feedback filter could be further refined based on lengthened platform pitch period due to the operating turbine. This may reduce negative damping in the wave energy region by more tightly focusing the feedback signal to ROSCO.
 - Retuning the ROSCO PI gains using the as-built rotor inertia would provide a more responsive controller
 - Adjusting the Pitch TMD target frequency to account for the lengthened platform pitch period may improve performance during turbine operation
- 3) Implement drivetrain models in ROSCO
- Including the standard OpenFAST generator models would help more accurately account for scale model drivetrain dynamics
- 4) Continue to improve OpenFAST hydrodynamic model to better represent “baseline” hull model with fixed TMDs
- Include viscous elements to represent viscous effects on the hull and tune using depth dependent coefficients per each sea state

6.5 Publications

Publications from the FOCAL program that have been published at the time of writing are:

Conference and Journal Papers

Fowler, M. L., Lenfest, E., Viselli, A., Goupee, A. J., Kimball, R. W., Zalkind, D., Wright, A., Bergua, R., Wang, L., & Robertson, A. (2023). *1:70-Scale Model Testing of the Reference OpenSource Controller (ROSCO) on the IEA-Wind 15MW Reference Wind Turbine Including Floating Feedback*. ISOPE-I-23-074.

Fowler, M., Lenfest, E., Viselli, A., Goupee, A., Kimball, R., Bergua, R., Wang, L., Zalkind, D., Wright, A., & Robertson, A. (2023). Wind/Wave Testing of a 1:70-Scale Performance-Matched Model of the IEA Wind 15 MW Reference Wind Turbine with Real-Time ROSCO Control and Floating Feedback. *Machines*, 11(9), Article 9. <https://doi.org/10.3390/machines11090865>

Wang, L., Bergua, R., Robertson, A., Jonkman, J., Ngo, T., Das, T., Sarker, D., Flavia, F., Harries, R., **Fowler, M.**, Lenfest, E., Muro, J. L., Burlion, L., & Bilgen, O. (n.d.). *Experimental Validation of Models of a Hull-Based Tuned Mass Damper System for a Semisubmersible Floating Offshore Wind Turbine Platform*.

Kimball, R., Robertson, A., **Fowler, M.**, Mendoza, N., Wright, A., Goupee, A., Lenfest, E., & Parker, A. (2022). Results from the FOCAL experiment campaign 1: Turbine control co-design. *Journal of Physics: Conference Series*, 2265(2), 022082. <https://doi.org/10.1088/1742-6596/2265/2/022082>

Mendoza, N., Robertson, A., Wright, A., Jonkman, J., Wang, L., Bergua, R., Ngo, T., Das, T., Odeh, M., Mohsin, K., Flavia, F. F., Child, B., Bangga, G., **Fowler, M.**, Goupee, A., Kimball, R., Lenfest, E., & Viselli, A. (2022). Verification and Validation of Model-Scale Turbine Performance and Control Strategies for the IEA Wind 15 MW Reference Wind Turbine. *Energies*, 15(20), 7649. <https://doi.org/10.3390/en15207649>

Parker, A. (2022). *Development and Testing of a 1:70 Scale Model Wind Turbine of the IEA Reference 15 MW Floating Offshore System* [The University of Maine]. <https://digitalcommons.library.umaine.edu/etd/3548>

Datasets

Robertson, A. (2023a). *FOCAL Campaign I: Advanced Wind Turbine Control Strategies* [dataset]. Atmosphere to Electrons (A2e) Data Archive and Portal, Pacific Northwest National Laboratory; PNNL. <https://doi.org/10.21947/1962594>

Robertson, A. (2023b). *FOCAL Campaign II/III: Applying Active Hull Controls Using Tuned-mass Dampers/Hull Flexibility and Internal Loads* [dataset]. Atmosphere to Electrons (A2e) Data Archive and Portal, Pacific Northwest National Laboratory; PNNL. <https://doi.org/10.21947/1968406>

Robertson, A. (2023c). *FOCAL Campaign IV: Integrated System Control: Turbine + Hull* [dataset]. Atmosphere to Electrons (A2e) Data Archive and Portal, Pacific Northwest National Laboratory; PNNL. <https://doi.org/10.21947/1972267>

BIBLIOGRAPHY

- Abbas, N. J., Jasa, J., Zalkind, D. S., Wright, A., & Pao, L. (2024). Control co-design of a floating offshore wind turbine. *Applied Energy*, 353, 122036. <https://doi.org/10.1016/j.apenergy.2023.122036>
- Abbas, N. J., Zalkind, D. S., Pao, L., & Wright, A. (2022). A reference open-source controller for fixed and floating offshore wind turbines. *Wind Energy Science*, 7(1), 53–73. <https://doi.org/10.5194/wes-7-53-2022>
- Abbas, N. J., Zalkind, D., Mudafort, R. M., Hylander, G., Mulders, S., Heffernan, D., & Bortolotti, P. (2023). *NREL/ROSCO: RAAW v1.4* (raaw1.4) [Computer software]. Zenodo. <https://doi.org/10.5281/ZENODO.8335624>
- Abbas, N., Zalkind, D., Pao, L., & Wright, A. (2021). *A Reference Open-Source Controller for Fixed and Floating Offshore Wind Turbines* [Preprint]. Control and system identification. <https://doi.org/10.5194/wes-2021-19>
- Allen, C., Viselli, A., Dagher, H., Goupee, A., Gaertner, E., Abbas, N., Hall, M., & Barter, G. (2020). *Definition of the UMaine VolturnUS-S Reference Platform Developed for the IEA Wind 15-Megawatt Offshore Reference Wind Turbine*. NREL/TP-5000-76773. <https://doi.org/10.2172/1660012>
- American Bureau of Shipping. (2020). *Guide for Building and Classing Floating Offshore Wind Turbines*. https://www.eagle.org/content/dam/eagle/rules-and-guides/current/offshore/195_fowti/fowt-guide-july20.pdf
- ARPA-e. (2019). ATLANTIS. US Department of Energy. <https://arpa-e.energy.gov/technologies/programs/atlantis>.
- Azcona, J.; Lemmer, F.; Matha, D.; Amann, F.; Bottasso, C.; Montinari, P.; Chassapoyannis, P.; Diakakis, K.; Voutsinas, S.; Pereira, R; et al. (2016). D4.24—Results of Wave Tank Tests; Technical Report D4.2.4; http://www.innwind.eu/-/media/sites/innwind/publications/deliverables/230117/d4-24_final_v2.pdf
- Bacelli, G., Coe, R., Patterson, D., & Wilson, D. (2017). System Identification of a Heaving Point Absorber: Design of Experiment and Device Modeling. *Energies*, 10(4), 472. <https://doi.org/10.3390/en10040472>
- Bachynski, E. E., Thys, M., Sauder, T., Chabaud, V., & Sæther, L. O. (2016, October 18). *Real-Time Hybrid Model Testing of a Braceless Semi-Submersible Wind Turbine: Part II — Experimental Results*. ASME 2016 35th International Conference on Ocean, Offshore and Arctic Engineering. <https://doi.org/10.1115/OMAE2016-54437>
- Bak, C., Zahle, F., Bitsche, R., Kim, T., Yde, A., Henriksen, L. C., ... & Natarajan, A. (2013). The DTU 10-MW reference wind turbine. In *Danish wind power research 2013*.
- Battistella, T., Paradinas, D. D. L. D., Urbán, A. M., & Garcia, R. G. (2018). High Fidelity Simulation of Multi-MW Rotor Aerodynamics by Using a Multifan. *Volume 10: Ocean Renewable Energy*, V010T09A074. <https://doi.org/10.1115/OMAE2018-77606>

Bayati, I., Belloli, M., Bernini, L., Mikkelsen, R., & Zasso, A. (2016). On the aero-elastic design of the DTU 10MW wind turbine blade for the LIFES50+ wind tunnel scale model. *Journal of Physics: Conference Series*, 753, 022028. <https://doi.org/10.1088/1742-6596/753/2/022028>

Bayati, I., Belloli, M., Facchinetti, A., & Giappino, S. (2013). Wind Tunnel Tests on Floating Offshore Wind Turbines. *Wind Engineering*, 37(6), 557–568. JSTOR.

Bayati, I., Bernini, L., Facchinetti, A., Fontanella, A., Giberti, H., Zasso, A., & Belloli, M. (2019). Hybrid HIL Testing of Floating Wind Turbines Within LIFES50+ Project. In F. Ricciardelli & A. M. Avossa (Eds.), *Proceedings of the XV Conference of the Italian Association for Wind Engineering* (Vol. 27, pp. 99–109). Springer International Publishing. https://doi.org/10.1007/978-3-030-12815-9_8

Beaudry-Losique, J., Boling, T., Brown-Saracino, J., Gilman, P., Hahn, M., Hart, C., Johnson, J., McCluer, M., Morton, L., Naughton, B., Norton, G., Ram, B., Redding, T., & Wallace, W. (2011). *A National Offshore Wind Strategy. Creating an Offshore Wind Energy Industry in the United States* (DOE/GO--102011-2988, 1219141; p. DOE/GO--102011-2988, 1219141). <https://doi.org/10.2172/1219141>.

Berthelsen, P. A., Bachynski, E. E., Karimirad, M., & Thys, M. (2016, October 18). *Real-Time Hybrid Model Tests of a Braceless Semi-Submersible Wind Turbine: Part III — Calibration of a Numerical Model*. ASME 2016 35th International Conference on Ocean, Offshore and Arctic Engineering. <https://doi.org/10.1115/OMAE2016-54640>

Bredmose, H., Lemmer, F., Borg, M., Pegalajar-Jurado, A., Mikkelsen, R. F., Larsen, T. S., Fjelstrup, T., Yu, W., Lomholt, A. K., Boehm, L., & Armendariz, J. A. (2017). The Triple Spar campaign: Model tests of a 10MW floating wind turbine with waves, wind and pitch control. *Energy Procedia*, 137, 58–76. <https://doi.org/10.1016/j.egypro.2017.10.334>

Broeren, A.P., Giguère, P., & Selig, M.S. (1996). Summary of Low-Speed Airfoil Data - Vol. 3.

Bureau of Ocean Energy Management. (2023, July). *Gulf of Maine / Bureau of Ocean Energy Management*. Retrieved October 8, 2023, from <https://www.boem.gov/renewable-energy/state-activities/maine/gulf-maine/>.

Cao, Q., Xiao, L., Cheng, Z., & Liu, M. (2020). An Experimental Study on Dynamic Behavior of a New Concept of 10MW Semi-Submersible Wind Turbine. ISOPE-I-20-1310.

Chakrabarti, S. K. (1994). Offshore structure modeling. World Scientific. Chapter 3

Chen, P., Chen, J., & Hu, Z. (2020). Review of Experimental-Numerical Methodologies and Challenges for Floating Offshore Wind Turbines. *Journal of Marine Science and Application*. <https://doi.org/10.1007/s11804-020-00165-z>.

Coudurier, C., Lepreux, O., & Petit, N. (2015). Passive and semi-active control of an offshore floating wind turbine using a tuned liquid column damper. *IFAC-PapersOnLine*, 48(16), 241–247. <https://doi.org/10.1016/j.ifacol.2015.10.287>

Coulling, A. J., Goupee, A. J., Robertson, A. N., & Jonkman, J. M. (2013, November 26). Importance of Second-Order Difference-Frequency Wave-Diffraction Forces in the Validation of a FAST Semi-

Submersible Floating Wind Turbine Model. ASME 2013 32nd International Conference on Ocean, Offshore and Arctic Engineering. <https://doi.org/10.1115/OMAE2013-10308>

Coulling, A. J., Goupee, A. J., Robertson, A. N., Jonkman, J. M., & Dagher, H. J. (2013). Validation of a FAST semi-submersible floating wind turbine numerical model with DeepCwind test data. *Journal of Renewable and Sustainable Energy*, 5(2), 023116. <https://doi.org/10.1063/1.4796197>

de Ridder, E.-J., Otto, W., Zondervan, G.-J., Huijs, F., & Vaz, G. (2014). Development of a Scaled-Down Floating Wind Turbine for Offshore Basin Testing. *Volume 9A: Ocean Renewable Energy*, V09AT09A027. <https://doi.org/10.1115/OMAE2014-23441>

Deb, K. (2004). Multi-objective optimization using evolutionary algorithms (Repr). Wiley.

DNV-GL. (2023). Bladed. <https://www.dnv.com/services/wind-turbine-design-software-bladed-3775>.

Facchinetti, A.; Di Carlo, S.; Fontanella, A.; Guanche, R.; Battistella, T.; Somoano, M.; Sarmiento, J.; Rodriguez, A. (2020). HIL 15MW Development; Technical Report D5.1. <https://corewind.eu/wp-content/uploads/files/delivery-docs/D5.1.pdf>

Fontanella, A., Liu, Y., Azcona, J., Pires, O., Bayati, I., Gueydon, S., Ridder, E. J. de, Wingerden, J. W. van, & Belloli, M. (2020). A hardware-in-the-loop wave-basin scale-model experiment for the validation of control strategies for floating offshore wind turbines. *Journal of Physics: Conference Series*, 1618(3), 032038. <https://doi.org/10.1088/1742-6596/1618/3/032038>

Fowler, M. J., Goupee, A. J., & Viselli, A. M. (2016). Advances in Model Scale Testing of Floating Offshore Wind Turbines Utilizing the W2 Wind/Wave Basin. *OTC-27258-MS*, 15. <https://doi.org/10.4043/27258-MS>

Fowler, M. J., Goupee, A. J., Allen, C., Viselli, A., & Dagher, H. (2017). 1:52 Scale Testing of the First US Commercial Scale Floating Wind Turbine, VolturnUS: Testing Overview and the Evolution of Scale Model Testing Methods. *Volume 10: Ocean Renewable Energy*, V010T09A078. <https://doi.org/10.1115/OMAE2017-61864>

Fowler, M. J., Kimball, R. W., Thomas, D. A., & Goupee, A. J. (2013). Design and Testing of Scale Model Wind Turbines for Use in Wind/Wave Basin Model Tests of Floating Offshore Wind Turbines. *Volume 8: Ocean Renewable Energy*, V008T09A004. <https://doi.org/10.1115/OMAE2013-10122>

Fowler, M. L., Lenfest, E., Viselli, A., Goupee, A. J., Kimball, R. W., Zalkind, D., Wright, A., Bergua, R., Wang, L., & Robertson, A. (2023a). *1:70-Scale Model Testing of the Reference OpenSource Controller (ROSCO) on the IEA-Wind 15MW Reference Wind Turbine Including Floating Feedback*. ISOPE-I-23-074.

Fowler, M., Lenfest, E., Viselli, A., Goupee, A., Kimball, R., Bergua, R., Wang, L., Zalkind, D., Wright, A., & Robertson, A. (2023b). Wind/Wave Testing of a 1:70-Scale Performance-Matched Model of the IEA Wind 15 MW Reference Wind Turbine with Real-Time ROSCO Control and Floating Feedback. *Machines*, 11(9), Article 9. <https://doi.org/10.3390/machines11090865>

Garcia-Sanz, M. (2019). Control Co-Design of Floating Offshore Wind Turbines, Presented at the 5th Wind Energy Systems Engineering Workshop, Pamplona, Spain,

<https://www.nrel.gov/wind/assets/pdfs/systems-engineering-workshop-2019-control-co-design-offshore.pdf>.

Garrett Barter, Pietro Bortolotti, Evan Gaertner, Jenni Rinker, Nikhar J. Abbas, Daniel Zalkind, Frederik Zahle, T-Wainwright, E. Branlard, Lu Wang, Luis A. Padrón, Matt Hall, & Issraman. (2023). IEAWindTask37/IEA-15-240-RWT: ROSCO v2.8 and minor fix in HAWCStab2 file. (v1.1.8). Zenodo. <https://doi.org/10.5281/zenodo.10031673>

GE. (2023). Haliade-X offshore wind turbine. <https://www.ge.com/renewableenergy/wind-energy/offshore-wind/haliade-x-offshore-turbine>

Glauert, H. (1983). *The Elements of Aerofoil and Airscrew Theory* (1st ed.). Cambridge University Press. <https://doi.org/10.1017/CBO9780511574481>

Goupee, A. J., Fowler, M. J., Kimball, R. W., Helder, J., & de Ridder, E.-J. (2014). Additional Wind/Wave Basin Testing of the DeepCwind Semi-Submersible With a Performance-Matched Wind Turbine. *Volume 9B: Ocean Renewable Energy*, V09BT09A026. <https://doi.org/10.1115/OMAE2014-24172>

Goupee, A. J., Kimball, R. W., & Dagher, H. J. (2017). Experimental observations of active blade pitch and generator control influence on floating wind turbine response. *Renewable Energy*, 104, 9–19. <https://doi.org/10.1016/j.renene.2016.11.062>

Groom, N. (2023, September 15). Biden's offshore wind target slipping out of reach as projects struggle. *Reuters*. <https://www.reuters.com/business/energy/bidens-offshore-wind-target-slipping-out-reach-projects-struggle-2023-09-15/>.

Guanche, R., Somoano, M., Battistella, T., Rodriguez, A., Fernandez, S., Sarmiento, J., Alvarez, A., Blanco, D., Facchinetti, A., Fontanella, A., Simoni Di Carlo, Arramounet, V., Castillo, F., Climent Molins, Trubat, P., Muñoz, S., Romero, I., Comas, F. J., Sisí, D., & Doole, S. (2023). *Integrated FOWT test report*. <https://doi.org/10.5281/ZENODO.7871090>.

Gueydon, S., Bayati, I., & De Ridder, E. J. (2020). Discussion of solutions for basin model tests of FOWTs in combined waves and wind. *Ocean Engineering*, 209, 107288. <https://doi.org/10.1016/j.oceaneng.2020.107288>

Gueydon, S., Duarte, T., & Jonkman, J. (2014). Comparison of Second-Order Loads on a Semisubmersible Floating Wind Turbine. *Volume 9A: Ocean Renewable Energy*, V09AT09A024. <https://doi.org/10.1115/OMAE2014-23398>

Hall, M. (2016). *Hybrid Modeling of Floating Wind Turbines* [The University of Maine]. <https://digitalcommons.library.umaine.edu/etd/2477>

Han, D., Wang, W., Li, X., & Su, X. (2022). Optimization design of multiple tuned mass dampers for semi-submersible floating wind turbine. *Ocean Engineering*, 264, 112536. <https://doi.org/10.1016/j.oceaneng.2022.112536>

Hill, Joshua S. (16 February 2018). "Hywind Scotland, World's First Floating Wind Farm, Performing Better Than Expected". CleanTechnica. Sustainable Enterprises Media, Inc. Retrieved 7 March 2018.

Hmedi, M., Uzunoglu, E., Zeng, C., Gaspar, J. F., & Guedes Soares, C. (2023). Experimental Challenges and Modelling Approaches of Floating Wind Turbines. *Journal of Marine Science and Engineering*, 11(11), 2048. <https://doi.org/10.3390/jmse11112048>

Jahangiri, V., & Sun, C. (2020). Three-dimensional vibration control of offshore floating wind turbines using multiple tuned mass dampers. *Ocean Engineering*, 206, 107196. <https://doi.org/10.1016/j.oceaneng.2020.107196>

Jamieson, P. (2011). *Innovation in Wind Turbine Design* (1st ed.). Wiley. <https://doi.org/10.1002/9781119975441>

Jonkman, B., Mudafort, R. M., Platt, A., E. Branlard, Sprague, M., Ross, H., Jjonkman, HaymanConsulting, Hall, M., Slaughter, D., Vijayakumar, G., Buhl, M., Russell19798, Bortolotti, P., Reos-Rerozier, Shreyas Ananthan, Michael, S., Rood, J., Rdamiani, ... Mattrphillips. (2023). *OpenFAST/openfast: V3.5.0* (v3.5.0) [Computer software]. Zenodo. <https://doi.org/10.5281/ZENODO.7942867>.

Jonkman, J., & Musial, W. (2010). *Offshore Code Comparison Collaboration (OC3) for IEA Wind Task 23 Offshore Wind Technology and Deployment* (NREL/TP-5000-48191, 1004009; p. NREL/TP-5000-48191, 1004009). <https://doi.org/10.2172/1004009>.

Jonkman, J., Butterfield, S., Musial, W., & Scott, G. (2009). *Definition of a 5-MW Reference Wind Turbine for Offshore System Development* (NREL/TP-500-38060, 947422; p. NREL/TP-500-38060, 947422). <https://doi.org/10.2172/947422>

Kimball, R. W., Goupee, A. J., Coulling, A. J., & Dahger, H. J. (2012, October 24). *Model Test Comparisons of TLP, Spar-buoy and Semi-submersible Floating Offshore Wind Turbine Systems*. SNAME Maritime Convention. <https://doi.org/10.5957/SMC-2012-A16>

Kimball, R., Goupee, A. J., Fowler, M. J., de Ridder, E.-J., & Helder, J. (2014). Wind/Wave Basin Verification of a Performance-Matched Scale-Model Wind Turbine on a Floating Offshore Wind Turbine Platform. *Volume 9B: Ocean Renewable Energy*, V09BT09A025. <https://doi.org/10.1115/OMAE2014-24166>

Koo, B. J., Goupee, A. J., Kimball, R. W., & Lambrakos, K. F. (2014). Model Tests for a Floating Wind Turbine on Three Different Floater. *Journal of Offshore Mechanics and Arctic Engineering*, 136(2). <https://doi.org/10.1115/1.4024711>.

Kvittem, M. I., Berthelsen, P. A., Eliassen, L., & Thys, M. (2018, September 25). *Calibration of Hydrodynamic Coefficients for a Semi-Submersible 10 MW Wind Turbine*. ASME 2018 37th International Conference on Ocean, Offshore and Arctic Engineering. <https://doi.org/10.1115/OMAE2018-77826>

Lackner, M. A., & Rotea, M. A. (2011). Structural control of floating wind turbines. *Mechatronics*, 21(4), 704–719. <https://doi.org/10.1016/j.mechatronics.2010.11.007>

Larsen, T. J., & Hanson, T. D. (2007). A method to avoid negative damped low frequent tower vibrations for a floating, pitch controlled wind turbine. *Journal of Physics: Conference Series*, 75, 012073. <https://doi.org/10.1088/1742-6596/75/1/012073>

Lee, C.H. and Newman, J.N. (2006) WAMIT User Manual, Versions 6.4, 6.4PC, 6.3S, 6.3S-PC. WAMIT, Inc., Cambridge, MA.

Lewis, Michelle. 2023. "GE is developing a massive 18 MW offshore wind turbine." Electrek. <https://electrek.co/2023/03/13/ge-is-developing-a-massive-18-mw-offshore-wind-turbine/>.

Lin, G.-L., Lu, L.-Y., Lei, K.-T., Liu, K.-Y., Ko, Y.-Y., & Ju, S.-H. (2021). Experimental study on seismic vibration control of an offshore wind turbine with TMD considering soil liquefaction effect. *Marine Structures*, 77, 102961. <https://doi.org/10.1016/j.marstruc.2021.102961>

Lopez, A., Green, R., Williams, T., Lantz, E., Buster, G., & Roberts, B. (2022). *Offshore Wind Energy Technical Potential for the Contiguous United States* (NREL/PR-6A20-83650). National Renewable Energy Laboratory. <https://doi.org/10.2172/1882929>.

Manjock, A. (2016) D4.22: Methods for Performing Scale-Tests for Method and Model Validation of Floating Wind Turbines; Technical Report; http://www.innwind.eu/-/media/sites/innwind/publications/deliverables/deliverabled4-22-rev021_innwind-eu.pdf

Manwell, J. F., McGowan, J. G., & Rogers, A. L. (2002). *Wind Energy Explained*. John Wiley & Sons, Ltd. <https://doi.org/10.1002/0470846127>

Martin, H. R., Kimball, R. W., Viselli, A. M., & Goupee, A. J. (2014). Methodology for Wind/Wave Basin Testing of Floating Offshore Wind Turbines. *Journal of Offshore Mechanics and Arctic Engineering*, 136(2), Article 2. <https://doi.org/10.1115/1.4025030>

Mendoza, N., Robertson, A., Wright, A., Jonkman, J., Wang, L., Bergua, R., Ngo, T., Das, T., Odeh, M., Mohsin, K., Flavia, F. F., Child, B., Bangga, G., Fowler, M., Goupee, A., Kimball, R., Lenfest, E., & Viselli, A. (2022). Verification and Validation of Model-Scale Turbine Performance and Control Strategies for the IEA Wind 15 MW Reference Wind Turbine. *Energies*, 15(20), 7649. <https://doi.org/10.3390/en15207649>

Musial, Walter, Spitsen, Paul, Beiter, Philipp, Duffy, Patrick, Mulas Hernando, Daniel, Hammond, Rob, Shields, Matt, & Marquis, Melinda. Offshore Wind Market Report: 2023 Edition. United States. <https://doi.org/10.2172/1997466>.

NREL. (2021). OpenFAST/openfast: V3.0.0 (v3.0.0) [Computer software]. <https://github.com/OpenFAST/openfast/tree/v3.0.0>

NREL. (2021). ROSCO. Version 2.4.1, <https://github.com/NREL/ROSCO>, 2021.

Olondriz, J., Elorza, I., Trojaola, I., Pujana, A., & Landaluze, J. (2016). On the effects of basic platform design characteristics on floating offshore wind turbine control and their mitigation. *Journal of Physics: Conference Series*, 753, 052008. <https://doi.org/10.1088/1742-6596/753/5/052008>

Parker, A. (2022). *Development and Testing of a 1:70 Scale Model Wind Turbine of the IEA Reference 15 MW Floating Offshore System* [The University of Maine]. <https://digitalcommons.library.umaine.edu/etd/3548>

Pegalajar-Jurado, A., & Bredmose, H. (2019). Reproduction of slow-drift motions of a floating wind turbine using second-order hydrodynamics and Operational Modal Analysis. *Marine Structures*, 66, 178–196. <https://doi.org/10.1016/j.marstruc.2019.02.008>

Platt, A., (2020). ServoDyn Structural control submodule (formerly TMD) #607. <https://github.com/OpenFAST/openfast/pull/607>

Randall, S. E., Halsted, D. M., & Taylor, D. L. (1981). Optimum Vibration Absorbers for Linear Damped Systems. *Journal of Mechanical Design*, 103(4), 908–913. <https://doi.org/10.1115/1.3255005>

Ransley, E. J., Brown, S. A., Edwards, E. C., Tosdevin, T., Monk, K., Reynolds, A. M., Greaves, D., & Hann, M. R. (2023). Real-Time Hybrid Testing of a Floating Offshore Wind Turbine Using a Surrogate-Based Aerodynamic Emulator. *ASME Open Journal of Engineering*, 2(021017). <https://doi.org/10.1115/1.4056963>

Robertson, A. (2023a). *FOCAL Campaign I: Advanced Wind Turbine Control Strategies* [dataset]. Atmosphere to Electrons (A2e) Data Archive and Portal, Pacific Northwest National Laboratory; PNNL. <https://doi.org/10.21947/1962594>

Robertson, A. (2023b). *FOCAL Campaign II/III: Applying Active Hull Controls Using Tuned-mass Dampers/Hull Flexibility and Internal Loads* [dataset]. Atmosphere to Electrons (A2e) Data Archive and Portal, Pacific Northwest National Laboratory; PNNL. <https://doi.org/10.21947/1968406>

Robertson, A. (2023c). *FOCAL Campaign IV: Integrated System Control: Turbine + Hull* [dataset]. Atmosphere to Electrons (A2e) Data Archive and Portal, Pacific Northwest National Laboratory; PNNL. <https://doi.org/10.21947/1972267>

Robertson, A. N., Gueydon, S., Bachynski, E., Wang, L., Jonkman, J., Alarcón, D., Amet, E., Beardsell, A., Bonnet, P., Boudet, B., Brun, C., Chen, Z., Féron, M., Forbush, D., Galinos, C., Galvan, J., Gilbert, P., Gómez, J., Harnois, V., ... Wohlfahrt-Laymann, S. (2020). OC6 Phase I: Investigating the underprediction of low-frequency hydrodynamic loads and responses of a floating wind turbine. *Journal of Physics: Conference Series*, 1618(3), 032033. <https://doi.org/10.1088/1742-6596/1618/3/032033>

Robertson, A. N., Wendt, F., Jonkman, J. M., Popko, W., Dagher, H., Gueydon, S., Qvist, J., Vittori, F., Azcona, J., Uzunoglu, E., Soares, C. G., Harries, R., Yde, A., Galinos, C., Hermans, K., De Vaal, J. B., Bozonnet, P., Bouy, L., Bayati, I., ... Debruyne, Y. (2017). OC5 Project Phase II: Validation of Global Loads of the DeepCwind Floating Semisubmersible Wind Turbine. *Energy Procedia*, 137, 38–57. <https://doi.org/10.1016/j.egypro.2017.10.333>

Robertson, A., & Wang, L. (2021). OC6 Phase Ib: Floating Wind Component Experiment for Difference-Frequency Hydrodynamic Load Validation. *Energies*, 14(19), 6417. <https://doi.org/10.3390/en14196417>

Robertson, A., Fowler, M., Wright, A., Wang, L. (2023d) FOCAL Project – Summary Presentation. Presented to ARPA-e (unpublished).

Robertson, A., Jonkman, J., Masciola, M., Song, H., Goupee, A., Coulling, A., & Luan, C. (2014a). *Definition of the Semisubmersible Floating System for Phase II of OC4* (NREL/TP-5000-60601, 1155123; p. NREL/TP-5000-60601, 1155123). <https://doi.org/10.2172/1155123>

Robertson, A., Jonkman, J., Vorpahl, F., Popko, W., Qvist, J., Frøyd, L., Chen, X., Azcona, J., Uzunoglu, E., Guedes Soares, C., Luan, C., Yutong, H., Pengcheng, F., Yde, A., Larsen, T., Nichols, J., Buils, R., Lei, L., Nygaard, T. A., ... Guérinel, M. (2014b). Offshore Code Comparison Collaboration Continuation Within IEA Wind Task 30: Phase II Results Regarding a Floating Semisubmersible Wind System. *Volume 9B: Ocean Renewable Energy*, V09BT09A012. <https://doi.org/10.1115/OMAE2014-24040>

Roddier, D., Cermelli, C., Aubault, A., & Weinstein, A. (2010). WindFloat: A floating foundation for offshore wind turbines. *Journal of Renewable and Sustainable Energy*, 2(3), 033104. <https://doi.org/10.1063/1.3435339>.

Sauder, T., Chabaud, V., Thys, M., Bachynski, E. E., & Sæther, L. O. (2016, October 18). *Real-Time Hybrid Model Testing of a Braceless Semi-Submersible Wind Turbine: Part I — The Hybrid Approach*. ASME 2016 35th International Conference on Ocean, Offshore and Arctic Engineering. <https://doi.org/10.1115/OMAE2016-54435>

Savenije, F. (2017). Model Testing of a Floating Wind Turbine Including Control, Presentation at Deepwind Conference - Trondheim, Norway.

Selig, M. S. (Ed.). (1995). *Summary of low speed airfoil data. Vol. 1*. SoarTech Publications.

Shields, M., Beiter, P., Nunemaker, J., Cooperman, A., & Duffy, P. (2021). Impacts of turbine and plant upsizing on the levelized cost of energy for offshore wind. *Applied Energy*, 298, 117189. <https://doi.org/10.1016/j.apenergy.2021.117189>.

Souza, C. E. S., & Bachynski, E. E. (2019). Changes in surge and pitch decay periods of floating wind turbines for varying wind speed. *Ocean Engineering*, 180, 223–237. <https://doi.org/10.1016/j.oceaneng.2019.02.075>

Stewart, G. M., & Lackner, M. A. (2014). The impact of passive tuned mass dampers and wind–wave misalignment on offshore wind turbine loads. *Engineering Structures*, 73, 54–61. <https://doi.org/10.1016/j.engstruct.2014.04.045>

Stiesdal, H. (2009). Hywind: The world's first floating MW-scale wind turbine. *Wind Directions*, 31, 52–53.

The White House. (2021, March 29). *FACT SHEET: Biden Administration Jumpstarts Offshore Wind Energy Projects to Create Jobs*. The White House. <https://www.whitehouse.gov/briefing-room/statements-releases/2021/03/29/fact-sheet-biden-administration-jumpstarts-offshore-wind-energy-projects-to-create-jobs/>.

The White House. (2022, September 15). *FACT SHEET: Biden-Harris Administration Announces New Actions to Expand U.S. Offshore Wind Energy*. The White House. <https://www.whitehouse.gov/briefing-room/statements-releases/2022/09/15/fact-sheet-biden-harris-administration-announces-new-actions-to-expand-u-s-offshore-wind-energy/>.

Thys, M., Chabaud, V., Sauder, T., Eliassen, L., Sæther, L. O., & Magnussen, Ø. B. (2018, December 13). *Real-Time Hybrid Model Testing of a Semi-Submersible 10MW Floating Wind Turbine and Advances in the Test Method*. ASME 2018 1st International Offshore Wind Technical Conference. <https://doi.org/10.1115/IOWTC2018-1081>

US Department of Energy. (September 2022). *Floating Offshore Wind ShotTM: Unlocking the Power of Floating Offshore Wind Energy*. Retrieved October 8, 2023, from <https://www.energy.gov/sites/default/files/2022-09/floating-offshore-wind-shot-fact-sheet.pdf>.

Van Der Veen, G. J., Couchman, I. J., & Bowyer, R. O. (2012). Control of floating wind turbines. *2012 American Control Conference (ACC)*, 3148–3153. <https://doi.org/10.1109/ACC.2012.6315120>

Wang, L., Bergua, R., Robertson, A., Jonkman, J., Ngo, T., Das, T., Sarker, D., Flavia, F., Harries, R., Fowler, M., Lenfest, E., Muro, J. L., Burlion, L., & Bilgen, O. (2023a). *Experimental Validation of Models of a Hull-Based Tuned Mass Damper System for a Semisubmersible Floating Offshore Wind Turbine Platform*. [in press]

Wang, L., Robertson, A., Jonkman, J., & Yu, Y.-H. (2022a). OC6 phase I: Improvements to the OpenFAST predictions of nonlinear, low-frequency responses of a floating offshore wind turbine platform. *Renewable Energy*, 187, 282–301. <https://doi.org/10.1016/j.renene.2022.01.053>

Wang, L., Robertson, A., Jonkman, J., Kim, J., Shen, Z.-R., Koop, A., Borràs Nadal, A., Shi, W., Zeng, X., Ransley, E., Brown, S., Hann, M., Chandramouli, P., Viré, A., Ramesh Reddy, L., Li, X., Xiao, Q., Méndez López, B., Campaña Alonso, G., ... Yu, K. (2022b). OC6 Phase Ia: CFD Simulations of the Free-Decay Motion of the DeepCwind Semisubmersible. *Energies*, 15(1), Article 1. <https://doi.org/10.3390/en15010389>

Wang, L.; Bergua, R.; Robertson, A.; Wright, A.; Zalkind, D.; Fowler, M.; Lenfest, E.; Viselli, A.; Goupee, A.; Kimball, R. (2023b). Experimental Investigation of Advanced Turbine Control Strategies and Load-Mitigation Measures with a Model-Scale Floating Offshore Wind Turbine System. *Applied Energy*

Wang, W., Li, X., Zhao, H., Wang, B., & Li, Y. (2020). Vibration control of a pentapod offshore wind turbine under combined seismic wind and wave loads using multiple tuned mass damper. *Applied Ocean Research*, 103, 102254. <https://doi.org/10.1016/j.apor.2020.102254>

Wen, B., Tian, X., Dong, X., Li, Z., Peng, Z., Zhang, W., & Wei, K. (2019). Design approaches of performance-scaled rotor for wave basin model tests of floating wind turbines. *Renewable Energy*. <https://doi.org/10.1016/j.renene.2019.10.147>

Wendt, F. F., Robertson, A. N., & Jonkman, J. M. (2019). FAST Model Calibration and Validation of the OC5-DeepCwind Floating Offshore Wind System Against Wave Tank Test Data. *International Journal of Offshore and Polar Engineering*, 29(01), 15–23. <https://doi.org/10.17736/ijope.2019.jc729>

Yu, W., Lemmer, F., Bredmose, H., Borg, M., Pegalajar-Jurado, A., Mikkelsen, R. F., Larsen, T. S., Fjelstrup, T., Lomholt, A. K., Boehm, L., Schlipf, D., Armendariz, J. A., & Cheng, P. W. (2017). The Triple Spar Campaign: Implementation and Test of a Blade Pitch Controller on a Scaled Floating Wind Turbine Model. *Energy Procedia*, 137, 323–338. <https://doi.org/10.1016/j.egypro.2017.10.357>

Yu, W., Lemmer, F., Schlipf, D., Cheng, P. W., Visser, B., Links, H., Gupta, N., Dankemann, S., Counago, B., & Serna, J. (2018). Evaluation of control methods for floating offshore wind turbines. *Journal of Physics: Conference Series*, 1104(1), 012033. <https://doi.org/10.1088/1742-6596/1104/1/012033>

Yu, W., Zhou, S. T., Lemmer, F., & Cheng, P. W. (2023). *Control Co-Design optimization of floating offshore wind turbines with tuned liquid multi-column dampers* [Preprint]. Wind technologies/Systems engineering. <https://doi.org/10.5194/wes-2023-131>

Zhao, Z., Wang, W., Han, D., Shi, W., Si, Y., & Li, X. (n.d.). Structural Control of an Ultra-large Semi-submersible Floating Offshore Wind Turbine. *Journal of Offshore Mechanics and Arctic Engineering*, 1–12. <https://doi.org/10.1115/1.4048880>

APPENDICES

APPENDIX A: CAMPAIGN 1 SUPPLEMENTALS

This appendix includes supplemental data relating to Campaign 1 to improve readability of the main text. Items are referenced directly in the text when possible.

Wind Time Series and PSDs from Section 2.3.3.

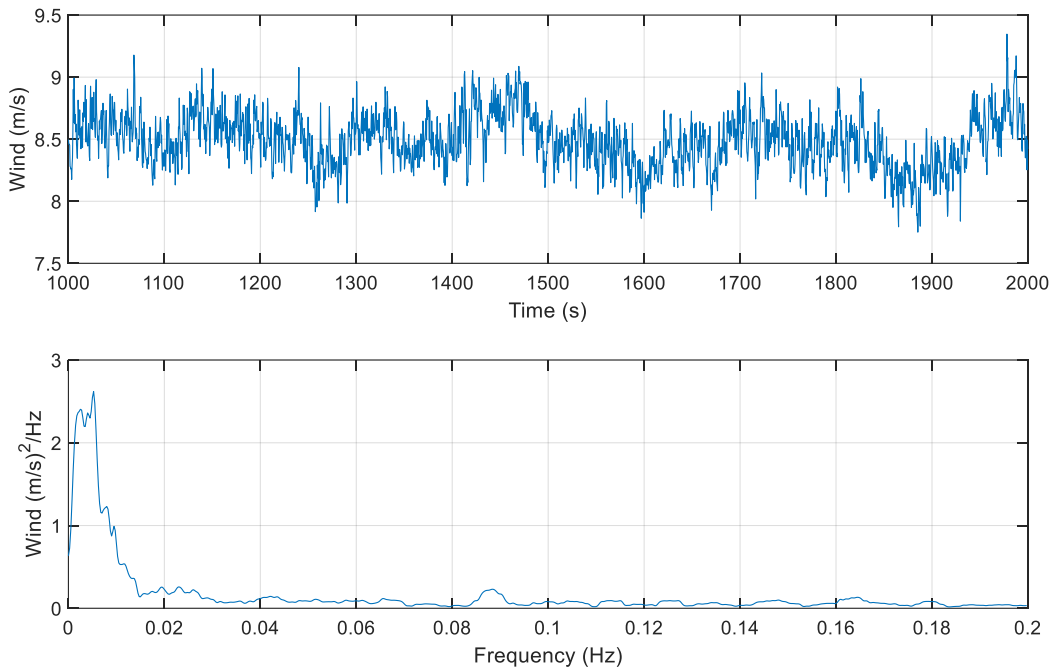


Figure A.1: BR1 Time History and Power Spectral Density Plots

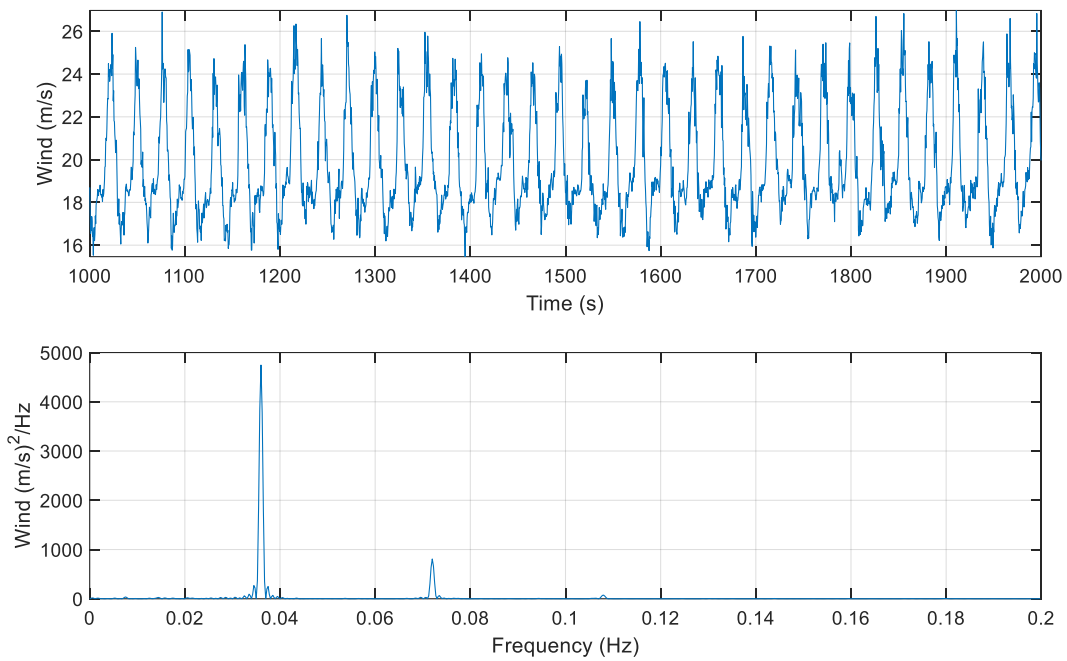


Figure A.2: TR1D Time History and Power Spectral Density Plots

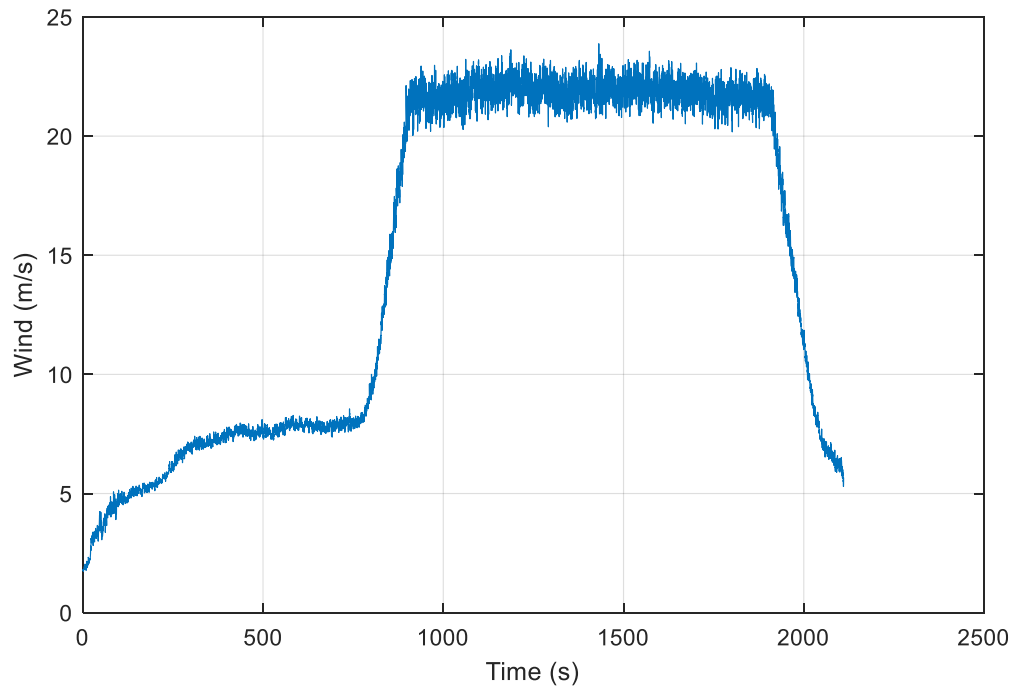


Figure A.3: TR1G Time History

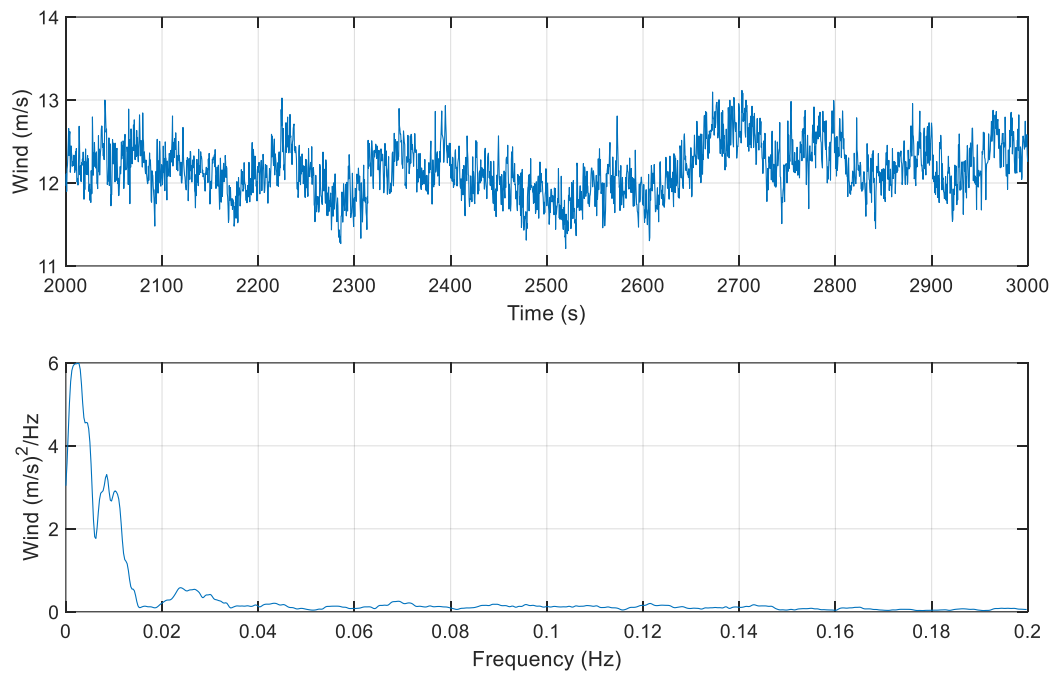


Figure A.4 : TR1S Time History and Power Spectral Density Plots

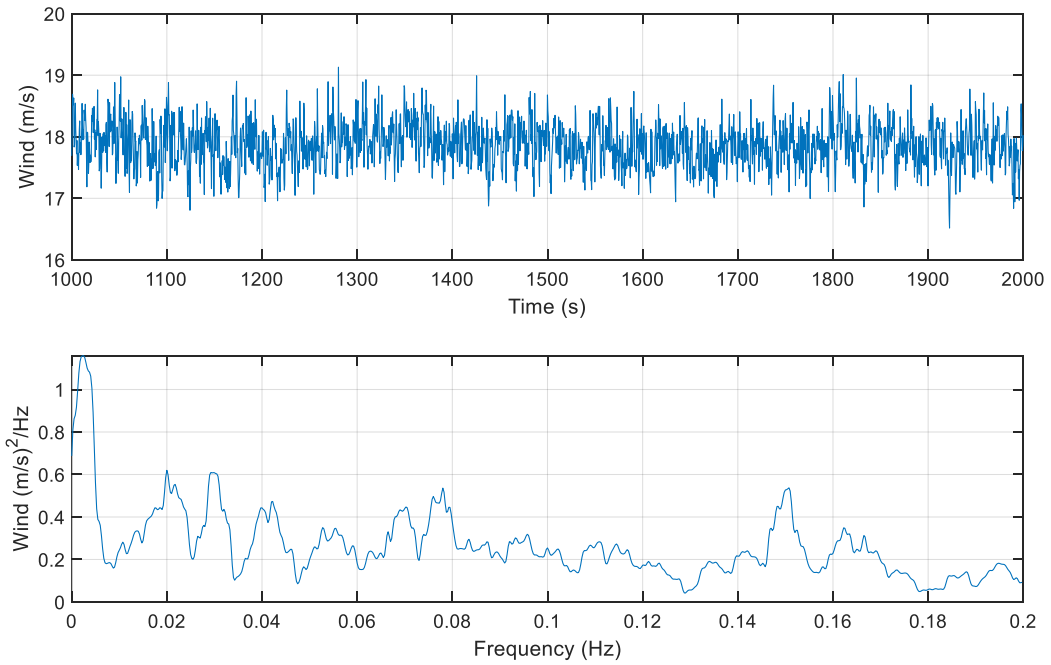


Figure A.5: AR1 Time History and Power Spectral Density Plots

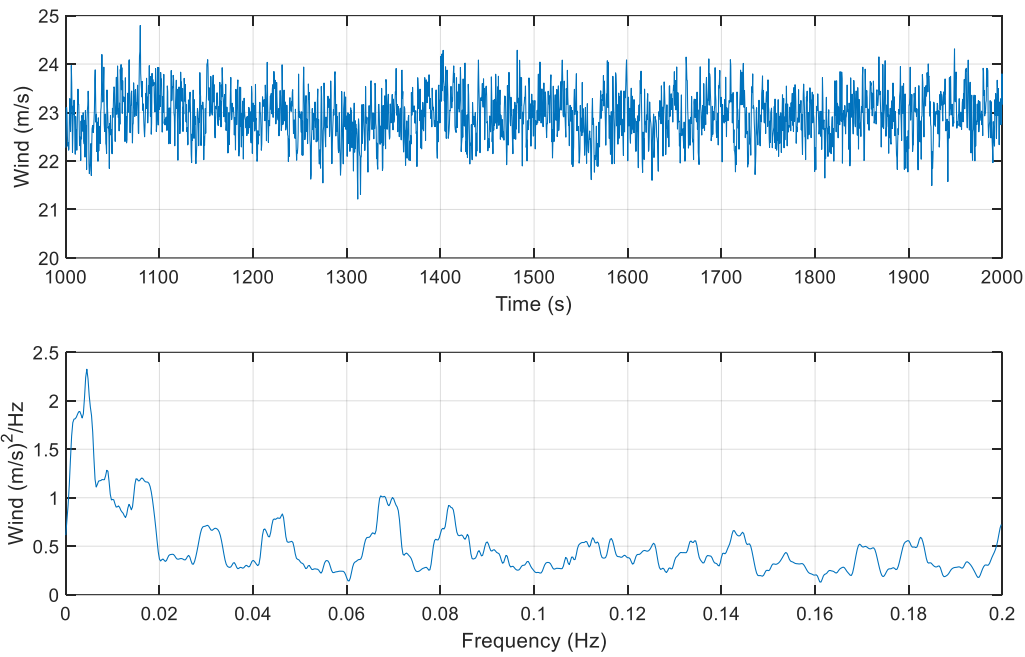


Figure A.6: AR2 Time History and Power Spectral Density Plots

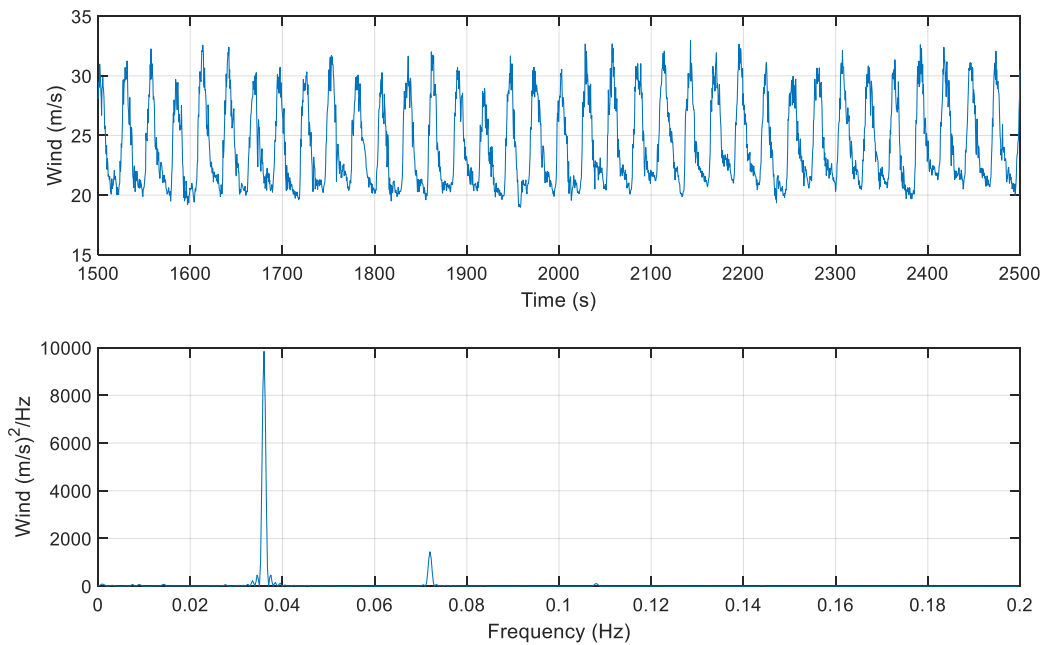


Figure A.7: AR2D Time History and Power Spectral Density Plots

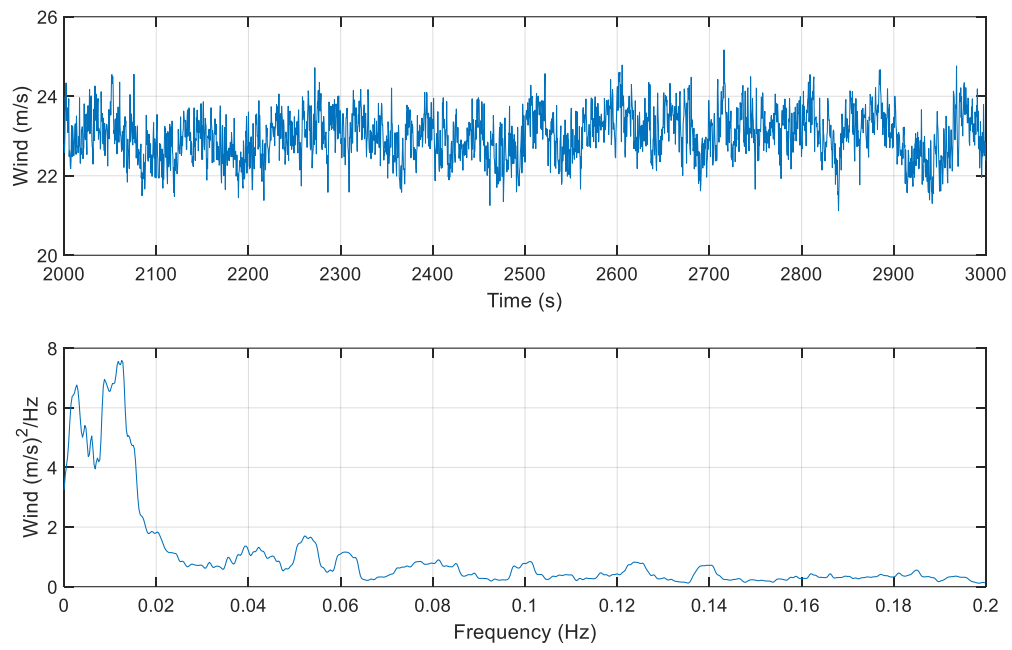


Figure A.8: AR2S Time History and Power Spectral Density Plots

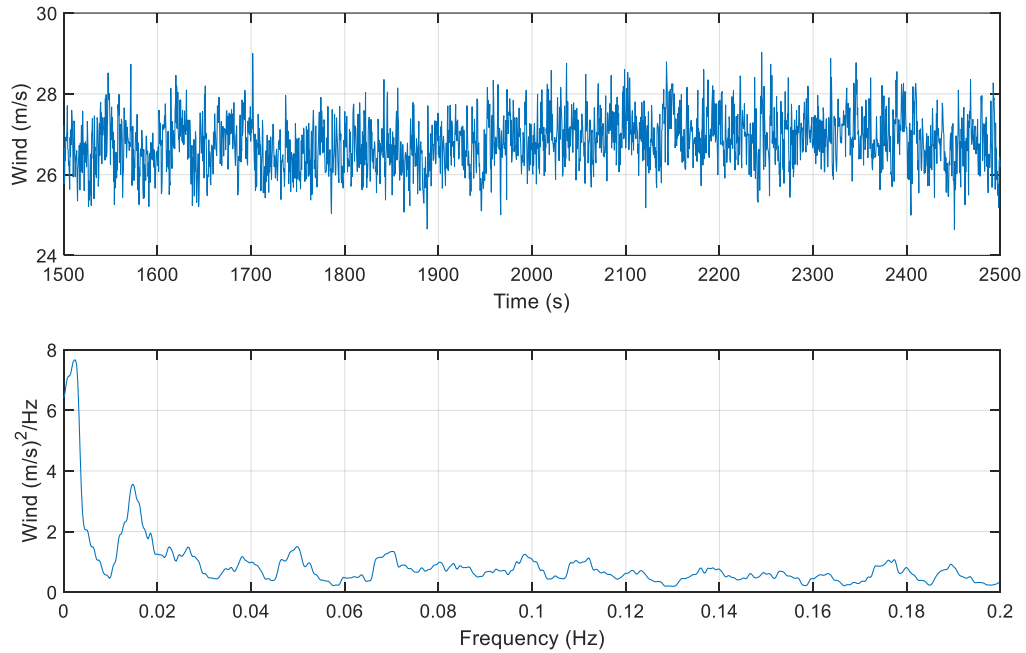


Figure A.9: CO Time History and Power Spectral Density Plots

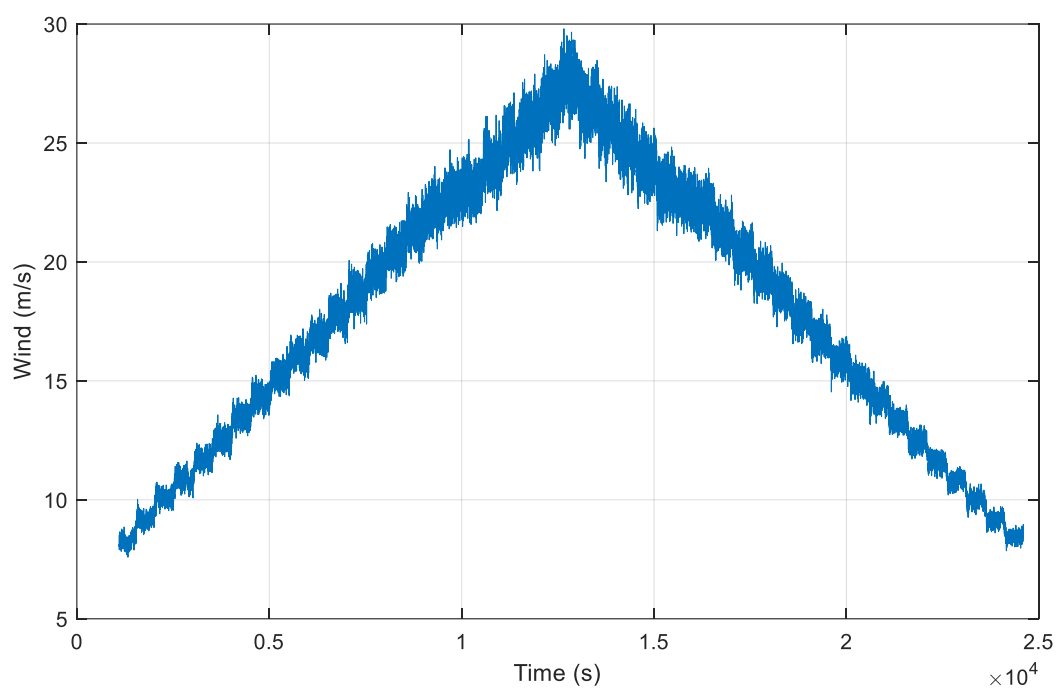


Figure A.10: Step Time History

APPENDIX B: CAMPAIGN 2/3 SUPPLEMENTS

This appendix includes supplemental data relating to Campaigns 2 and 3 to improve readability of the main text. Items are referenced directly in the text when possible.

System geometry and figures from Section 3.3.1

Table B.1: Geometry of Structure

Dimension	Symbol	Reference Figure	Units	As-Built Full Scale	Value Origin
Diameter of Outer Columns	BCD	Figure B.	m	12.23	Measured
Total height of Outer Columns	BCH	Figure B.	m	34.88	Measured
Outer Column Center to Center Column Center	BCC	Figure B.	m	51.67	Measured
Diameter of Center Column	CCD	Figure B.	m	9.85	Measured
Total height of Center Column	CCH	Figure B.	m	35.25	Measured
Width of Pontoon Leg	PLW	Figure B.	m	12.43	Measured
Height of Pontoon Leg	PLH	Figure B.	m	7.08	Measured
Diameter of Tower	TD	Figure B.	m	3.57	Measured
Height of Tower	TH	Figure B.	m	123.55	Measured
Keel to SWL (Adjusted +/-0.18m during testing)	Zswl	Figure B.	m	20.00	Nominal
Keel to Tower Base Flange bottom	Ztb	Figure B.	m	38.34	Measured
Center Column Top to Tower Base height	HFtb	Figure B.	m	3.09	Measured
Fairlead height above keel	FLH	Figure B.	m	5.64	Measured
Hull Force Gauge interface to Column Center	RFLEG	Figure B.	m	15.05	Measured
Hull force gauge CL to Keel height	HFLEG	Figure B.	m	3.51	Measured
Tower Base force gauge interface to Keel	HFTB	Figure B.	m	37.88	Measured
Tower base accelerometer to Keel height	AccTBz	Figure B.	m	37.18	Measured
Nacelle base accelerometer to Keel height	AccNBz	Figure B.	m	170.35	Measured
TMD Mass CG Nominal Position to Keel height	RCz	Figure B.	m	12.97	Nominal
TMD Mass CG Radial Distance to Center Column	RCx	Figure B.	m	51.67	Measured

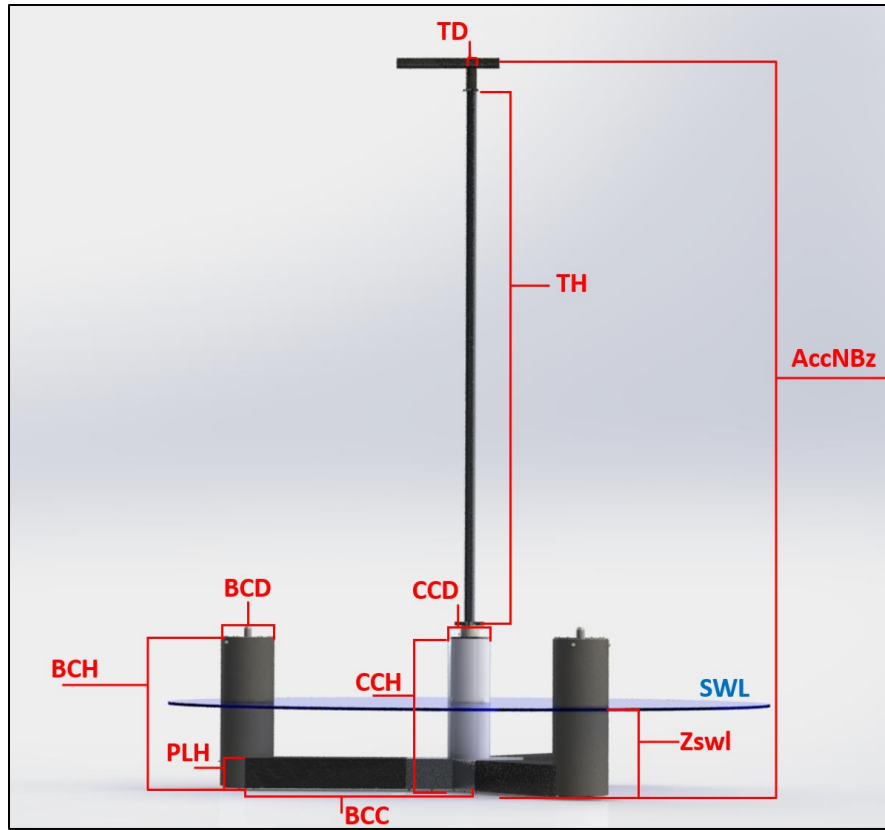


Figure B.1: System Geometry Definitions

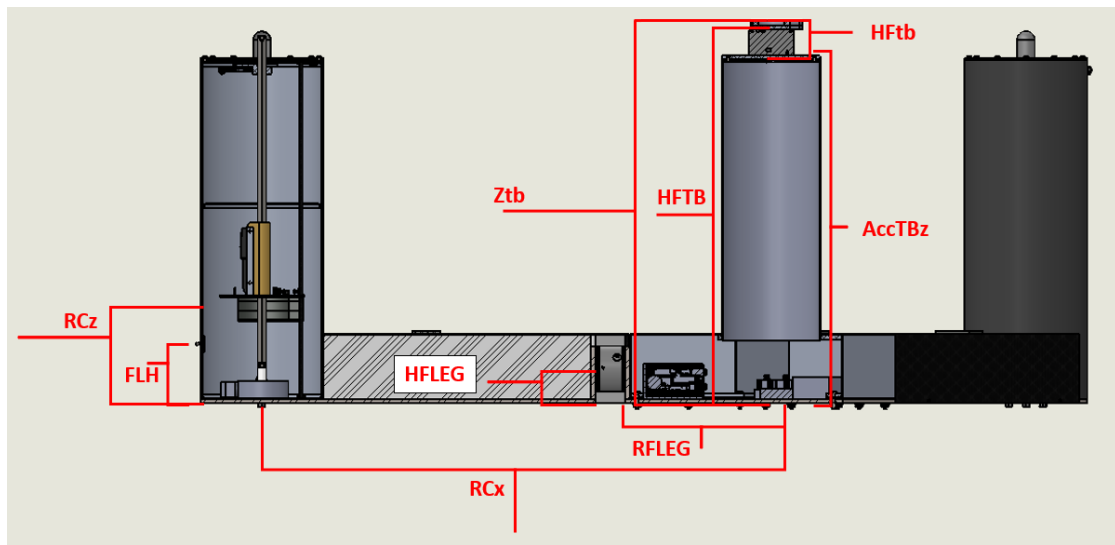


Figure B.2: Hull Geometry Definitions- Side View



Figure B.3: Hull Geometry Definitions- Top View

Calibrated wave environments, from Section 3.6.3.

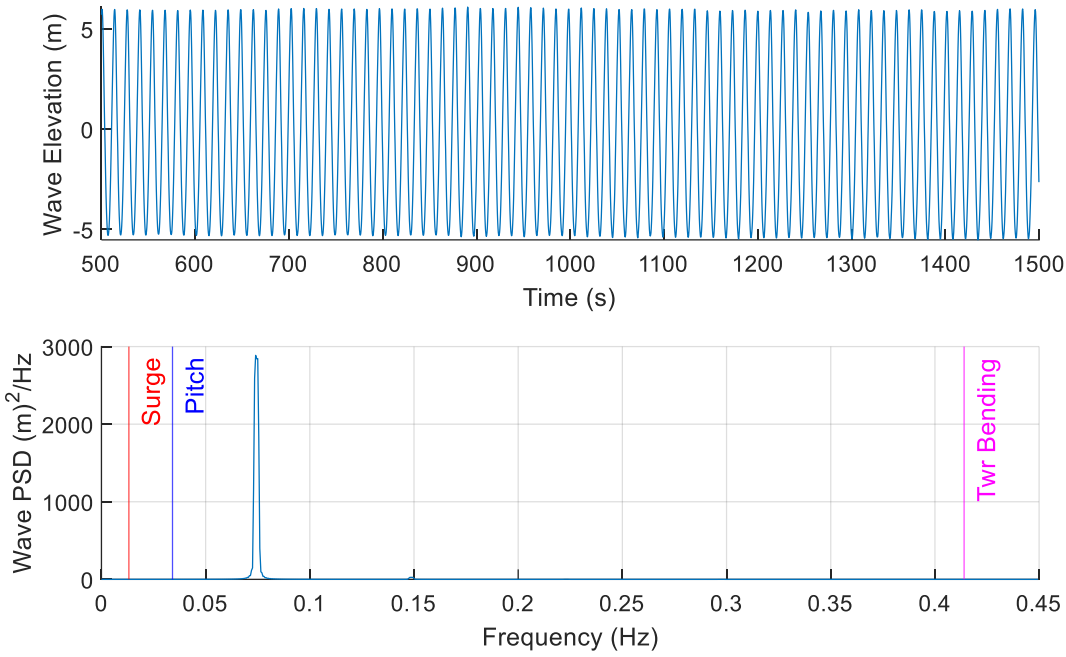


Figure B.4: R2 Time History and Power Spectral Density Plots

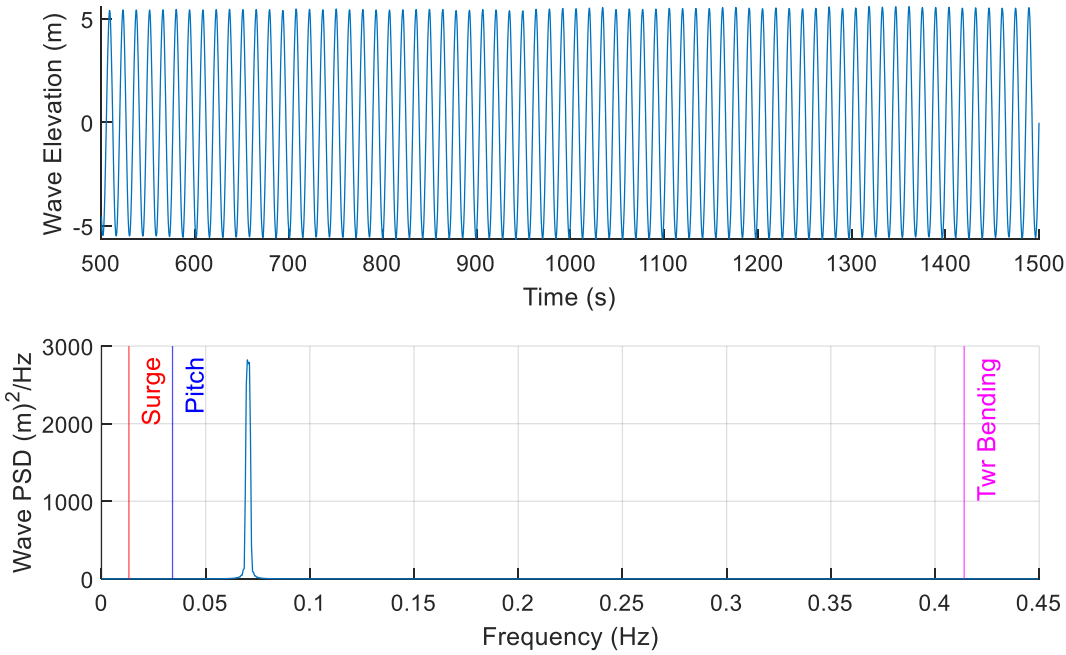


Figure B.5: R3 Time History and Power Spectral Density Plots

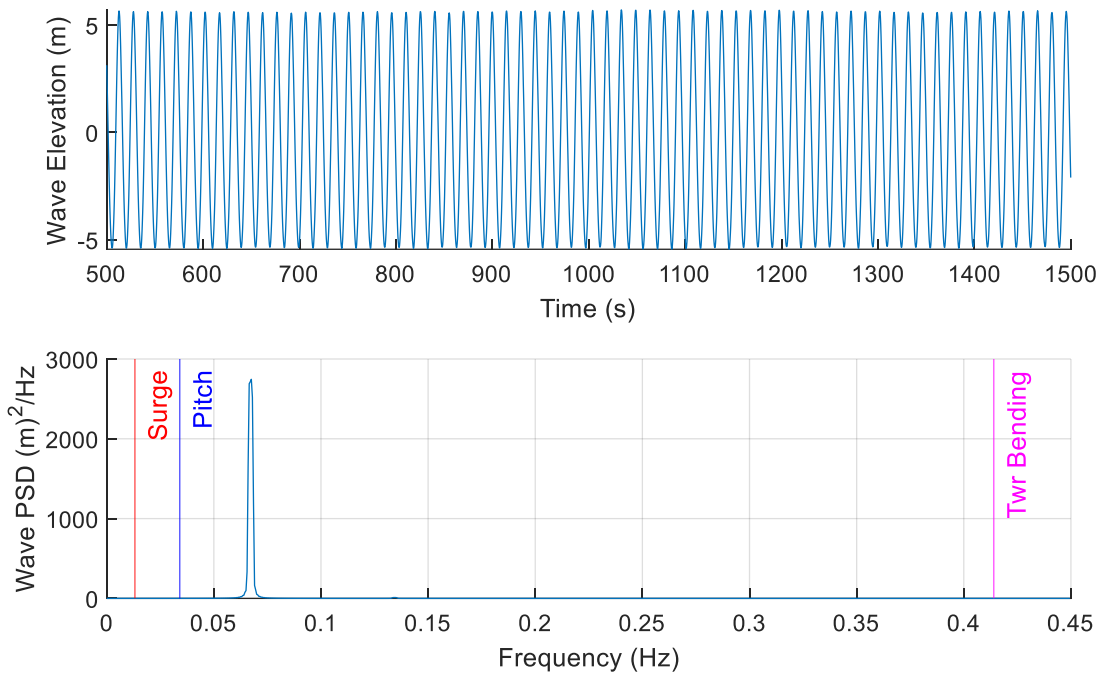


Figure B.6: R4 Time History and Power Spectral Density Plots

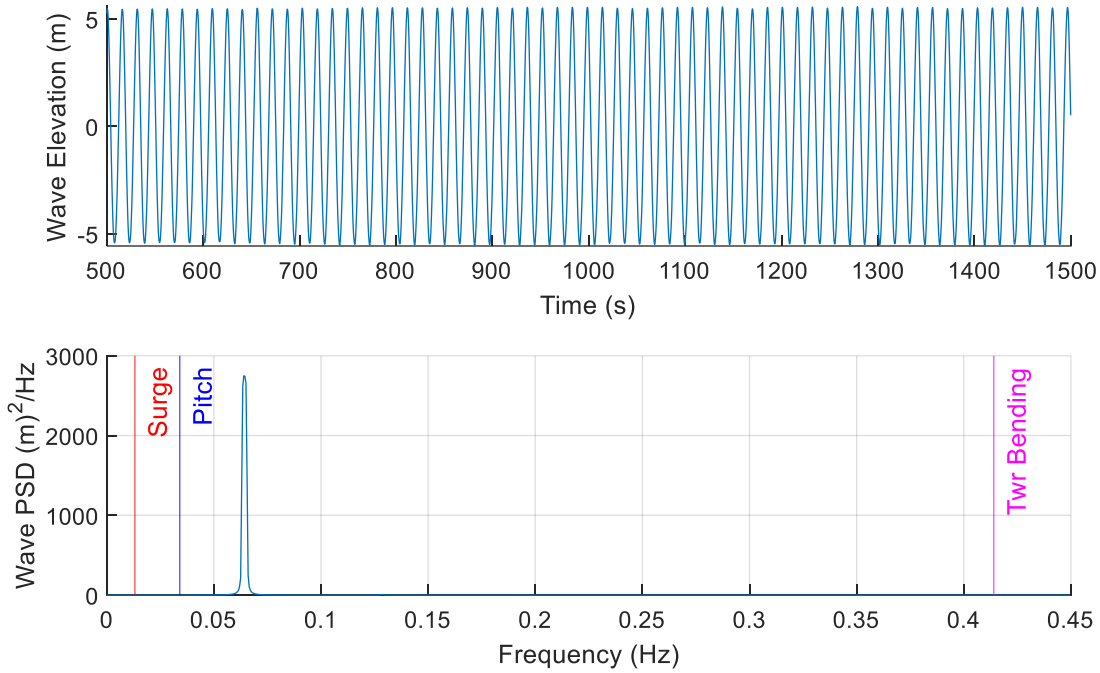


Figure B.7: R5 Time History and Power Spectral Density Plots

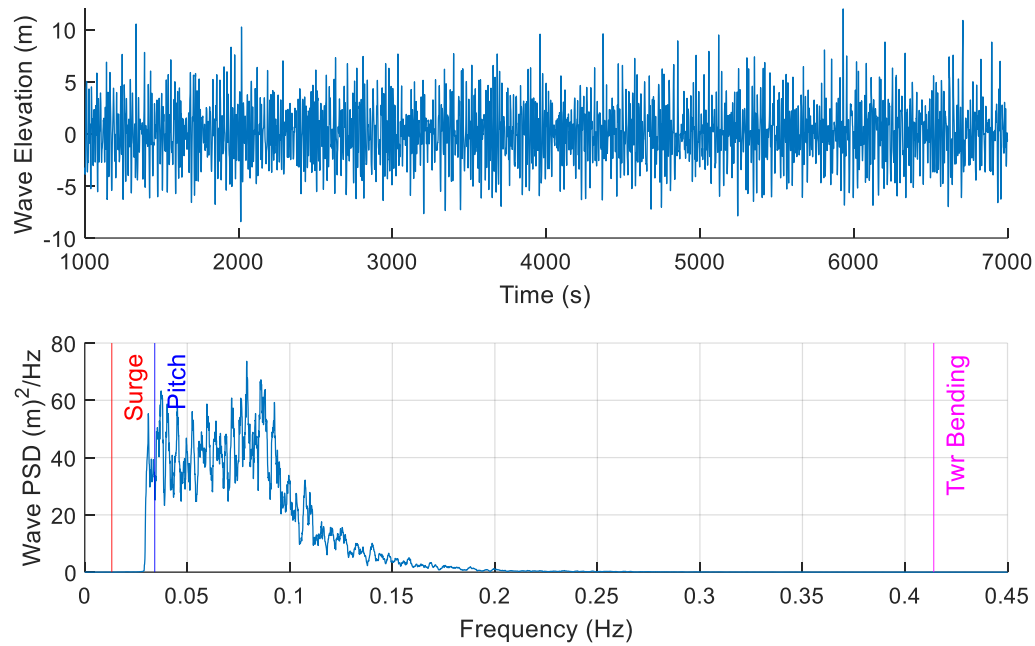


Figure B.8: PN2 Time History and Power Spectral Density Plots

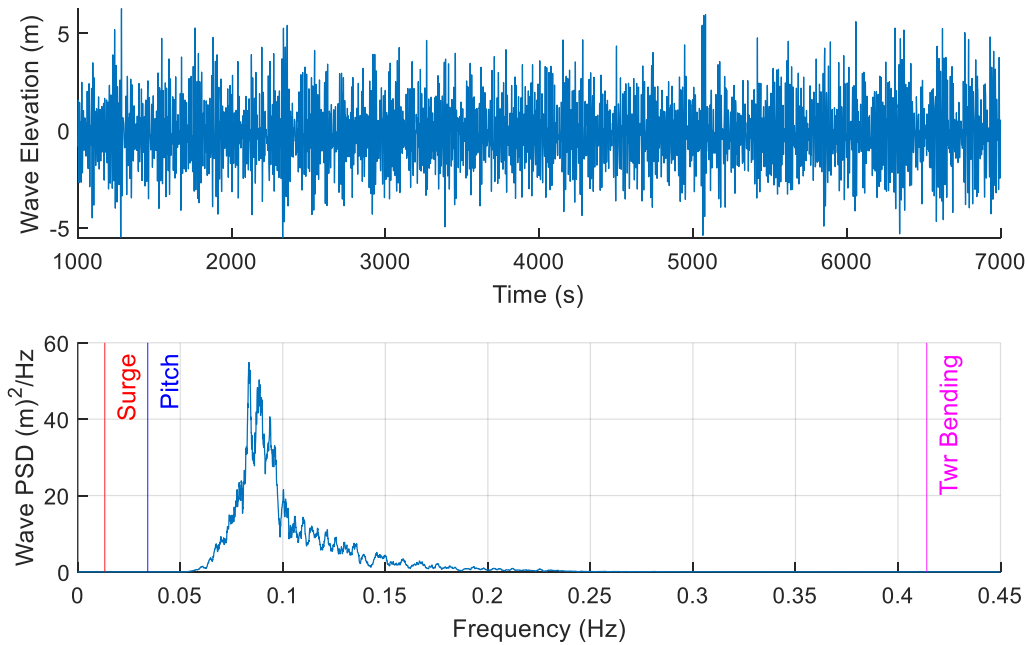


Figure B.9: I2 Time History and Power Spectral Density Plots

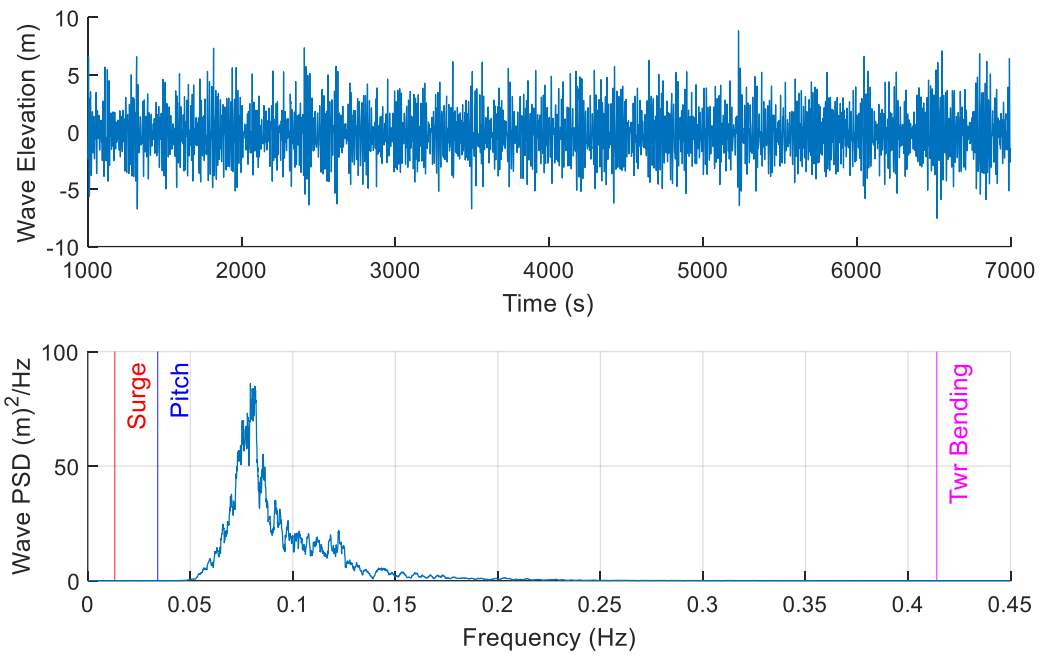


Figure B.10: I3 Time History and Power Spectral Density Plots

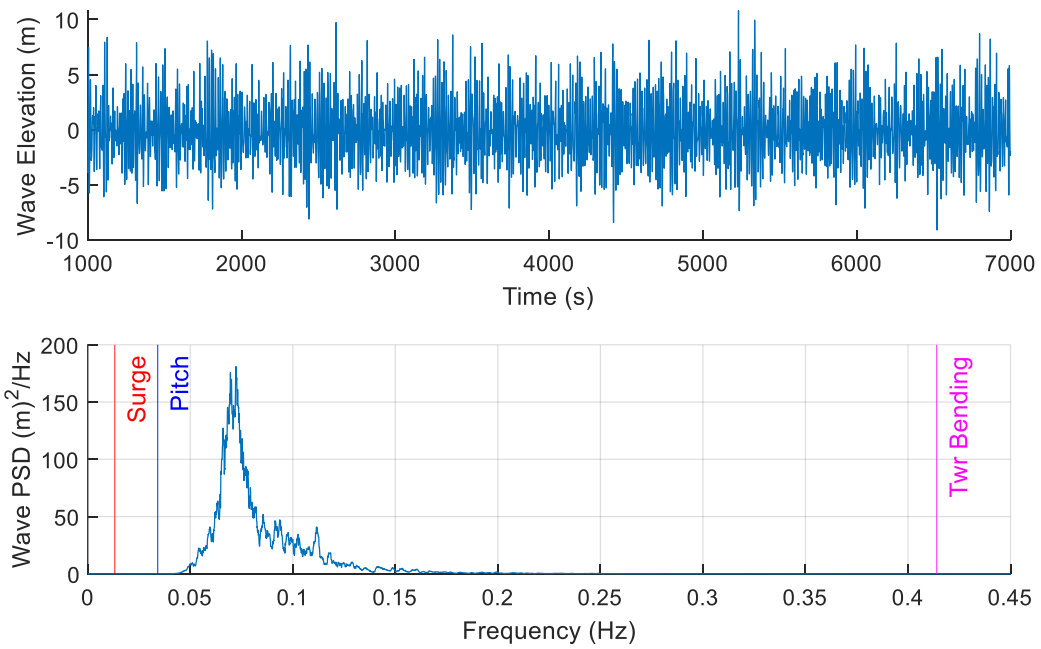


Figure B.11: I4S1 Time History and Power Spectral Density Plots

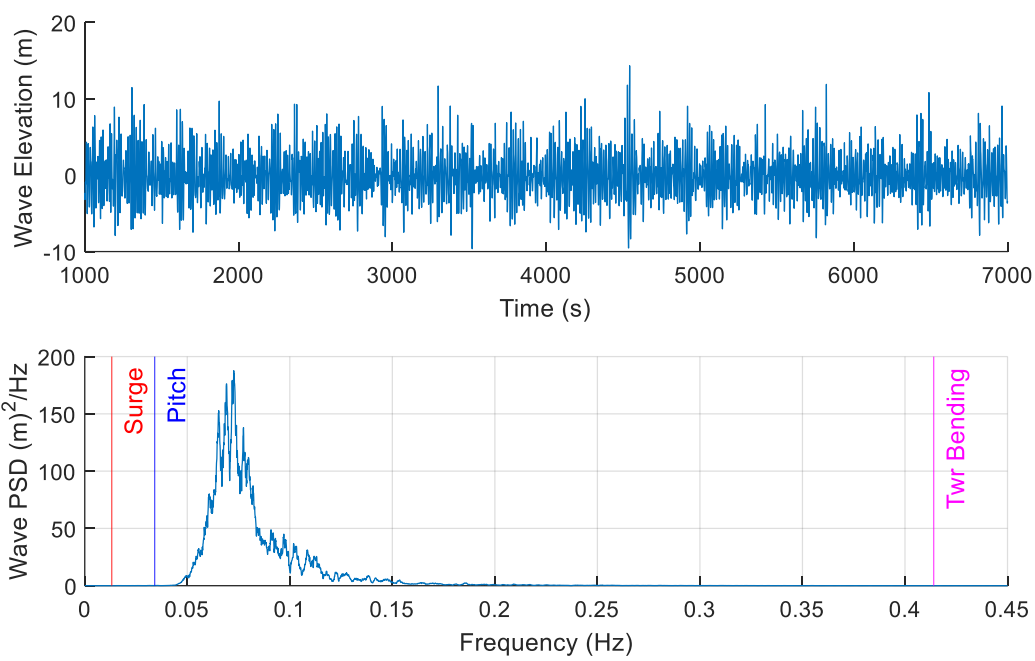


Figure B.12: I4S2 Time History and Power Spectral Density Plots

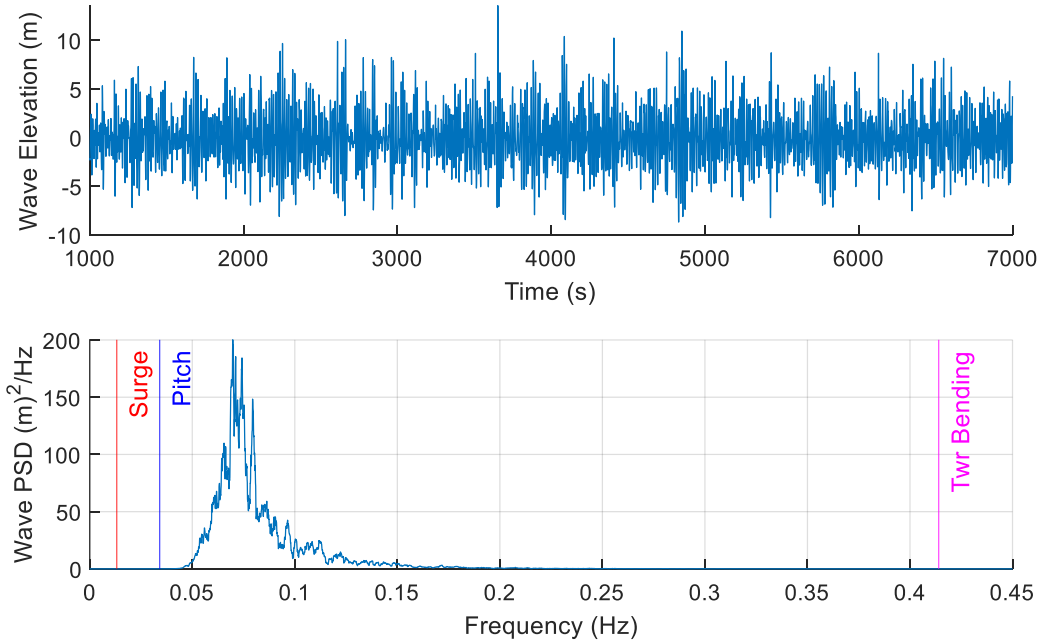


Figure B.13: I4S3 Time History and Power Spectral Density Plots

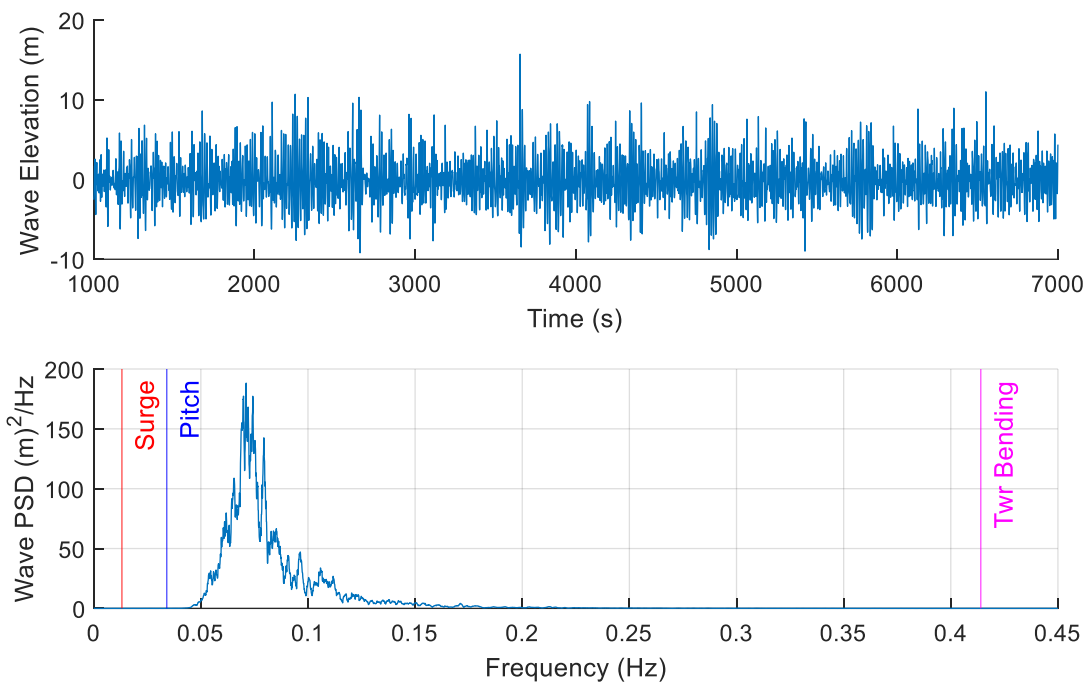


Figure B.14: I4S4 Time History and Power Spectral Density Plots

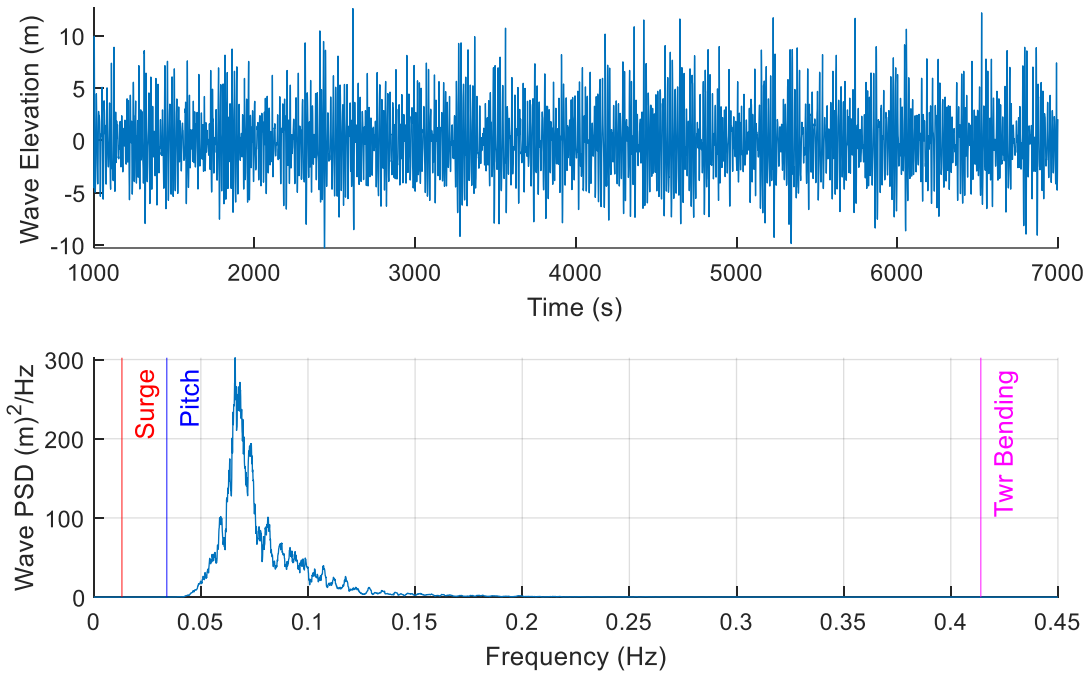


Figure B.15: I5 Time History and Power Spectral Density Plots

APPENDIX C: CAMPAIGN 4 SUPPLEMENTALS

This appendix includes supplemental data relating to Campaign 4 to improve readability of the main text.

Items are referenced directly in the text when possible.

Geometric properties of the floating turbine system, from Section 4.5.

Table C.1: Floating System Geometric Properties

Dimension	Symbol	Reference Figure	Units	Value
Outer Columns Diameter	BCD	Figure C.	m	12.23
Outer Columns Total Height	BCH	Figure C.	m	34.88
Outer Column Center to Center Column Center	BCC	Figure C.	m	51.67
Center Column Diameter	CCD	Figure C.	m	9.85
Center Column Total Height	CCH	Figure C.	m	35.25
Pontoon Leg Width	PLW	Figure C.	m	12.43
Pontoon Leg Height	PLH	Figure C.	m	7.08
Tower Diameter	TD	Figure C.	m	3.57
Tower Height	TH	Figure C.	m	123.55
Keel to Tower Base Flange Bottom	Ztb	Figure C.	m	38.34
Center Column Top to Tower Base Flange Bottom	Hftb	Figure C.	m	3.09
Keel to Fairlead	FLH	Figure C.	m	5.64
Hull Force Gauge Interface to Column Center	RFLEG	Figure C.	m	15.05
Hull Force Gauge CL to Keel	HFLEG	Figure C.	m	3.51
Tower Base Force Gauge Interface to Keel	HFTB	Figure C.	m	37.88
Tower Base Accelerometer to Keel	AccTBz	Figure C.	m	37.18
Nacelle Base Accelerometer to Keel	AccNBz	Figure C.	m	165.23
TMD Mass CG Nominal Position to Keel	RCz	Figure C.	m	12.97
TMD Mass CG Radial Distance to Center Column	RCx	Figure C.	m	51.67
Hub Height to Keel	HH	Figure C.	m	169.74
Rotor Diameter	RD	Figure C.	m	242.8
Hub Diameter	HD	Figure C.	m	11.08
Overhang ¹	OH	Figure C.	m	10.86
Shaft Tilt	ST	Figure C.	deg	6
Coning Angle ²	-	-	deg	0
Tower to Shaft ³	TTS	Figure C.	m	6.715

¹ Overhang = horizontal distance from yaw axis to rotor apex

² Note: Model blades are rigid, coning is 0° to account for reduced blade deflection during testing.

³ Twr2Shft = vertical distance from top of tower-top flange to the rotor shaft

The coordinate systems referenced in Table C. are shown in Figure C. to Figure C..

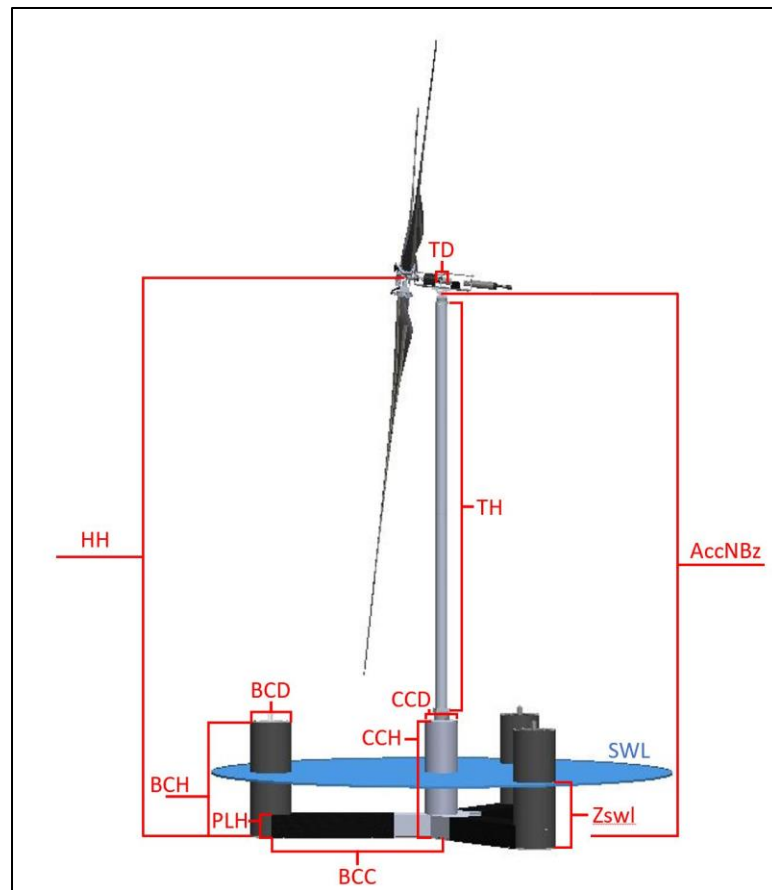


Figure C.1: System Geometry Definitions

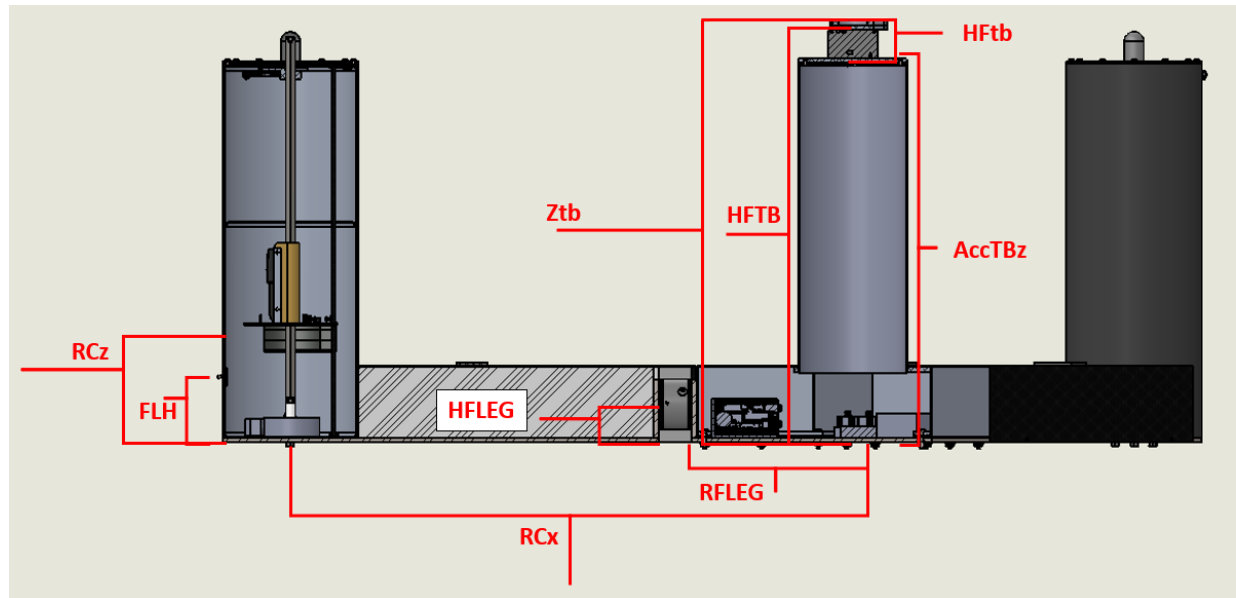


Figure C.2: Hull Geometry Definitions- Side View



Figure C.3: Hull Geometry Definitions- Top View

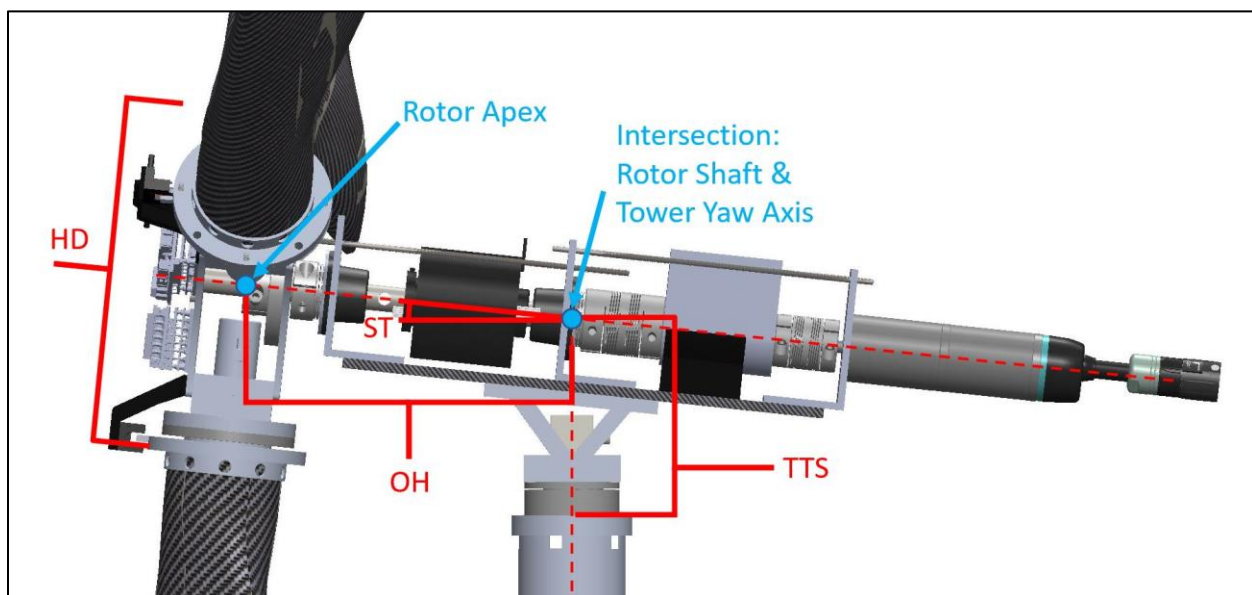


Figure C.4: System Geometry Definitions- RNA Detail

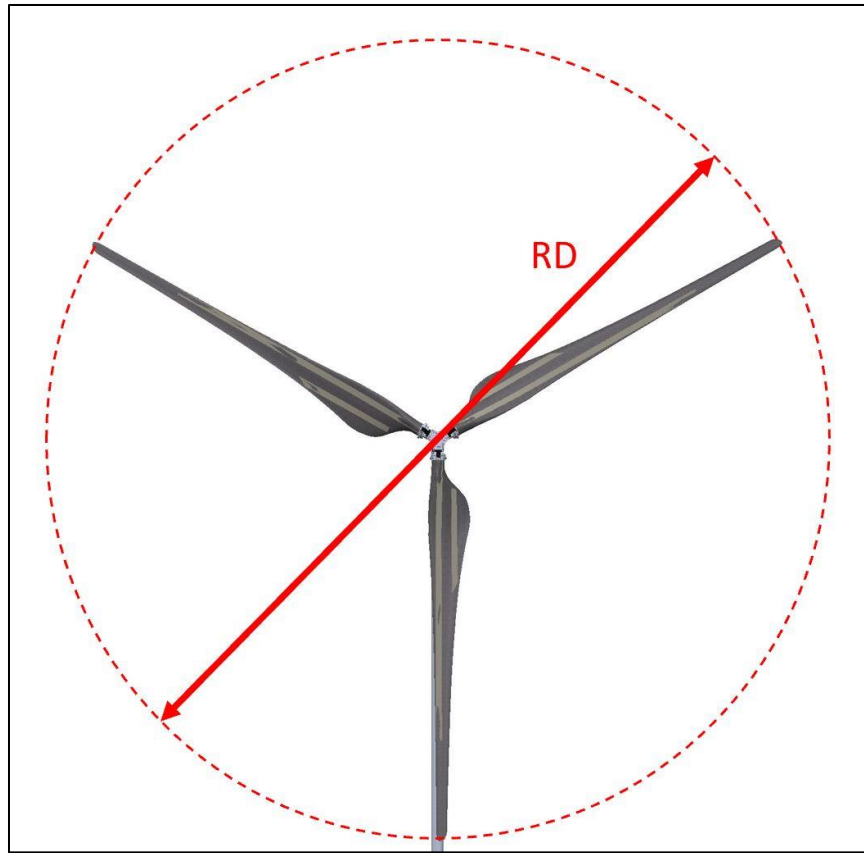


Figure C.5: System Geometry Definitions- Front View

Table C.2: Umbilical Mass Properties

Property	Units	Value
Mass	kg	240,100
CG z distance from keel	m	-7.60
CG x-offset	m	28.00
CG y-offset	m	0

BIOGRAPHY OF THE AUTHOR

Matthew Fowler was born in Presque Isle, Maine on June 13, 1987. He enjoyed growing up in northern Maine and attended the University of Maine to obtain his Bachelor of Science degree in Mechanical Engineering in 2009. He then worked in Groton, CT at General Dynamics Electric Boat performing structural analysis on nuclear-powered submarines before returning to the University of Maine to pursue a graduate degree focusing on floating offshore wind technology and renewable energy. He obtained his Master of Science degree in Mechanical Engineering in 2014 and his Master of Business Administration from the Maine Business School in 2018. He is currently employed as the Scale Model Testing Manager for the Alfond Wind/Wave Ocean Engineering Laboratory at the University of Maine's Advanced Structures and Composites Center. Matthew is a candidate for the Doctor of Philosophy degree in Mechanical Engineering from the University of Maine in December 2023.